

Abstract

Title of Dissertation: A Coupled CFD/CSD Investigation of the
Effects of Leading Edge Slat on Rotor Performance

Asitav Mishra, Doctor of Philosophy, 2012

Dissertation directed by: Associate Professor James D. Baeder
Department of Aerospace Engineering

A coupled Computational Fluid Dynamic (CFD) and Computational Structural Dynamics (CSD) methodology is extended to analyze the effectiveness of a leading edge slat (LE-Slat) for mitigating the adverse effects of dynamic stall on rotor blade aerodynamic and dynamic response. This involved the following improvements over the existing CFD methodology to handle a multi-element airfoil rotor: incorporating the so-called Implicit Hole Cutting method for inter-mesh connectivity, implementing a generalized force transfer routine for transferring LE-Slat loads onto the main blade, and achieving increased parallelization of the code.

Initially, the structured overset mesh CFD solver is extensively validated against available 2-D experimental wind tunnel test cases in steady and unsteady flight conditions. The solver predicts the measurements with sufficient accuracy for test cases with both the baseline airfoil and that with two slat configurations, S-1 and S-6. As expected, the addition of the slat is found to be highly effective

in delaying stall until larger angles for the case of a static airfoil and ameliorating the effects of dynamic stall for a 2-D pitching airfoil. The 3-D coupled CFD/CSD model is extensively validated against flight test data of a UH-60A rotor in a high-altitude, high-thrust flight condition, namely C9017, characterized by distinct dynamic stall events in the retreating side of the rotor disk.

The validated rotor analysis tool is then used to successfully demonstrate the effectiveness of a LE-Slat in mitigating (or eliminating) dynamic stall on the rotor retreating side. The calculations are performed with a modified UH-60A blade with a 40%-span slatted airfoil section. The addition of the slat is effective in the mitigation (and/or elimination) of lift and moment stall at outboard stations, which in turn is accompanied by a reduction of torsional structural loads (upto 73%) and pitch link loads (upto 62%) as compared to the baseline C9017 values.

The effect of a dynamically moving slat, actuating between slat positions S-1 and S-6, is thoroughly investigated, firstly on 2-D airfoil dynamic stall, and then on the UH-60A rotor. Three slat actuation strategies with upto $[1, 3, 5]/rev$ harmonics, respectively, are considered. However, it is noted that the dynamic slat does not necessarily result in better rotor performance as compared to a static slat configuration.

The coupled CFD/CSD platform is further used to successfully demonstrate the capability of the slat (S-6) to achieve upto 10% higher thrust than C9017, which is beyond the conventional thrust limit imposed by McHugh's stall boundary. Stall mitigation due to the slat results in a reduction of torsional load upto 54% and reduction of pitch link load upto 32% as compared to the baseline C9017 flight test values, even for an increase in thrust of 10%.

A Coupled CFD/CSD Investigation of the Effects of Leading Edge Slat on Rotor Performance

by

Asitav Mishra

Dissertation submitted to the Faculty of the Graduate School of the
University of Maryland at College Park in partial fulfillment
of the requirements for the degree of
Doctor of Philosophy
2012

Advisory Committee:

Associate Professor James D. Baeder, Chairman/Advisor
Dr. Inderjit Chopra
Dr. Kenneth Yu
Dr. Anya Jones
Dr. Ramani Duraiswami, Dean's Representative

© Copyright by

Asitav Mishra

2012

Dedication

To the two greatest people I know, my kind and loving parents.

Acknowledgements

I would like to express my sincere gratitude to my thesis advisor, Dr. James D. Baeder, for his unfathomable patience, remarkable kindness and committed dedication to see me through my doctoral work. While being always very lenient on me, his timely guidance and advice surely helped me overcome many hurdles I faced during the research work. I was lucky to have him as a guide who gives his students a lot of freedom during the course of their research and also instils in them a sense of inquisitiveness towards engineering problems.

I would also like to thank Dr. Inderjit Chopra for providing his useful comments and suggestions on my dissertation. In that regard I also appreciate the other committee members, Dr. Kenneth Yu, Dr. Ramani Duraiswami and Dr. Anya R. Jones for their useful comments on my thesis.

This dissertation was possible due to significant interactions I had with UTRC and other helicopter industry personnels. I sincerely thank Dr. Brian Wake and Dr. Peter Lorber for providing me with required data for the work, their timely suggestions and guidance during the course of my PhD.

I sincerely thank Jaina (Dr. Jayanarayanan Sitaraman) for initiating me on the PhD work. His guidance during the initial phase of my research through his insightful suggestions were really helpful in getting me started off with the work. I would also like to thank Karthik (Dr. Karthik Duraisami) for guiding me on various aspects of research. I have a great sense of appreciation for the help Shreyas (Dr. Shreyas Ananthan) offered throughout my doctoral work (from working for papers to fixing bugs in the code). I really appreciate his continued help and suggestions even after leaving our CFD lab. I would also like to thank

Anubhav (Dr. Anubhav Datta) for providing me with timely help and guidance at various stages of my research.

My graduate life at UMD could not have been fun without the presence of friends such as Vinod, Arun (my friends from undergrad days) and Vik. Their company in both the academic as well as non-academic aspects of my graduate life made it very enjoyable. I also appreciate other colleagues, Abhishek, Monica, Ria, Shivaji, Brandon and Ben Silbaugh for their support and company during the PhD work.

I have my heartfelt appreciation for my roommates and close friends, Mehul, Bhaskar and Vamshi, for being very supportive throughout. I should also appreciate the other Grad Hills friends, Ajuer, Kanika, Priya, Kota, Moble, and my music buddies, Aminul and Adil, for their enjoyable company.

I am very grateful to my close friend Ravi for always being there. His objective outlook towards all sorts of problems in life has helped me at various stages of difficulties during my graduate life. I would also like to thank my long time friends Ambi and Aneesh for their cheerful presence and immense support all along.

Finally, I could not acknowledge enough the extent of sacrifice and dedication my parents have shown for my education and for my PhD. I deeply appreciate their continued support and patience throughout the doctoral studies. I have dedicated this thesis work to them. At this point I would also like to mention my brothers, Ajitabh, Amitav and my sister Aparna, for their unconditional love and support all through out my academic life, from undergraduate through graduate days.

Table of Contents

List of Tables	ix
List of Figures	x
Nomenclature	xxiii
1 Introduction	1
1.1 Flight Envelope	2
1.2 Dynamic Stall in Helicopters	2
1.3 High Lift Concepts	4
1.3.1 High-lift Airloads	7
1.3.2 Multi-element Flow Physics	9
1.4 Previous Work	13
1.4.1 Fundamental Understanding of Dynamic Stall	14
1.4.2 Three Dimensional Dynamic Stall: Wings and Rotors	15
1.5 Stall Alleviation Techniques	16
1.5.1 Innovative Airfoil Design	16
1.5.2 Passive Control Techniques	17
1.5.3 Active Control Methods	18

1.6	Motivation	24
1.7	Objective	25
1.8	Contribution of Thesis	28
1.9	Scope and Organization of the Thesis	29
2	Methodology	31
2.1	Fluid Flow Modeling	31
2.1.1	Navier-Stokes Equations	32
2.1.2	Reynolds Averaged Navier-Stokes Equations	39
2.1.3	Initial and Boundary Conditions	41
2.1.4	Numerical Algorithm	42
2.1.5	Mesh Generation	49
2.1.6	Overset Mesh and Grid Connectivity	50
2.1.7	Aeroelastic Deformation of a Multi-element Rotor Blade	53
2.2	Structural Dynamics and Vehicle Trim	56
2.2.1	Comprehensive Rotor Analysis	56
2.2.2	Finite element discretization of the rotor blade	57
2.2.3	Vehicle Trim	58
2.2.4	Uncoupled and Coupled Trim Procedure	59
2.3	Coupling Structural Dynamics and Fluid Dynamics	60
2.4	Limitations of Current Methodology	62
2.5	Technical Challenges and Improvements	64
2.5.1	Implicit Hole Cutting	64
2.5.2	Slat Actuation	67
2.5.3	Multi-element Mesh Deformation	68
2.5.4	Force Calculations on a Multi-Element Rotor Blade	68

2.6	Summary	71
3	Validation	74
3.1	Steady State Airfoil: SC2110 with S-1 and S-6	75
3.1.1	Flow Physics: Presence of Leading Edge Vortex	80
3.1.2	Boundary Layer Profile: Effect of Slat	88
3.1.3	Limitations of CFD Prediction: Turbulence Transition?	91
3.2	Pitching Airfoil: SC2110 with S-1 and S-6	94
3.2.1	Pitching Amplitude 10°: Baseline Airfoil SC2110	95
3.2.2	Pitching Amplitude 10°: Slatted Airfoil	97
3.2.3	Pitching Amplitude 20°: Baseline and Slatted Airfoil	104
3.3	Unsteady Rotor: UH-60A Flight Test C9017	108
3.3.1	Quantitative Validation: Airloads	109
3.3.2	Grid Convergence Study	116
3.3.3	Qualitative Verification: Streamlines and Vorticity Contours	118
3.3.4	More Quantitative Validation	120
3.4	Summary	129
4	Rotor Performance Improvement using LE Slats	131
4.1	Effect of Thrust Setting on Dynamic Stall	132
4.2	Analysis of UH-60A with Slat	139
4.2.1	Modified UH-60A Rotor Blade with Slat	140
4.2.2	2-D Dynamic Slat Actuation	142
4.2.3	Effectiveness of Slat on Dynamic Stall Mitigation	145
4.2.4	Performance Improvement due to Slat	159
4.3	Dynamic Slat Strategies	160

4.3.1	Phase Offset of Dynamic Slat Actuation on SC2110 Airfoil	160
4.3.2	Higher Harmonic Slat Actuation on SC2110 Airfoil	164
4.3.3	Higher Harmonic Slat Actuation on Modified UH-60A Rotor	166
4.4	Effectiveness of Slat on Achieving Higher Thrust	170
4.4.1	Quantifying Stall at Higher Thrust settings: Pitch Link Load and Root Torsional Moment	177
4.5	Performance Prediction for Slatted Rotor	179
5	Conclusion	181
5.1	Summary	182
5.2	Observations and Conclusions	183
5.2.1	Methodology	183
5.2.2	Validation of CFD Solver	184
5.2.3	Rotor Performance Improvement using LE Slats	186
5.3	Significance of the Work	188
5.4	Recommendations and Future Work	189
5.4.1	Future Work	190
A	LE-Slat versus Other High-lift Devices: A Numerical Investiga- tion	192
B	Numerical Studies of the Unsteady Effects in a Pitching Airfoil	200
B.1	Effect of Varying Mean Pitching Angle	200
B.2	Quasi-steady Versus Dynamic Slat Actuation	202
B.3	Unsteady Effect of Slat Actuation	202
	Bibliography	206

List of Tables

1.1	Comparison of Active Control Devices	22
3.1	Final trim control angles and the predicted rotor power for the baseline using the free-flight and wind-tunnel trim algorithms . .	115
3.2	Final trim control angles and the predicted rotor power for the baseline for different grid sizes	118
4.1	CFD Predicted Trim Control Angles and Power for Three Thrust Cases	138
4.2	Final trim control angles and the predicted rotor power for the baseline and the modified UH-60A rotor geometries without the slat.	142
4.3	Comparison of the final trimmed control pitch settings and the net rotor power for the modified UH-60A configurations and the baseline UH-60A rotor.	154
4.4	Comparison of the final trimmed control pitch settings and the net rotor power for different slat actuations.	170
4.5	Comparison of the final trimmed control pitch settings and the net rotor power of higher thrust settings with the baseline thrust.	177

List of Figures

1.1	Thrust limit on a UH-60A rotor [1]	3
1.2	Stages of Dynamic Stall [2]	5
1.3	High-lift concepts. Courtesy NASA	6
1.4	Clark Y wing with 21.1% chord split flap and 30% chord Maxwell slat [7]	7
1.5	Airloads on Clark Y wing with split flap and Maxwell slat [7] . . .	8
1.6	Lift contribution of flap and slat to total lift of an MEA airfoil. [5]	10
1.7	Inviscid Effects of Gap	11
1.8	Viscous Effects of Gap	11
1.9	Process of formation of CBL in a typical multi-element airfoil [6].	13
1.10	Innovative Airfoil and passive Blade Design	17
1.11	S-1 and S-6 slat configurations with respect to the baseline air- foil [55].	23
1.12	Elastomeric bearing concept for slat actuation [53].	27
2.1	Schematic showing computational cell.	43
2.2	C-O mesh on UH-60A blade	51
2.3	Cylindrical rotor wake mesh.	52
2.4	Conventional overset mesh	54

2.5	Loose Coupling Flow Chart	63
2.6	Overset meshes in 2-D and 3-D using Implicit Hole-Cutting	66
2.7	Slat deformation	69
2.8	Slat Force Transfer to Main Element on (a)2D Airfoil and (b)Rotor	72
2.9	Flow Chart describing force transfer for Multi-element Rotor . . .	73
3.1	S-1 and S-6 slat configurations with respect to the baseline air- foil [55].	76
3.2	SC2110 airfoil computational mesh with and without the slat mesh embedded in the background wind-tunnel mesh at an angle of attack $\alpha = 18^\circ$	77
3.3	Effect of wind tunnel wall correction on lift and pitching moment coefficients of the main airfoil section, $Re = 4.14 \times 10^6$, $M_\infty = 0.3$.	77
3.4	Steady airload validation on baseline airfoil and baseline with S-1 and S-6 slat configurations for $Re = 4.14 \times 10^6$, $M_\infty = 0.3$	79
3.5	Variation of the non-dimensional pressure coefficient over the air- foil surface with and without the slat, $Re = 4.14 \times 10^6$, $M_\infty =$ 0.3 , $\alpha = 10^\circ$	80
3.6	Skin friction coefficient (C_f) over the airfoil surface with and with- out the slat, $Re = 4.14 \times 10^6$, $M_\infty = 0.3$, $\alpha = 10^\circ$	81
3.7	Variation of the non-dimensional pressure coefficient over the air- foil surface with and without the slat, $Re = 4.14 \times 10^6$, $M_\infty =$ 0.3 , $\alpha = 15^\circ$	82
3.8	Streamlines with pressure contours; $Re = 4.14 \times 10^6$, $M_\infty =$ 0.3 , $\alpha = 15^\circ$	83

3.9	Streamlines with pressure contours on slats; $Re = 4.14 \times 10^6, M_\infty = 0.3, \alpha = 15^\circ$	84
3.10	Skin friction coefficient (C_f) over the airfoil surface with and without the slat, $Re = 4.14 \times 10^6, M_\infty = 0.3, \alpha = 15^\circ$	85
3.11	Variation of the non-dimensional pressure coefficient over the airfoil surface with and without the slat, $Re = 4.14 \times 10^6, M_\infty = 0.3, \alpha = 18^\circ$	86
3.12	Streamlines with pressure contours; $Re = 4.14 \times 10^6, M_\infty = 0.3, \alpha = 18^\circ$	87
3.13	Streamlines with pressure contours on slats; $Re = 4.14 \times 10^6, M_\infty = 0.3, \alpha = 18^\circ$	88
3.14	Skin friction coefficient (C_f) over the airfoil surface with and without the slat, $Re = 4.14 \times 10^6, M_\infty = 0.3, \alpha = 18^\circ$	89
3.15	Comparing BL profile on baseline airfoil and that with slat S-6, $Re = 4.14 \times 10^6, M_\infty = 0.3, \alpha = 10^\circ$ and 18°	90
3.16	Cl/Cd for baseline and S-6	91
3.17	Effect of transition fix on slatted S-6 airfoil; $Re = 4.14 \times 10^6, M_\infty = 0.3$	92
3.18	Skin friction with fully turbulent and with laminar-turbulent transition fixed flow on slatted S6 airfoil at $\alpha = 15^\circ$	92
3.19	Comparing airload predictions from fully turbulent and laminar-turbulent transition fixed flow on slatted S6 airfoil	94
3.20	Periodic variation of the non-dimensional lift and pitching moment coefficients as a function of angle of attack for the baseline 2-D airfoil element, $M_\infty = 0.3, k = 0.07, \alpha = 15^\circ - 5^\circ \cos(\omega t)$. . .	96

3.21	Streamlines on baseline SC2110 airfoil near stall region: Dynamic Stall.	98
3.22	Surface pressure on baseline SC2110 airfoil near stall region [53]. . .	99
3.23	Periodic variation of the non-dimensional lift, pitching moment and drag coefficients as a function of angle of attack for the multi-element airfoil with the slat at S-6 configuration, $M_\infty = 0.3$, $k = 0.07$, $\alpha = 15^\circ - 5^\circ \cos(\omega t)$ [53].	100
3.24	Periodic variation of the non-dimensional lift and pitching moment coefficients as a function of angle of attack for the multi-element airfoil with the slat at S-1 configuration, $M_\infty = 0.3$, $k = 0.07$, $\alpha = 15^\circ - 5^\circ \cos(\omega t)$ [53].	101
3.25	Streamlines on Slat-S6 SC2110 airfoil at high angles: mitigation of dynamic stall.	102
3.26	Surface pressure on Slat-S6 SC2110 airfoil at high angles [53]. . .	103
3.27	Periodic variation of the non-dimensional lift and pitching moment coefficients as a function of angle of attack for the baseline airfoil section, $M_\infty = 0.4$, $k = 0.07$, $\alpha = 10^\circ - 10^\circ \cos(\omega t)$ [53]. . .	104
3.28	Periodic variation of the non-dimensional lift and pitching moment coefficients as a function of angle of attack for the multi-element airfoil with the slat at S-1 configuration, $M_\infty = 0.4$, $k = 0.07$, $\alpha = 10^\circ - 10^\circ \cos(\omega t)$	105
3.29	Periodic variation of the non-dimensional lift and pitching moment coefficients as a function of angle of attack for the multi-element airfoil with the slat at S-6 configuration, $M_\infty = 0.4$, $k = 0.07$, $\alpha = 10^\circ - 10^\circ \cos(\omega t)$	106

3.30	Mach contours on baseline and slatted airfoils at upstroke $\alpha = 14.1^\circ$ during pitching cycle; $M_\infty = 0.4$, $k = 0.07$, $\alpha = 10^\circ - 10^\circ \cos(\omega t)$	107
3.31	Mach contours on baseline and slatted airfoils at upstroke $\alpha = 20^\circ$ during pitching cycle; $M_\infty = 0.4$, $k = 0.07$, $\alpha = 10^\circ - 10^\circ \cos(\omega t)$	107
3.32	McHugh Lift Boundary [88]	109
3.33	Overset mesh system used in the simulation of the UH-60A rotor in forward flight showing the body-fitted blade meshes embedded within a cylindrical background mesh.	110
3.34	UH-60A flight test data stations [91].	111
3.35	Time histories of the non-dimensional sectional normal forces at different radial stations along the span for the baseline UH-60A rotor in C9017 flight condition. Black dot: Flight test data, Blue solid: CFD-CSD with shaft-fixed trim, Red dash: CFD-CSD with free-flight trim.	111
3.36	Time histories of the non-dimensional sectional pitching moment coefficients (means removed) at different radial stations along the span for the baseline UH-60A rotor in C9017 flight condition. Black dot: Flight test data, Blue solid: CFD-CSD with shaft-fixed trim, Red dash: CFD-CSD with free-flight trim.	112

3.37	Time histories of sectional pitching moment coefficients (means removed) at three outboard radial stations for the baseline UH-60A rotor in C9017 flight condition taken from previous CFD-CSD work by Sitaraman et. al. [90]. Black solid : Flight test data, Blue solid: CFD-CSD with shaft-fixed trim, Red dash-dot: previous CFD-CSD with shaft-fixed trim.	113
3.38	Comparison of the predicted pitching moment variation across the rotor disk with flight test data for baseline UH-60A rotor.	113
3.39	Lift stall (LS) and Moment stall (MS) map on the UH-60A rotor.	114
3.40	Time histories of the non-dimensional sectional normal forces at different radial stations along the span for the baseline UH-60A rotor in C9017 flight condition. Black dot: Flight test data, Blue solid: Grid size $133 \times 130 \times 61$, Green dash: Grid size $133 \times 197 \times 61$, Red dash-dot: Grid size $133 \times 259 \times 61$, Cyan dots: Grid size $199 \times 130 \times 61$	116
3.41	Time histories of the non-dimensional sectional pitching moment coefficients (means removed) at different radial stations along the span for the baseline UH-60A rotor in C9017 flight condition. Black dot: Flight test data, Blue solid: Grid size $133 \times 130 \times 61$, Green dash: Grid size $133 \times 197 \times 61$, Red dash-dot: Grid size $133 \times 259 \times 61$, Cyan dots: Grid size $199 \times 130 \times 61$	117
3.42	Streamlines (undeformed frame) at $r/R = 80\%$ station near <i>first</i> lift stall event for the baseline UH-60A rotor in C9017 flight condition.	119

3.43	Streamlines (undeformed frame) at $r/R = 93\%$ station near <i>second</i> lift stall event for the baseline UH-60A rotor in C9017 flight condition.	119
3.44	Dynamic stall vortex on UH-60A blade at azimuth, $\psi = 270^\circ$. . .	120
3.45	Surface pressure coefficient at different radial stations near <i>first</i> lift stall event for the baseline UH-60A rotor in C9017 flight condition. Black dot: Flight test data, Blue solid: CFD-CSD with shaft-fixed trim.	122
3.46	Surface pressure coefficient at different radial stations near <i>second</i> lift stall event for the baseline UH-60A rotor in C9017 flight condition. Black dot: Flight test data, Blue solid: CFD-CSD with shaft-fixed trim.	123
3.47	Surface pressure coefficient at different radial stations on advancing side of baseline UH-60A rotor in C9017 flight condition. Black dot: Flight test data, Blue solid: CFD-CSD with shaft-fixed trim.	124
3.48	Comparison of CFD/CSD predicted sectional torsional moments with C9017 flight test data.	126
3.49	Comparison of CFD/CSD predicted amplitudes of harmonics of sectional torsional moments with C9017 flight test data.	127
3.50	Comparison of CFD/CSD predicted pitch link load with C9017 flight test data.	128
4.1	Variation of UMARC linearized aerodynamic airloads with thrust. $C_T/\sigma = 0.1325$; $C_T/\sigma = 0.1258$; $C_T/\sigma = 0.1190$	133
4.2	Variation of CFD normal loads with thrust. Blue solid: $C_T/\sigma = 0.1325$; Green dash: $C_T/\sigma = 0.1258$; Red dash-dot: $C_T/\sigma = 0.1190$	134

4.3	Variation of CFD pitching moments with thrust. Blue solid: $C_T/\sigma = 0.1325$; Green dash: $C_T/\sigma = 0.1258$; Red dash-dot: $C_T/\sigma = 0.1190$	134
4.4	Variation of CFD chord wise forces with thrust. Blue solid: $C_T/\sigma = 0.1325$; Green dash: $C_T/\sigma = 0.1258$; Red dash-dot: $C_T/\sigma = 0.1190$	135
4.5	Sectional 4 – 17/rev torsional moments at $r/R = 22.5\%$: effect of thrust on stall; Blue solid: $C_T/\sigma = 0.1325$; Green dash: $C_T/\sigma = 0.1258$; Red dash-dot: $C_T/\sigma = 0.119$	136
4.6	Pitch link loads: effect of thrust on stall; Blue solid: $C_T/\sigma = 0.1325$; Green dash: $C_T/\sigma = 0.1258$; Red dash-dot: $C_T/\sigma = 0.119$	137
4.7	CFD predicted 4/rev Hub loads; $C_T/\sigma = 0.1325$; $C_T/\sigma = 0.1258$; $C_T/\sigma = 0.119$	138
4.8	Variation of CFD vibratory normal loads (3–20/rev) with thrust. Blue solid: $C_T/\sigma = 0.1325$; Green dash: $C_T/\sigma = 0.1258$; Red dash-dot: $C_T/\sigma = 0.119$	139
4.9	Modified UH60 Blade with Slat S-6	140
4.10	Predicted and measured sectional normal loads for C9017. Black dot: Flight Test Data; Blue solid: CFD UH60A Blade; Red dash: CFD UH60A-mod Blade.	141
4.11	Predicted and measured sectional moment loads for C9017. Black dot: Flight Test Data; Blue solid: CFD UH60A Blade; Red dash: CFD UH60A-mod Blade.	142
4.12	Time history of slat angle over one cycle ($-\Delta\theta_s$ versus ψ) due to 1/rev slat actuations	143
4.13	Airload comparisons for static and dynamic slat cases	144

4.14	Slat S-6 Geometry	145
4.15	Computational time speed up for Np processors with respect to the corresponding minimum number of processors ($Np0$) used for baseline as well as slatted (S-6) rotors	147
4.16	Schematic of slat actuation over a rotor revolution with appropriate phase offset.	148
4.17	Time history of CFD normal loads with dynamic slat. Blue solid: no slat; Green dash: steady slat S-6; Red dash dot: steady slat S-1; Black dot: dynamic slat.	149
4.18	Time history of CFD pitching moments with dynamic slat. Blue solid: no slat; Green dash: steady slat S-6; Red dash dot: steady slat S-1; Black dot: dynamic slat.	150
4.19	Time history of CFD chord wise forces with dynamic slat. Blue solid: no slat; Green dash: steady slat S-6; Red dash dot: steady slat S-1; Black dot: dynamic slat.	151
4.20	Comparison of the pitching moment variation across the rotor disk for the static and dynamic slat analyses with the baseline no-slat rotor.	152
4.21	Time history of CFD vibratory normal loads ($3 - 20/rev$) with dynamic slat. Blue solid: no slat; Green dash: steady slat S-6; Red dash dot: steady slat S-1; Black dot: dynamic slat.	153
4.22	Variation of the effective geometric angle of attack as a function of azimuth at different radial stations. Blue solid: no slat; Green dash: steady slat S-6; Red dash dot: dynamic slat; Black dot: steady slat S-1.	153

4.23	Streamlines comparisons for baseline and slatted rotor cases at three outboard stations, $r/R = 73\%$, 75% , and 79%	155
4.24	Comparison of Q-criterion iso-surface contours of baseline rotor with that having static S-6 slat.	156
4.25	Mitigation of pressure peaks near leading edge of main blade due to slat S-6 in slat region.	156
4.26	Mitigation of pressure peaks near leading edge of main blade due to slat S-6 outboard of slat.	157
4.27	Comparison of the vibratory torsional loads ($4 - 17/\text{rev}$) and predicted pitch link loads showing the effect of slat on rotor structural loads. Blue solid: no slat; Green dash: steady slat S-6; Red dash dot: dynamic slat. ; Black dash: steady slat S-1	157
4.28	CFD/CSD predicted peak-to-peak vibratory root torsional and pitch link loads for various blade configurations.	158
4.29	CFD predicted $4/\text{rev}$ Hub loads; no slat; Steady Slat S-6; Dynamic Slat	158
4.30	Non-dimensional torque and thrust time history over one rotor revolution.	159
4.31	Time history of change of slat angle with respect to S-1 position over one cycle ($\Delta\theta_s$ versus ψ) due to three different phasing ($\phi = -60^\circ, -90^\circ, -120^\circ$) of slat actuation	161
4.32	Airload comparisons of the three phasing ($\phi = -60^\circ, -90^\circ, -120^\circ$) of slat actuations	162

4.33	Time history of change of slat angle with respect to S-1 over one cycle ($\Delta\theta_s$ versus ψ) due to three (up to 1, 3, 5/rev) slat actuations and build up of the $\Delta\theta_{s5}$ slat actuation	164
4.34	Airload comparisons of the three (up to 1, 3, 5/rev) harmonic dynamic slat actuations	166
4.35	Slat actuation (up to 1, 3, 5/rev) with respect to S-1 position over one rotor revolution ($\Delta\theta_s$ vs ψ)	167
4.36	Time history of CFD normal loads all dynamic slat actuations. Blue solid: no slat; Green dash: 1/rev dynamic slat; Red dash dot: up to 3/rev dynamic slat; Black dot: up to 5/rev dynamic slat.	167
4.37	Time history of CFD pitching moments with dynamic slat actuations. Blue solid: no slat; Green dash: 1/rev dynamic slat; Red dash dot: up to 3/rev dynamic slat; Black dot: up to 5/rev dynamic slat	168
4.38	Comparison of the vibratory torsional loads (4 – 17/rev) and predicted pitch link loads showing the effect of dynamic slat actuations on rotor structural loads. Blue solid: no slat; Green dash: 1/rev dynamic slat; Red dash dot: up to 3/rev dynamic slat; Black dot: up to 5/rev dynamic slat.	169
4.39	CFD/CSD predicted peak-to-peak vibratory root torsional and pitch link loads for various slat actuations.	169
4.40	Variation of predicted normal loads with thrust setting; Blue solid: $Ct/\sigma = 0.1325$ baseline; Green dash: $Ct/\sigma = 0.1391$ with S-6; Red dash dot: $Ct/\sigma = 0.1458$ with S-6	171

4.41	Variation of predicted pitching moment with thrust setting; Blue solid: $C_T/\sigma = 0.1325$ baseline; Green dash: $C_T/\sigma = 0.1391$ with S-6; Red dash dot: $C_T/\sigma = 0.1458$ with S-6	172
4.42	Variation of predicted chordwise force with thrust setting; Blue solid: $C_T/\sigma = 0.1325$ baseline; Green dash: $C_T/\sigma = 0.1391$ with S-6; Red dash dot: $C_T/\sigma = 0.1458$ with S-6	173
4.43	Variation of predicted normal ($3 - 20/rev$) loads with thrust setting; Blue solid: $C_T/\sigma = 0.1325$ baseline; Green dash: $C_T/\sigma = 0.1391$ with S-6; Red dash dot: $C_T/\sigma = 0.1458$ with S-6	174
4.44	Variation of the polar normal load over whole rotor disk with higher thrust values	175
4.45	Comparison of the polar pitching moment (mean removed) load over whole rotor disk of higher thrust settings with the baseline thrust.	176
4.46	Comparison of the vibratory torsional loads ($4 - 17/rev$) and predicted pitch link loads of higher thrust settings with the baseline thrust. Blue solid: $C_T/\sigma = 0.1325$ baseline; Green dash: $C_T/\sigma = 0.1391$ with S-6; Red dash dot: $C_T/\sigma = 0.1458$ with S-6.	178
4.47	Comparing CFD/CSD predicted peak-to-peak vibratory root torsional and pitch link loads of higher thrust settings with the baseline thrust.	178
4.48	Comparing L/D_e for baseline rotor with that having slats S-6 and S-1	180
A.1	Various high lift devices	193

A.2	Comparing airloads on various high lift devices ($M = 0.3, Re = 4.14 \times 10^6$)	194
A.3	C_p on various high lift devices at free stream $M = 0.3, Re = 4.14 \times 10^6$	195
A.4	Boundary layer profile on various high lift devices at $M = 0.3, Re = 4.14 \times 10^6, \alpha_{eff} = 12.0^\circ$	197
A.5	Boundary layer profile on various high lift devices at $M = 0.3, Re = 4.14 \times 10^6, \alpha_{eff} = 18.0^\circ$	197
A.6	Stream lines on various high lift devices at $M = 0.3, Re = 4.14 \times 10^6, \alpha_{eff} = 18.0^\circ$	199
B.1	Effect of varying mean angle of pitching	201
B.2	Comparing airloads of dynamic slat actuation with corresponding quasi-steady run	203
B.3	Comparing mean removed airloads of unsteady slat on static main airfoil at $\alpha = [0^\circ, 10^\circ, 15^\circ]$	204
B.4	Comparing C_p and lift values of unsteady slat on static main airfoil with steady values of the corresponding slat configurations at $\alpha = 15^\circ$	205

Nomenclature

a	Speed of sound, ft s^{-1}
A	Rotor disk area, πR^2 , ft^2
c	Rotor chord, ft
C_D	2-D drag coefficient
Cd_0	Profile drag coefficient
C_L	2-D lift coefficient
C_M	2-D pitching moment coefficient
C_m	Blade pitching moment coefficient
C_n	Blade normal force coefficient
C_p	Pressure coefficient
C_f	Skin friction coefficient
C_T	Rotor thrust coefficient, $T/(\rho A \Omega^2 R^2)$
C_Q	Rotor shaft torque coefficient, $Q/(\rho A \Omega^2 R^3)$
C_P	Rotor power coefficient, $P/(\rho A \Omega^3 R^3)$
k	Reduced frequency, $\omega c/2V$
N_b	Number of blades
r	Radial distance of a rotor spanwise station, ft
R	Rotor radius, ft
Re	Reynolds number, Vc/ν
V	Velocity, ft s^{-1}
u_t	Tangential velocity, ft s^{-1}
U_∞	Freestream velocity, ft s^{-1}
M	Mach number, V/a

M_∞	Freestream Mach number, U_∞/a
α	Sectional angle of attack, deg
α_s	Shaft tilt angle, deg
θ_0	Collective pitch, deg
θ_{1c}, θ_{1s}	Lateral and longitudinal cyclic, deg
μ	Advance ratio, $V_\infty/\Omega R$
ν	Kinematic viscosity, ft^2s^{-1}
ρ	Flow density, slugs ft^{-3}
σ	Rotor solidity, $N_b c/\pi R$
ψ	Azimuth angle, deg
Ω	Rotor rotational speed, rad s^{-1}

Chapter 1

Introduction

Modern rotorcrafts today face many challenges to meet ever-increasing demands from their military and civilian customers. This reflects on increasing requirements for larger payload weight, range, endurance or reduced fuel consumption, as well as better maneuverability and agility, i.e. the ability to sustain larger g-force. These demands translate to an increased thrust requirement besides demanding a larger overall lift-to-drag (L/D) ratio. In addition to the above stated demands, helicopters have contrasting aerodynamic requirements on the advancing and retreating sides. For efficient operation, the advancing side requires thinner blades for lower profile drag (Cd_0), which is strongly influenced by transonic/compressible effects. But, to balance the lift on the advancing side the retreating side requires thicker blades which would allow larger sectional lift (Cl_{max}) values; but these values are limited by stall phenomena. The following sections further discuss how these contrasting aerodynamic needs limit the rotor flight envelope.

1.1 Flight Envelope

In general for a helicopter at a nominal forward flight speed the need for a larger thrust requires an increase in rotor collective (θ_0). To balance out the advancing side lift, the local angle of attack (α) on the retreating side blade section becomes higher. Increasingly higher α ultimately leads to stall. This has several consequences: a) the local lift no longer increases, b) the local drag increases greatly, and c) the local nose-down pitching moment penalty becomes larger which generates larger blade section torsional loads. The moment also gets transmitted to the pitch-link which leads to blade pitch link load fatigue and eventually failure. These aerodynamic and structural phenomena ultimately contribute to various forms of flight envelope limits, e.g. thrust limit (due to loss of lift), torsional limit (due to large nose-down pitching moment) or power limit (resulting from large drag penalty). Figure 1.1 shows an example of thrust limit on a UH-60A rotor for a range of forward flight speed. The arrow shows the direction of increasing collective at a given forward speed and the thrust value is limited by the so-called McHugh's Stall Boundary [1].

1.2 Dynamic Stall in Helicopters

The discussion in the previous section on flight envelope clearly shows the significant role of stall in defining the flight envelope boundary. Unlike fixed wing, the helicopter rotor experiences a highly unsteady aerodynamic environment. The unsteady effects are severe, especially on the retreating side of the rotor disk, because the blade sections operate at low dynamic pressures and high angles of attack in this region. In forward flight there is the potential for a lift imbalance

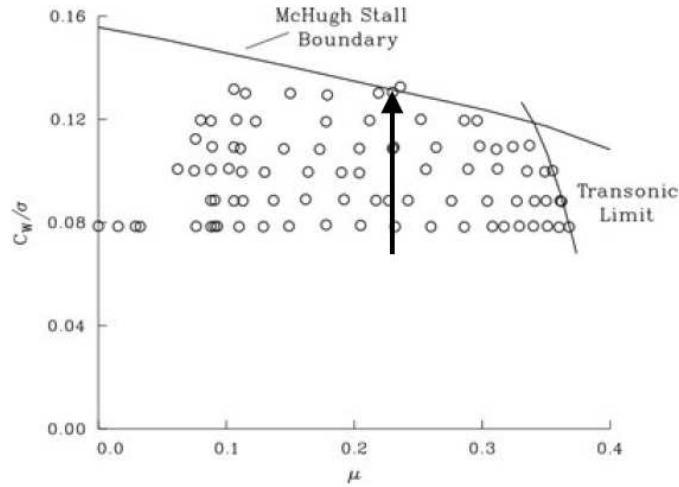


Figure 1.1: Thrust limit on a UH-60A rotor [1]

between the advancing and retreating sides of the rotor disk. To compensate for the asymmetry the flexible rotor blades usually flap up on the advancing side and flap down on the retreating side. The effect of the flap motion along with the differential in pitch, due to the cyclic pitch inputs, on the advancing and retreating sides results in a lower effective angle of attack on the advancing side and higher angle of attack on the retreating side. The unsteady operation of the blade sections on the retreating side near the airfoil stall boundary leads to a phenomenon called dynamic stall (DS). Figure 1.2 describes the stages of DS on a 2-D airfoil undergoing cyclic pitching. Dynamic stall is characterized by the following sequence of events:

1. With increasing angle the flow stays attached to a higher α than what is usually observed for the steady stall case.
2. Further increase in α results in the formation of an energetic leading edge vortex which after detaching from the leading edge, convects down stream

above the upper surface of the airfoil.

3. The downstream movement of the vortex along the upper surface causes large aft movement of the center of pressure on the airfoil, which in turn results in a large nose-down pitching moment.
4. Once the vortex convects past the trailing edge, the flow separates and the airfoil goes into lift stall.

The dramatic fluctuations of the blade pitching moments during dynamic stall lead to severe vibratory hub loads, which limits the operational envelope of helicopter rotors. A detailed discussion on DS is found in the book by Leishman [2].

It must be noted that DS flow behavior is strongly influenced by static stall behavior of an airfoil. For example, Fig. 1.2 shows that the static airload stall limits in lift, moment and drag are lower bounds to dynamic stall lift, moment and drag, respectively. Moreover, many DS models, e.g. Leishman-Beddos, Beddos etc., are based on information extracted from static airfoil data. This emphasizes the importance of understanding the fundamental static airfoil properties before predicting and/or determining dynamic stall flow behavior.

1.3 High Lift Concepts

In the past, there has been extensive research and development in low speed fixed wing high lift designs, a brief summary of which is presented in Fig 1.3. Broadly speaking the design concepts were in the form of:

1. Mechanical or conformal morphing designs, such as, variable camber, integrated trailing edge flap (TEF), drooping or deforming leading edge (LE),

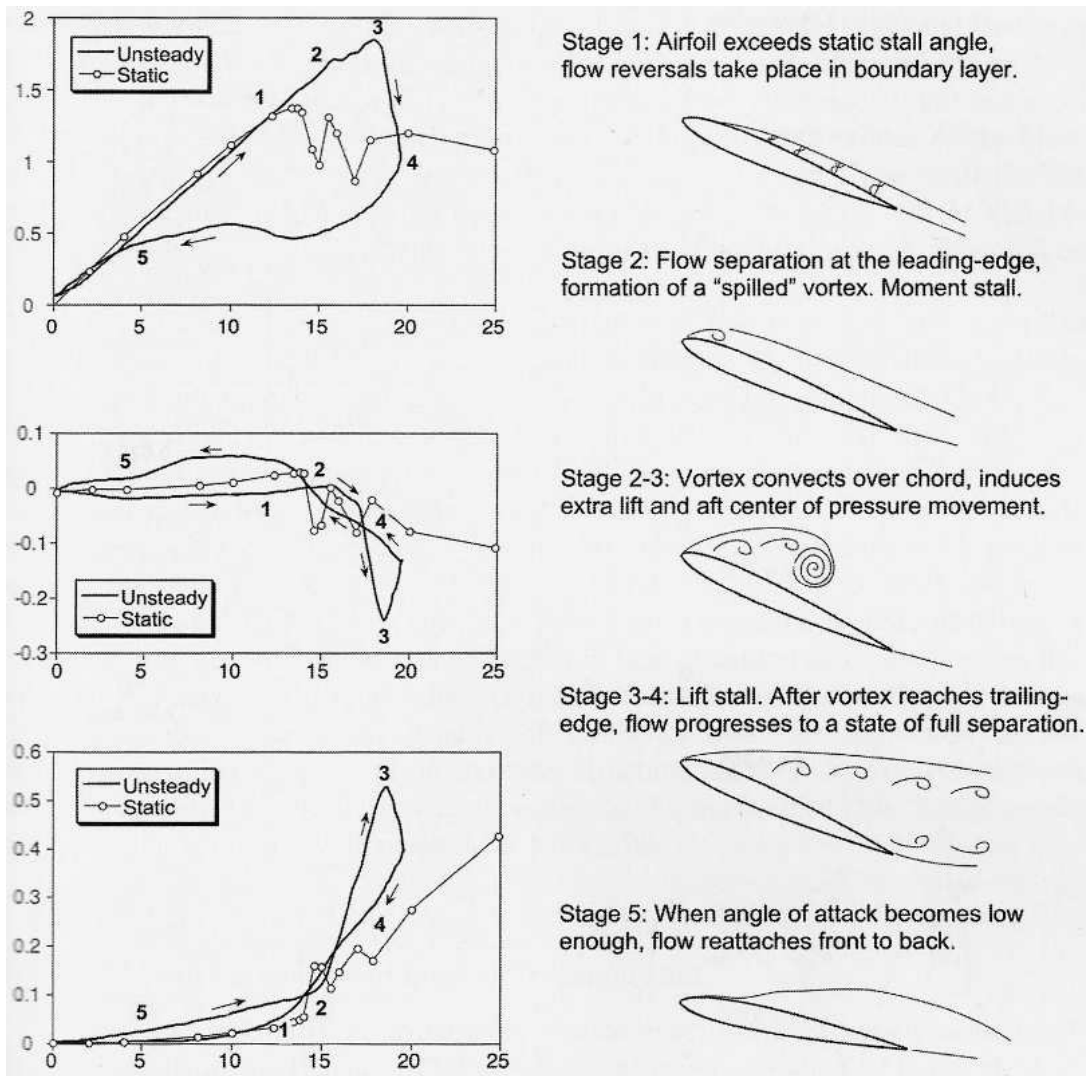


Figure 1.2: Stages of Dynamic Stall [2]

etc.

2. Multi-element concepts, such as, TEF, LE-slats or combination of both.
3. Flow control techniques, such as, direct flow (blowing/suction), zero mass flux (synthetic jets), vortex generators, etc.

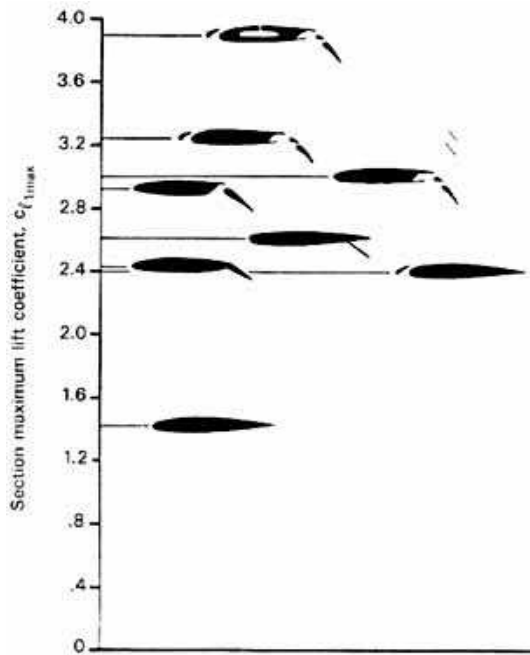


Figure 1.3: High-lift concepts. Courtesy NASA

The trend observed in these broad class of high lift concepts is that the increasing need for high lift benefits requires increasingly complex designs. There exists a trade off between complexity of the design versus its potential benefits, and in that regard multi-element concepts perform well in maintaining a good balance of the two. The following section discusses the airload characteristics of two typical multi-element designs, namely, a TEF and a LE-slat.

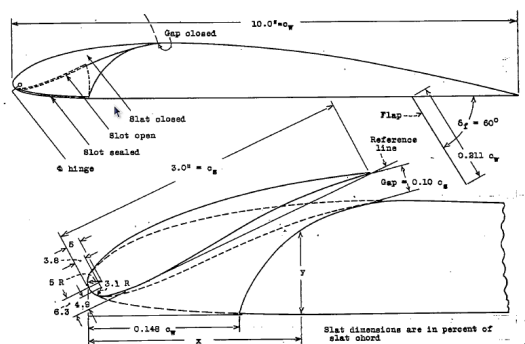
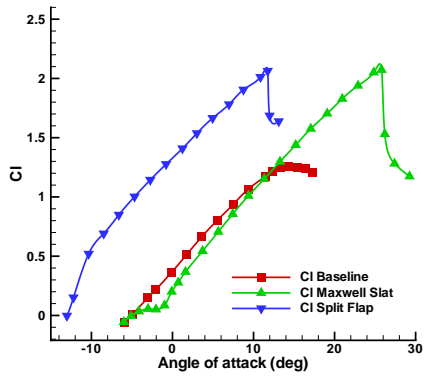


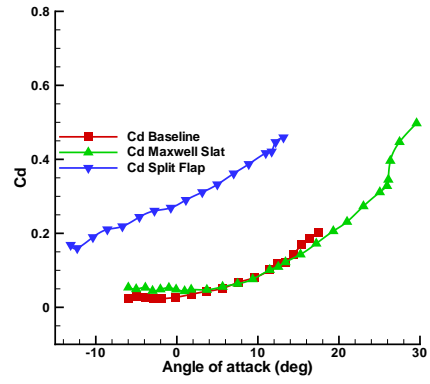
Figure 1.4: Clark Y wing with 21.1% chord split flap and 30% chord Maxwell slat [7]

1.3.1 High-lift Airloads

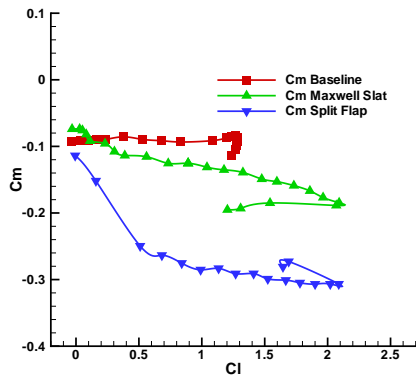
As mentioned before, the popular multi-element concepts in the past were: trailing edge flaps (TEF) and leading edge-slats (LE-slats). Comparison of their relative airload characteristics would throw light on their relative performance in relation to today's modern helicopter demands. As an example, various airfoil characteristics of a plain Clark Y airfoil geometry (Figure 1.4), with that from the same airfoil but with either a 21.1% chord split flap or a Maxwell 30% chord slat with gap [7], are compared in Figure 1.5. Figure 1.5(a) shows the improved Cl_{max} for the split flap compared to the baseline airfoil. But, due to the flap the effective angle of attack is increased, and therefore the airfoil undergoes stall at a lower angle of attack and the stall is much sharper than for the baseline case. Adding the LE-slat not only improves the Cl_{max} value, it also increases the stall boundary by approximately $5 - 6^\circ$ angle of attack as compared to the baseline airfoil and more than around 8° as compared to the split flap. The flap is also found to incur more of a drag penalty (around 0.2) as compared to both



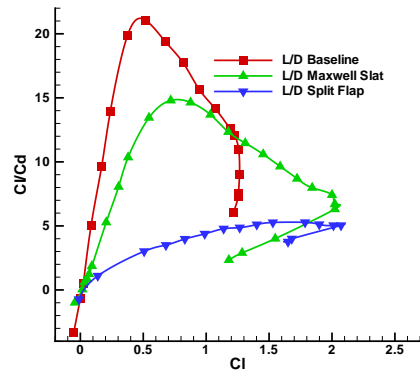
(a) C_l versus α



(b) C_d versus α



(c) C_m versus C_l



(d) C_l/C_d versus C_l

Figure 1.5: Airloads on Clark Y wing with split flap and Maxwell slat [7]

the plain and the slatted airfoil. Moreover, the flap results in a larger nose-down pitching moment than the slatted airfoil, for the same lift value (Fig. 1.5(c)). Finally, Fig. 1.5(d) shows that overall performance of the slatted airfoil, in terms of lift-to-drag ratio (Cl/Cd), is better than that of both the plain and split flap airfoil.

For the split flap, although the flap increases the lift, the increase in drag is even greater such that the lift-to-drag ratio is decreased, as compared to the plain airfoil. For the slatted airfoil, the lift-to-drag ratio is greater at the large angles of attack. Moreover, with increasing angle the lift carrying capacity of the element itself diminishes for the flap, but increases for the slat. For example, see Fig. 1.6. At the lower angles of attack the slat is less effective. In fact, near zero degree angle of attack, separated flow may occur on the lower surface of the slat, resulting in increased drag. It should be noted that this would be ameliorated if the angle of the slat was increased; however, that would decrease the effectiveness of the slatted airfoil at high angles of attack. Thus, the shown fixed slatted airfoil geometry is a compromise.

To better understand the airload behavior of multi-element airfoils, such as the ones discussed above, it is necessary to study their underlying physics. The following sections discuss the basic flow physics of multi-element airfoils and their advantages over conventional single element high lift concepts.

1.3.2 Multi-element Flow Physics

In a historical review paper [3] on high lift aerodynamics, A.M.O. Smith characterized the maximum lift carrying capacity of a natural boundary layer (BL). He emphasized the theory that any multi-element airfoil would produce higher

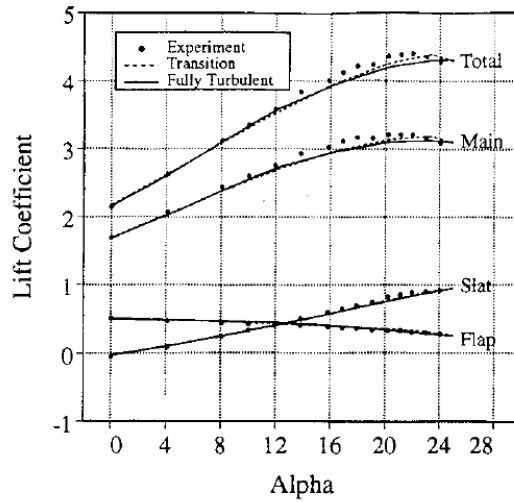


Figure 1.6: Lift contribution of flap and slat to total lift of an MEA airfoil. [5] lift than a single element airfoil. The theory in general states that lift due to $n + 1$ elements is greater than n elements. In this paper, Smith laid out five predominant favorable effects of gaps or slots in multi-element airflows, three of which are inviscid effects (Fig. 1.7) and the rest are viscous (Fig. 1.8).

1. Slat effect (inviscid)
2. Circulation effect (inviscid)
3. Dumping effect (inviscid)
4. Off-surface pressure recovery effect (viscous)
5. Fresh boundary layer effect (viscous)

From inviscid theory, any finite lift producing airfoil element can be approximated by a point vortex with finite circulation value (neglecting the thickness effect). See Fig. 1.7(a). This approximation helps in understanding the flow physics behind the first three (inviscid) effects.

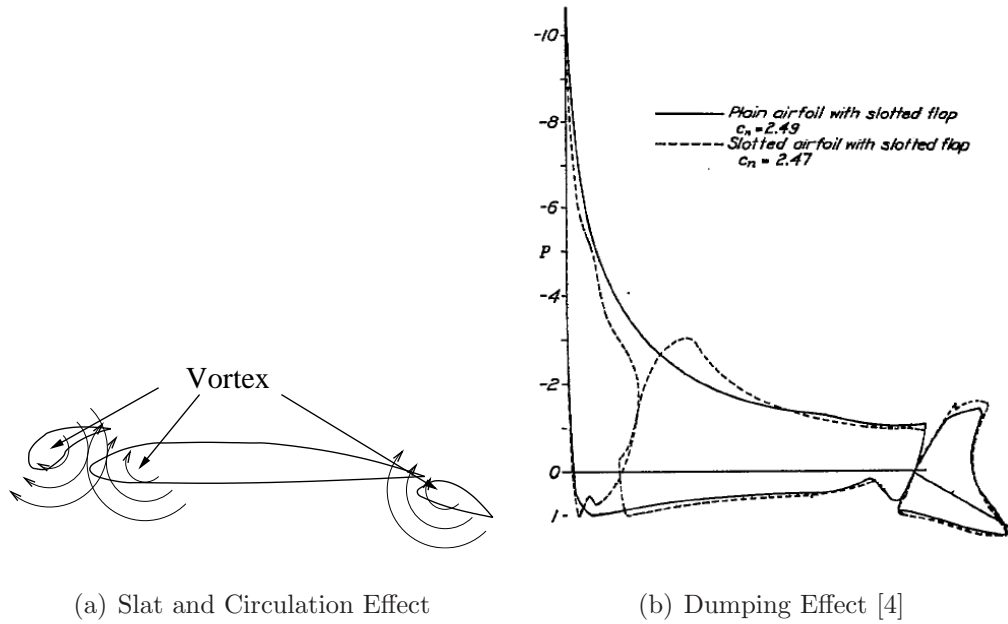


Figure 1.7: Inviscid Effects of Gap

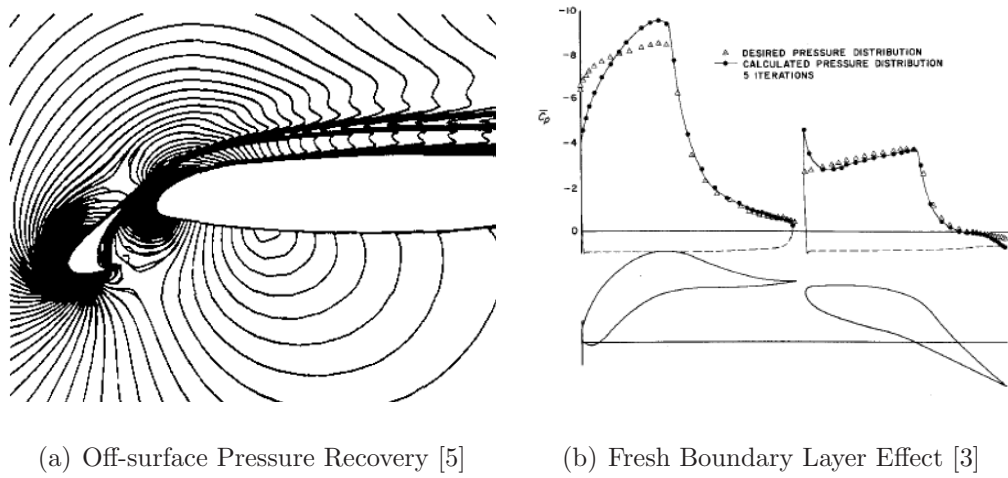


Figure 1.8: Viscous Effects of Gap

The *slat effect* from the forward element, due to its finite circulation vortex, causes decreased flow angle at the downstream element leading edge (LE). This reduces the pressure peak on the downstream LE and thus protects the element from flow separation. *Circulation effect* due to the down stream element causes an increased flow angle on the forward element at the trailing edge (TE). To maintain the Kutta condition, the circulation on the forward element becomes larger which results in larger lift. Since, the pressure peak on the forward element increases, it can be placed at a lower physical angle. The high velocity flow on the upper surface of the trailing element allows the flow to leave the forward element at a higher speed. This *dumping effect* (Fig. 1.7(b)) reduces the pressure recovery of the forward element as well as allowing for improved lift due to the larger area under the pressure curve on the forward element.

The first of the viscous effects is the *off-surface pressure recovery* effect, which states that the pressure recovery in a wake is more efficient than one in a boundary layer (BL) on wall. See Fig. 1.8(b). The wake of the slat merges with the BL on the wall and forms a Confluent Boundary Layer (CBL) as illustrated in Fig. 1.9. If the boundary layer and wake have a large enough separation between them, then there is also a layer or layers of unretarded air from the upstream gaps, which usually disappear further downstream as the layers merge. The CBL can be very thick and extend from the surface well into the flow field (e.g., 20% chord). The CBL can generally withstand a larger adverse pressure gradient (avoiding separation) than a standard boundary layer.

The other viscous effect is related to the ‘age’ of a boundary layer itself. Each element has a *fresh boundary layer* which originates on that element. A thin, turbulent boundary layer can withstand stronger pressure gradients than a thick

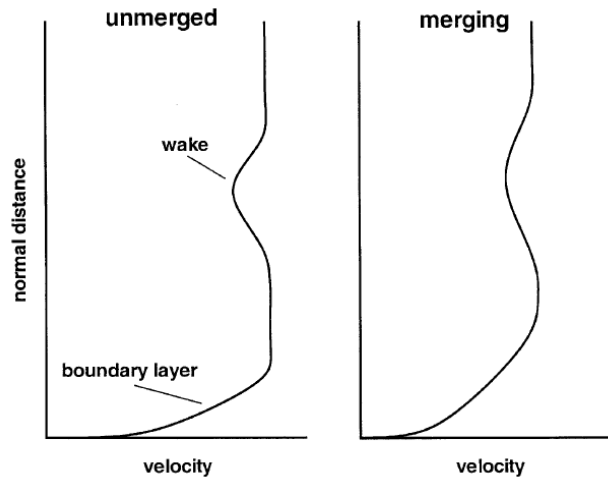


Figure 1.9: Process of formation of CBL in a typical multi-element airfoil [6].

one and is less likely to separate. See Fig. 1.8(b). If the development of the boundary layer on an airfoil is compared to that on a multi-element system of elements with an equivalent combined chord length, the overall pressure recovery of the multi-element system is, effectively, divided among all the elements. At the same time, the boundary layer does not continuously grow along the effective chord as it would on the single element. Moreover, a fresh boundary layer (BL) allows for region of laminar flow on downstream elements, favoring reduced drag values.

1.4 Previous Work

The problem of relating rotor thrust capability to airfoil section characteristics becomes difficult when it is recognized that the rotor thrust is not dependent upon the maximum static airfoil lift, but that there is an unsteady or dynamic component [8] that increases the thrust capability. Similar to the findings in

two-dimensional airfoils observed earlier, measurements of the rotor thrust of a full-scale H21 rotor in the 40- by 80-Foot Wind Tunnel by McCloud and McCullough [9] demonstrated that a rotor can provide more thrust than that which would be calculated using just the static airfoil lift coefficient. This additional lift, as mentioned earlier, can be attributed to the phenomenon called dynamic stall.

1.4.1 Fundamental Understanding of Dynamic Stall

Dynamic stall has been the subject of extensive research in the past [10, 11]. There has been a lot of experiments to understand the fundamental nature of dynamic stall, including wind tunnel tests on two-dimensional airfoils. Experiments were conducted by McCroskey and his colleagues [12–14] exclusively to understand dynamic stall characteristics of eight airfoil sections in the 7- by 10-Foot Wind Tunnel at NASA Ames Research Center. Bousman [1] used these data to come up with a dynamic stall function. He studied the effects of various parameters, namely, amplitude, frequency of airfoil oscillations, Reynolds number, boundary layer and Mach number, on the dynamic stall function. In his limited experimental and analytical efforts in improving dynamic stall performance he concluded that variable geometry or multi-element airfoil designs would provide improved lift without a severe moment or drag penalty.

The knowledge obtained on dynamic stall from 2D wind tunnel testing provides a useful basis for understanding dynamic stall on a helicopter rotor in forward flight and maneuvers. However, significant differences exist between the two environments and it is useful to mention some of these differences. The angle of attack on an airfoil can be expressed as: $\alpha = \theta_{const} + \theta_{elast} - \phi$. In a

conventional 2D wind tunnel test, the model is made rigid so that elastic motion (θ_{elast}), even at the highest frequencies, is one to two orders of magnitude smaller than the control angle (θ_{const}). Similarly, the induced flow angle (ϕ) is normally small and is neglected. For a helicopter in flight, however, all three of these angles are of approximately the same size. It is possible in flight to measure the control angle of a rotor with reasonable accuracy and, with some care, derive the elastic deformation in the blade from strain gauge measurements. However, the induced flow angle is dependent upon the trailed and shed wake of the blade, the inflow induced by all the other blades and the flow induced by the fuselage. Therefore, there is a need for the three dimensional study of dynamic stall in fixed wings and/or rotors.

1.4.2 Three Dimensional Dynamic Stall: Wings and Rotors

3D wing stall has been studied through extensive experiments by Lorber [15], and Lorber et al. [16] for SSC-A09 thin airfoil and Piziali [17] for a NACA 0015 airfoil. Lorber et al. studied the unsteady separation and dynamic stall process along with the effects of compressibility, pitch rate, wave rate, and geometry on dynamic stall of an oscillating wing with varying wing sweep angles. The flight condition spanned Mach numbers of 0.2 – 0.6 and Reynolds numbers of 2 – 6 million which broadly simulates all the flow conditions that a helicopter usually experiences during one rotor revolution. A comprehensive review of experimental investigations up to 1996 can be found in Carr and Chandrasekhara [18]. This review of research on the effect of compressibility on dynamic stall showed that compressibility effects can have a major impact on dynamic stall events, and

can even completely change the physics of the stall process that occurs at low Mach number. They emphasized that future research effort should go into areas of control, alleviation, or avoidance of dynamic stall.

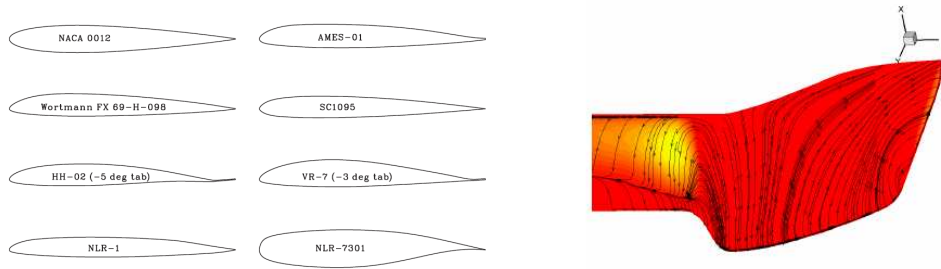
Spentzos et al [19] conducted a CFD based study of three dimensional dynamic stall of various fixed wing plan form shapes. The main conclusion of this work was that similarity between 2-D and 3-D calculations is good only in the mid-span area of the wing while the outboard section is dominated by the omega-shaped vortex. The flow configuration near the wing tip is far more complex with the tip vortex and the Dynamic Stall Vortex (DSV) starting from the wing tip.

1.5 Stall Alleviation Techniques

Alleviation of dynamic stall has been one of the biggest concerns among helicopter researchers. Earlier stall alleviation concepts involved fixed geometry innovative airfoil and passive control designs.

1.5.1 Innovative Airfoil Design

McCroskey and colleagues at NASA carried out extensive experimental tests wherein they examined the dynamic stall characteristics of several airfoil designs [12–14] in the 7- by 10-Foot Wind Tunnel at NASA Ames Research Center. The airfoils they tested were: NACA0012, AMES-01, Wortmann FX 69H098, SC1095, Hughes Helicopters HH02, VR7, NLR1 and NLR-7301 (see Figure 1.10(a)). Bousman [1] used the Ames test data to better understand the airfoil design characteristics that affect the augmented lift in dynamic stall and



(a) Airfoils tested in the NASA Ames $7' \times 10'$ Wind Tunnel [12–14]

(b) BERP Rotor [20]

Figure 1.10: Innovative Airfoil and passive Blade Design

the associated moment and drag penalties. Those data were used to understand what parameters most strongly influence the dynamic stall loading and provided some indications about the use of multi-element and variable geometry airfoils in rotors for enhanced dynamic stall performances.

1.5.2 Passive Control Techniques

Popular passive techniques used in the past to improve rotor performance were: modification of rotor sweep, taper, twist, anhedral or tip shape. Innovative rotor designs such as the BERP [20] rotor (with its RAE9645/48 airfoil sections) have been successful in pushing the dynamic stall limit (Figure 1.10(b)) by incorporating a spanwise variation in airfoil geometry in combination with a modified tip shape. Fradenberg et al [21] patented a helicopter blade of high twist with an improved tip that incorporated a combination of sweep, taper, and anhedral to improve the hover performance by unloading the tip and reducing the tip vortex strength as well as displacing the vortex away from the returning approaching blade surface. However, an experimental investigation on a “BERP-type” rotor

by Yeager et al. [22] showed no performance gain either in hover or in forward flight, although this innovative rotor design showed good reduced hub and pitch-link load characteristics. Gurney flaps [23] have been found to be effective in maximizing lift and lift-to-drag ratio with reduced drag and moment penalty, but only at light dynamic stall [24]. Moreover, several studies [25] have shown that it requires a combination of passive flow control devices, instead of just one, to attain an optimum configuration for stall alleviation.

1.5.3 Active Control Methods

The flight envelope expansion that can be achieved by innovative blade design alone is limited, because of their passive nature for blade control. The passive devices typically effective on fixed wings are impractical on helicopter rotors because they would have to be deployed in a rapid, time-dependent manner in the rotor cycle. On the other hand, active control strategies, unlike passive control elements, can be switched on and off instantly. Thus, the active control mechanisms do not degrade the operational performance when they are not needed. Therefore, recently active control methods have gained more popularity than passive control methods.

One kind of stall control mechanism involves direct influence on fluid flow using flow control mechanisms such as: boundary layer suction [26], blowing or air injection [27], vortex generation [28], plasma actuation of flow [29, 30], or mass-less “synthetic-jet” [31–33]. These control devices help maintain leading edge suction by energizing the boundary layer, which delays boundary layer separation and stall. Although these flow control techniques have direct influence on the flow and hence are more effective on dynamic stall (DS) control, implement-

ing them on a rotor, however, is very complex. For example, direct fluid flow control would require fluid transfer from the hub to the rotating elements, which would be very power demanding. Even in the case of zero-mass flow methods, such as, synthetic jets, the mechanism involved in cavity actuation is highly complex for a rotating element. Therefore, actively controlled blade element design concepts, such as a) TEFs b) Variable Geometry LE and c) LE-Slats, have become more popular among researchers for rotor DS alleviation.

With the advances in smart material actuators researchers have investigated the use of active flow control techniques using trailing edge flaps to dynamically control the rotor flow field [34–36]. Mechanically an active trailing edge flap is easier to design and implement, and is a suitable alternative because of its high control authority, low actuation power, and low aerodynamic drag. But, its effectiveness in DS mitigation or alleviation is only mild due to its indirect influence on the leading edge aerodynamics. TEFs achieve DS mitigation/alleviation either by: a) modifying the dynamic stall vortex trajectory by shifting the trailing edge vortex [37] or by b) aeroelastically reducing the elastic twist through its moment flap effect [38]. In this context, active control concepts that modify the leading edge flow directly, especially the deforming leading edge airfoil concepts, are more effective and hence are becoming more popular.

In the recent past, various control strategies involving deforming leading edge concepts have been investigated in regards to dynamic stall control in high-lift configurations. Two such concepts are: dynamically deforming leading-edge (DDLE) [39,40], and variable droop leading-edge (VDLE) [24,41–43]. With variable droop, the flow acceleration is slowed down prior to reaching the leading edge and hence the adverse pressure gradient is much smoother and mitigated.

This results in a mitigated compressibility effect too. While it helps reduce stall intensities in regards to moment and drag, it shows little or no mitigation of lift stall events. This results in reduced lift-to-drag ratio at larger angles. Similar arguments explains the limited stall alleviation capability of DDLE devices. Although VDLEs and DDLEs have direct control on the leading edge flow resulting in dynamic stall alleviation, the effect is still mild. Moreover, implementation of deforming geometry devices is limited by the complexity involved in the integration of the active fiber or active patches to the blade surface. Leading edge slats, in comparison, hold better promise as a dynamic stall control device as they directly modify the boundary layer flow on the upper surface of the airfoil, without requiring any special blade surface material for their implementation.

Leading Edge Slats

A leading-edge slat delays the onset of boundary layer separation on the main airfoil section and therefore provides a higher stall margin, which is critical for the blade sections operating on the retreating side of the rotor disk. However, studies have shown that this high lift capability is accompanied with an increased drag penalty. For example, steady and unsteady results from high lift airfoil sections, such as, VR-7 with the NACA-15320 as a leading edge slat (LE-Slat), showed improved steady lift and reduced hysteresis during dynamic stall, but increased drag at low angles of attack [44, 45]. Noonan et al. [46] investigated two forward-slotted configurations (C106 and C210) based on the RC(6)-08 tip airfoil. By comparing against a viscous transonic code, they observed an increase of 29 – 61% in the maximum lift capability in comparison to the baseline single-element airfoil, and a 150% increase in the drag. These slatted airfoils (RC(4)-10

airfoils) in the HIMARCS-I rotor [47] showed a 15 – 20% improvement in the rotor stall boundary accompanied by a reduction in the rotor torque at high thrusts, and high advance ratios, but was accompanied with a 10 – 20% torque penalty at lower thrust conditions. Carr et al. [48] have conducted detailed flow measurements demonstrating the effectiveness of these slat configurations on RC(6)-08/106 and -08/210 airfoils in suppressing the dynamic stall.

Several computational studies have been conducted to design slat configurations that can overcome the airfoil drag and torque penalties at low angles of attack. Narramore et al. [49] combined a potential flow/integral boundary layer solver with an inverse design tool to develop airfoil geometries which were later analyzed using a thin layer Navier Stokes solver. A comprehensive rotor dynamics solver, using a lift and drag table generated from the solver, was used to develop a new slat design, A3C. This new design demonstrated a 3% increase in maximum lift and a 47% decrease in minimum drag over the earlier C106 airfoil. This design was later successfully applied in a tilt rotor study to improve its maximum thrust capability [50]. Computations using CAMRAD [51] on the UH-60A rotor with A3C slats showed a 25% increase in the maximum thrust capability of the rotor, but it incurred a significant power penalty at lower thrust. A separate design effort applied adjoint optimization and an unstructured Navier Stokes code and achieved drag reductions at lower lift coefficient by reducing the flow separation on the slat lower surface [52]. A detailed discussion of the flow on the optimum slot design showed that the design was effective in suppressing the dynamic stall vortex, even at the high Mach numbers that have tended to negate the effectiveness of many flow control concepts. Table 1.1 compares various active control devices and shows how LE-slats fair better than others on

Properties	TEF	VDLE	Flow Control	LE Slat
Camber	High	High	Low	High
Energize BL	Low	Low	Moderate	High
Transition Delay	Low	Low	Moderate	High
Drag Penalty	Low	Moderate	Low	Moderate
Mech. Complexity	Low	Moderate	High	Moderate
Lift/Drag	Moderate	Low	Moderate	High
Stall mitigation	Low	Low	Moderate	High

Table 1.1: Comparison of Active Control Devices

many aspects, especially in terms of lift-to-drag ratio and stall characteristics.

To summarize various LE-slat benefits:

1. LE-slats directly influence boundary layer development on the upper surface of the main airfoil through favorable *gap effects* (inviscid/viscous), and thus sustain attached flow until larger angles.
2. LE-slats are very effective in increasing stall margin.
3. They provide higher sustained lift (C_{lmax}), reduced pitch down moment compared to other multi-element airfoils such as TEFs, and therefore reduced blade section torsional and pitch link loads.
4. With an *actively* moving slat, blade geometric properties can be slowly varied across the rotor azimuth and as a function of changing flight conditions.

Most recently, researchers at Sikorsky and UTRC have been able to improve

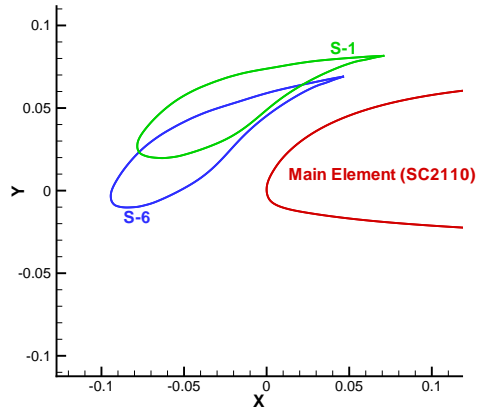


Figure 1.11: S-1 and S-6 slat configurations with respect to the baseline airfoil [55].

the Multi-Element Airfoil (MEA) fixed geometry designs to overcome the advancing side drag penalty by incorporating an active slat actuation and control concept [53]. Amongst the several slat configurations proposed by Lorber et al., two slat positions S-1 and S-6 (see Fig. 1.11) were used for this study. The S-1 position was specifically designed to achieve a compromise between high-lift and low-drag, while the S-6 position provided higher maximum lift characteristics on the retreating side, and was not expected to perform well on the advancing side due to high drag. The performance benefits of these configurations on a model Sikorsky rotor blade were analyzed using transonic wind tunnel measurements [54] and later compared with an analytical study. Results indicated that a modified S6-1 position (derived from the S-6 configuration) was the best configuration because of its high stall-extension capabilities and minimum torque penalty at lower thrusts.

1.6 Motivation

Robust, reliable analysis methodologies are critical in evaluating the merits of novel rotor design configurations involving active control surfaces, such as leading edge slats, on helicopter performance. Traditional analysis methodologies rely on simple, lower-order aerodynamic models to predict the aerodynamics of the rotor blade-wake system, primarily because of their low computational footprint allowing these models to be used as practical design tools. However, these empirical models were derived from experiments performed on simple airfoil configurations, and lacked the fundamental capability to model the complex flow environment observed in multi-element airfoil configurations. Furthermore, the use of active control surfaces allow the designer considerable flexibility in the shape, sizing, and the amplitude and phasing of the actuation. Conducting experiments across this entire design space, necessary to develop empirical, low-order models of these configurations, is impractical. Any analysis of such exotic configurations must, therefore, rely on high-fidelity CFD models which can calculate the aerodynamic environment associated with complex aerodynamic surfaces from first principles by direct solution of the Navier-Stokes equations.

To obtain reliable predictions of the helicopter performance and the detailed aerodynamic environment surrounding the rotor blades, both the fluid and the structural domains need to be modeled accurately. Solving the two domains in a single monolithic solver is impractical, instead a coupled simulation using specialized solvers allows the modeling of the domain-specific features in a simpler, efficient manner. Interactions between the fluid and the structural surface can then be modeled by exchanging information at the fluid-structure interface. Earlier studies concentrated on the use of CFD for optimizing airfoil configurations

by generating airload tables, such as, lift and drag tables. The computational structural dynamics (CSD) analysis was then used to carry out an aeroelastic study on rotor performances [51]. In this regard an approach that couples CFD and computational structural dynamics (CSD) is more appropriate to capture the aeroelastic effects of the mentioned active control methods.

1.7 Objective

The focus of the current research is to develop and validate a coupled Computational Fluid Dynamics (CFD) and Computational Structural Dynamic (CSD) model to investigate the effectiveness of the LE-slat concept in delaying the onset of dynamic stall on rotors and thus its effectiveness in expanding the rotor flight envelope.

First, this requires the CFD based aerodynamic model to be rigorously validated against available 2-D wind-tunnel measurements on LE slats in both static and dynamic flow conditions. Then, the validated CFD aerodynamic model can be coupled with a CSD model capable of predicting the dynamics of a flexible rotor blade and computing the vehicle trim solution. The coupled simulation should be used to analyze the baseline UH-60A rotor in a high-altitude, high-thrust flight condition and validate against available flight test data. The flight condition can then be analyzed with a slightly modified UH-60A blade that includes slatted airfoil sections in the mid span region. Different slat configurations, for example, S-1, S-6 and prescribed slat actuations should be used to examine the effectiveness of leading-edge slats in mitigating the dynamic stall on the retreating side.

Among various challenges encountered by such a CFD solver in a MEA frame-

work, connectivity between grids in the overset mesh systems is a notable one. In the conventional overset mesh system, the bodyfitted blade meshes were embedded inside a cylindrical off body mesh to capture the entire rotor blade-wake aerodynamics. The hole-cutting and the data-exchange routines in the baseline solver were limited to simple rotor blade-wake mesh configurations and would not be capable of modeling the three mesh system when used with a leading-edge slat. Therefore, the overset methodology needs to be modified to use a novel Implicit Hole-Cutting (IHC) technique [56]. The current work will look into the advantages and effectiveness of the IHC technique for MEA rotor analysis.

Although, there have been efforts on understanding the effects of LE slats on rotors, including the recent ones at UTRC, these efforts were restricted to slats remaining static with respect to the main blade. In order to minimize the drag penalty, it is necessary to actively control the position of the LE slat as a function of the blade azimuthal position. The objective is to orient the slat in a position that delivers the maximum lift capability on the retreating side, while reorienting it in a way that minimizes the drag penalty incurred on the advancing side. Initial efforts in achieving actuation of slat on rotor were taken by Torok et al. [57, 58]. A novel span wise actuation concept for an active slat was developed by Bernhard et al. in [59], and is illustrated in Figure 1.12. But, the analysis of this moving slat concept is very limited in the literature. The current work hopes to contribute to an improved understanding of the dynamic slat concept by exploring its aerodynamic and structural implication on rotors in detail.

Detailed objectives of the thesis are:

1. An existing coupled CFD/CSD platform will be modified to incorporate

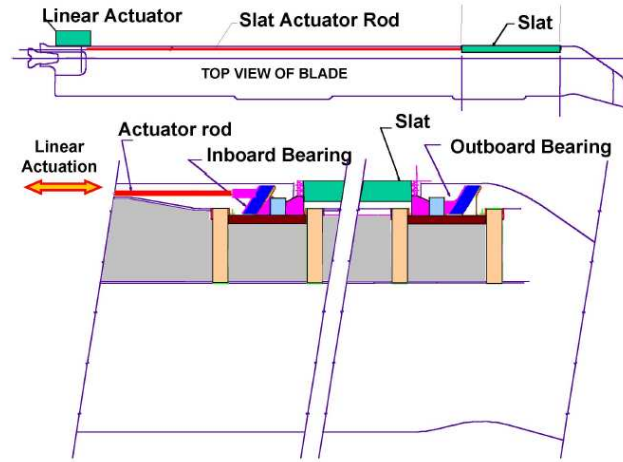


Figure 1.12: Elastomeric bearing concept for slat actuation [53].

an actively controlled LE-slat system.

2. LE-Slats actuation will be incorporated to achieve variable rotor blade geometry to effectively deal with the azimuthally varying rotor aerodynamic environment.
3. A novel hole cutting technique, IHC, will be incorporated to efficiently achieve grid connectivity in a complex multi-element overset mesh system.
4. This CFD solver will be validated with respect to two dimensional wind tunnel experimental data with and without slats and further more the CFD/CSD solver will be validated with a three dimensional UH60 rotor flight test case: C9017.
5. Slat effectiveness will be demonstrated by:
 - (a) Achieving dynamic stall alleviation on UH60 rotor with reduced drag penalty.

- (b) Showing performance benefits through slat actuation.
6. This MEA CFD/CSD platform will be used to demonstrate that the flight envelope can be pushed to higher thrust (C_T/σ) values by making use of actively controlled LE-Slats.

1.8 Contribution of Thesis

The key contributions of this thesis can be classified into two major parts. A brief description of these contributions are:

1. Methodology Development:
 - (a) Extension of existing CFD/CSD platform to analyze MEA design, namely, LE-slats. It involves implementation of dynamic LE Slat actuation on the helicopter blade.
 - (b) Development of a generalized force transfer routine for MEA configurations.
 - (c) Implementation of IHC methodology for improved connectivity across meshes and optimization of the hole cutting procedure by appropriate parallel implementation in an overset frame work required for a multi-element bladed rotor.
2. Computational validation and determining physical mechanisms and benefits:
 - (a) Improved prediction and understanding of two dimensional MEA airfoils as well as a three dimensional rotor (UH60 flight test case C9017)

undergoing dynamic stall phenomena with improved aerodynamic modeling. This includes realizing the need for accurate modeling of turbulence and turbulence transition for improved prediction of the solver.

- (b) Implementation of static and dynamic LE slat mechanisms to mitigate and/or eliminate rotor dynamic stall.
- (c) Determining increase in stall margin and quantifying performance and pitch link load benefits.

1.9 Scope and Organization of the Thesis

The research work in the thesis is focused on extending, developing and validating a coupled CFD/CSD model to investigate the effectiveness of active control elements, such as TEFs and LE slats, on expanding the helicopter flight envelope as well as improving its performance in high lift flight conditions. With an improved connectivity algorithm (IHC) the solver can be a useful tool in analysing any multi-element rotor system or more generally speaking, any multi-body mesh system.

Chapter 2 describes the methodology used for this research. The novel hole cutting strategy (IHC) with its merits over existing conventional hole cutting is discussed. Further, actuation strategies for both TEF and LE slat on rotor blade are described.

The computational model for the analysis is validated and discussed in Chapter 3. The validation cases span two dimensional wind tunnel experiments through full scale model rotor flight tests, i.e. C9017 flight test.

Chapter 4 looks into the effectiveness of LE Slats on improving rotor performance by alleviating retreating side DS. It also explores the effectiveness of a dynamically moving slat on alleviating DS both on a 2-D airfoil as well as on rotors and their overall performance improvement.

The observations and conclusions from the present research in the thesis are summarized in Chapter 5.

Chapter 2

Methodology

The methodology used for the current analysis mainly consists of hi-fidelity aerodynamic tools used for predicting complex three-dimensional flow features and procedures for fluid-structure coupling. The methodology can be broadly divided into: aerodynamic prediction using Computation Fluid Dynamics (CFD), structural dynamics analysis using Computational Structural Dynamics (CSD) and finally fluid-structure coupling. In this chapter, each of these aspects of methodology is described in brief. Then, limitations of the existing methodology are discussed. The technical challenges to improve upon the limitations are discussed next.

2.1 Fluid Flow Modeling

The fluid flow properties are governed by the three-dimensional Navier-Stokes (NS) equations. The equations are numerically discretized at finite mesh points and are solved using specified boundary conditions for the specific geometry and starting from given initial conditions. The NS equations are a unified mathematical representation of the major conservation laws of physics, i.e. conservation

of mass, momentum and energy. For closure, additional algebraic or differential equations (e.g. equation of state, Stokes hypothesis or turbulent eddy viscosity equation) are required.

2.1.1 Navier-Stokes Equations

The Navier-Stokes equations are the fundamental partial differential equations which describe the flow of compressible fluids. The strong conservation-law form of the NS equations in Cartesian coordinates can be written as:

$$\frac{\partial Q}{\partial t} + \frac{\partial F_i}{\partial x} + \frac{\partial G_i}{\partial y} + \frac{\partial H_i}{\partial z} = \frac{\partial F_v}{\partial x} + \frac{\partial G_v}{\partial y} + \frac{\partial H_v}{\partial z} + S \quad (2.1)$$

where Q is the vector of conserved variables, F_i , G_i , H_i are vectors representing inviscid fluxes, F_v , G_v , H_v are vectors that represent the viscous fluxes, and S represents the source terms that have to be included to account for the centrifugal and Coriolis accelerations if the equations are formulated in a non-inertial frame of reference. The vector of conserved variables is given by

$$Q = \left\{ \begin{array}{c} \rho \\ \rho u \\ \rho v \\ \rho w \\ e \end{array} \right\} \quad (2.2)$$

where ρ is the density, (u, v, w) are the Cartesian velocity components and e is the total energy per unit volume. The flux vectors are given by

$$F_i = \left\{ \begin{array}{c} \rho u \\ \rho u^2 + p \\ \rho uv \\ \rho uw \\ u(e + p) \end{array} \right\} \quad (2.3)$$

$$G_i = \left\{ \begin{array}{c} \rho v \\ \rho vu \\ \rho v^2 + p \\ \rho vw \\ v(e + p) \end{array} \right\} \quad (2.4)$$

$$H_i = \left\{ \begin{array}{c} \rho w \\ \rho wu \\ \rho wv \\ \rho w^2 + p \\ w(e + p) \end{array} \right\} \quad (2.5)$$

$$F_v = \left\{ \begin{array}{c} 0 \\ \tau_{xx} \\ \tau_{yx} \\ \tau_{zx} \\ u\tau_{xx} + v\tau_{xy} + w\tau_{xz} - q_x \end{array} \right\} \quad (2.6)$$

$$G_v = \left\{ \begin{array}{c} 0 \\ \tau_{xy} \\ \tau_{yy} \\ \tau_{zy} \\ u\tau_{yx} + v\tau_{yy} + w\tau_{yz} - q_y \end{array} \right\} \quad (2.7)$$

$$H_v = \left\{ \begin{array}{c} 0 \\ \tau_{xz} \\ \tau_{yz} \\ \tau_{zz} \\ u\tau_{zx} + v\tau_{zy} + w\tau_{zz} - q_z \end{array} \right\} \quad (2.8)$$

where q_x , q_y and q_z are the thermal conduction terms, which can be represented in terms of temperature (T) and coefficient of thermal conductivity (k), given by:

$$q_i = -k \frac{\partial T}{\partial x_i} \quad (2.9)$$

The pressure (p) is determined by the equation of state for a perfect gas, given by

$$p = (\gamma - 1) \left\{ e - \frac{1}{2} \rho (u^2 + v^2 + w^2) \right\} \quad (2.10)$$

where γ is the ratio of specific heats, generally taken as 1.4. For a perfect gas, $T = \frac{p}{\rho R}$, where R is the gas constant. With the assumption of Stokes' hypothesis [60], the mean stresses can be represented by:

$$\tau_{ij} = \mu \left[\left(\frac{\partial u_i}{\partial x_j} + \frac{\partial u_j}{\partial x_i} \right) - \frac{2}{3} \frac{\partial u_k}{\partial x_k} \delta_{ij} \right] \quad (2.11)$$

where μ is the laminar viscosity, which can be evaluated using simple algebraic Sutherland's Law [60].

Non-dimensionalization of Navier-Stokes Equations

Non-dimensionalization of the governing equations is useful in achieving dynamic and energetic similarity solutions for geometrically similar situations. Once the solution is achieved, it provides exact solutions for all the flows satisfying the same boundary and initial conditions and having the same values of the dynamic and energetic non-dimensional parameters. The solutions thus obtained are of a non-dimensional nature and are on the order of one. Generally, a characteristic dimension such as the chord of an airfoil is selected to non-dimensionalize the length scale, while free-stream conditions are used to non-dimensionalize the dependant variables. The non-dimensional variables (denoted by superscript *) are given below:

$$\begin{aligned} t^* &= \frac{ta_\infty}{c} & x^* &= \frac{x}{c} & y^* &= \frac{y}{c} & z^* &= \frac{z}{c} \\ \mu^* &= \frac{\mu}{\mu_\infty} & u^* &= \frac{u}{a_\infty} & v^* &= \frac{v}{a_\infty} & w^* &= \frac{w}{a_\infty} \\ \rho^* &= \frac{\rho}{\rho_\infty} & T^* &= \frac{T}{T_\infty} & p^* &= \frac{p}{\rho_\infty a_\infty^2} & e^* &= \frac{e}{\rho_\infty a_\infty^2} \end{aligned} \quad (2.12)$$

where c is the chord of the airfoil, a is the speed of sound and subscript ∞ represents free-stream condition.

The non-dimensional parameters are defined as:

$$\begin{aligned}
\text{Reynolds Number :} & \quad Re_\infty = \frac{\rho_\infty V_\infty c}{\mu_\infty} \\
\text{Mach Number :} & \quad M_\infty = \frac{V_\infty}{a_\infty} \\
\text{Prandtl Number :} & \quad Pr = \frac{\mu C_p}{k} \tag{2.13}
\end{aligned}$$

where C_p is the specific heat at constant pressure. For all computations in this work, $Pr = 0.72$ is assumed. V_∞ is the free-stream total velocity given by $\sqrt{u_\infty^2 + v_\infty^2 + w_\infty^2}$.

The Navier-Stokes equations in non-dimensional form can again be represented as eqn. 2.1, if the superscript $*$ is ignored. The non-dimensional inviscid and viscous flux terms will also have identical form as before. Differences arise in the non-dimensional stress and conduction terms, which now become a function of the non-dimensional parameters (Reynolds number and Prandtl number). Neglecting the superscript $*$, the non-dimensional mean stresses and thermal conduction terms, respectively, are given by:

$$\tau_{ij} = \frac{\mu M_\infty}{Re_\infty} \left[\left(\frac{\partial u_i}{\partial x_j} + \frac{\partial u_j}{\partial x_i} \right) - \frac{2}{3} \frac{\partial u_k}{\partial x_k} \delta_{ij} \right] \tag{2.14}$$

$$q_i = - \frac{\mu M_\infty}{Re_\infty Pr (\gamma - 1)} \frac{\partial T}{\partial x_i} \tag{2.15}$$

Rotating Reference Frame

The governing equations, usually solved in the inertial reference frame, can alternatively be solved in a non-inertial reference frame. Although choosing non-inertial over inertial reference frame has significant advantages in hover calculations [61, 62], it can have noticeable impact on solution convergence even in

forward flight calculations. To account for a non-inertial reference frame, the fluxes in eqn. 2.1 become:

$$F_i = \left\{ \begin{array}{c} \rho(u - u_g) \\ \rho u(u - u_g) + p \\ \rho(u - u_g)v \\ \rho(u - u_g)w \\ (u - u_g)(e + p) \end{array} \right\} \quad (2.16)$$

$$G_i = \left\{ \begin{array}{c} \rho(v - v_g) \\ \rho(v - v_g)u \\ \rho(v - v_g)v + p \\ \rho(v - v_g)w \\ (v - v_g)(e + p) \end{array} \right\} \quad (2.17)$$

$$H_i = \left\{ \begin{array}{c} \rho(w - w_g) \\ \rho(w - w_g)u \\ \rho(w - w_g)v \\ \rho(w - w_g)w + p \\ (w - w_g)(e + p) \end{array} \right\} \quad (2.18)$$

where, $U = \{u, v, w\}$ is the vector of physical velocities in the inertial frame and $U_g = \{u_g, v_g, w_g\} = \Omega \times r$ is the rotational velocity vector. Ω is the angular velocity vector $\{0, 0, \Omega_z\}$, rotating about z -axis and r is the relative position vector from the axis of rotation. Thus, $U_g = \{-\Omega_z y, \Omega_z x, 0\}$. In addition, the relative acceleration terms (due to coriolis force) have to be included as a source term vector S in eqn. 2.1:

$$S = \begin{pmatrix} 0 \\ \rho v \Omega_z \\ -\rho u \Omega_z \\ 0 \\ 0 \end{pmatrix} \quad (2.19)$$

Note that the source term vector added to the right hand side of the NS equations is an analytic expression. This enables better representation of the rotational effect in the non-inertial reference frame than in the inertial reference frame.

Transformation to Generalized Curvilinear Coordinates

The governing equations can be expressed in strong conservation law form in a generalized body-conforming curvilinear coordinate system with the aid of the chain rule of partial derivatives. In effect, the equations after being transformed to the computational coordinates ξ, η, ζ are as follows:

$$\frac{\partial \hat{Q}}{\partial t} + \frac{\partial \hat{F}}{\partial \xi} + \frac{\partial \hat{G}}{\partial \eta} + \frac{\partial \hat{H}}{\partial \zeta} = \hat{S} \quad (2.20)$$

where,

$$\hat{Q} = \frac{1}{J}Q \quad (2.21)$$

$$\hat{F} = \frac{1}{J}[\xi_t Q + \xi_x(F_i - F_v) + \xi_y(G_i - G_v) + \xi_z(H_i - H_v)] \quad (2.22)$$

$$\hat{G} = \frac{1}{J}[\eta_t Q + \eta_x(F_i - F_v) + \eta_y(G_i - G_v) + \eta_z(H_i - H_v)] \quad (2.23)$$

$$\hat{H} = \frac{1}{J}[\zeta_t Q + \zeta_x(F_i - F_v) + \zeta_y(G_i - G_v) + \zeta_z(H_i - H_v)] \quad (2.24)$$

$$\hat{S} = \frac{1}{J}S \quad (2.25)$$

where J is the Jacobian of the coordinate transformation (i.e., $J = \det \left(\frac{\partial(\xi, \eta, \zeta)}{\partial(x, y, z)} \right)$)

2.1.2 Reynolds Averaged Navier-Stokes Equations

The governing NS stokes equations 2.20 are sufficient for solving inviscid or laminar flows, but present difficulties in turbulent regimes. Turbulent flow motions occur in the vast majority of fluid applications encountered in engineering problems, especially in external aerodynamics involving helicopter rotors. Turbulent fluid motion is an irregular condition of flow in which the various quantities show a random variation with time and space coordinates, so that statistically distinct average values can be discerned [63].

The most elegant solution to any turbulent flow is via the Direct Numerical Simulation (DNS) of turbulence. This approach is implemented by discretizing the Navier-Stokes equations 2.20 with a higher order accurate numerical scheme and solved using an extremely fine grid mesh and hence can be computationally very expensive. An alternative approach to the DNS technique would be the adoption of Large Eddy Simulation (LES), which draws upon the advantages of the direct simulation of turbulence flows and the solution of the Reynolds averaged equations through closure assumptions. Although the popularity of

DNS and LES have become noticeable due to rapid development of high performance computing technology, the general trend of computing turbulent flows still remains with the solution of the Reynolds-Averaged Navier-Stokes (RANS) equations with the inclusion of Reynolds stresses into the original full Navier-Stokes equations. Resolving the turbulent flows via this means proves to be computationally much less expensive.

The RANS approach, which was presented by Reynolds in 1895, is based upon the decomposition of the flow variables into mean and fluctuating parts. The motivation behind this is that in most engineering and physical processes, one is only interested in the mean quantities. Therefore, any flow variable, ϕ , can be written as:

$$\phi = \bar{\phi} + \phi' \tag{2.26}$$

where $\bar{\phi}$ is the mean part and ϕ' is the fluctuating part. The mean part, $\bar{\phi}$, is obtained using Reynolds averaging given by

$$\bar{\phi} = \frac{1}{\bar{\chi}} \lim_{\Delta t \rightarrow \infty} \frac{1}{\Delta t} \int_0^{\Delta t} \chi \phi(t) dt \tag{2.27}$$

where $\chi = 1$, if ϕ is density or pressure and $\chi = \rho$, if ϕ is other variables such as velocity, internal energy, enthalpy and temperature. By definition, the Reynolds average of the fluctuating part is zero.

The decomposed variables are then inserted into the Navier-Stokes equations (eqn. 2.20) and the equations are Reynolds averaged to obtain the mathematical description of the mean flow properties. If the overbar on the mean flow variables is dropped, the resulting equations are identical to the instantaneous Navier-Stokes equations with the exception of additional terms in the momen-

tum equation and the energy equation (not present if heat transfer is neglected). The extra terms in the momentum equation accounts for the additional stress due to turbulence and are called the **Reynolds-stress tensor**. These stresses add to the viscous stress terms given in eqn. 2.11 and are given by:

$$\tau_{ij}^R = -\rho \overline{u'_i u'_j} \quad (2.28)$$

However, with the introduction of the Reynolds-stress terms, we obtain six additional unknowns in the Reynolds-averaged momentum equations. In order to close the RANS equation, the Reynolds stress terms are approximated using a turbulence model. Details of turbulence modeling will be briefly discussed in section 2.1.4.

2.1.3 Initial and Boundary Conditions

RANS equations discussed in the previous section can be used to analyze any general problem. To characterize and define a particular fluid flow problem, initial and boundary conditions are required. Initial conditions refers to the state of flow before the solution procedure starts and boundary condition refers to the physical as well as numerical conditions imposed on the flow domain boundaries. A particular choice or combination of boundary and/or initial conditions can have a considerable influence on the accuracy or even the stability properties of a numerical scheme.

Typically for a forward flight rotor simulation, the initial conditions of fluid properties such as density, pressure and velocities can either be set to the freestream values or to a previously converged solution state.

The two common boundary conditions for an external flow are the wall boundary condition and the far-field boundary condition. Wall boundaries are natural boundaries of the physical domain which arise from the wall surfaces being exposed to the flow. For a viscous fluid which passes a solid wall, the relative velocity between the surface and the fluid directly at the surface is zero. The truncation of the physical domain or system for the purpose of numerical simulation leads to artificial far-field boundaries, where certain physical quantities have to be prescribed. The far-field boundary condition has to fulfill two basic requirements. First, the truncation of the domain should have no notable effects on the flow solution as compared to the infinite domain. Second, any outgoing disturbances must not be reflected back into the flow-field.

2.1.4 Numerical Algorithm

The solver used in this work is the overset structured mesh solver OVERTURNS [64] (OVERset Transonic Unsteady Rotor Navier-Stokes). OVERTURNS solves the compressible RANS equations on two or three dimensional single block structured grids.

The inviscid fluxes are evaluated using a finite volume upwind numerical algorithm. The upwind biased flux-difference scheme used is that proposed by Roe [65] and later extended to three-dimensional conservation laws by Vatsa et al. [66]. The use of upwinding eliminates the addition of explicit numerical dissipation, which is often required in central difference schemes. Upwind schemes have been demonstrated to produce less dissipative numerical solutions compared to their central difference counterparts. First order schemes have unrealistic mesh discretization requirements. Therefore, the Van Leer [67] Monotone

Upstream-Centered Scheme for Conservation Laws (MUSCL) approach is used to obtain higher order accuracy. Appropriate flux limiting is used to make the scheme total variation diminishing (TVD). The Lower-Upper-Symmetric Gauss-Seidel (LU-SGS) scheme, suggested by Jameson and Yoon [68,69] is used as the implicit operator.

The differential eqn. 2.20 is discretized in space and time in a finite volume approach. In this approach, fictitious volumes are created around each grid point. A fictitious volume is created around a point using the midpoints of the lines joining the adjacent grid points to the grid point. The faces of this new volume lie exactly in the middle of two grid points. The faces of this new volume lie exactly in the middle of two grid points. This volume is treated as a control volume and fluxes are evaluated at the faces of the volume, resulting in conservation equations for the volume.

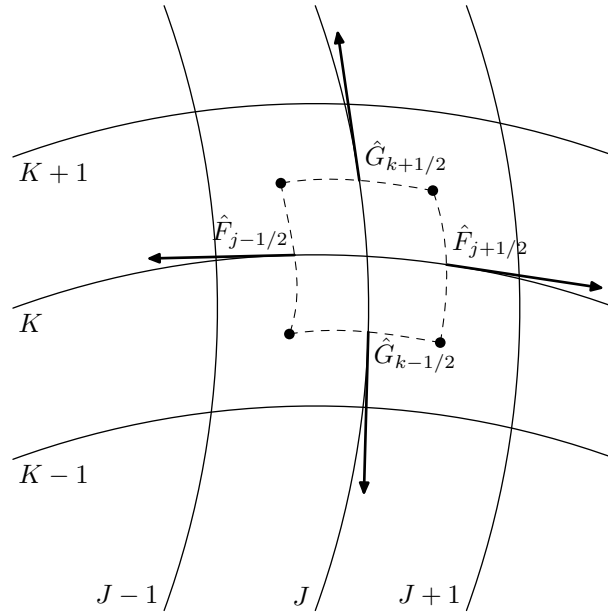


Figure 2.1: Schematic showing computational cell.

The semi-discrete conservative approximation of eqn. 2.20 can be written as:

$$\frac{\partial \hat{Q}}{\partial t} = -\frac{\hat{F}_{j+\frac{1}{2}} - \hat{F}_{j-\frac{1}{2}}}{\Delta \xi} - \frac{\hat{G}_{k+\frac{1}{2}} - \hat{G}_{k-\frac{1}{2}}}{\Delta \eta} - \frac{\hat{H}_{l+\frac{1}{2}} - \hat{H}_{l-\frac{1}{2}}}{\Delta \zeta} + \hat{S}_{j,k,l} \quad (2.29)$$

where, (j, k, l) are the indices corresponding to the (ξ, η, ζ) directions in the transformed coordinate system and $(j \pm \frac{1}{2}, k \pm \frac{1}{2}, l \pm \frac{1}{2})$ define the cell-interfaces of the control volumes as shown in Fig. 2.1 (2D cell shown for simplicity). The spatial discretization (consisting of the inviscid and viscous fluxes) reduces to evaluating the interfacial fluxes $\hat{F}_{j+\frac{1}{2}}, \hat{G}_{k+\frac{1}{2}}, \hat{H}_{l+\frac{1}{2}}$ for every cell (j, k, l) in the domain.

Inviscid Terms

The inviscid part of the interfacial flux is computed using upwind schemes [67]. Upwind schemes have the advantage that the wave propagation property of the inviscid equations is accounted for (albeit approximately) in the flux calculation. To evaluate the interfacial fluxes, the Monotone Upstream-Centered Scheme for Conservation Laws (MUSCL) [67] approach is used. This procedure involves two steps. First, the left and right states at each interface are reconstructed from the corresponding cells using piecewise cubic reconstruction with Koren's limiter [70]. Next, these right and left states are used to define a local Riemann problem and the interfacial flux is obtained by using Roe flux difference splitting [65]:

$$F(q^L, q^R) = \frac{F(q^L) + F(q^R)}{2} - |\hat{A}(q^L, q^R)| \frac{q^R - q^L}{2} \quad (2.30)$$

where \hat{A} is the Roe-averaged Jacobian matrix.

Viscous Terms

Helicopter rotor experiences flow conditions ranging from high Reynolds number attached flow to low Reynolds number highly separated flow. The thin-layer assumption, appropriate only for attached flow calculations, becomes invalid for separated flows (encountered near root and at large blade sectional angles). Therefore, in OVERTURNS, full viscous terms are considered without any thin-layer approximations. Numerical discretization of these terms involve expressions of the form [71]:

$$\frac{\partial}{\partial \xi} \left(\alpha \frac{\partial \beta}{\partial \eta} \right) \quad (2.31)$$

These terms are computed using second order accurate central differencing. Thus, the above expression will be discretized as:

$$\frac{1}{\Delta \xi} \left(\left[\alpha_{j+\frac{1}{2},k} \frac{\beta_{j+\frac{1}{2},k+1} - \beta_{j+\frac{1}{2},k}}{\Delta \eta} \right] - \left[\alpha_{j-\frac{1}{2},k} \frac{\beta_{j-\frac{1}{2},k} - \beta_{j-\frac{1}{2},k-1}}{\Delta \eta} \right] \right) \quad (2.32)$$

where

$$\delta_{j+\frac{1}{2},k} = \frac{\delta_{j,k} + \delta_{j+1,k}}{2}, \quad (\delta = \alpha, \beta) \quad (2.33)$$

Time Integration

Time evolution of the conservative variables, Q , in the equation 2.29 can be achieved using either explicit or implicit methods. Explicit methods have restrictions on time step size based on the mesh size and flow quantities. However, most implicit methods do not have such restrictions. Hence, implicit methods are preferred for RANS calculations with fine meshes at the wall surfaces.

The OVERTURNS code uses the implicit Lower Upper Symmetric Gauss Siedel Scheme (LUSGS) [68, 69] along with Newton sub-iterations [72] in order to remove factorization errors and to fully recover time accuracy.

If an index for time step is included in equation 2.29, an implicit scheme can be written as the following.

$$\frac{\partial \hat{Q}^{n+1}}{\partial t} = -\frac{\hat{F}_{j+\frac{1}{2}}^{n+1} - \hat{F}_{j-\frac{1}{2}}^{n+1}}{\Delta \xi} - \frac{\hat{G}_{k+\frac{1}{2}}^{n+1} - \hat{G}_{k-\frac{1}{2}}^{n+1}}{\Delta \eta} - \frac{\hat{H}_{l+\frac{1}{2}}^{n+1} - \hat{H}_{l-\frac{1}{2}}^{n+1}}{\Delta \zeta} + \hat{S}_{j,k,l}^{n+1} \quad (2.34)$$

In the above equations, fluxes and conservative variables are known at time step (n) and these quantities are desired to be evaluated at the new time step ($n + 1$). Fluxes at ($n + 1$) time step need to be linearized and expressed in terms of fluxes and conservative variables at step (n). The nonlinear terms are linearized in time about \hat{Q}^n by Taylor Series as:

$$\hat{F}^{n+1} = \hat{F}^n + \hat{A} \Delta \hat{Q}^n + O(h^2) \quad (2.35)$$

$$\hat{G}^{n+1} = \hat{G}^n + \hat{B} \Delta \hat{Q}^n + O(h^2) \quad (2.36)$$

$$\hat{H}^{n+1} = \hat{H}^n + \hat{C} \Delta \hat{Q}^n + O(h^2) \quad (2.37)$$

where $\hat{A} = \frac{\partial \hat{F}}{\partial \hat{Q}}$, $\hat{B} = \frac{\partial \hat{G}}{\partial \hat{Q}}$ and $\hat{C} = \frac{\partial \hat{H}}{\partial \hat{Q}}$. The source terms can also be linearized with respect to the conservative variables. Note that the linearization are second order accurate and so if a second order time scheme is chosen (typically used in OVERTURNS), the linearization would not degrade the time accuracy.

With the flux linearization and assumed first order Euler implicit time discretization, ($\partial_t \hat{Q}^{n+1} = \frac{\Delta \hat{Q}^n}{\Delta t}$), the equation. 2.34 can be written in 'delta form' as:

$$\left[I + \Delta t(\delta_\xi \hat{A}^n + \delta_\eta \hat{B}^n + \delta_\zeta \hat{C}^n) \right] \Delta \hat{Q}^n = -\Delta t \left[\delta_\xi \hat{F}^n + \delta_\eta \hat{G}^n + \delta_\zeta \hat{H}^n - \hat{S}^n \right] \quad (2.38)$$

which is simplified as

$$\text{LHS } \Delta \hat{Q}^n = -\Delta t \text{ RHS} \quad (2.39)$$

The RHS represents the physics of the problem and the left hand side (LHS) the numerics. Therefore, the LHS determines the rate of convergence of the solution. In an implicit time integration method, the LHS is a large banded system of algebraic equations and is solved using LUSGS. In the LUSGS algorithm, LHS is factored into three matrices, namely, lower (L), upper (U) and diagonal (D) matrices. Using first order split flux Jacobians and neglecting the viscous contribution, these matrices can be represented as:

$$L = \Delta t(-\hat{A}_{j-1,k,l}^+ - \hat{B}_{j,k-1,l}^+ - \hat{C}_{j,k,l-1}^+) \quad (2.40)$$

$$D = I + \Delta t(\hat{A}_{j,k,l}^+ - \hat{A}_{j,k,l}^- + \hat{B}_{j,k,l}^+ - \hat{B}_{j,k,l}^- + \hat{C}_{j,k,l}^+ - \hat{C}_{j,k,l}^-) \quad (2.41)$$

$$U = \Delta t(\hat{A}_{j+1,k,l}^- + \hat{B}_{j,k+1,l}^- + \hat{C}_{j,k,l+1}^-) \quad (2.42)$$

This can be solved by a forward and a backward sweep using a two-factor scheme that can be written as:

$$\begin{aligned} [D + L]\Delta \bar{Q} &= -\Delta t[\text{RHS}] \\ [D + U]\Delta \hat{Q} &= D\Delta \bar{Q} \end{aligned} \quad (2.43)$$

Further simplifications involve approximating the split flux Jacobians, e.g. $\hat{A}^\pm = \frac{1}{2}(\hat{A} \pm \sigma_\xi)$, σ_ξ being the spectral radius. This reduces D to a diagonal matrix and its inversion reduces to just a scalar inversion. The contribution of viscous fluxes can be approximated by adding a scalar term to the spectral radius (e.g. $\sigma_\xi + \sigma_\xi^v$), where

$$\sigma_\xi^v = \frac{2\mu (\xi_x^2 + \xi_y^2 + \xi_z^2)}{\rho} \quad (2.44)$$

In OVERTURNS, the factorization errors due to the approximations on the LHS is removed by using Newton sub-iterations at each physical time step. This also removes the linearization errors. Furthermore, the 2^{nd} order backward difference in time (BDF2) is implemented by substituting $\partial_t \hat{Q}^{n+1} = \frac{3\hat{Q}^{n+1} - 4\hat{Q}^n + \hat{Q}^{n-1}}{2\Delta t}$

Turbulence Modeling

With the introduction of the **Reynolds stress term** (eqn. 2.28), more variables are introduced into the RANS equation. Turbulence modeling fixes this problem by finding closure to the RANS equation by approximating the Reynolds stress term. Assuming isotropic eddy viscosity, the stress term can be represented by:

$$\tau_{ij}^R = \mu_t \left[\left(\frac{\partial u_i}{\partial x_j} + \frac{\partial u_j}{\partial x_i} \right) - \frac{2}{3} \frac{\partial u_k}{\partial x_k} \delta_{ij} \right] \quad (2.45)$$

where μ_t is the turbulent viscosity. Various turbulence models have been developed to obtain the turbulent viscosity field. The models range from zero equation algebraic turbulence models (Baldwin-Lomax [73]), four equation turbulence models ($\nu^2 - f$ model [74]) to Reynolds Stress models. The four equation $\nu^2 - f$ model by Durbin, besides incurring increased stiffness to the differential

equations, demands extremely high computational time for solving the turbulent viscosity field.

OVERTURNS uses the Baldwin-Lomax model, but it is restricted mostly to steady and attached flows ([75]). For more general flows, OVERTURNS uses the one equation model of Spalart and Allmaras [76]. The Spalart-Allmaras (SA) model is popular in aerospace flow problems because it was developed with such applications in mind, and therefore it is used in OVERTURNS for all computations in the present work. In the SA model, the Reynolds stresses are related to the mean strain by the isotropic relation, $\overline{u'_i u'_j} = -2\nu_t S_{ij}$, where ν_t is the turbulent eddy viscosity, which is obtained by solving a one equation PDE for a related variable, $\bar{\nu}$ (and $\nu_t = f(\bar{\nu})$).

Another popular turbulence model used in OVERTURNS is the SST k- ω turbulence model [77], a two-equation eddy-viscosity model. The shear stress transport (SST) formulation ensures that the model behaves according to k- ω formulation in the inner boundary layer and switches to k- ϵ formulation in the free-stream. Thus this model avoids the common k- ω problem associated with its sensitivity to the inlet free-stream turbulence properties. The two extra transportation equations are for solving two extra variables, namely, a) turbulent kinetic energy, κ , determining the energy of the turbulence, and b) specific dissipation, ω , determining the scale of the turbulence.

2.1.5 Mesh Generation

To accurately represent blade surfaces, body conforming structured curvilinear meshes are required. The blade surface geometry properties such as sweep, non-linear twist, non-linear dihedral/anhedral, and chord distribution can be

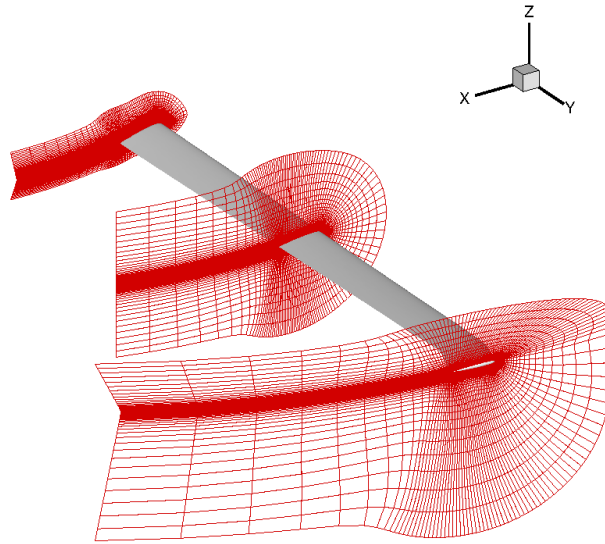
represented as a function of span. Therefore, mesh generation in a spanwise manner would be more appropriate for rotor blades. In this study, a hyperbolic mesh generation technique [78] is used to generate 2D C-type meshes around the airfoil sections at the various spanwise locations, shown in Fig. 2.2(a). The C-type meshes are free of a geometrical singularity at the trailing edge, which is a major disadvantage of O-type meshes. Moreover, the C-type mesh allows for appropriate clustering at the trailing edge which provides good resolution for capturing the shed wake. The 2D C-meshes are stacked in the spanwise direction. For the root and the tip region, a C-O topology is used, i.e. the spanwise sections are rotated and collapsed. See Fig. 2.2(b).

For rotor problems, the blade mesh itself is overset in one or more background meshes, in order to model rotor blade-wake system. In the current work, a background mesh consists of identical planes that are rotated in the azimuthal direction and hence is cylindrical. A sample background mesh for a four bladed single rotor is shown in Fig. 2.3.

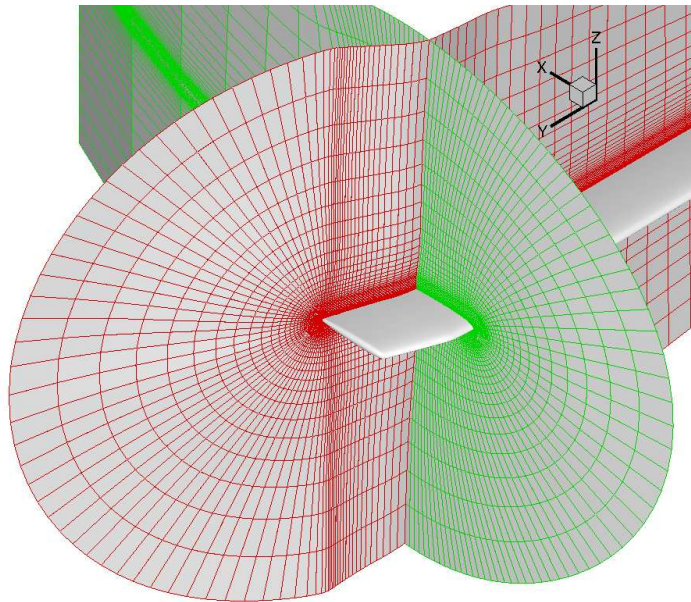
2.1.6 Overset Mesh and Grid Connectivity

Once the overlapping meshes are generated, the data exchange to establish connectivity between the meshes is achieved by making use of *chimera* or overset methods. The chimera methodology involves three distinct steps, namely: i) hole cutting, ii) identification of hole fringe and chimera boundary points and finally, iii) finding donor cells and interpolation factors.

The hole cutting step involves defining arbitrary *hole* regions describing the blade surface geometries, and identifying the points that lie inside these holes. These points are not involved in the flow solution. More specifically, in a typical

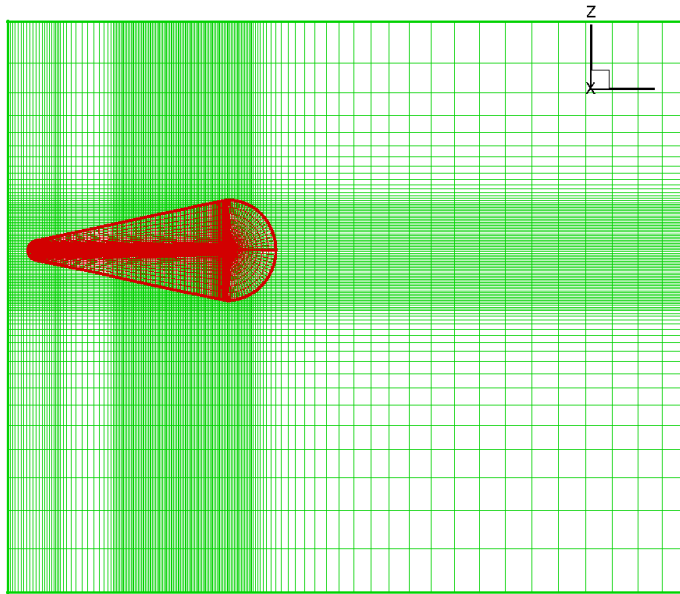


(a) Spanwise 2-D C-mesh

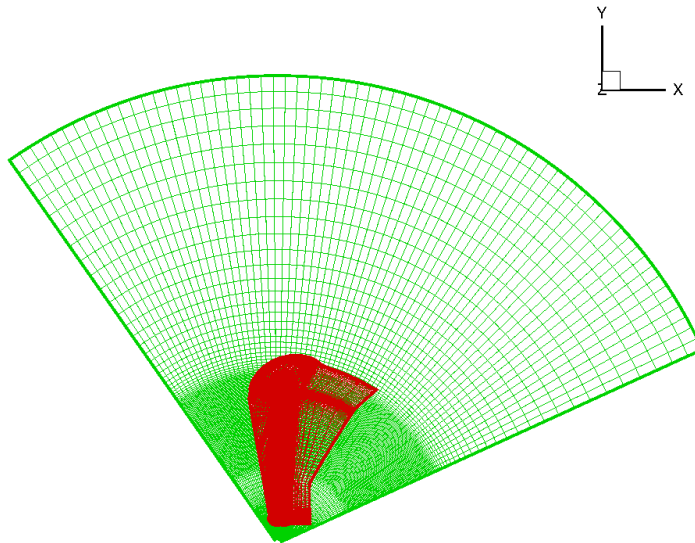


(b) C-O mesh at rotor tip

Figure 2.2: C-O mesh on UH-60A blade



(a) Wake mesh azimuthal plane



(b) Wake mesh top view

Figure 2.3: Cylindrical rotor wake mesh.

rotor simulation, the blade mesh is overset in a background mesh. Knowing the approximate dimensions of the solid body, a box enclosing the solid body is defined in the background grid. All the points inside this box are checked as to whether they lie inside the overset grid and the points that do not are labeled as hole points. Using the neighbor information, this hole region is extended at least one layer outwards.

After obtaining the hole points, a list of hole fringe points that require information from other grids to serve as boundary conditions are extracted. As the next step, the chimera points, defined as the boundary points on the body mesh that require information from the background mesh, are specified by user. The size of fringe and chimera points layer is dependent on the stencil size of the spatial scheme.

The last step involves finding the donor cells of the other grid and the information is interpolated, usually linearly, using the interpolation factors. The donor cell search uses the so-called “stencil-walk” [79] procedure. Figure 2.4 shows a typical wake mesh with hole for a UH60 rotor blade with C-O mesh. More elaborate discussion can be found in Ref. [62, 80].

2.1.7 Aeroelastic Deformation of a Multi-element Rotor Blade

To simulate the actual flow for a given steady flight condition, the base blade geometry (UH-60A in our case) needs to be dynamically deformed consistent with the blade response that conforms to a trimmed state over one rotor revolution. This blade dynamic response which includes both rigid and elastic flap, lag and torsion deformations is obtained from the structural dynamics analysis. Among

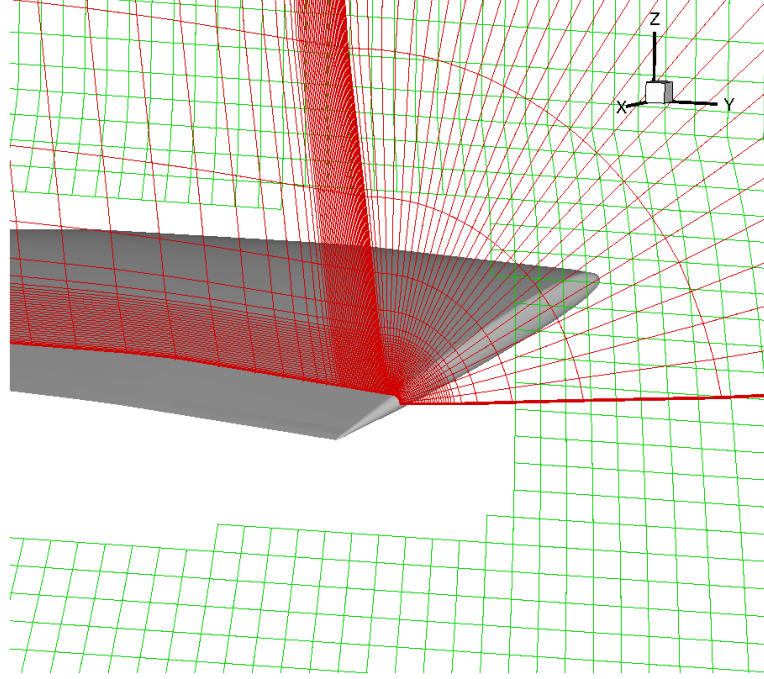


Figure 2.4: Conventional overset mesh

different ways of expressing this elastic deformations, the most popular is using Euler parameters $[e_1, e_2, e_3, e_4, e_5, e_6]$, which are nothing but linear and rotational displacements. These parameters are radially and azimuthally varying functions i.e. $e_i(r, \psi), i = 1, 2, \dots, 6$, where $i = 1, 2, 3$ refer to linear motion and $i = 4, 5, 6$ to rotations.

The rotation matrix used for deforming an undeformed blade can be composed by using e_4, e_5, e_6 as follows:

$$e_0 = \sqrt{1 - e_4^2 - e_5^2 - e_6^2} \quad (2.46)$$

$$T_{DU} = \begin{bmatrix} 1 - e_5^2 - e_6^2 & 2(e_4e_5 + e_0e_6) & 2(e_4e_6 - e_0e_5) \\ 2(e_4e_5 - e_0e_6) & 1 - e_4^2 - e_6^2 & 2(e_5e_6 + e_0e_4) \\ 2(e_4e_6 + e_0e_5) & 2(e_5e_6 - e_0e_4) & 1 - e_4^2 - e_5^2 \end{bmatrix} \quad (2.47)$$

In the present work the deformations are provided in the form $[u, v, w, v', w', \phi]$, where u , v and w are the linear deformations in the axial, lag and flap directions, v' and w' are the radial derivatives for lag and flap degrees and ϕ is the elastic torsional deformation. The Euler parameters can be expressed in terms of these parameters [81] and then T_{DU} can be expressed as:

$$T_{DU} = \begin{bmatrix} 1 - \frac{v'^2}{2} - \frac{w'^2}{2} & v' & w' \\ -v' \cos \theta_1 - w' \sin \theta_1 & (1 - \frac{v'^2}{2}) \cos \theta_1 - v' w' \sin \theta_1 & (1 - \frac{w'^2}{2}) \sin \theta_1 \\ -v' \sin \theta_1 - w' \cos \theta_1 & -(1 - \frac{v'^2}{2}) \sin \theta_1 - v' w' \cos \theta_1 & (1 - \frac{w'^2}{2}) \cos \theta_1 \end{bmatrix} \quad (2.48)$$

The variable θ_1 represents the total pitch of the blade, i.e. $\theta_1 = \theta_c + \phi$, where θ_c are the control deflections and ϕ is the elastic torsional deflection.

Mesh Deformation

The final step of mesh deformation consists of deforming the undeformed mesh coordinates to the deformed state using the transformation matrix T_{DU} . The deformed mesh coordinates in the hub fixed frame are obtained by:

$$\begin{bmatrix} x' \\ y' \\ z' \end{bmatrix} = [T_{DU}]^T \begin{bmatrix} x \\ y \\ z \end{bmatrix} + \vec{x}_{lin} \quad (2.49)$$

where $[x, y, z]^T$ represents the undeformed mesh and $[x', y', z']^T$ the deformed mesh in the hub fixed frame. The vector \vec{x}_{lin} is linear deformations ($[e_1, e_2, e_3]^T$ for Euler and $[u, v, w]^T$ for the present work). To ensure that the outer boundary of the meshes stay stationary a cosine decay function was used for the deformations [82].

2.2 Structural Dynamics and Vehicle Trim

The rotor system can be modeled as a second order system, similar to mass-spring-damper, which is harmonically excited by an unsteady forcing, i.e. aerodynamic loading in the rotor problem. The blade motions (both rigid and elastic) need to be calculated such that they simultaneously satisfy the vehicle trim equations and blade periodic response equations.

Finite element based methods are known to accurately model kinematic and elastic behavior in bending and torsion of slender beams. A single rotor blade, because of its large aspect ratio, can be considered as a slender beam. The rotor blade has all the 6 degrees of freedom and undergoes simultaneous flap, lag and torsion deformations. Due to non-linear coupling between various degrees of freedom, the governing equations for such a system is very complex. This coupling between the various degrees of freedom appear as cross-coupling terms in mass, stiffness and damping matrices.

2.2.1 Comprehensive Rotor Analysis

The comprehensive rotor analysis consists of four major parts. First part involves structural modeling of the rotor blade, i.e., finite element discretization of

the blade and subsequent analysis of their natural frequencies and mode shapes. The second part involves computing the unsteady forcing and aerodynamic mass, stiffness and damping matrices. In the third part, the blade equations of motion are reduced to the modal form, which are then solved using temporal finite element method. The fourth and the last part involves calculation of the control parameters generating a rotor response which would give a set of average rotor forces and moments that would satisfy the vehicle trim equations. A more detailed description of the analysis can be found in thesis work of Sitaraman, J. [82], but a brief overview is presented here.

2.2.2 Finite element discretization of the rotor blade

For a rotor with only flap bending, the blade can be discretized into two noded beam elements with two degrees of freedom per node, i.e. displacement, w and slope, w' . For a given displacement vector for the end points, $[q_1, q_2, q_3, q_4]$, such that, $q_1 = w_1, q_2 = w_1', q_3 = w_2, q_4 = w_2'$, the displacement can be written as:

$$w(x, t) = \sum_{i=1}^4 H_i q_i \quad (2.50)$$

where, H_i are the shape functions, otherwise known as Hermite polynomials [81].

To derive the system of equation of motion, Hamilton's variational principle is used. The principle can be mathematically represented as:

$$\delta \Pi = \int_{t_1}^{t_2} (\delta U - \delta T - \delta W) = 0 \quad (2.51)$$

where δU is the virtual variation of strain energy, δT is the virtual variation of kinetic energy and δW is the work done by external forces. The element mass and stiffness matrices are derived based on this principle and are given as:

$$[m_{ij}] = \int_0^1 m H_i H_j ds \quad (2.52)$$

$$[k_{ij}] = \int_0^1 (F_A H'_i H'_j + (EI_z \sin^2(\theta_o) + EI_y \cos^2(\theta_o))(H''_i H''_j)) ds \quad (2.53)$$

where EI_y and EI_z are flexural rigidities in the longitudinal and transverse directions and $F_A = \int_x^1 m x dx$. The eigen values of the resulting mass and stiffness matrices are the square of the natural frequencies of this system of equations, while the eigen vectors represent the natural vibration mode shapes.

2.2.3 Vehicle Trim

Trimming the rotor means achieving an equilibrium in space so that the net forces and moments about any point is zero. Broadly speaking, trim solutions are of two types: a) free flight trim and b) wind tunnel trim.

Free Flight Trim

For free flight or propulsive trim, it is assumed that the engine can supply the necessary power required to maintain the flight condition. The target rotor forces and moments are equal and opposite to those produced by the rest of the aircraft. For a steady flight, the comprehensive propulsive trim solution can be obtained by satisfying the three force (vertical, longitudinal and lateral), three moment (pitch, roll and yaw) vehicle equilibrium equations, flap equation and inflow equation. For example, for a specified gross weight and level flight speed, the trim solution gives the rotor pitch controls (collective θ_0 , cyclic θ_{1c} and θ_{1s}), rotor dynamics e.g. flapping ($\beta(\psi)$), vehicle orientation (longitudinal shaft tilt α_s and lateral shaft tilt ϕ_s), tail rotor pitch (collective θ_{tr}) and inflow (λ).

Wind Tunnel Trim

Wind tunnel trim (isolated rotor trim) is a simplified trim procedure where the three rotor controls are adjusted to achieve specified free flight condition. With the shaft angle always prescribed, the target values are either: a) target thrust and the hub roll and pitch moments or b) target thrust, 1/rev longitudinal and lateral flapping (β_{1c} and β_{1s}).

While a free-flight trim is a more accurate representation of the helicopter in flight, it requires a good confidence in estimating the forces and moments experienced by the fuselage, the empennage, and the tail rotor, which are often not available to the computational model. In contrast, the rotor operating thrust, and the rolling and pitching moments are more easily available.

2.2.4 Uncoupled and Coupled Trim Procedure

The method of achieving periodic blade response for a fixed control setting is known as *uncoupled trim*. This method coupled with the requirement that specific targets are met is known as *coupled trim*. For example, obtaining a rotor response such that a set of steady rotor forces and moments maintain vehicle equilibrium is a coupled approach to trim a helicopter [82]. As the trim analysis is non-linear in nature a reasonably accurate initial guess is a necessity. A trim analysis of a rigid rotor blade is conducted to find the initial control estimate. The vehicle force and moment equations and the blade flapping equations are solved using an appropriate non-linear equation solver. The response of the rotor to the initial control estimate is found by solving the rotor equations using the temporal finite element method. A force summation is conducted on the basis of the blade response obtained to yield the aerodynamic forces and moments

produced by the deformed blade. The time averaged values (over one rotor revolution) of rotor forces and moments are substituted in the appropriate vehicle trim equations to obtain the residuals of these equations. The final aim of the coupled trim procedure is to find the control estimate which drives these residuals towards zero. Newtons method, based on the evaluation of a trim Jacobian matrix, is used to find the final control estimate. A finite difference approximation is used to calculate the control Jacobian. The initial controls are perturbed one at a time and the variation of the residuals are used appropriately to find individual terms of the control Jacobian. The control settings are updated using the control Jacobian and the value of the residual vector. The whole process is conducted in a loop until the residues to the vehicle trim equations are below a specified error bound.

2.3 Coupling Structural Dynamics and Fluid Dynamics

The information exchange between the two solvers, structural dynamics and fluid dynamics, occurs at the fluid-structure interface. This transfer of information at every rotor revolution is achieved using a *Loose Coupling* [83] approach.

In the literature, there have been many studies on loose coupling. Initial studies on the UH-60A faced convergence problems due to inaccurate pitching moments which would lead to divergence of the torsional response. Earlier efforts used full potential CFD analysis which overpredicted the pitching moment magnitudes and led that divergence. In the loose coupling approach used in the present study, CFD generated normal force, pitching moments and chord force

are consistently coupled at all radial and azimuthal stations (i.e. $C_{nr}, \psi, C_{cr}, \psi$ and C_{mr}, ψ) to obtain stable high-speed solutions for the UH-60A helicopter. These aerodynamic forces are obtained in the deformed blade frame and transformed to the undeformed frame for structural analysis. The control angles are calculated using full CFD airloads and thus ensures simultaneous convergence of trim, structural dynamics and fluid dynamics. The current coupling approach uses a full wake capturing method as against the wake coupling method which was used in earlier studies [82, 84].

The loose coupling algorithm, as shown in flow chart Fig. 2.5, can be described by the following steps:

1. Initial guess for control angles and blade motions are obtained using UMARC comprehensive analysis solution. Initial lifting line airloads are also calculated $((F/M)_{LL}^{N-1})$.
2. CFD airloads $((F/M)_{CFD}^{N-1})$ are obtained using the above blade deformations and trim angles. These airloads are expected to be more reliable than the lower order lifting line airloads $((F/M)_{LL}^{N-1})$.
3. The difference between the CFD and lifting line airloads, defined as *delta* airloads, is obtained. The lifting line airload of the current iteration is corrected using this delta airload.

$$\begin{aligned}\Delta(F/M)^N &= (F/M)_{CFD}^{N-1} - (F/M)_{LL}^{N-1} \\ (F/M)^N &= (F/M)_{LL}^N + \Delta(F/M)^N\end{aligned}$$

4. The comprehensive analysis solution is now re-run with the corrected airload $((F/M)^N)$. The delta air loads are held fixed over the trim iterations.

The lifting-line air loads change from one coupled trim iteration to another and provide the air load sensitivities required to trim the rotor (control jacobian). The lifting-line air loads provide aerodynamic damping which makes the procedure stable.

5. Check for blade response and trim convergence. If the convergence condition is not satisfied return to step 2.

The final air loads are the CFD air loads and equal the sum of lifting-line air loads and the converged delta air loads. While the lifting-line airloads and delta airloads may vary, their sum, i.e. the CFD airload remain independent of the initial lifting solution.

2.4 Limitations of Current Methodology

The existing CFD/CSD coupling platform assumed a single element blade rotor and hence the fluid dynamics model had limited application on rotors. The accompanying overset mesh combination of fine blade in a coarser wake mesh could make use of the conventional hole cutting efficiently. But the conventional hole cutting could handle only a two mesh system and required that the finer blade mesh be totally embedded inside the coarse wake mesh. Thus this hole cutting method was found incapable of handling an extra mesh element due to a LE-slat. Moreover, if the slat were to be actuated with respect to the main blade for active control, it would be even more inefficient to achieve dynamic hole cutting using a conventional method. Therefore, handling a multi-element bladed rotor demanded a novel hole cutting scheme (IHC). This scheme not only can handle a multiple mesh overset system, and therefore can be more

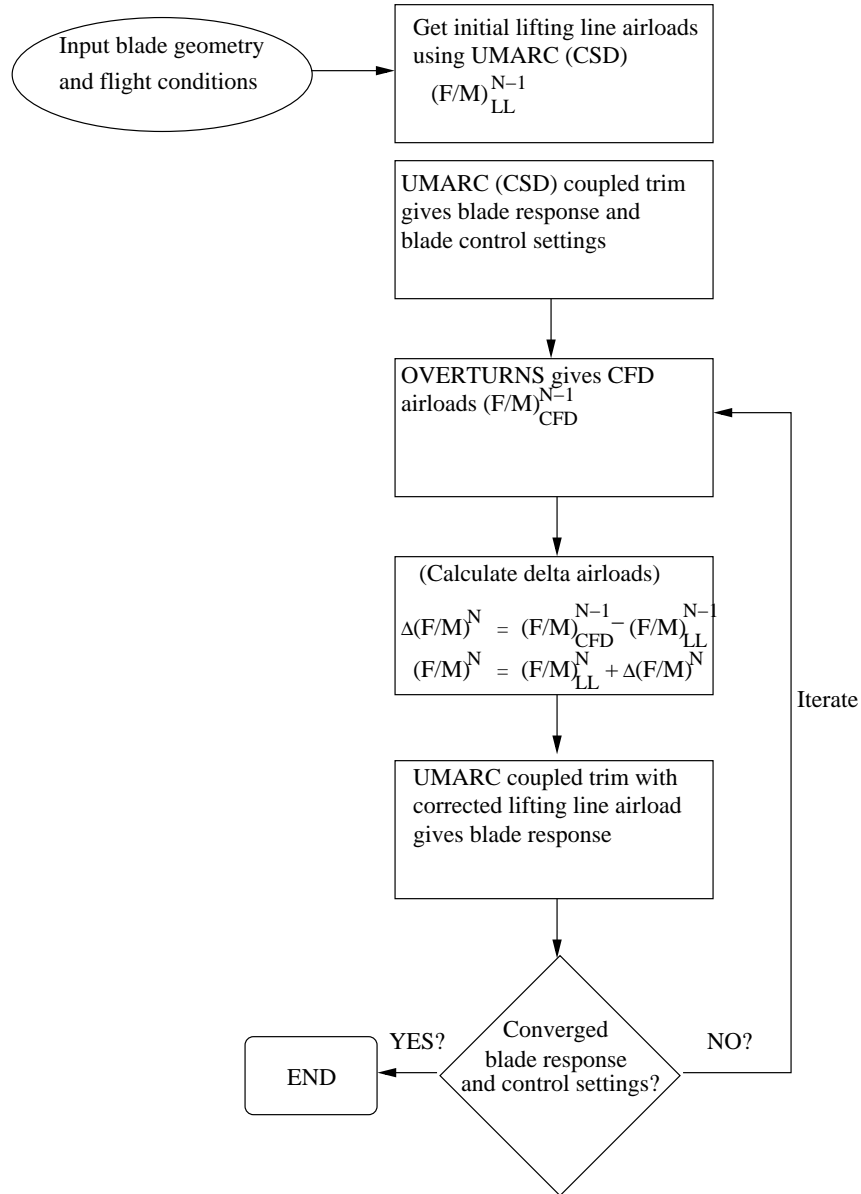


Figure 2.5: Loose Coupling Flow Chart

generic, but it also can perform more efficient dynamic hole cutting when the slat actuates. Details of this hole cutting scheme will be discussed in the following section.

The other shortcoming accompanying the assumption of single element blade

rotor was that the existing force calculation method could not handle more than one load carrying element per blade, such as in multi-element bladed rotors. The LE-Slat significantly modifies the flow physics around the main blade besides producing its own independent airloads. Therefore, its affect on the main blade airloads needs to be accounted for. This is achieved through a generalized force transfer routine that can be applied to a multi-element blade with as many elements as are attached to the main blade. This will be discussed more elaborately in the following section.

2.5 Technical Challenges and Improvements

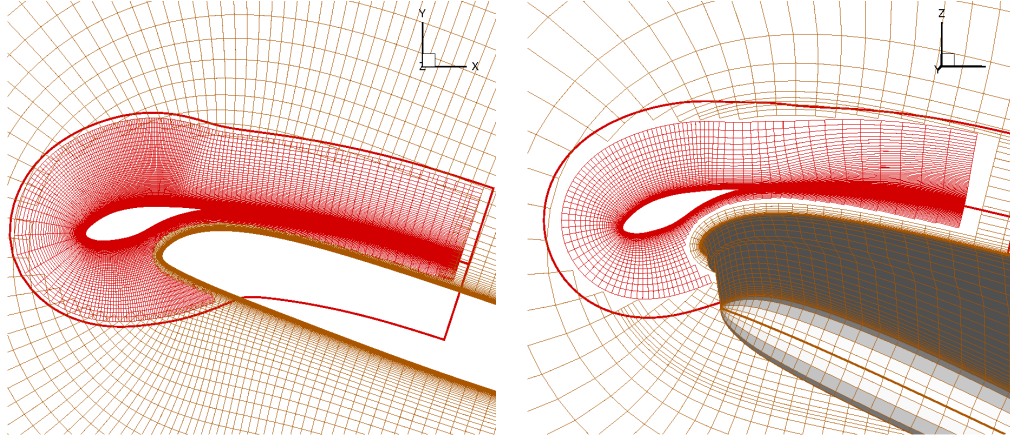
Several modifications were made to the existing OVERTURNS CFD tool to handle multi-element bladed rotors in forward flight, some of which are already mentioned in the previous section. The IHC hole cutting was implemented to handle more than a two grid overset system to establish connectivity across grids. To be able to accommodate various actuation schemes for a LE-slat, a general N/rev ($N \geq 1$) slat actuation scheme with appropriate phase offset capability is designed. Since the slat is another element rigidly attached to the main blade, it too undergoes deformation along with the main blade over the whole rotor revolution. The code is modified to handle multi-element deformation. These modifications and improvements are discussed in this section.

2.5.1 Implicit Hole Cutting

The conventional hole cutting, as described in 2.1.6, has certain limitations. Firstly, the algorithm can handle only two overset meshes and requires that one

mesh be completely embedded in the other. Therefore, this algorithm is not general enough and imposes limitations on the kinds of meshes used in the case of more complex problems when more than one body exist, as in slatted airfoil flows. Secondly, the hole cutting algorithm used in conventional hole cutting required explicit specification of the box around the bodies. This introduces complexities when the body geometry is not well defined. Moreover, when more than one bodies exist and lie close to each other (as in slatted blades), the boundaries of these boxes would overlap or intersect. This makes the problem even harder because special care must be taken to ensure no overlap between these hole cutting boxes. It is also noted that, since the box size is explicitly defined, it does not necessarily take into account the grid compatibility between the hole fringe points and the donor cells. If the grid sizes are hugely different, this might result in huge interpolation error in accuracy. Although, the hole size can be expanded outward from the body to attain grid compatibility across grid boundaries, it incurs extra computational cost. Moreover, it is not a fail proof method to ensure grid compatibility.

The implicit hole cutting (IHC) method for overset meshes developed recently by Lee and Baeder [56,85] overcomes the above mentioned problems and limitations. The advantage of the IHC algorithm is it can handle more than two meshes and therefore, is most ideally suited for problems involving multi-element airfoils, such as slatted airfoils. The IHC method does not require explicit specification of a box for hole cutting nor does it need to expand the hole size. Unlike conventional hole cutters which determine *hole* and *fringe* boundaries, IHC steps through every point in the grid system to test and select the best quality cells in multiple overlapped regions, leaving the rest as hole points. It designates the



(a) 2-D hole-cutting for MEA

(b) 3-D hole-cutting for MEA

Figure 2.6: Overset meshes in 2-D and 3-D using Implicit Hole-Cutting

mesh whose cell has the smallest volume as the *field* point at any given point in the flow domain, all other meshes are marked as *receivers*. In other words, at any point, the solution is computed on the cell having the smallest volume and interpolated at other points. The presence of the body is felt either by the progressively smaller cell sizes towards the wall or by the grid topology (for example, if all walls are located at $k = 1$). Since the hole cutting is determined by cell size, the resultant hole from the IHC algorithm is automatically optimum. More detailed comparison between the conventional and implicit hole cutting can be found in Ref. [62].

Figure 2.6 shows examples of the holes cut using the IHC technique in two-dimensional and three-dimensional grids. Notice how the mesh containing the field point switches smoothly in the region between the slat and the main airfoil sections near the leading edge of the blade airfoil.

2.5.2 Slat Actuation

The primary purpose of using a LE-slat in rotor in forward flight is to alleviate dynamic stall. This phenomenon being unsteady in nature, an actively controlled LE-slat can be expected to be more effective than a static slat. By dynamically actuating it with respect to the main blade, the rotor blade sectional property can be varied across the rotor azimuth to improve rotor performance. A general N/rev ($N \geq 1$) slat actuation mechanism is incorporated to accommodate more than $1/\text{rev}$ slat actuation. Over one period (one pitching cycle or one rotor revolution), the slat oscillates between two predefined optimum slat configurations (discussed more in the results sections). This requires the movement of the slat in two degrees of freedom,

1. periodic rotation (pitch up and down) of the slat about a predefined pivot point with an amplitude defined by the optimum slat configurations and,
2. periodic translation of the pivot point with an amplitude defined again by the optimum slat configurations.

The equation of motion of actuation mechanism is:

$$\Delta\theta = \sum_1^N \theta_i \cos(i\psi + \phi_i) \quad (2.54)$$

$$\theta = \theta_0 + \Delta\theta \quad (2.55)$$

$$\Delta xc = \sum_1^N xc_i \cos(i\psi + \phi_i) \quad (2.56)$$

$$\Delta yc = 0 \quad (2.57)$$

$$\Delta zc = \sum_1^N zc_i \cos(i\psi + \phi_i) \quad (2.58)$$

$$[xc, yc, zc] = [xc_0, yc_0, zc_0] + \Delta [xc, yc, zc] \quad (2.59)$$

$$(2.60)$$

where, θ_i is the i th harmonic component of the total slat angle displacement $\Delta\theta$, and θ_0, θ are the initial and absolute slat angles, respectively, defined with respect to the main blade chord. Similarly, $\Delta [xc, yc, zc]$ is the i th harmonic component of the total displacement of the slat rotation pivot point, and $[xc_0, yc_0, zc_0], [xc, yc, zc]$ are the initial and absolute co-ordinates, respectively, of the pivot point. The components xc, yc and zc refer to the chordwise, spanwise and blade normal directions, respectively.

2.5.3 Multi-element Mesh Deformation

The deformation procedure applied to the other elements, such as a LE-slat rigidly attached to the main blade, is the same as that of the main blade itself. The deformations of these elements are consistently done with respect to the main blade elastic axis. This allows the use of the same transformation matrix $[[T_{DU}]^T$ as that used for the main blade to deform the slats (see Fig. 2.7).

2.5.4 Force Calculations on a Multi-Element Rotor Blade

The comprehensive analysis used in the present study does not incorporate the slat dynamics. It interacts with the blade structure through its airload contribution evaluated through CFD computations. The LE-slat being a separate blade element, experiences its own airloads. For the present CFD/CSD modeling purpose, it is assumed that the main blade experiences these airloads on the slat. The airloads (forces and moments) of the slat need to be transferred to the main element through appropriate means. The following sections describe the force transfer procedure for two dimensional airfoils and for a three dimensional rotor.

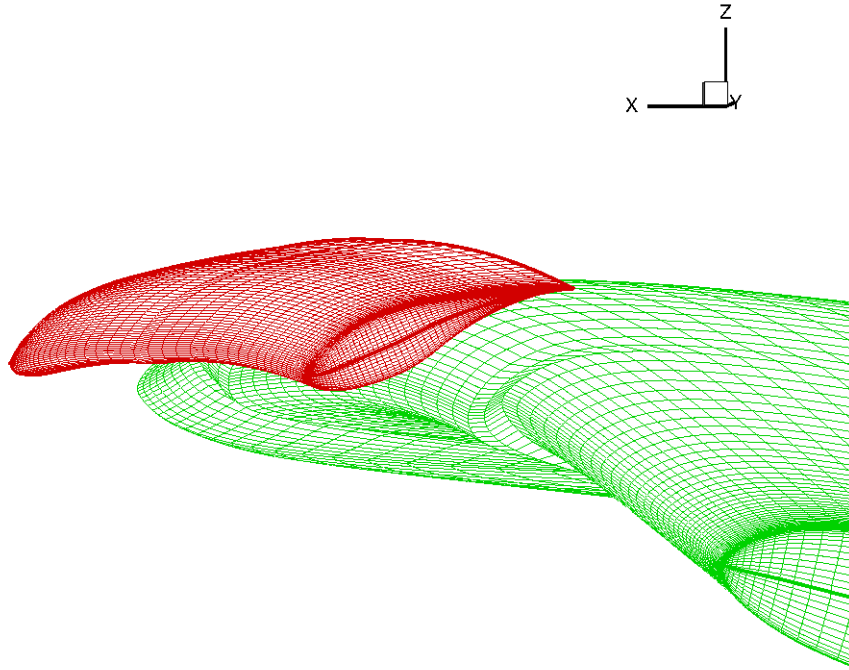


Figure 2.7: Slat deformation

Force Transfer in 2D Airfoil

The force transfer from the slat to the main element follows the following steps (see Fig. 2.8(a)):

1. Forces and moments of all the elements (LE-slats and main element) are calculated with respect to the main element quarter chord, $[x_{qc1}, y_{qc1}]$.
2. For the ease of analysis and comparison with the baseline airfoil, the combined slat and main element are treated as one element. In that case, the forces and moments are transferred to the effective quarter chord, $[x_{qc2}, y_{qc2}]$.

Forces get added and transferred to this quarter chord:

$$F_{\{x,y\}-tot} = F_{\{x,y\}-s} + F_{\{x,y\}-m} \quad (2.61)$$

3. The moment calculated in step 1 ($M_{z,1}$), already includes the contribution from the slat airloads. If required for the analysis, the moment is now transferred to the effective quarter chord:

$$M_{z,2} = M_{z,1} - (F_{x,s} + F_{x,m})\Delta x + (F_{y,s} + F_{y,m})\Delta y \quad (2.62)$$

where, $\Delta(\cdot) = (\cdot)_{qc2} - (\cdot)_{qc1}$.

Non-dimensional parameters such as, Cl, Cd, Cm , are now defined with respect to the effective combined chord of the element.

Force Transfer in Rotor

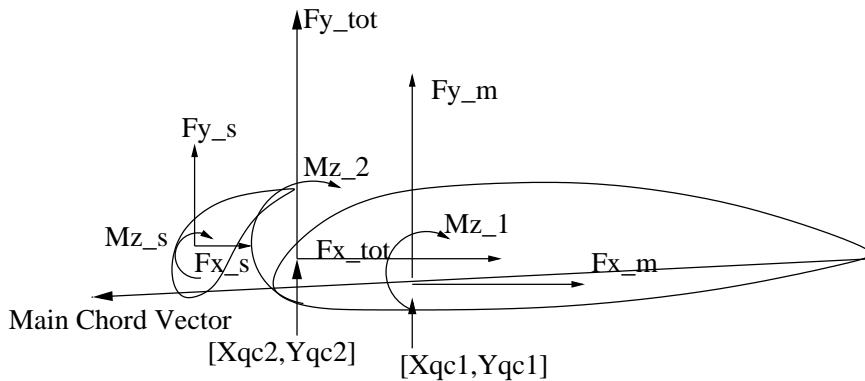
The force transfer procedure for a multi-element rotor blade is described in the flow chart presented in Fig. 2.9. The procedure can be summarized by the following steps:

1. Define the elastic axis (E.A.) line of the rotor main blade.
2. Compute the forces/moments with respect to the rotor blade E.A.
3. If the element considered is a main blade, transfer loads from the main blade to the deformed E.A.
4. If the element is a slat (or other external element other than the main blade) identify its spanwise stations nearest to the deformed E.A. stations.
5. Linearly interpolate in span the slat loads from the identified stations to their corresponding deformed E.A. stations.

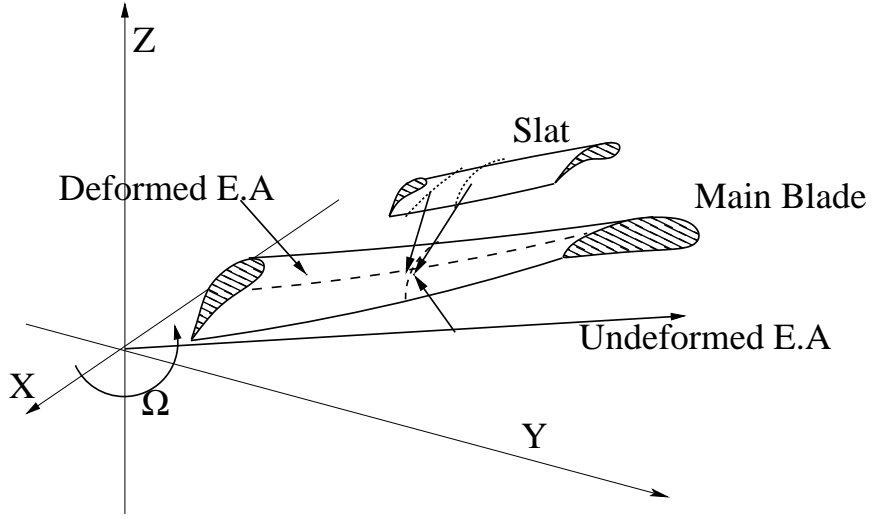
6. Add the loads from all the elements (including the main blade) at E.A. stations and then transfer them back to the main blade stations.

2.6 Summary

In this chapter, we discussed the three major aspects of methodology, namely, the fluid dynamics, the structural dynamics and the fluid-structure interaction. The limitations of the existing model are discussed and the implemented improvements required to handle multi-element bladed rotors were described.



(a) Force Transfer on 2D Airfoil



(b) Force Transfer on Rotors

Figure 2.8: Slat Force Transfer to Main Element on (a)2D Airfoil and (b)Rotor

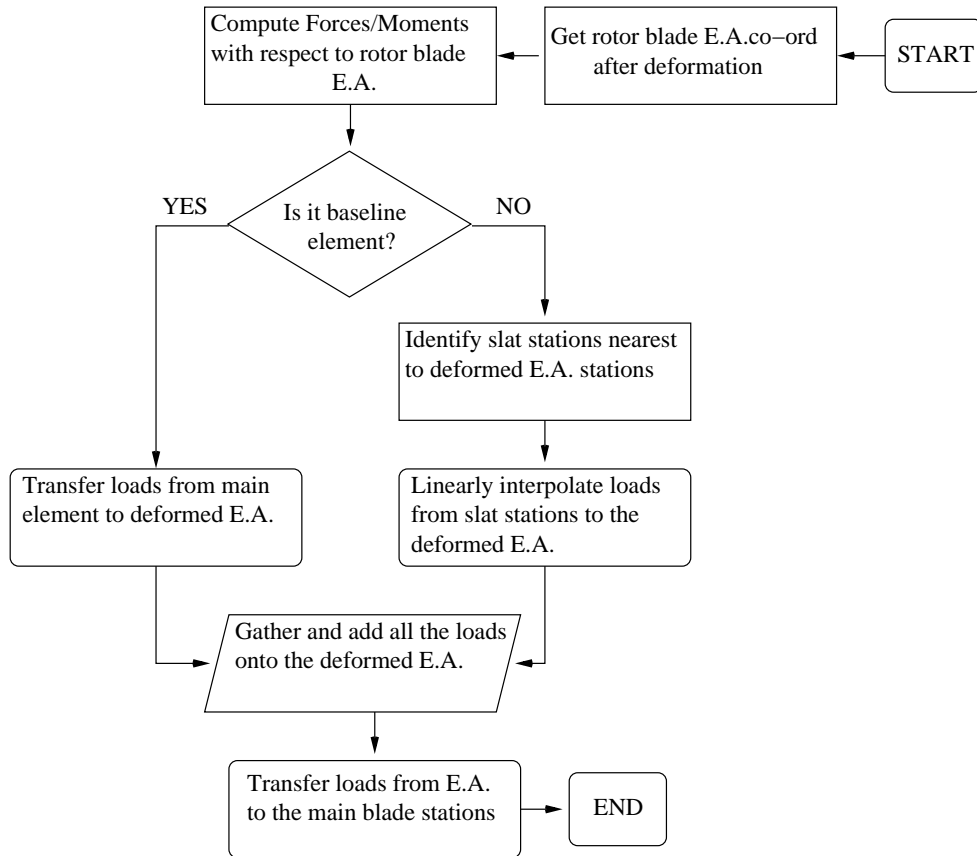


Figure 2.9: Flow Chart describing force transfer for Multi-element Rotor

Chapter 3

Validation

One of the major objectives of the present work is the development of a CFD overset-mesh solver for simulating multi-element airfoil (MEA) rotor blades. Unfortunately, there is currently no test data available that is suitable for fully validating such a CFD solver. However, there are available 2-D wind tunnel experimental data for validating airfoils with slats and full-scale flight test data for validating rotor blades without slats. Therefore, the validation will be performed in two stages:

1. Validation of the CFD solver with available 2-D wind-tunnel experiments in static and dynamic flight conditions, and
2. Validation of the 3D CFD solver (coupled with a structural solver) against available helicopter flight test data.

The wind tunnel experiment considered for the first stage of validation of the solver is a compressible and high Reynolds Number (on the order of a few millions) flow on SC2110 airfoil. Lorber et al. [53] conducted extensive 2-D wind-tunnel experiments on an SC2110 airfoil with a slat, in both steady and unsteady flight conditions. The tests were conducted in the UTRC Main Wind Tunnel,

using the 33in wide by 8ft high Two Dimensional Channel (TDC). The model chord was 24in. The test Mach number range was 0.2 to 0.75, but for the present work, the test data for only the Mach numbers of 0.3 and 0.4 are considered. The slat geometry was carefully designed to promote better tailoring of the flow around the leading edge of the main airfoil section and, therefore, achieve high $C_{l_{max}}$ values compared to the baseline airfoil. The experiments present an ideal dataset to determine the capabilities of the CFD solver. Computations are performed to match the measured conditions of the experiments in steady angle-of-attack sweeps as well as a dynamic pitching airfoil with static slat.

The second stage of validation first involves extension of the CFD solver to handle multi-element (slat) bladed rotor flows. This 3-D CFD solver is the Overset Transonic Unsteady Reynolds-averaged Navier-Stokes (OverTURNS). The next step is the *loose* coupling of the solver with a comprehensive Computational Structural Dynamics (CSD) solver, namely University of Maryland Advanced Rotorcraft Code (UMARC). Final step is the validation of the coupled CFD/CSD platform with available flight test data for a moderate speed high altitude flight condition, C9017. This chapter describes the aforementioned stages of validation in detail.

3.1 Steady State Airfoil: SC2110 with S-1 and S-6

This section compares the airload predictions by CFD for slatted airfoils with steady experimental data. It also investigates the physical nature of the flow on the airfoil and the favorable influence of slats on the flow towards performance

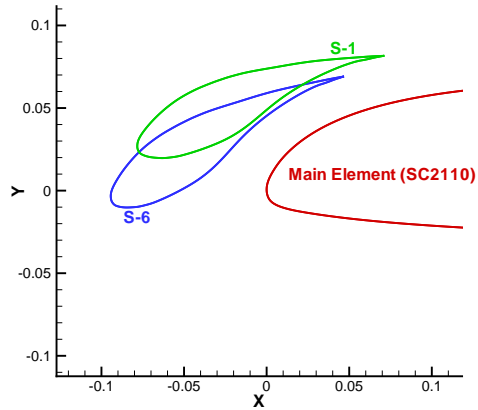


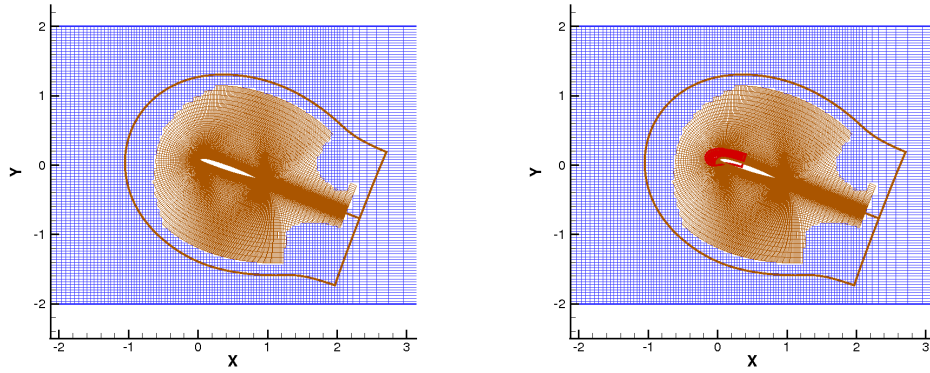
Figure 3.1: S-1 and S-6 slat configurations with respect to the baseline airfoil [55].

improvements.

The steady state computations performed on the SC2110 baseline airfoil are with two different slat configurations, namely, S-1 and S-6 (see Fig. 3.1), for which experimental measurements are available. As mentioned previously, these configurations represent the low-drag and the high-lift slat orientations for the multi-element airfoil section. Note that a lower-drag position can be achieved by moving the slat further up (with reduced maximum lift, e.g. see Ref. 53). Steady lift and pitching moment coefficients are computed for angle of attack sweeps over a range of $\alpha = [-4^\circ : 24^\circ]$ at $Re = 4.14 \times 10^6$, $M_\infty = 0.3$.

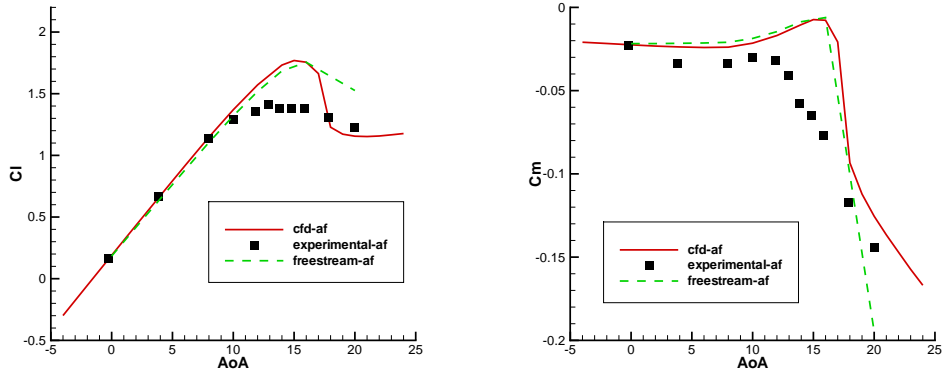
Figure 3.2 shows the overset computational meshes used in the current work. The slat and the blade meshes are body-fitted C-grids with, respectively, 317×97 and 365×138 points in the wraparound and normal direction, respectively. These body-fitted grids are embedded in a background wind-tunnel mesh with grid size 151×101 to study the effects of the wind-tunnel wall on the aerodynamic behavior of the multi-element airfoil.

The experimental data was obtained in a wind-tunnel where the height of the



(a) Baseline airfoil in Wind Tunnel (b) Slat and Main Element in Wind Tunnel

Figure 3.2: SC2110 airfoil computational mesh with and without the slat mesh embedded in the background wind-tunnel mesh at an angle of attack $\alpha = 18^\circ$.



(a) C_L vs α

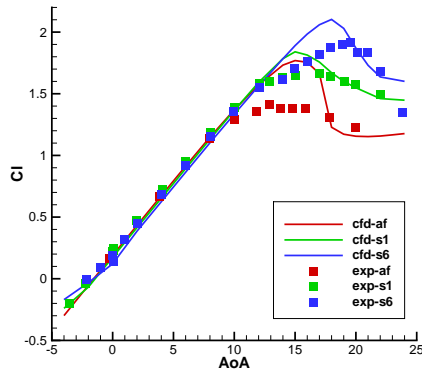
(b) C_M vs α

Figure 3.3: Effect of wind tunnel wall correction on lift and pitching moment coefficients of the main airfoil section, $Re = 4.14 \times 10^6$, $M_\infty = 0.3$.

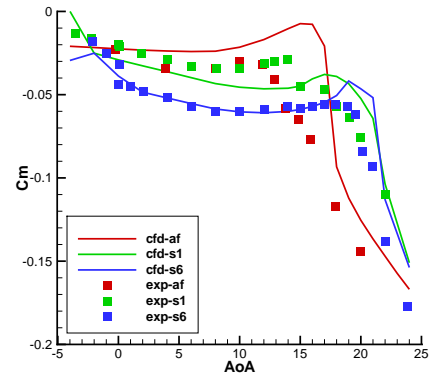
wind-tunnel was four main airfoil element chords. It is, therefore, necessary to account for the wind-tunnel wall effects on the measurements. To gain a better insight into the wind-tunnel interference effects, computations are performed for angle of attack sweeps with and without the wind-tunnel background mesh

for the main airfoil element. Figure 3.3 compares the relative lift and moment coefficients on the main element in free stream and that in the wind tunnel with experimental measurements. The results indicate that there is considerable wind-tunnel interference on the measurements especially near the static stall region. Accounting for these effects, improves the predictions of the sectional lift coefficients considerably. Marginal improvements are observed in the prediction of the moment stall break point for the airfoil in the wind tunnel compared to that in the free stream. However, observing the notable effect of wind tunnel on lift prediction, all further validation studies are done in a wind tunnel.

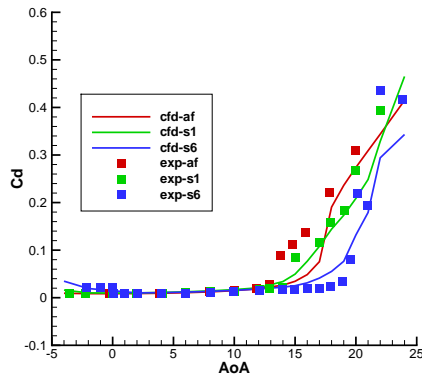
Figure 3.4 compares the computational predictions of the lift and pitching moment coefficients for the airfoil section with and without the leading-edge slat over a range of angle of attack. In the figures, the non-dimensional Cl and Cm values for the multi-element airfoil is obtained by normalizing the forces and moments using the effective chord of the combined slat-airfoil. The benefits of the S-6 configuration is evident from both the experiments and the computations of the lift coefficients. However, the 33% increase in the stall margin comes at an increased nose-down pitching moment penalty over the entire angle of attack range. This is not surprising if it is noted that the introduction of a slat increases the effective camber of the combined airfoil section. Further, because of the augmented lift due to favorable gap effects of slat, e.g. reduced separated flow, the pitch down moment about the effective quarter chord of the slatted airfoil is larger than the baseline airfoil. The computed lift coefficients show good agreement with measured values at lower angles of attack for both with and without the slat, but the values are over predicted near the lift stall event. For the baseline airfoil, the lift stall point is predicted slightly late. The mo-



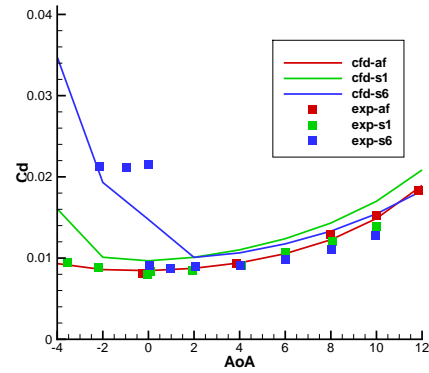
(a) C_l vs α



(b) C_m vs α



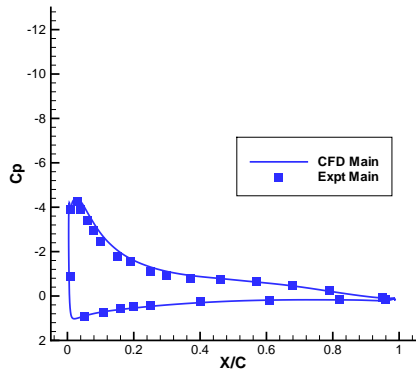
(c) C_d vs α



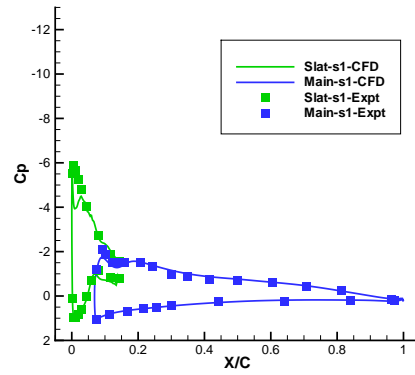
(d) C_d vs α (zoomed)

Figure 3.4: Steady airload validation on baseline airfoil and baseline with S-1 and S-6 slat configurations for $Re = 4.14 \times 10^6$, $M_\infty = 0.3$

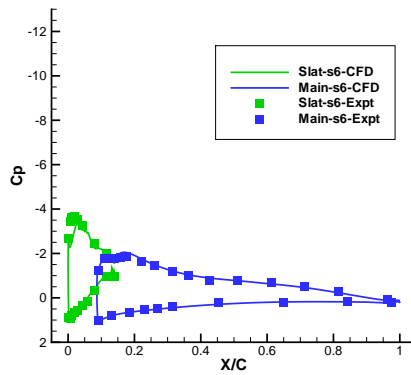
ment predictions show a slight delay in the onset of moment stall for all airfoil configurations, with baseline moment stall prediction being the most delayed. From the drag plot it is observed that while the slatted airfoils consistently over predict drag values, especially at lower angles (see Fig. 3.4(d)), the baseline, on the other hand, slightly under predicts the drag values at these lower angles, i.e. for the range of $\alpha \in [4^\circ, 10^\circ]$.



(a) Baseline surface C_p



(b) Slat-S1 surface C_p

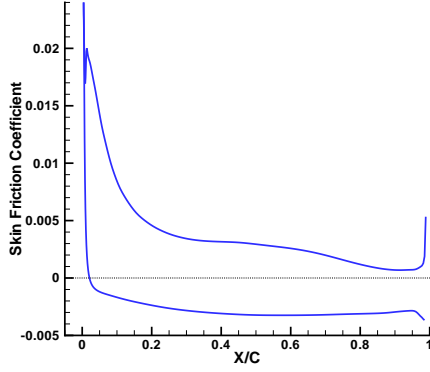


(c) Slat-S6 surface C_p

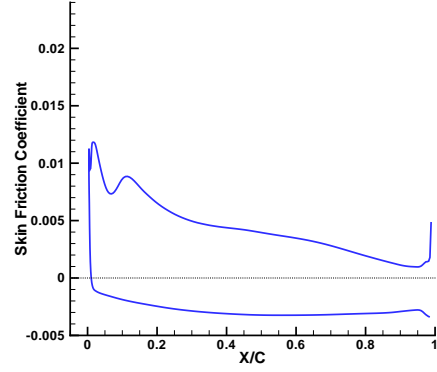
Figure 3.5: Variation of the non-dimensional pressure coefficient over the airfoil surface with and without the slat, $Re = 4.14 \times 10^6$, $M_\infty = 0.3$, $\alpha = 10^\circ$

3.1.1 Flow Physics: Presence of Leading Edge Vortex

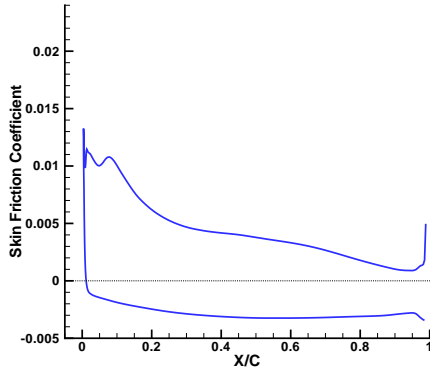
The physics governing the aerodynamics of a slatted airfoil can be understood better by examining the surface pressure coefficients and the streamlines. Figure 3.5 compares the predictions with the experiments for an angle of attack that is away from baseline stall point, at $\alpha = 10^\circ$. As the plots show, the predictions are in good agreement with the experiment and therefore the airloads, especially



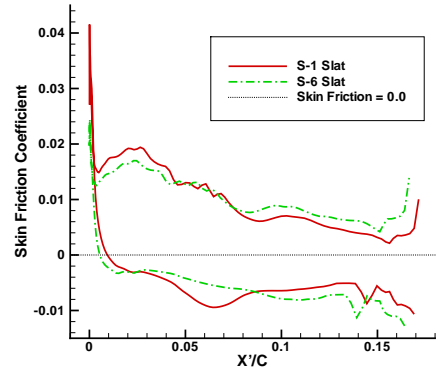
(a) Baseline airfoil C_f



(b) Slat-S1 main element C_f



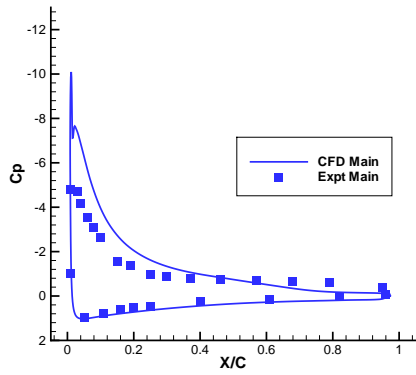
(c) Slat-S6 main element C_f



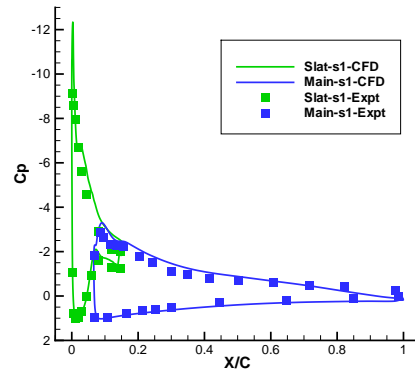
(d) Slat S-1 and S-6 C_f

Figure 3.6: Skin friction coefficient (C_f) over the airfoil surface with and without the slat, $Re = 4.14 \times 10^6$, $M_\infty = 0.3$, $\alpha = 10^\circ$.

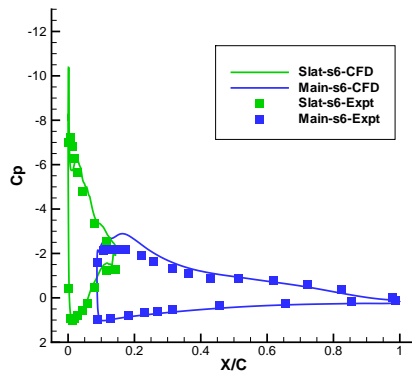
lift and drag values, are also well predicted. The flow is fully attached for all the configurations and hence the CFD performs well at such lower angles. The predicted surface skin friction values, shown in Fig. 3.6 further confirm the attached behavior of the flows on all configurations. It must be mentioned here that, for the sake of comparison, the slats are rigidly translated such that their leading edge is at the origin, i.e. $X' = X - X_{LE}$ for the slat in Fig. 3.6(d), X_{LE} being



(a) Baseline surface C_p



(b) Slat-S1 surface C_p

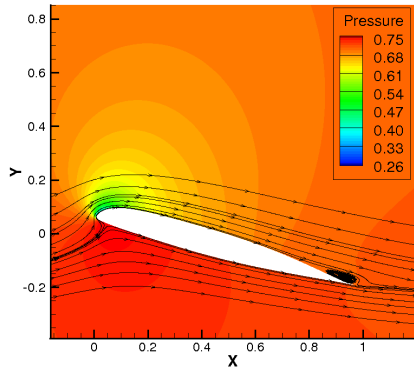


(c) Slat-S6 surface C_p

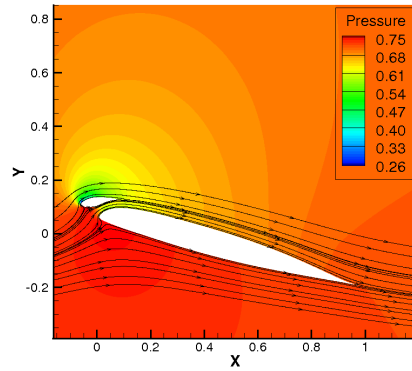
Figure 3.7: Variation of the non-dimensional pressure coefficient over the airfoil surface with and without the slat, $Re = 4.14 \times 10^6$, $M_\infty = 0.3$, $\alpha = 15^\circ$.

the actual X -co-ordinate of the corresponding slats. The figures clearly show that skin friction peak is significantly reduced (approximately by 50%) near the main element leading edge due to the slat.

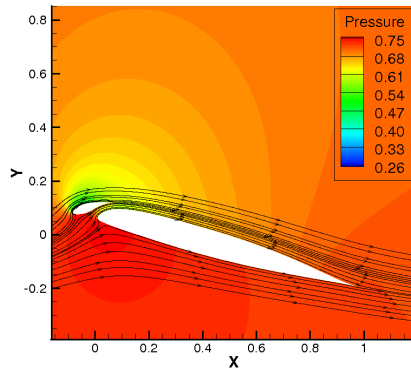
Figures 3.7 and 3.8 show the C_p distribution and the streamlines with pressure contours in the flow field for an angle of attack that is near the baseline stall point, at $\alpha = 15^\circ$. The over prediction of the suction peak near the baseline leading



(a) Baseline: Limited BL Separation



(b) Slat-S1: No BL Separation



(c) Slat-S6: No BL Separation

Figure 3.8: Streamlines with pressure contours; $Re = 4.14 \times 10^6$, $M_\infty = 0.3$, $\alpha = 15^\circ$.

edge clearly explains its over prediction of lift at this point. It is observed that the discrepancy in surface pressure prediction with experiment for the slatted airfoil cases is not large enough to cause noticeable disagreement in their integrated airload values. It is further observed that at this angle of attack, the boundary layer (BL) on the baseline airfoil is already beginning to separate at the trailing edge (TE) (Fig. 3.8(a)), whereas that on the slatted airfoils is still attached throughout (Fig. 3.8(b), 3.8(c)). However, a closer look at the streamlines near

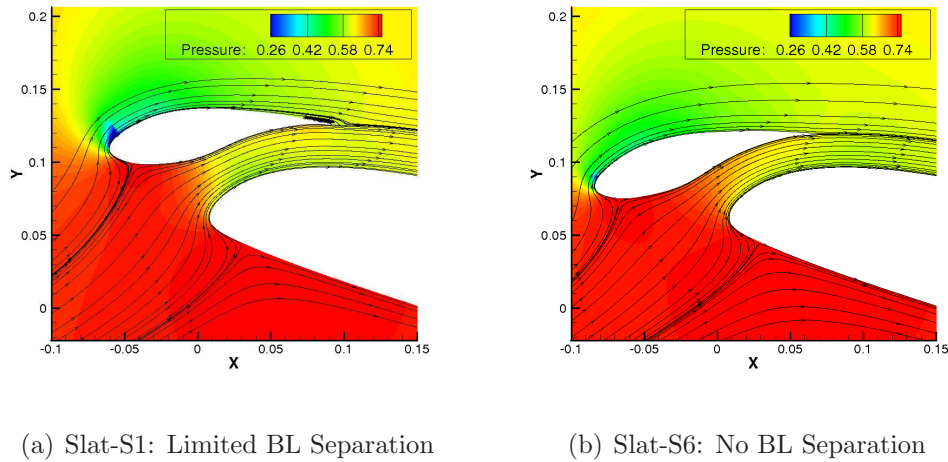
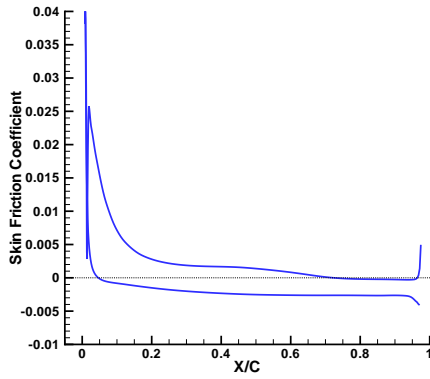


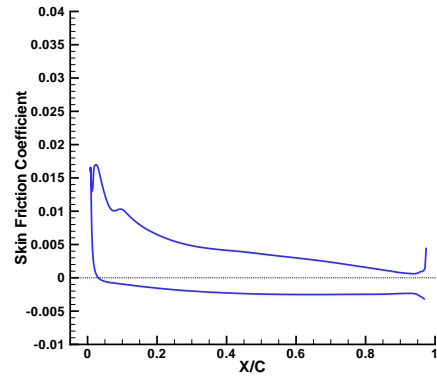
Figure 3.9: Streamlines with pressure contours on slats; $Re = 4.14 \times 10^6$, $M_\infty = 0.3$, $\alpha = 15^\circ$.

the slats shows that while S-1 experiences a light TE separation (Fig. 3.9(a)), S-6 still maintains an attached BL. A further point to note here is that, even though the slat experiences light stall on itself, it still helps sustain attached flow on the main element. These observations correspond well with the skin friction values shown in Fig. 3.10. The zero or negative skin friction values near the trailing edge of baseline airfoil suggests a trailing edge separation at this angle. But, the skin friction values on the main airfoil with slat S-1 and S-6 are consistently positive, suggesting a fully attached behavior of the flow on the main element, although separated (and reverse) flow regions on the upper surface (especially on S-1) may exist (see Fig. 3.10(d)). The slat S-1 shows more separation than S-6.

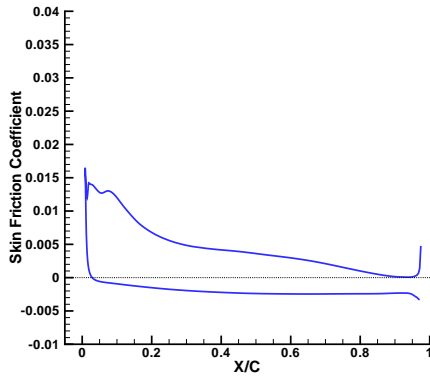
Figures 3.11 and 3.12 show the C_p distribution and the streamlines with pressure contours, respectively, in the flow field at a high angle of attack ($\alpha = 18^\circ$). A steep adverse pressure gradient is observed on the upper surface of the baseline main airfoil element (Fig. 3.11(a)), the flow is unable to negotiate the adverse



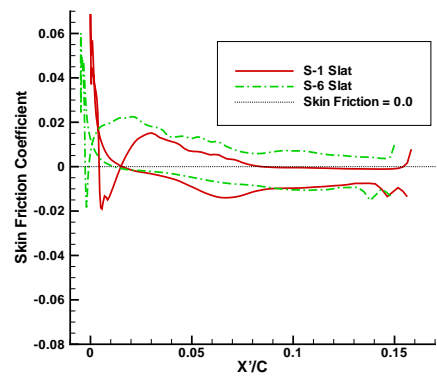
(a) Baseline airfoil C_f



(b) Slat-S1 main element C_f



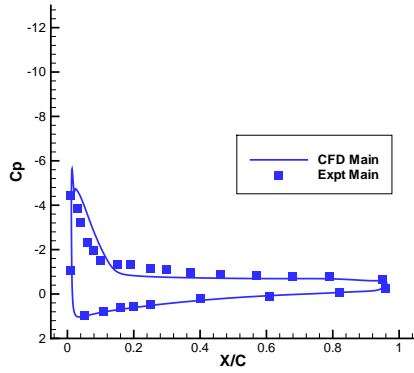
(c) Slat-S6 main element C_f



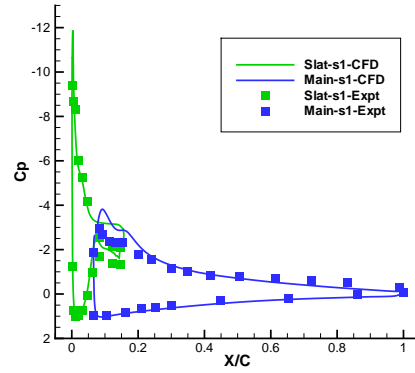
(d) Slat S-1 and S-6 C_f

Figure 3.10: Skin friction coefficient (C_f) over the airfoil surface with and without the slat, $Re = 4.14 \times 10^6$, $M_\infty = 0.3$, $\alpha = 15^\circ$.

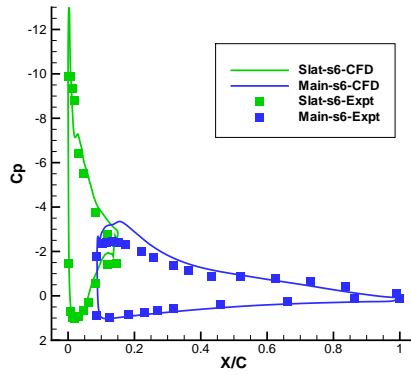
pressure gradient and the boundary layer is completely separated as seen in Fig. 3.12(a). In contrast, the introduction of a slat element relieves the huge suction peak off the main element leading edge (LE) to the slat element LE, i.e. the slat ‘protects’ the main element LE, and thus the main airfoil element sees a considerably moderate pressure gradient on its upper surface at the same angle of attack – see Fig. 3.11(c). This is one of the favorable gap effects due to a



(a) Baseline surface C_p



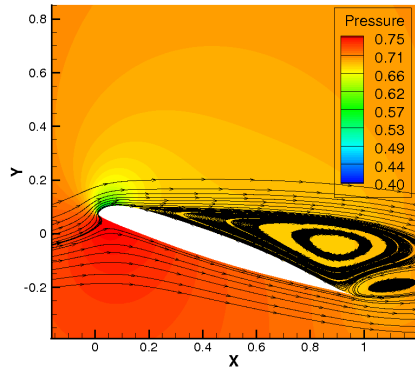
(b) Slat-S1 surface C_p



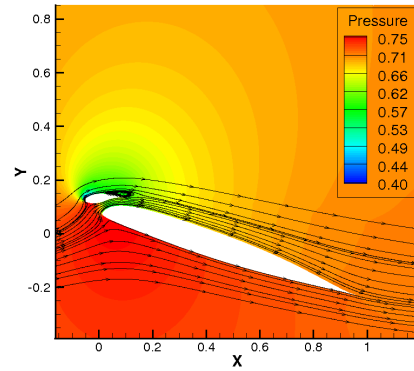
(c) Slat-S6 surface C_p

Figure 3.11: Variation of the non-dimensional pressure coefficient over the airfoil surface with and without the slat, $Re = 4.14 \times 10^6$, $M_\infty = 0.3$, $\alpha = 18^\circ$

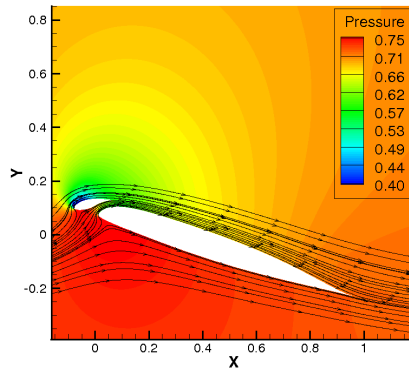
slat discussed in the Introduction chapter. Figure. 3.12 further corroborates the observations made from the surface pressure plots. While, Fig. 3.12(a) shows the presence of a strong stall vortex, and hence a separated flow at $\alpha = 18^\circ$, the other two Figs. 3.12(b) and 3.12(c) show a very well attached flow on the main element. Figure 3.12(b) shows, although slat S-1 experiences a mild stall and separated flow (Fig. 3.13(a)), the BL on the main element still stays attached,



(a) Baseline: BL Separation



(b) Slat-S1: Limited BL Separation



(c) Slat-S6: No BL Separation

Figure 3.12: Streamlines with pressure contours; $Re = 4.14 \times 10^6$, $M_\infty = 0.3$, $\alpha = 18^\circ$

demonstrating again how the slat 'protects' the main element from BL separation. The flow remains attached on slat S-6 in Fig. 3.13(b) because the slat is oriented at a lower free stream angle than S-1, thereby showing that S-6 is more effective at larger angles. Skin friction plots in Fig. 3.14 corroborate the observation about the flow physics made above. The baseline upper surface experiences zero or negative values over a wide area, which suggests deep stall, but both the S-1 and S-6 slatted main element shows positive skin friction values even at this

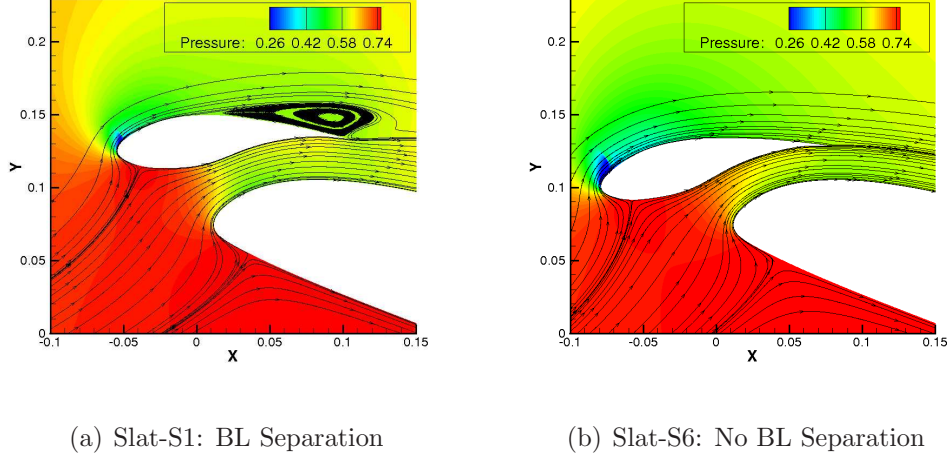
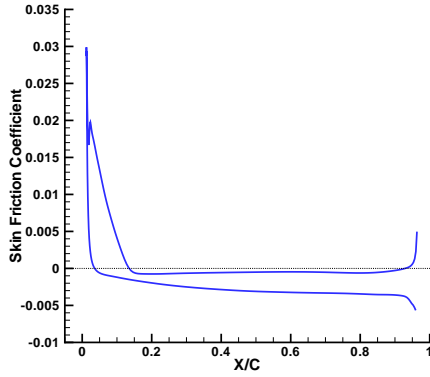


Figure 3.13: Streamlines with pressure contours on slats; $Re = 4.14 \times 10^6$, $M_\infty = 0.3$, $\alpha = 18^\circ$.

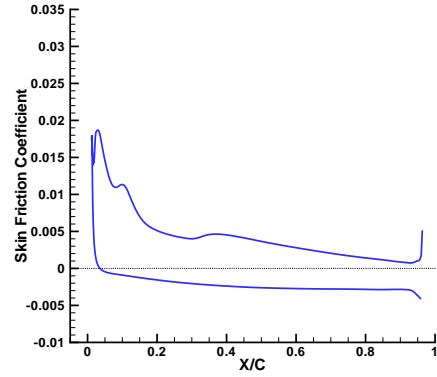
large angle. Although, the slat S-1 upper surface experiences negative values (shown in Fig. 3.14(d)) over a wider range (consistent with Fig. 3.12(b)), the S-6 upper surface skin friction is dominantly positive and hence more attached than the S-1 slat. Finally, the slat skin friction peaks are drastically reduced, which plays a crucial role in over all airfoil drag reduction.

3.1.2 Boundary Layer Profile: Effect of Slat

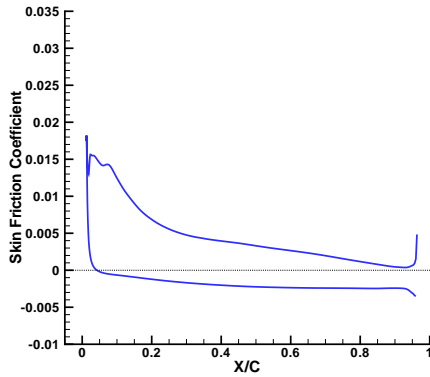
The favorable gap effects of a slat can be better appreciated if the boundary layer profile on the main airfoil is examined. Figure 3.15 shows how the slat significantly changes the BL characteristics. The 'slat effect' (described in Introduction chapter) at both 10° and 18° angles, results in reduced velocity near the main element leading edge (at 5% chord from LE) which results in its reduced pressure peaks (Figs. 3.5(c) and 3.11(c)). The tangential velocity (U_t) profiles at $\alpha = 10^\circ$ (Fig. 3.15(a)) at 10% and 50% chord locations show the process of



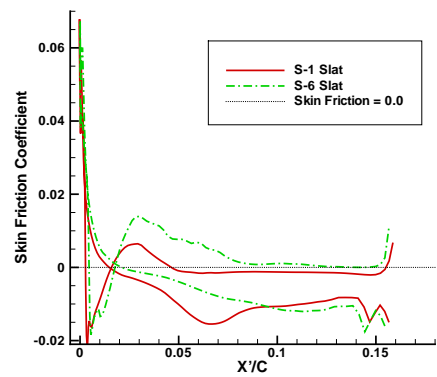
(a) Baseline airfoil C_f



(b) Slat-S1 main element C_f



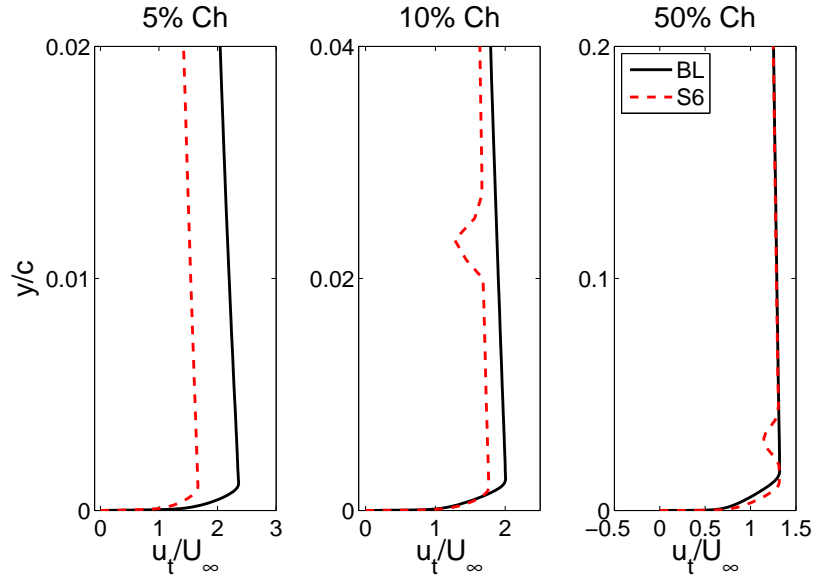
(c) Slat-S6 main element C_f



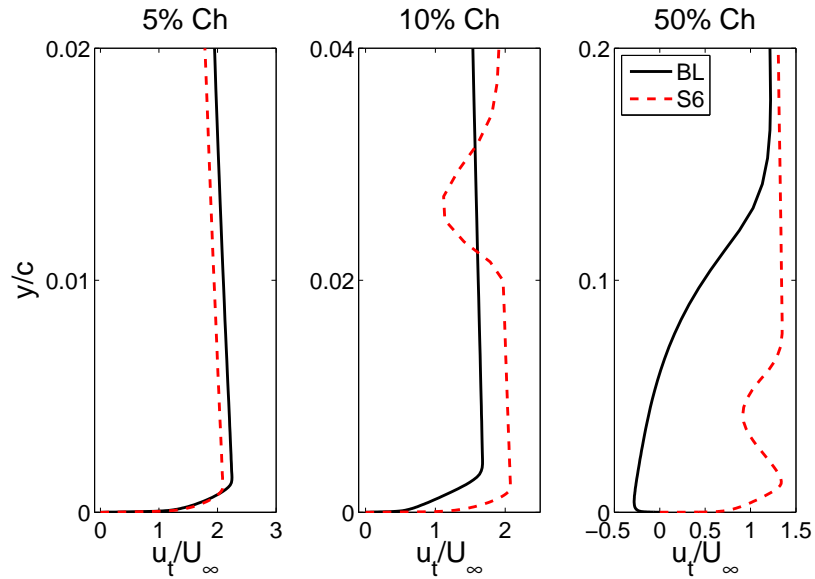
(d) Slat S-1 and S-6 C_f

Figure 3.14: Skin friction coefficient (C_f) over the airfoil surface with and without the slat, $Re = 4.14 \times 10^6$, $M_\infty = 0.3$, $\alpha = 18^\circ$

the slat wake interacting and finally merging with the main element boundary layer to develop into a confluent boundary layer (CBL). At this angle, the flow remains attached for both the baseline and the slatted S-6 main element. Similar wake-boundary layer interaction is observed for the slatted S-6 main element for $\alpha = 18^\circ$ (Fig. 3.15(b)), resulting in a CBL which extends deeper into the flow from the wall as compared to the flow at 10° . This thick CBL is effective in



(a) U_t/U_∞ profile at 10°



(b) U_t/U_∞ profile at 18°

Figure 3.15: Comparing BL profile on baseline airfoil and that with slat S-6, $Re = 4.14 \times 10^6$, $M_\infty = 0.3$, $\alpha = 10^\circ$ and 18° .

withstanding a larger pressure gradient over the main element boundary than the boundary layer of the baseline airfoil. Therefore the flow remains attached

for the slatted main element even at the 50% chord location, while the flow is already well separated for the baseline main element at this location.

3.1.3 Limitations of CFD Prediction: Turbulence Transition?

The assumption of fully turbulent flow in the present study may not resolve the right physics if the actual flow has certain laminar regions on the airfoil, which may exist near the leading edges of the main element and slat. Identifying the correct laminar regions is essential to predicting a laminar separation bubble, especially at larger angles, and consequently in predicting the right stall break points in lift, moment or drag airloads. This section investigates the effect of prescribed turbulent transition regions in the flow, and sees if it explains the lack of good CFD prediction at larger angles and near stall, e.g. surface pressure figures in Fig. 3.7.

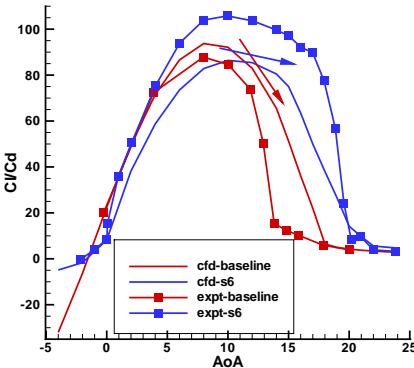
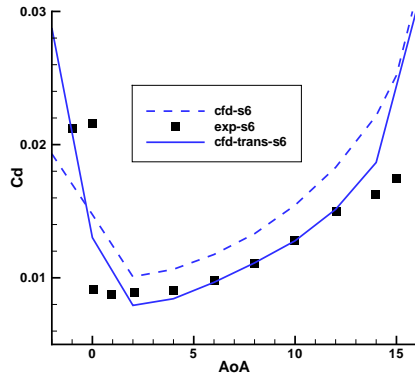
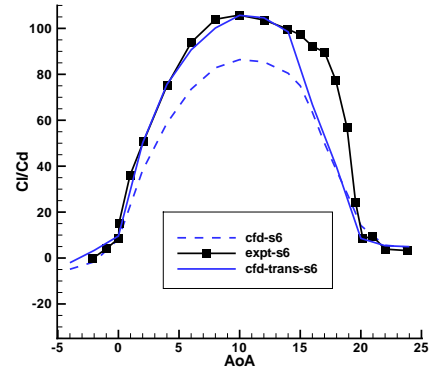


Figure 3.16: Cl/Cd for baseline and S-6

Considering the Cl/Cd curve for the baseline and a slatted S-6 configuration, we observe from Fig. 3.16 that the CFD over predicts airload values on the

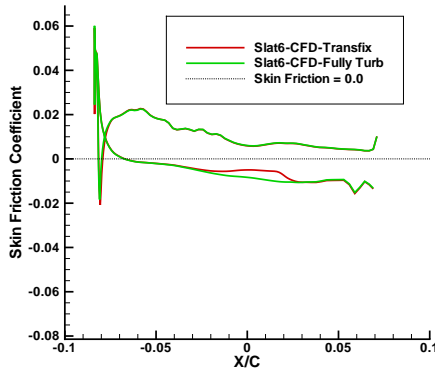


(a) C_d for S-6 with transition fix

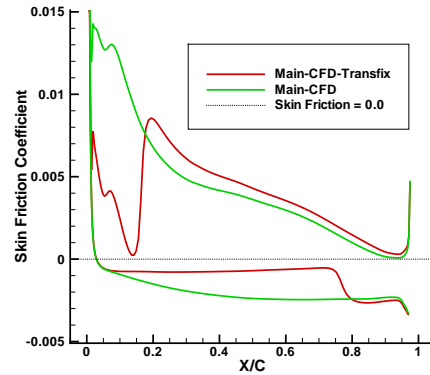


(b) Cl/Cd for S-6 with transition fix

Figure 3.17: Effect of transition fix on slatted S-6 airfoil; $Re = 4.14 \times 10^6$, $M_\infty = 0.3$



(a) Skin Friction on slat S-6



(b) Skin Friction on main element

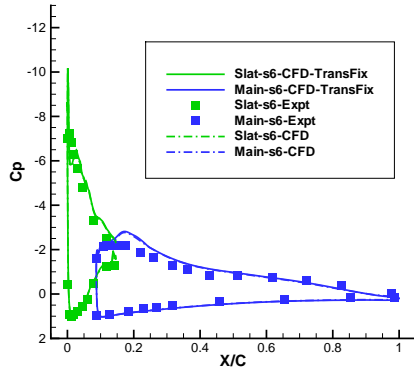
Figure 3.18: Skin friction with fully turbulent and with laminar-turbulent transition fixed flow on slatted S6 airfoil at $\alpha = 15^\circ$

baseline and under predict that on the slat-S6 airfoil. The higher Cl/Cd values for the baseline case can be explained by large Cl values predicted by CFD (Fig. 3.4(a)). But it does not explain the lower computed values of Cl/Cd for the slat-S6 airfoil. More careful examination reveals that the Cd values for the

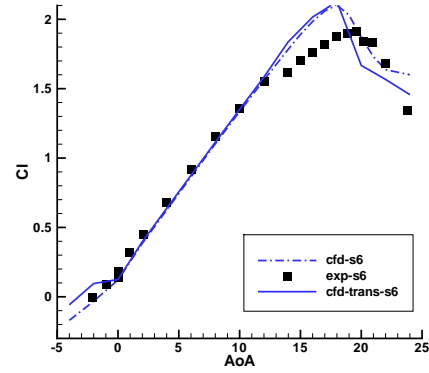
slatted airfoil are predicted higher than the experiment, which contributes to lower computed values of lift-to-drag ratio. Assuming laminar flows on certain appropriate areas on an airfoil, e.g. near the leading edges of slat and main element, would result in reduced values of skin friction, which in turn would result in reduced drag prediction. The laminar region is expected to vary with angle of attack and therefore the solver makes use of a 'table look up' approach to ascribe laminar and turbulent regions on both the elements (slat and main airfoil) for different α values. Using an appropriate fix for laminar-turbulent regions, the drag prediction can be improved, as shown in Fig. 3.17(a). This results in more accurate prediction of Cl/Cd values, at least at lower angles. See Fig. 3.17(b).

Figure 3.18 compares the skin friction values on S-6 and main element for the two flow conditions. The figures clearly show the effect of fixing the laminar region in the vicinity of the leading edge regions of the airfoil elements. The laminar-to-turbulent transition region is characterised by the sudden jump in the skin friction values both on the upper and lower surfaces. The reduced skin friction value influences the drag prediction by a significant amount, as observed in Fig. 3.17.

However, as Figure. 3.19 demonstrates, the effect of transition fix on surface pressure, and hence on lift, is very limited. This suggests that the fully turbulent flow assumption suffices to predict the lifting airloads to an acceptable accuracy, while the turbulent transition fix still does not necessarily yield more accurate lift airloads. A more rigorous turbulent transition modeling may provide better solution to this problem, but that is beyond the scope of the thesis. Therefore, for all the analyses through the rest of the thesis, the flow is assumed fully



(a) Pressure Co-efficient at $\alpha = 15^\circ$



(b) Lift Co-efficient vs α

Figure 3.19: Comparing airload predictions from fully turbulent and laminar-turbulent transition fixed flow on slatted S6 airfoil

turbulent.

3.2 Pitching Airfoil: SC2110 with S-1 and S-6

In this section, the MEA CFD solver is further validated, this time for an unsteady pitching airfoil (SC2110) flight condition. Both the baseline airfoil and the airfoil with static slat configurations, S-1 and S-6 are analyzed. This section studies the favorable gap effects of slats on suppression of a dynamic stall vortex and the consequent performance improvement of the slatted airfoil load characteristics.

Two C-mesh topologies, consisting of 385×138 points (along wrap around and normal direction, respectively) on the main element and 317×97 points on the slat, are used to model this flight condition. Wind tunnel interference effects are accounted for by using a background wind tunnel mesh of the size 151×101 , along streamwise and stream normal direction, respectively.

Two unsteady pitching motions are considered at a reduced frequency $k = \omega c / 2V_\infty = 0.07$.

$$\alpha_1(t) = 15^\circ - 5^\circ \cos(\omega t)$$

$$\alpha_2(t) = 10^\circ - 10^\circ \cos(\omega t)$$

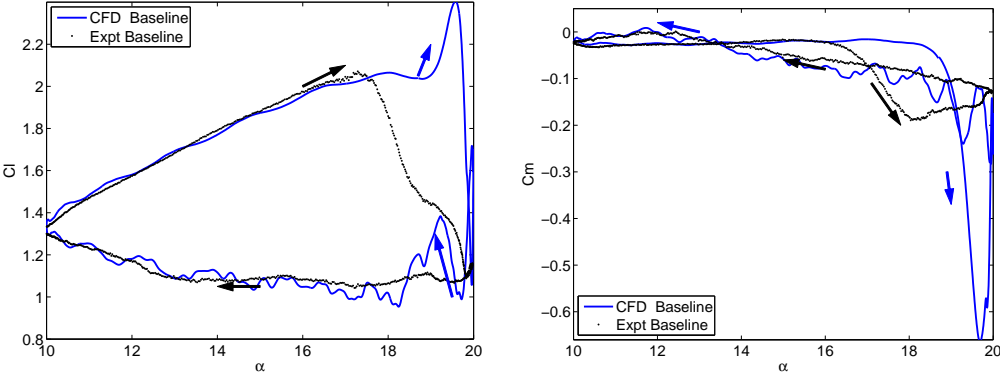
Pitching motion of $\alpha_1(t)$ is considered at a Reynolds number $Re = 4.14 \times 10^6$, and a freestream Mach number $M_\infty = 0.3$ and that of $\alpha_2(t)$ is considered at a Reynolds number $Re = 5.52 \times 10^6$, and a free stream Mach number $M_\infty = 0.4$. These flight conditions are typical of those encountered at mid-span stations on the retreating side of a rotor in forward flight.

3.2.1 Pitching Amplitude 10° : Baseline Airfoil SC2110

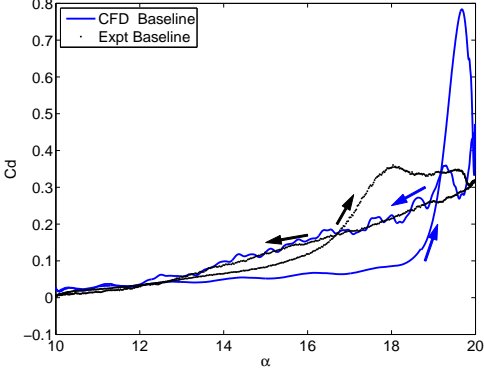
The comparison of the computational lift and pitching moment values with experimental measurements for the first unsteady pitching motion ($\alpha_1(t)$) for just the baseline airfoil element are shown in Fig. 3.20. The overall trend of the predicted values seem to be somewhat oscillatory in nature, which could arise from the wind tunnel wall effect. Compared to experiment, at lower angles the lift-curve slope is well captured, but the stall event is predicted late. Moreover, CFD predicts a sharp lift overshoot near stall, probably due to the presence of the dynamic stall vortex (DSV).

Similar observations can be made about pitching moment and drag predictions, i.e. fair correlation in upstroke phase in attached region at lower angles, followed by delayed prediction of stall events. The process of formation of the DSV followed by the process of vortex shedding and then its convection over the airfoil results in pitching moment stall due to the movement of center of pressure. This also explains why moment stall occurs earlier than lift stall. Lift

stall occurs only when the DSV moves past the TE. Similar to lift prediction, a huge overshoot of moment and drag values is observed near stall.



(a) C_L (b) C_M



(c) C_D

Figure 3.20: Periodic variation of the non-dimensional lift and pitching moment coefficients as a function of angle of attack for the baseline 2-D airfoil element, $M_\infty = 0.3$, $k = 0.07$, $\alpha = 15^\circ - 5^\circ \cos(\omega t)$.

Baseline Flow Physics: Presence of DSV

Figure 3.21 shows various stages of the baseline airfoil undergoing the pitching cycle. The Fig. 3.22 shows the corresponding surface pressure plots. At lower angles such as the one shown in Fig. 3.21(a) at $\alpha = 15^\circ$, the flow is still attached

as corroborated by the corresponding surface pressure plot (Fig. 3.22(a)). The gradient of pressure rise from the suction peak near the LE is still smooth which maintains attached flow. In such attached flow at lower angles, it can be observed that the predicted values correlate very well with the experimental values. With increasing angle the suction peak near the LE keeps increasing until finally the DSV forms and sheds from the LE (Figs. 3.21(b) and 3.21(c)). This results in separated flow, characterized by a large adverse pressure gradient (pressure rise) near the LE followed by flat regions of constant pressure values as shown in Figs. 3.22(b) and 3.22(c). A region of suction pressure rise in Fig. 3.22(b) is due to the presence of the DSV near the airfoil surface.

In the down stroke phase, when the angle is low again, the flow reattaches (Fig. 3.21(d) and 3.22(d)). But, due to the unsteady effect, the reattachment is delayed till much lower angles and therefore a reverse flow region near the TE still exists at 15° in Fig. 3.21(d). It is also noted that when the flow is initially separated, the predicted surface pressure values do not correlate well with the experimental values (Fig. 3.22(b)). This partly explains the inaccurate and over prediction of airloads compared to the experiment.

3.2.2 Pitching Amplitude 10° : Slatted Airfoil

Figure 3.23 compares the predicted and measured periodic variation of unsteady lift, pitching moment and drag for the multi-element airfoil with the slat at S-6 configuration. CFD does well in predicting the lift curve slope during the upstroke, but does not capture the exact trend of the lift variation in the down stroke, e.g. the nature of hysteresis loop post stall is itself different than what is observed in the experiment. The moment prediction is good in both the up and

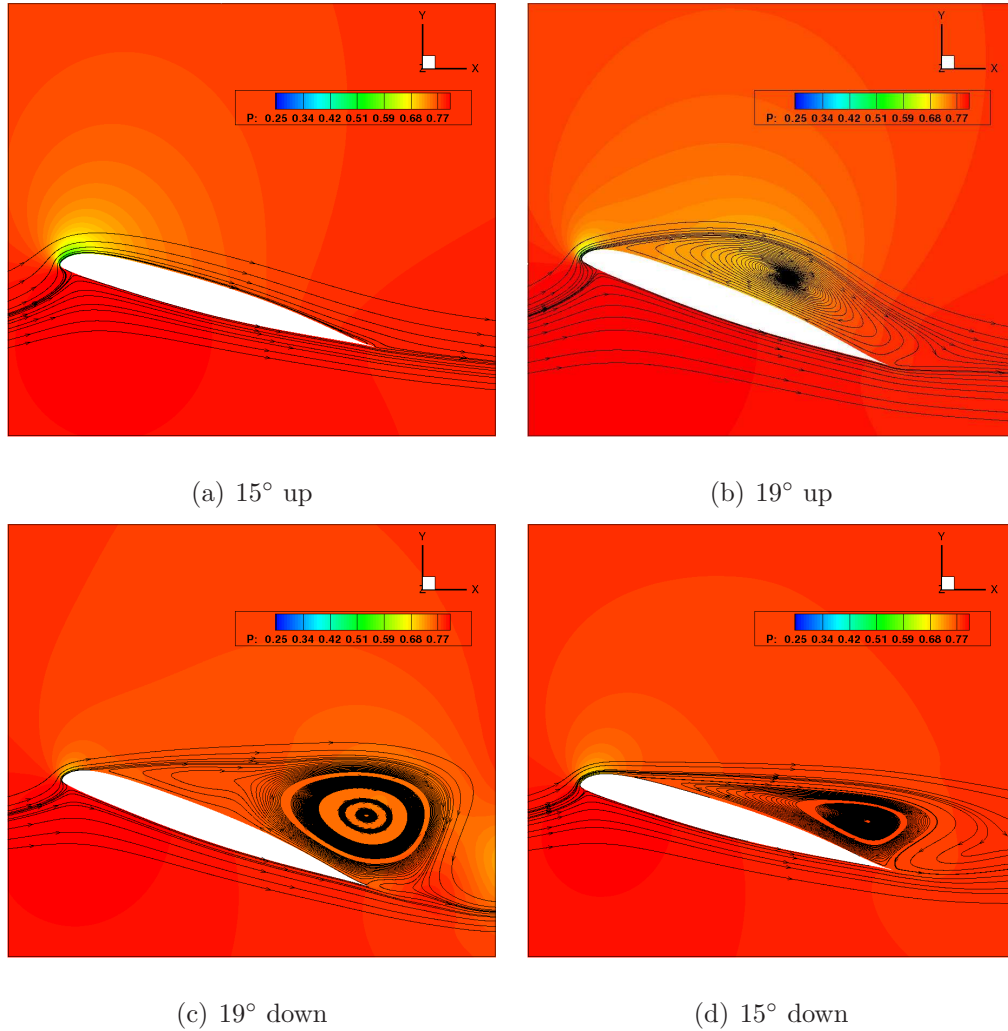
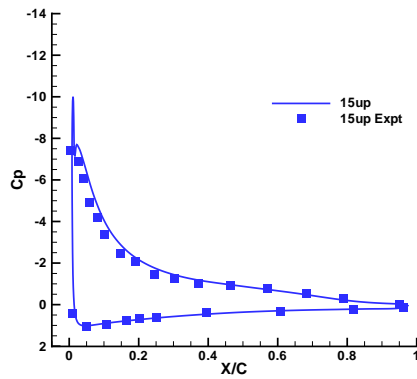


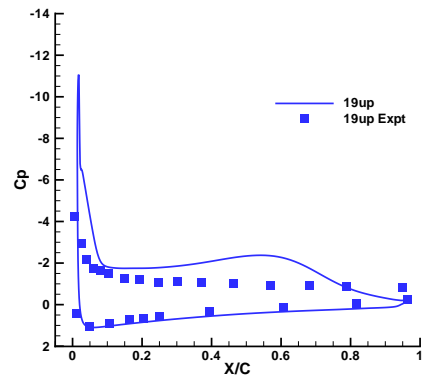
Figure 3.21: Streamlines on baseline SC2110 airfoil near stall region: Dynamic Stall.

down stroke phases of pitching cycle at lower angles when the flow is attached, but not right near stall. Similar to the baseline case, CFD over predicts the moment stall extent for the slatted airfoil. Drag values, on the other hand, are over predicted over most part of the pitching cycle (possibly due to the assumption of fully turbulent flow).

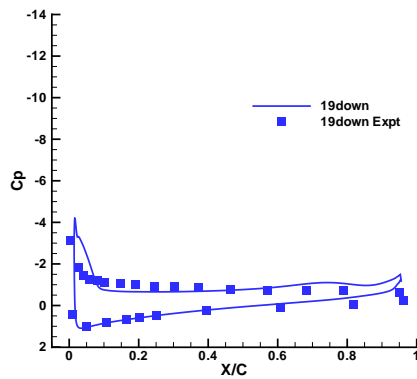
The predicted airload values for S-1 slat configuration are compared against experimental values in Fig. 3.24. The overall trend in all the airload predictions



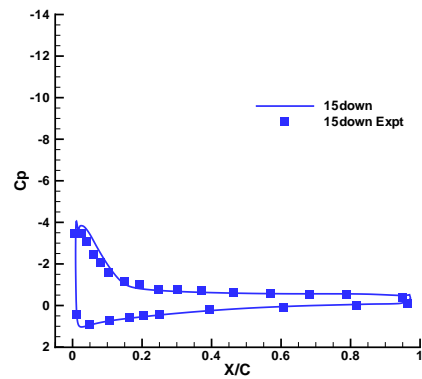
(a) 15° up



(b) 19° up



(c) 19° down



(d) 15° down

Figure 3.22: Surface pressure on baseline SC2110 airfoil near stall region [53].

is that CFD captures the trend of airload variation during the pitching cycle observed in experiment. The lift curve slope is well predicted but the values are under predicted. Although the stall break point is fairly well captured by CFD, the reattachment region post stall is not. The moment values compare well with experiment at lower angles and predict moment stall break point reasonably well. However, post stall the predicted values deviate from experimental values, although the nature of the hysteresis loop remains similar to that of experiment.

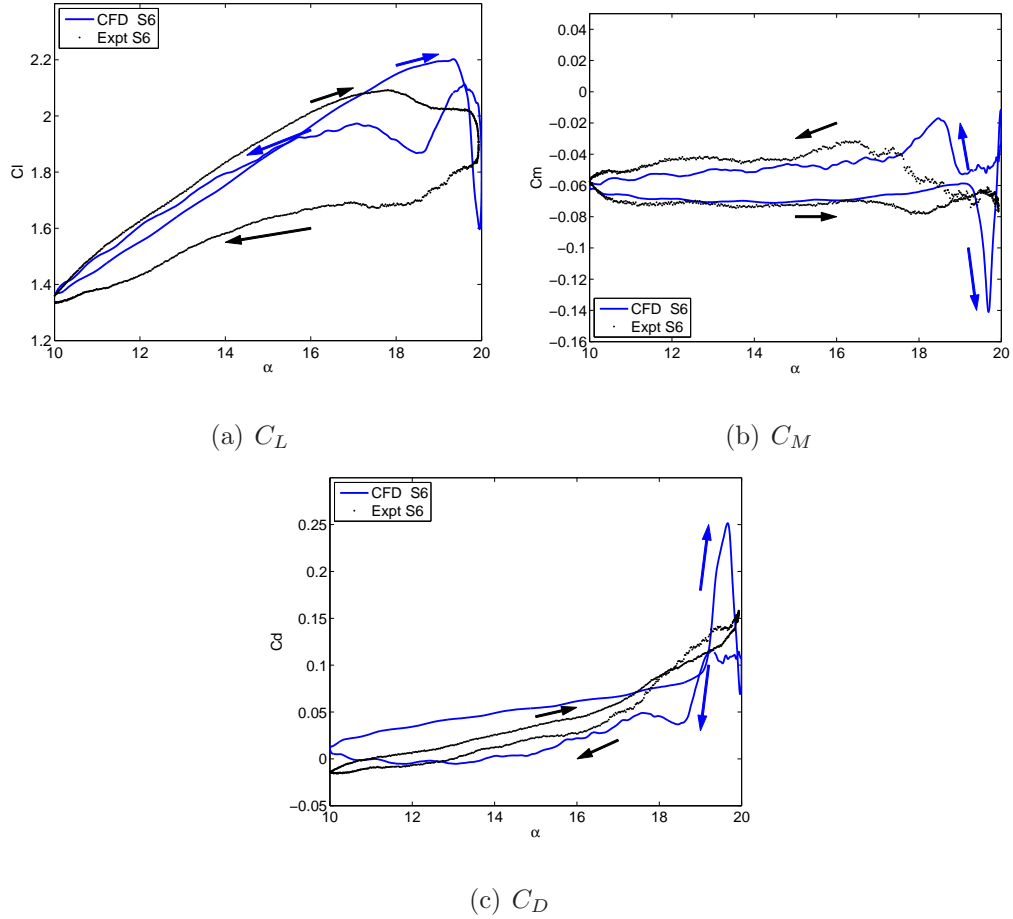


Figure 3.23: Periodic variation of the non-dimensional lift, pitching moment and drag coefficients as a function of angle of attack for the multi-element airfoil with the slat at S-6 configuration, $M_\infty = 0.3$, $k = 0.07$, $\alpha = 15^\circ - 5^\circ \cos(\omega t)$ [53].

CFD predicts the drag stall event to a good accuracy and maintains the right trend of the hysteresis loop, but over predicts the values in the up stroke and under predicts in the down stroke phase of the pitching cycle.

The two figures discussed above demonstrate the effectiveness of a slatted airfoil in mitigating dynamic stall by completely eliminating the DSV. Comparing the Figs. 3.24 and 3.23, it is clear that S6 has better stall characteristics than S1 and hence is more effective at larger angles. However, at lower angles, S1 is more

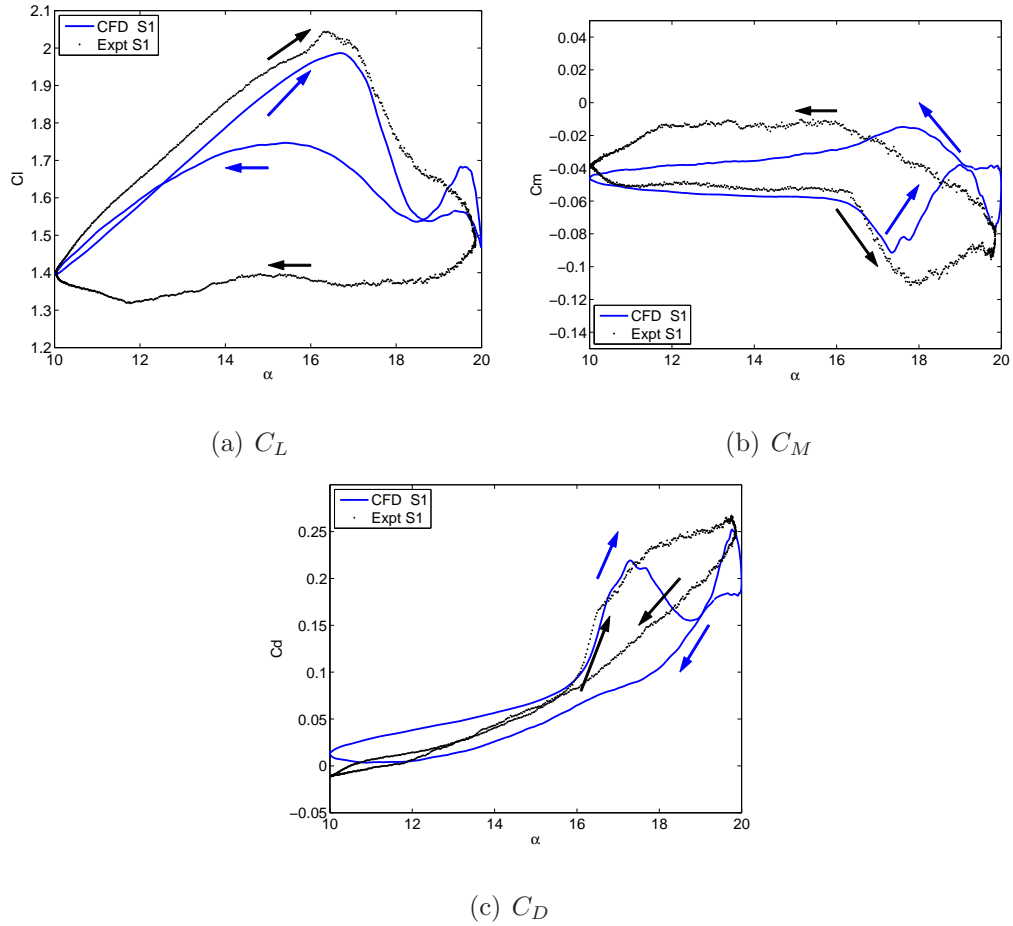


Figure 3.24: Periodic variation of the non-dimensional lift and pitching moment coefficients as a function of angle of attack for the multi-element airfoil with the slat at S-1 configuration, $M_\infty = 0.3$, $k = 0.07$, $\alpha = 15^\circ - 5^\circ \cos(\omega t)$ [53].

effective than S6 in overcoming the moment penalty. The S6 configuration not only sustains larger Cl_{max} till larger angles compared to the baseline airfoil, it also results in complete elimination of a coherent DSV, due to the favorable gap effects of the slat discussed in the Introduction chapter. This results in milder lift and moment stall events.

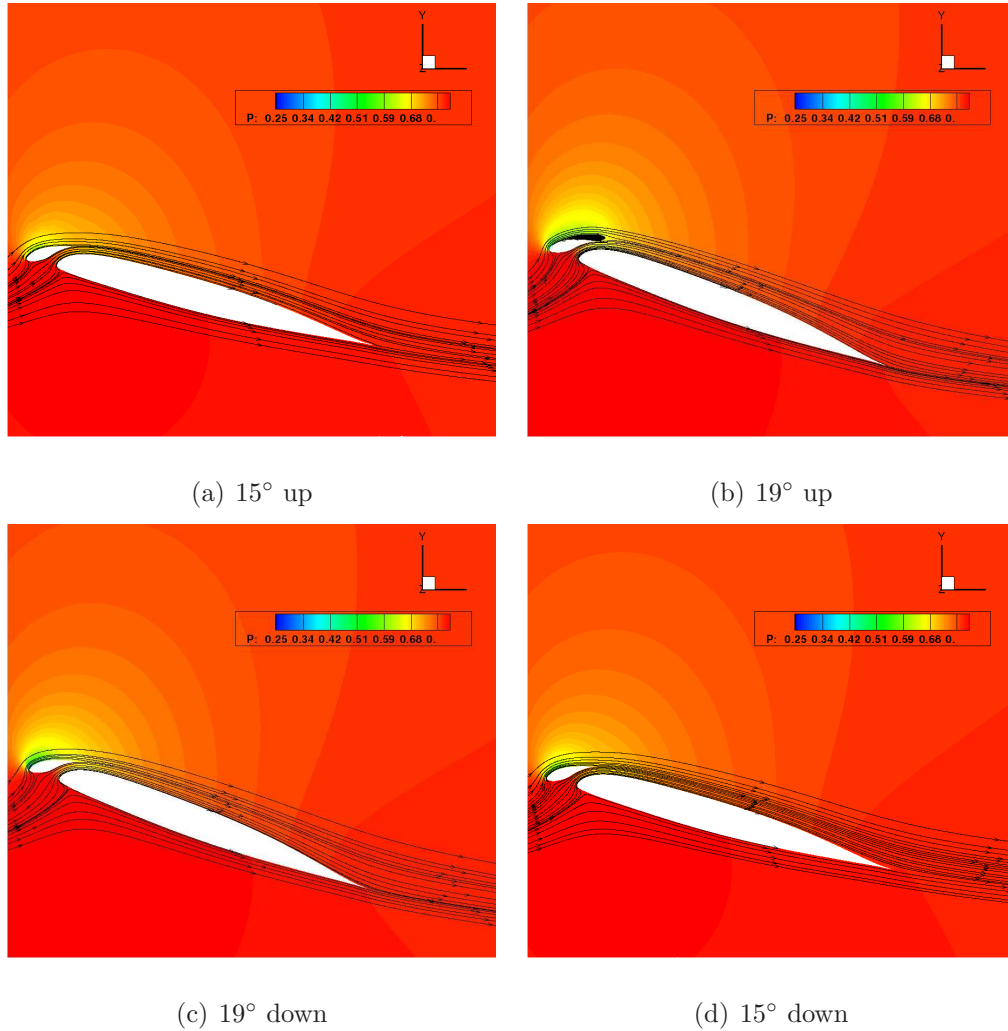
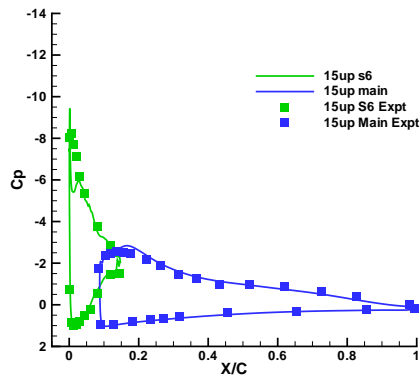


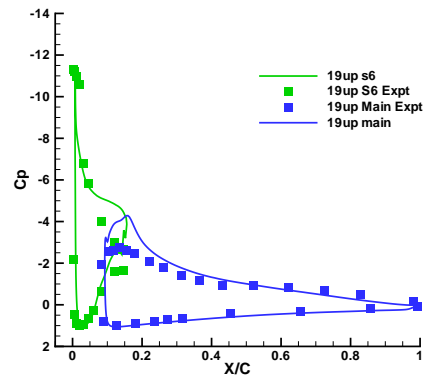
Figure 3.25: Streamlines on Slat-S6 SC2110 airfoil at high angles: mitigation of dynamic stall.

Flow Physics: Suppression of DSV with Slat

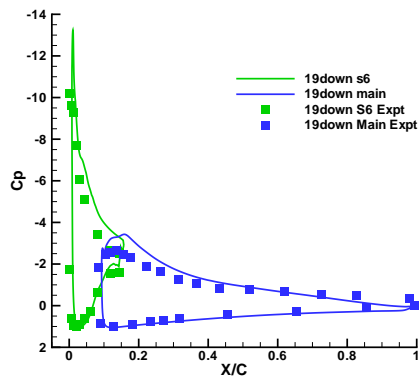
Figure 3.25 shows various stages (at the same angles considered for the baseline airfoil in 3.21) of the slatted airfoil (with slat S-6) undergoing a pitching cycle. The slatted airfoil results in mitigation of huge DS vortices allowing for attached flow throughout the pitching cycle, although the flow separates slightly on the slat at large angles (Fig. 3.25(b)). Figures 3.26 further explain how the pressure



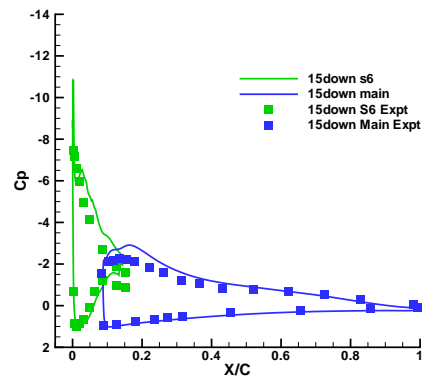
(a) 15° up



(b) 19° up



(c) 19° down



(d) 15° down

Figure 3.26: Surface pressure on Slat-S6 SC2110 airfoil at high angles [53].

suction peaks found on the baseline airfoil are reduced at the LE of the slatted airfoil main element due to the favorable slat effect. The slat bears the suction peak rise, but due to dumping effect (discussed in Introduction chapter), which allows the slat wake to dump flow at larger velocity than freestream, even this pressure rise on the slat is relieved. This allows the slat to bear a larger suction pressure peak than the main element and still have attached flow. The resulting surface pressure has much smoother pressure gradients on the slatted airfoil main

element than that found on the baseline airfoil at the same stage even at large angles, e.g. compare Figs. 3.26(b) and 3.22(b). The over predicted suction values on the main as well as the slat element of the slatted airfoil results in the over prediction of lift values at larger angles and post stall.

3.2.3 Pitching Amplitude 20° : Baseline and Slatted Airfoil

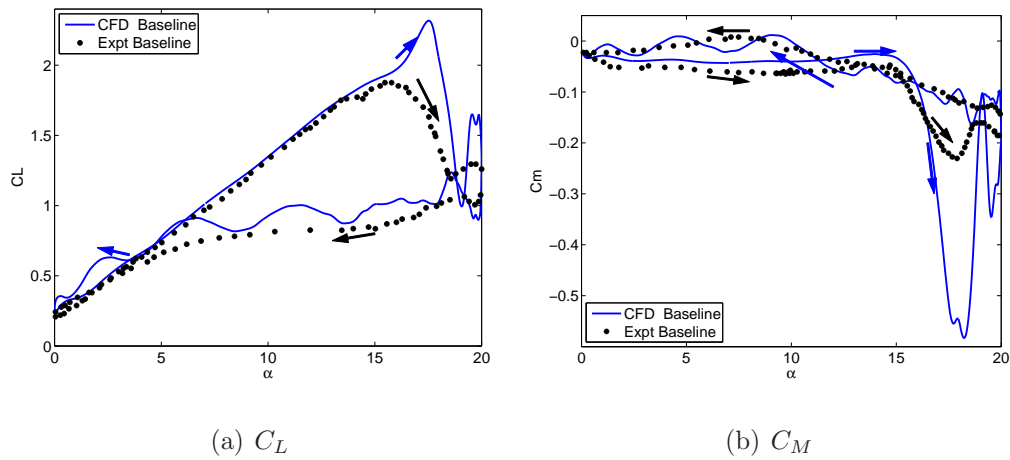


Figure 3.27: Periodic variation of the non-dimensional lift and pitching moment coefficients as a function of angle of attack for the baseline airfoil section, $M_\infty = 0.4$, $k = 0.07$, $\alpha = 10^\circ - 10^\circ \cos(\omega t)$ [53].

Computations are then performed for another unsteady pitching motion ($\alpha_2(t)$) using both the baseline airfoil and the slatted airfoil with the slat at S-6 configuration for $M = 0.4$ and $Re = 5.52 \times 10^6$. Figure 3.27 shows the lift and pitching moment cycles for the baseline airfoil for this pitching motion. The computations capture the overall trend of the pitching cycles of the airloads very well and the predictions are quite accurate in the attached region before stall. However, similar to what was observed for the case at $M = 0.3$, the airloads

show an up shoot in maximum lift prediction near stall and an over prediction of the drop in moment stall. The moment stall point, however, is predicted fairly well. Both the lift and moment loads show some oscillatory behavior in the down stroke phase.

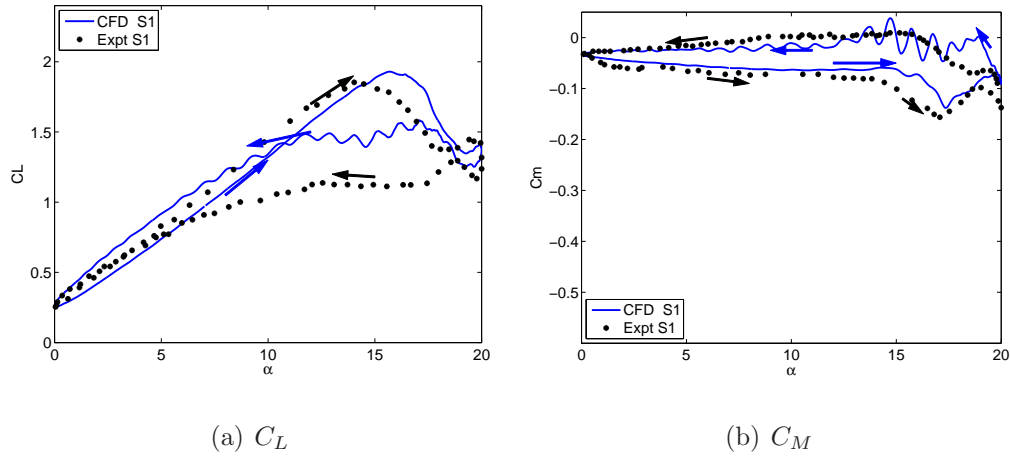


Figure 3.28: Periodic variation of the non-dimensional lift and pitching moment coefficients as a function of angle of attack for the multi-element airfoil with the slat at S-1 configuration, $M_\infty = 0.4$, $k = 0.07$, $\alpha = 10^\circ - 10^\circ \cos(\omega t)$.

Both the lift and moment stall break points are predicted later than experiment when S-1 slat is added to the main airfoil. On the upstroke the lift is under predicted. Even the lift curve slope is under predicted. In the down stroke phase, while the predicted lift values are not correct, the predicted moment loads are fairly well captured, especially near the flow reattachment region. See Fig. 3.28. Similar to S-1 slat results, with the S-6 slat, the CFD lift and moment values do not correlate as well with those from experiment in the upstroke phase even in the attached region. The stall predictions are delayed for both the airloads. See Fig. 3.29. The correlation is even worse for lift values in the downstroke phase, but it is fairly good for the moment values. Essentially the CFD simu-

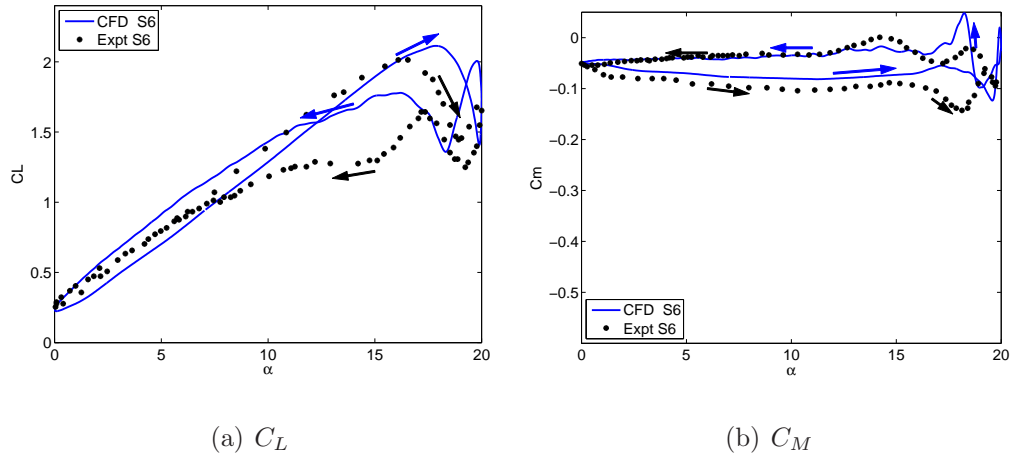


Figure 3.29: Periodic variation of the non-dimensional lift and pitching moment coefficients as a function of angle of attack for the multi-element airfoil with the slat at S-6 configuration, $M_\infty = 0.4$, $k = 0.07$, $\alpha = 10^\circ - 10^\circ \cos(\omega t)$.

lations seem to slightly overpredict the effectiveness of the slats in ameliorating the light stall.

An interesting observation that can be made about this case is the flow separation is shock induced, and therefore is influenced by compressibility effects. For example, Fig. 3.30(a) shows that the baseline airfoil experiences a weak but noticeable shock near $\alpha = 14^\circ$, which seems to initiate flow separation. Eventually, when the angle of attack reaches 20° , the BL is fully separated and the baseline is in deep stall (Fig. 3.31(a)). Delay of boundary layer separation due to the slats is very clearly observed from the remaining figures in Fig. 3.30 and Fig. 3.31. The slat not only offloads the shock from the main airfoil onto its own upper surface, it also maintains attached flow on the main airfoil till larger angles. At $\alpha = 14^\circ$ the slats experience light (Fig. 3.30(b)) to no stall (Fig. 3.30(c)). Slat S-6 still sustains attached flow even at 20° , even though S-1 experiences a deep stall on the slat (Fig. 3.31). However, both the slatted airfoils

maintain attached flow on the main element.

In general it is observed that with the slat the stall event is strongly mitigated. The most significant gain of using the slat is the large reduction of moment penalty due to the absence of stall on the main element, and in that regard the S-6 slat is more effective than the S-1 slat.

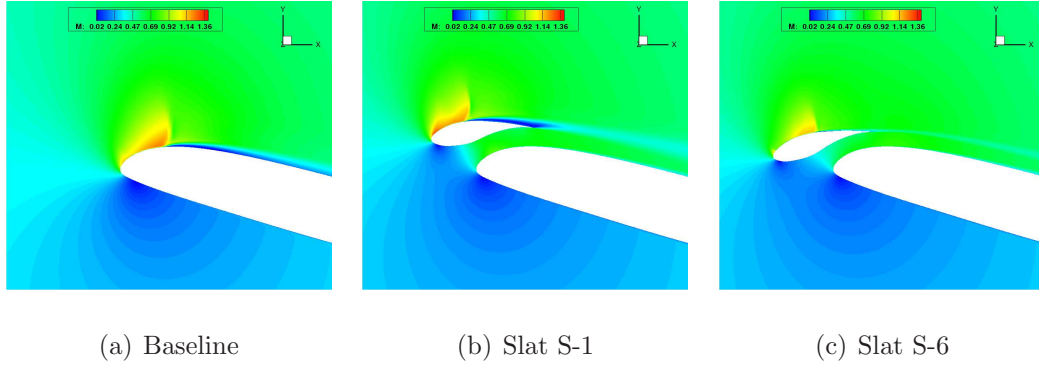


Figure 3.30: Mach contours on baseline and slatted airfoils at upstroke $\alpha = 14.1^\circ$ during pitching cycle; $M_\infty = 0.4$, $k = 0.07$, $\alpha = 10^\circ - 10^\circ \cos(\omega t)$.

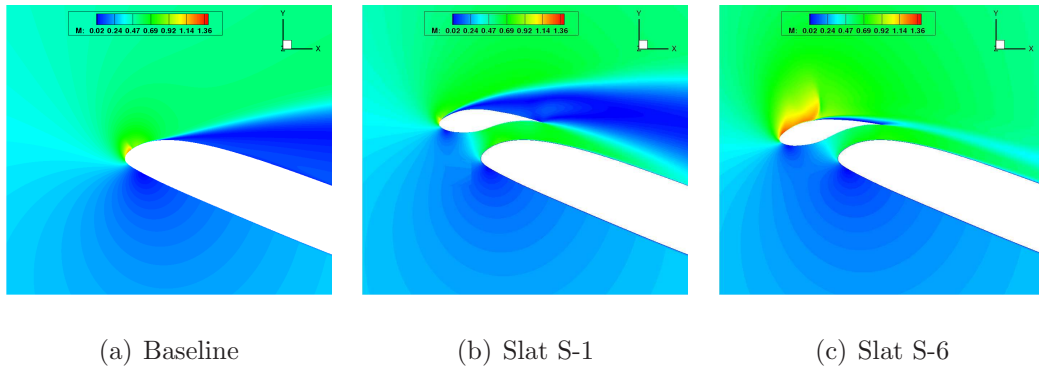


Figure 3.31: Mach contours on baseline and slatted airfoils at upstroke $\alpha = 20^\circ$ during pitching cycle; $M_\infty = 0.4$, $k = 0.07$, $\alpha = 10^\circ - 10^\circ \cos(\omega t)$.

3.3 Unsteady Rotor: UH-60A Flight Test C9017

Since the ultimate aim of the work is to analyze rotor aerodynamics, the CFD solver, having been validated against 2-D flight conditions, is extended to handle 3-D slatted rotor flows. As mentioned before, the solver is then coupled with a comprehensive CSD solver. This section, carries out detailed validation of the coupled CFD/CSD analysis with available data for flight test C9017.

The high altitude Flight 9017, at a vehicle weight coefficient of $C_T/\sigma = 0.1325$, is a flight condition characterized by severe dynamic stall events on the retreating side of the rotor disk. This flight counter is one of the several flight tests conducted by the NASA-Army UH-60A Airloads Program [86] on a four-bladed UH-60A aircraft in the early nineties. The flight condition is at an intermediate advance ratio of $\mu = 0.237$. The free stream Mach number is $M_\infty = 0.157$, and the tip Mach number is $M_{\text{tip}} = 0.665$. It is close to the McHugh's lift boundary (Fig. 3.32). The McHugh's lift boundary is shown for a qualitative assessment of the stall level. The boundary depicts the measured steady thrust limit of a 10-foot diameter CH-47B model rotor in the Boeing 20-by 20-ft V/STOL Wind Tunnel [87].

Rotor dynamic stall differs from airfoil and 3D wing stall due to additional excitations caused by wake induced inflow and high frequency elastic twist deformations. The stall response occurs at Reynolds numbers of 1 to 6 million. The local Mach numbers can be as high as 0.7 to 0.8 on the advancing blade and 0.2 to 0.4 on the retreating blade. High Mach numbers are relevant for the advancing blade stall cycle but for the level flight case, such as C9017, this stall cycle is not present. This flight condition, C9017, is characterized by severe dynamic stall events on the retreating side of the rotor disk and presents an ideal test

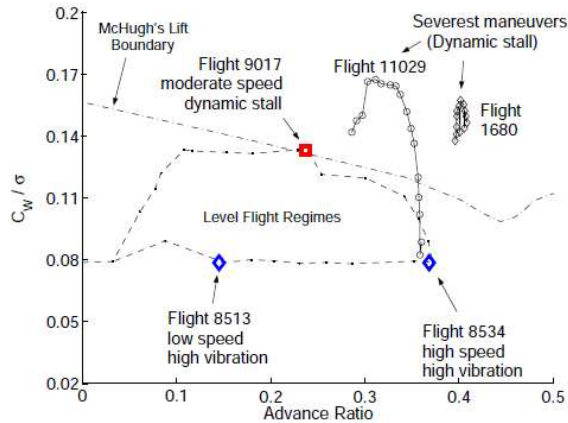


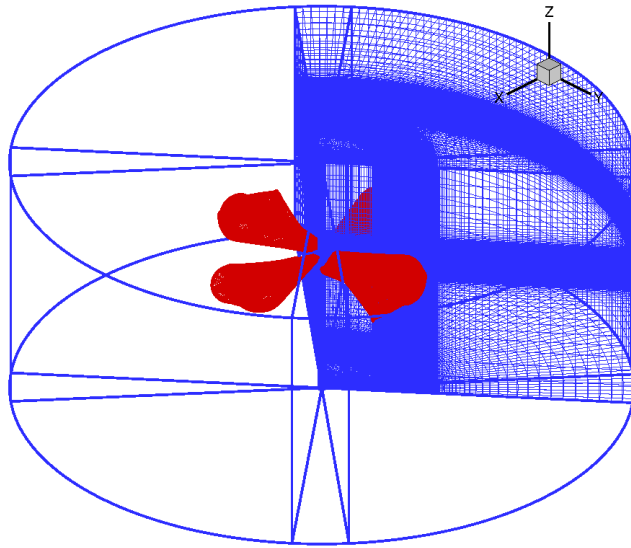
Figure 3.32: McHugh Lift Boundary [88]

case for the purposes of the present study, and is, therefore, an ideal candidate to investigate the effectiveness of leading-edge slats in mitigating the retreating blade dynamic stall.

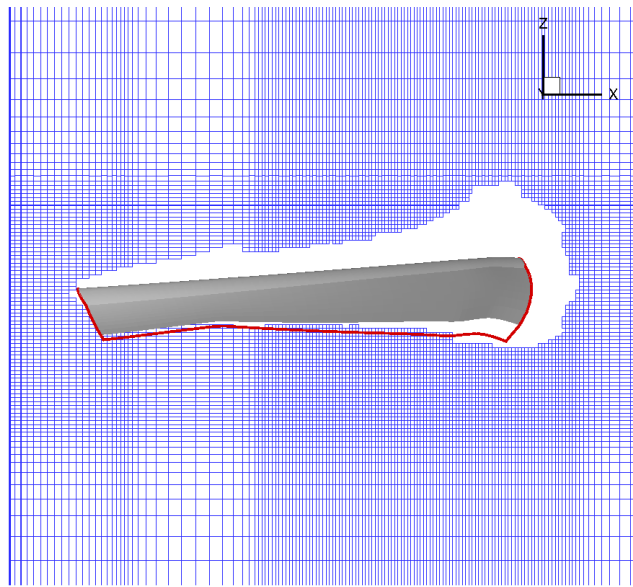
The near-body flowfield is modeled using a C–O type body conforming mesh with $133 \times 130 \times 61$ points (in chord wise, span wise and normal direction, respectively). The blade surface spacing in the normal direction is 5×10^{-6} chords (required for viscous calculations) and the mesh outer boundary is at a distance $25\%R$ away from the blade surface. The entire rotor blade-wake system is modeled by embedding the blade meshes in a cylindrical off body mesh with 4.4 million points (four wake meshes of size $133 \times 130 \times 61$) — see Fig. 3.33.

3.3.1 Quantitative Validation: Airloads

Flight test data are available for the C9017 flight condition at various spanwise stations on the UH-60A as shown in Fig. 3.34. Figures 3.35 and 3.36 show the comparison of the predicted normal force and pitching moment time histories at



(a) Computational domain with eight mesh system



(b) Background mesh near blade wake

Figure 3.33: Overset mesh system used in the simulation of the UH-60A rotor in forward flight showing the body-fitted blade meshes embedded within a cylindrical background mesh.

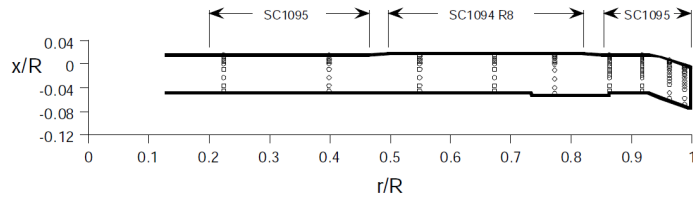


Figure 3.34: UH-60A flight test data stations [91].

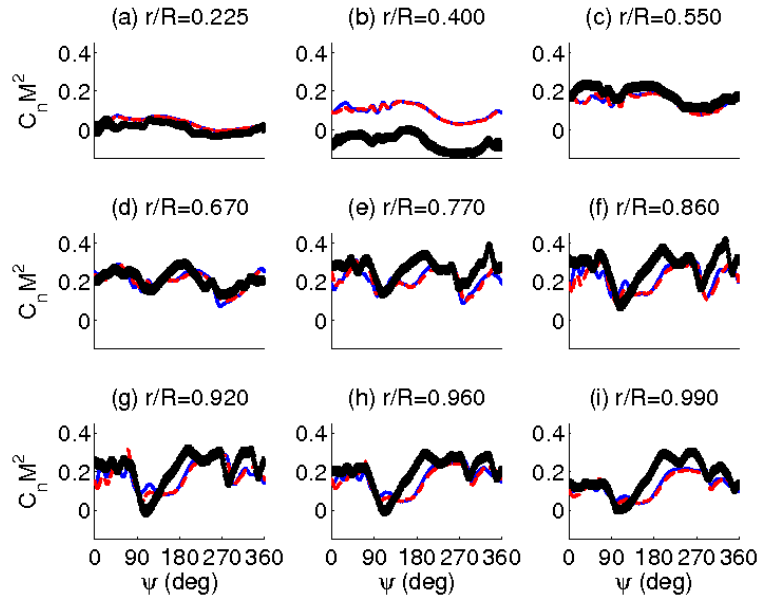


Figure 3.35: Time histories of the non-dimensional sectional normal forces at different radial stations along the span for the baseline UH-60A rotor in C9017 flight condition. Black dot: Flight test data, Blue solid: CFD-CSD with shaft-fixed trim, Red dash: CFD-CSD with free-flight trim.

the nine radial stations for the baseline UH-60A rotor with the flight test data. Results from the coupled simulation using the two trim algorithms are shown here. The calculations show good overall agreement with the measurements. The results obtained in the present analysis are consistent with those obtained with previous other CFD-CSD coupled simulations [88–90,92] (see Fig. 3.37). It

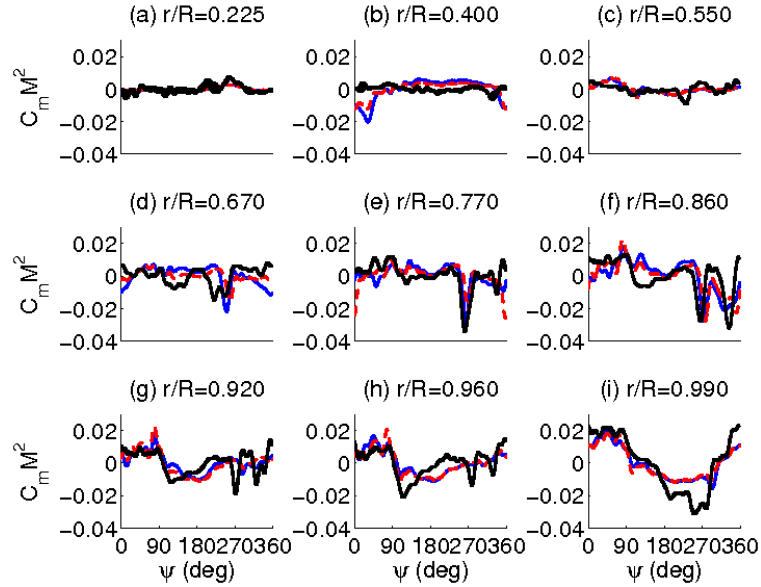


Figure 3.36: Time histories of the non-dimensional sectional pitching moment coefficients (means removed) at different radial stations along the span for the baseline UH-60A rotor in C9017 flight condition. Black dot: Flight test data, Blue solid: CFD-CSD with shaft-fixed trim, Red dash: CFD-CSD with free-flight trim.

must be noted here that the pitching moment values in Fig. 3.37 are dimensional. The pitching moment trend of the twin stall events, especially at $r/R = 0.86$, are captured in the current work as well, but with a phase offset of the second stall event as compared to the previous computation. In Fig. 3.35, the flight test data indicates a large span wise discontinuity at $40\%R$ which is most probably a manifestation of steady offsets present in the flight test data. The pitching moment variations at the outboard sections of the rotor blade are characterized by two distinct stall events. The first stall event is caused by an increase in the angle of attack induced by control inputs. The resulting large nose-down pitching moment causes an elastic torsional response (dominantly 5/rev) leading to flow

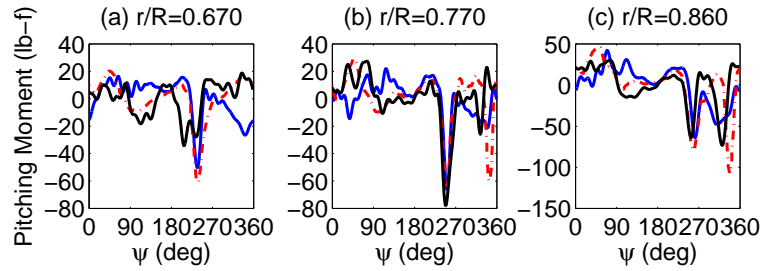


Figure 3.37: Time histories of sectional pitching moment coefficients (means removed) at three outboard radial stations for the baseline UH-60A rotor in C9017 flight condition taken from previous CFD-CSD work by Sitaraman et. al. [90]. Black solid : Flight test data, Blue solid: CFD-CSD with shaft-fixed trim, Red dash-dot: previous CFD-CSD with shaft-fixed trim.

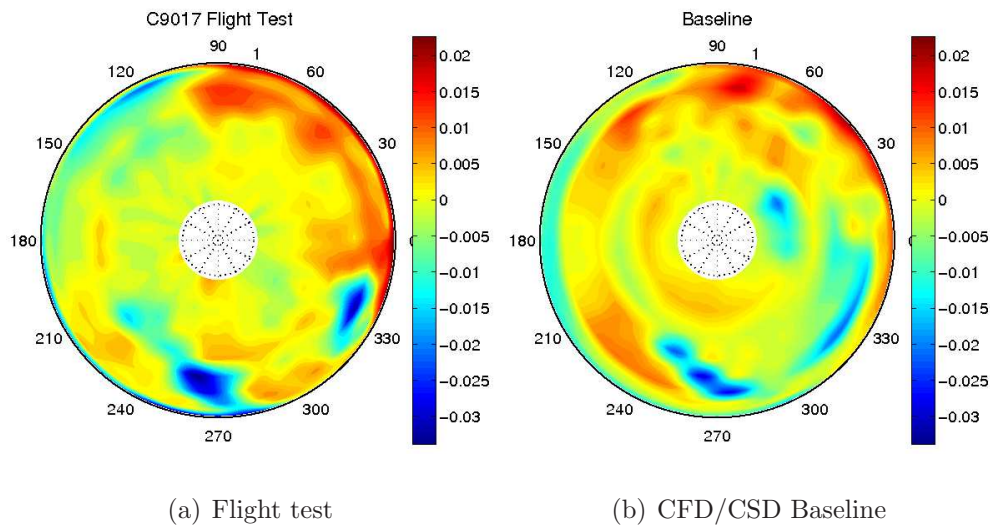


Figure 3.38: Comparison of the predicted pitching moment variation across the rotor disk with flight test data for baseline UH-60A rotor.

attachment and stall recovery. This is followed by a second stall event in the retreating side of the rotor disk. The coupled simulation captures the two stall events, although not resolved accurately in amplitude or phasing. This is clearly understood from Fig. 3.38, which compares the predicted pitching moment (mean

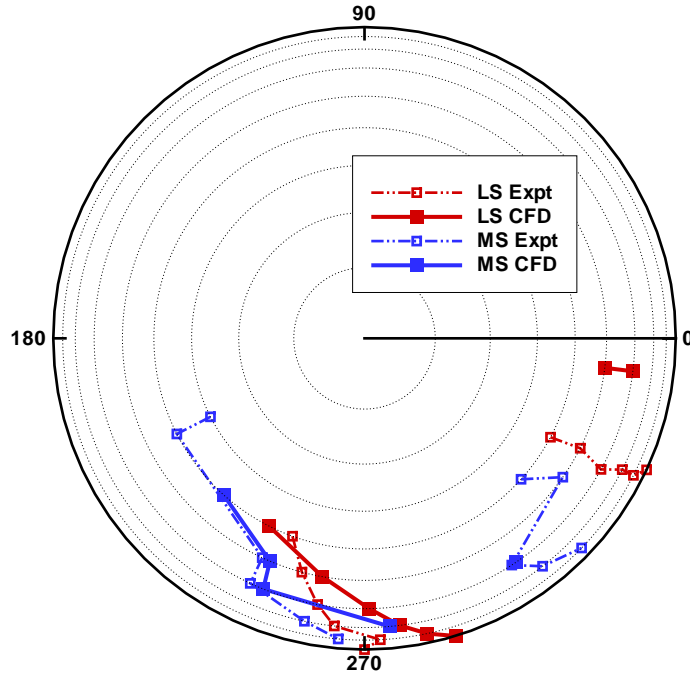


Figure 3.39: Lift stall (LS) and Moment stall (MS) map on the UH-60A rotor.

removed) with flight test data over the rotor disk. Finally Fig. 3.39 summarizes the lift as well as moment stall points on the rotor disk at various azimuthal and radial station in a polar plot. The general observation that can be made about both kinds of stall events (lift and moment) is that most often the stall event predictions are delayed. In addition, the model is unable to predict the full radial extent of the second stall events observed in the test data. For example, the computational model predicts only two of the radial locations for the second lift stall events and only one for the second moment stall events. However, the agreement is still considered satisfactory.

Free Flight Trim versus Wind Tunnel Trim

Examining the results from the two different trim procedures closely shows that the dynamic stall events, particularly the magnitude and phasing of the mo-

Blade Type	θ_0	θ_{1c}	θ_{1s}	α	C_Q/σ
C9017 Free-flight trim	13.66	6.49	-8.47	-1.98	0.00959
C9017 Wind-tunnel trim	14.86	7.01	-8.55	-2.85	0.01120

Table 3.1: Final trim control angles and the predicted rotor power for the baseline using the free-flight and wind-tunnel trim algorithms

ment stall, is much better resolved by the wind-tunnel trim algorithm. While there is no noticeable difference in the normal force predictions by the two trim procedures, the pitching moment shows wind tunnel trim resolves the first stall events better at stations $r/R = 0.77$ and 0.86 , both in magnitude and phasing. Moreover, the free flight trim leads to incorrect and over predicted second stall events at these stations. Table 3.1 shows the comparison of the final trimmed control pitch settings and the corresponding power predictions obtained from the analysis using the two different trim methodologies. It is observed that the wind-tunnel trim requires a lower cyclic input, and shows a slightly lower power requirement at this flight condition. In contrast, the free-flight trim converges to a higher shaft tilt angle resulting in larger inflow and, therefore, lower angles of attack on the retreating blade sections. Although the free-flight trim is a more realistic model of the actual UH-60A flight trim, the discrepancies found in the results can be attributed to the errors associated with simplistic models for the fuselage, empennage and the tail rotor that is used in the analysis. Because of the aforementioned reasons, all further analyses discussed in this paper will be obtained using the wind-tunnel trim algorithm.

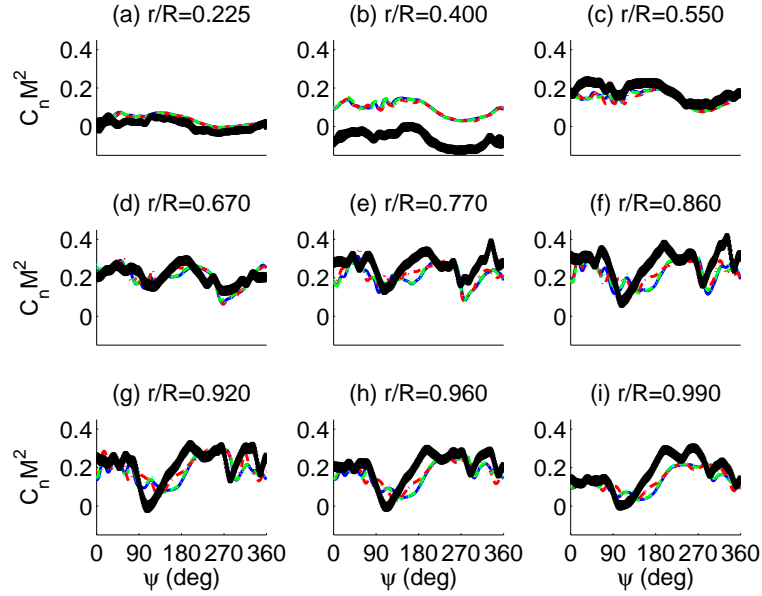


Figure 3.40: Time histories of the non-dimensional sectional normal forces at different radial stations along the span for the baseline UH-60A rotor in C9017 flight condition. Black dot: Flight test data, Blue solid: Grid size $133 \times 130 \times 61$, Green dash: Grid size $133 \times 197 \times 61$, Red dash-dot: Grid size $133 \times 259 \times 61$, Cyan dots: Grid size $199 \times 130 \times 61$.

3.3.2 Grid Convergence Study

Appropriate grid size is essential in capturing the right physics of the flow, especially when it involves unsteady aerodynamics varying across the span. To arrive at the appropriate grid size, grid sizes with varying numbers of spanwise and wrap around grid stations are considered. Their grid dimensions are: $133 \times 130 \times 61$, $133 \times 197 \times 61$, $133 \times 259 \times 61$, and $199 \times 130 \times 61$ along wraparound, spanwise and normal directions to the blade.

Figs. 3.40 and 3.41 compare the airloads due to these three grids. It is clearly noted that the coarsest grid itself suffices to resolve the salient characteristics of

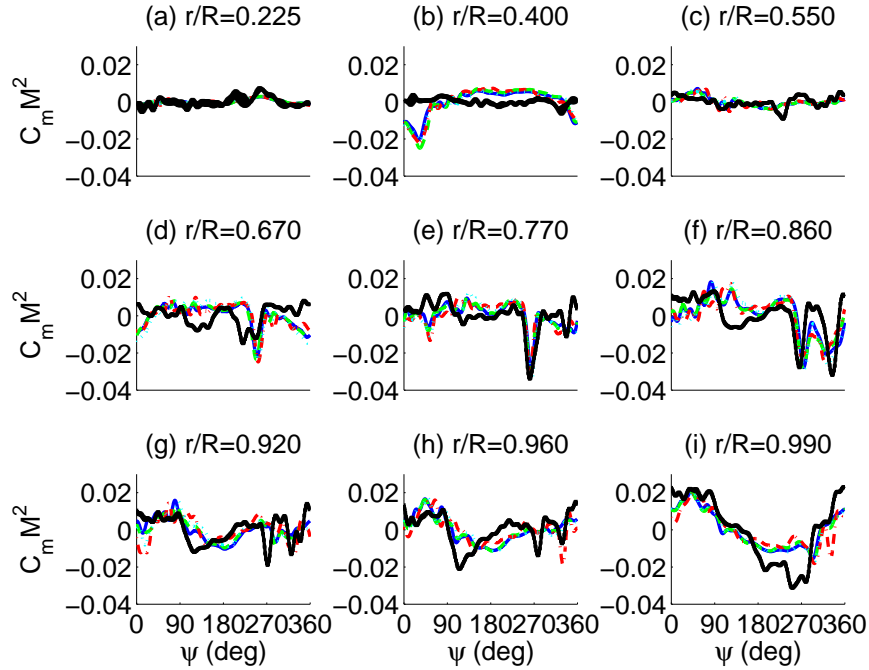


Figure 3.41: Time histories of the non-dimensional sectional pitching moment coefficients (means removed) at different radial stations along the span for the baseline UH-60A rotor in C9017 flight condition. Black dot: Flight test data, Blue solid: Grid size $133 \times 130 \times 61$, Green dash: Grid size $133 \times 197 \times 61$, Red dash-dot: Grid size $133 \times 259 \times 61$, Cyan dots: Grid size $199 \times 130 \times 61$.

the time history airload plots. For example, the spanwise coarsest grid already predicts the two moment stall events at the outboard stations, especially the one at $r/R = 0.86$, besides predicting the lift stall events to a reasonable accuracy. The finer grid resolution, with as much as half the grid spacing at the inboard stations as the coarsest one, does not help improve either the phasing or the extent of stall events by a significant amount. Moreover, the higher inboard grid resolution is still unable to pick up the smaller stall events at the inboard stations ($r/R = 0.55$) besides over predicting the second moment stall events at

Grid size	θ_0	θ_{1c}	θ_{1s}	α	C_Q/σ
$133 \times 130 \times 61$	14.86	7.01	-8.55	-2.85	0.01120
$133 \times 197 \times 61$	15.24	7.42	-8.70	-2.85	0.01172
$133 \times 259 \times 61$	15.40	7.87	-8.59	-2.85	0.01230
$199 \times 130 \times 61$	15.49	7.95	-8.48	-2.85	0.01235

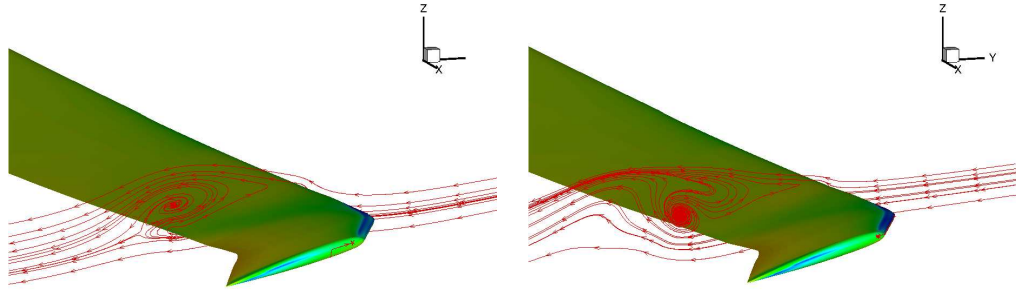
Table 3.2: Final trim control angles and the predicted rotor power for the baseline for different grid sizes

certain outboard stations ($r/R = 0.96$).

Table 3.2 compares the predicted trim control angles and power for all grid sizes. This further corroborates the findings from the airload time history plots. It shows that finer grid resolution has only moderate influence on trim angles and power prediction values, although it results in an increasing trend in the collective angles. But, observing only moderate advantages of further grid refinement compared to the initial coarse mesh size, the grid size of $133 \times 130 \times 61$ is consistently used for all the studies done hereafter in the thesis.

3.3.3 Qualitative Verification: Streamlines and Vorticity Contours

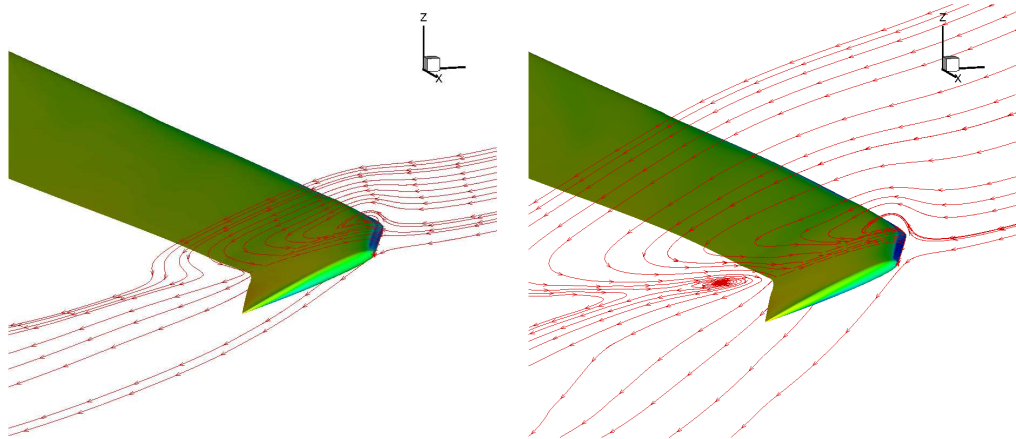
To understand the flow physics of the 3-D dynamic stall phenomenon, streamlines are examined at relevant azimuth locations at a few radial stations. Figure 3.42 shows streamlines near the first stall event ($\psi = 270^\circ$ and 282°) at 80% radial location. It clearly shows the presence of a vortex near the trailing edge which progressively moves away from the airfoil resulting in the first moment stall and then followed by a lift stall (deep stall). This is in agreement with the



(a) $r/R = 80\%$, $\psi = 274^\circ$

(b) $r/R = 80\%$, $\psi = 282^\circ$

Figure 3.42: Streamlines (undeformed frame) at $r/R = 80\%$ station near *first* lift stall event for the baseline UH-60A rotor in C9017 flight condition.



(a) $r/R = 93\%$, $\psi = 318^\circ$

(b) $r/R = 93\%$, $\psi = 330^\circ$

Figure 3.43: Streamlines (undeformed frame) at $r/R = 93\%$ station near *second* lift stall event for the baseline UH-60A rotor in C9017 flight condition.

trend and phasing of the first stall event normal load predictions. Figure 3.43 shows streamlines near the second stall event ($\psi = 318^\circ$ and 330°) at a more outboard station of 93% r/R . The dynamic stall vortex is only starting to form near $\psi = 318^\circ$, but has already convected past the trailing edge by the time the

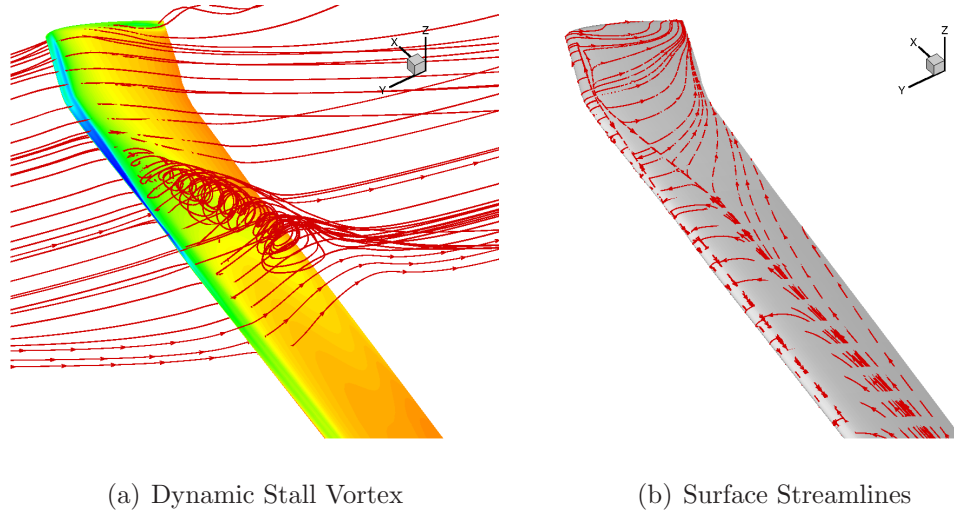


Figure 3.44: Dynamic stall vortex on UH-60A blade at azimuth, $\psi = 270^\circ$

blade reaches $\psi = 330^\circ$. These flow physics correspond well with the azimuthal location of the predicted second stall event.

Figure 3.44 shows volume and surface streamlines on the blade near the first dynamic stall. Figure 3.44(a) clearly verifies the presence of a strong dynamic stall vortex on the UH-60A blade at this azimuth location, $\psi = 270^\circ$. This correlates well with the test data confirming the presence of the first strong (moment as well as lift) dynamic stall events. Figure 3.44(b) shows the corresponding surface streamlines which clearly shows the separated flow regions and the separation lines. The λ -shaped separation region, which starts near $r/R \cong 0.95$ and spreads inboard of the blade, goes on to suggest the DSV grows in size from outboard to inboard as observed in Fig. 3.44(a).

3.3.4 More Quantitative Validation

This section quantitatively evaluates the credibility of the CFD/CSD model for analysing the high altitude high thrust rotor flight conditions. First, the

predicted aerodynamics of the rotor is quantitatively compared against existing experimental aerodynamic data, namely the surface pressure profiles. Then the predicted structural behavior is studied. Predicted rotor aeroelastic quantities, such as blade torsional moment, pitch link loads etc., are compared with available data from the flight test.

Aerodynamics: Surface Pressure

Previously, Figs. 3.35 and 3.36 showed discrepancies in the airload predictions as compared to experimental data. This discrepancy can be better explained if the surface pressure values are examined. As discussed before, the C9017 flight condition is characterised by two stall events: one occurring near 270° and the other near 330° . Figures 3.45 and 3.46 compare the predicted surface pressure coefficient with the flight test data at these two stall events. The predictions are fairly good over most of the radial stations except for the first few inboard stations ($r/R < 0.55$) where the suction pressure is over-predicted. Flat suction pressure profiles on the upper surface suggests highly separated flow, consistent with the stall event. It is also observed in Fig. 3.45 that the flow progresses from initial stages of stall to deeper stall from 270° to 282° azimuth, characterised by even flatter upper surface pressures and reduced areas under the pressure curves. Further, it is noticed that the size of the region of separation is decreasingly smaller towards the outboard stations, which is consistent with the observation made in the surface streamlines Fig. 3.44(b), at this azimuthal station.

A similar trend is observed in Fig. 3.46 as the flow progresses from mild stall at 318° to deep stall at 330° . The consistent under-predicted suction values at the outboard stations (Fig. 3.46) reflects the under-prediction of the normal load

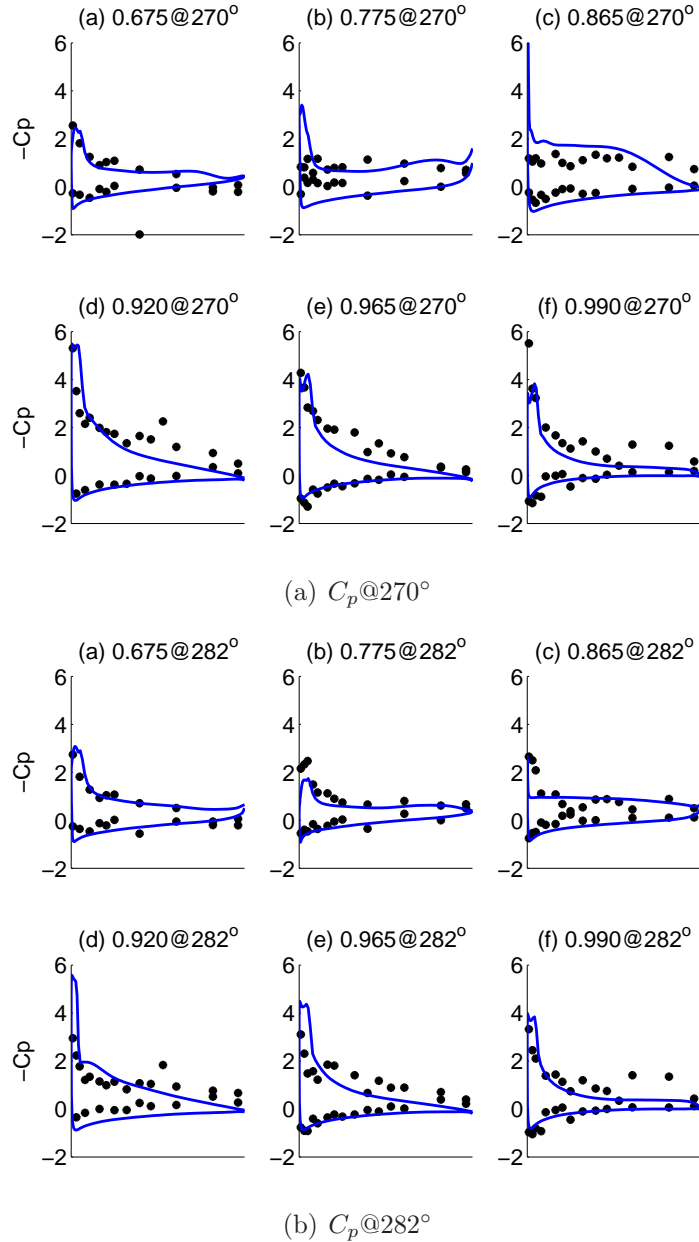


Figure 3.45: Surface pressure coefficient at different radial stations near *first* lift stall event for the baseline UH-60A rotor in C9017 flight condition. Black dot: Flight test data, Blue solid: CFD-CSD with shaft-fixed trim.

values and the phase offsets of the stall events. It is also observed that the airload predictions are better in the regions where the flow is mostly attached (e.g. at

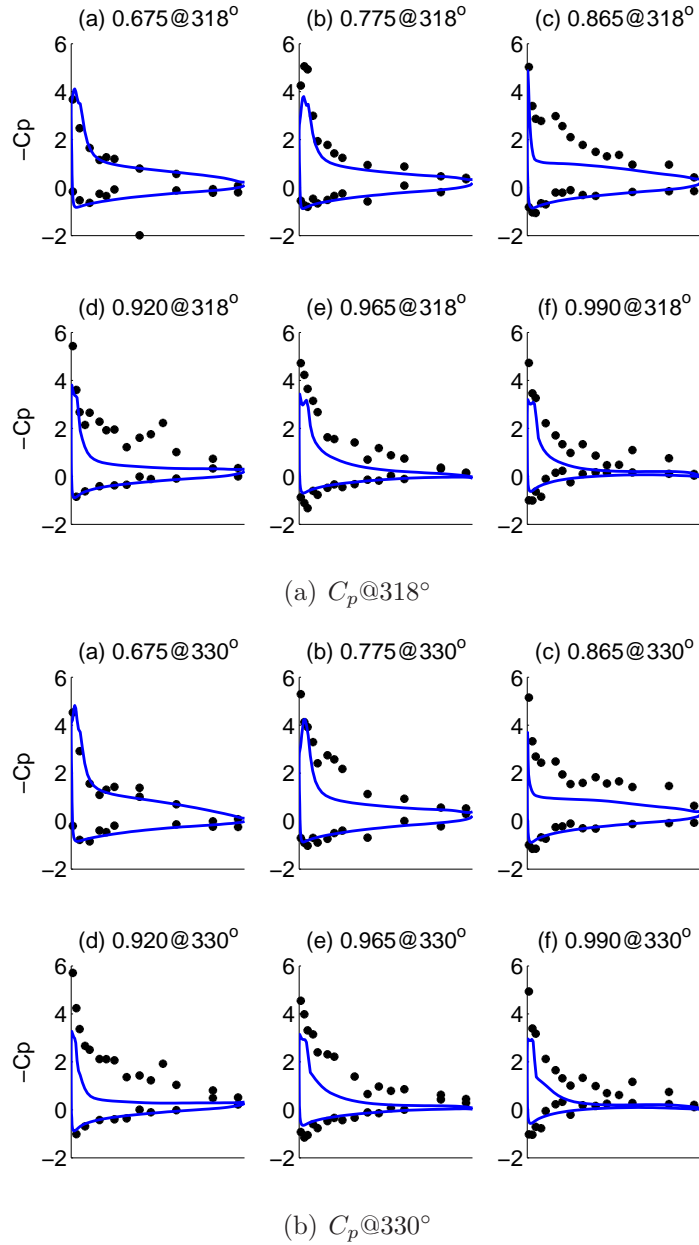


Figure 3.46: Surface pressure coefficient at different radial stations near *second* lift stall event for the baseline UH-60A rotor in C9017 flight condition. Black dot: Flight test data, Blue solid: CFD-CSD with shaft-fixed trim.

$r/R = 0.675$) and tends to deviate from the flight test data near inception of stall events (e.g at the outboard stations), that is, when the flow is separated.

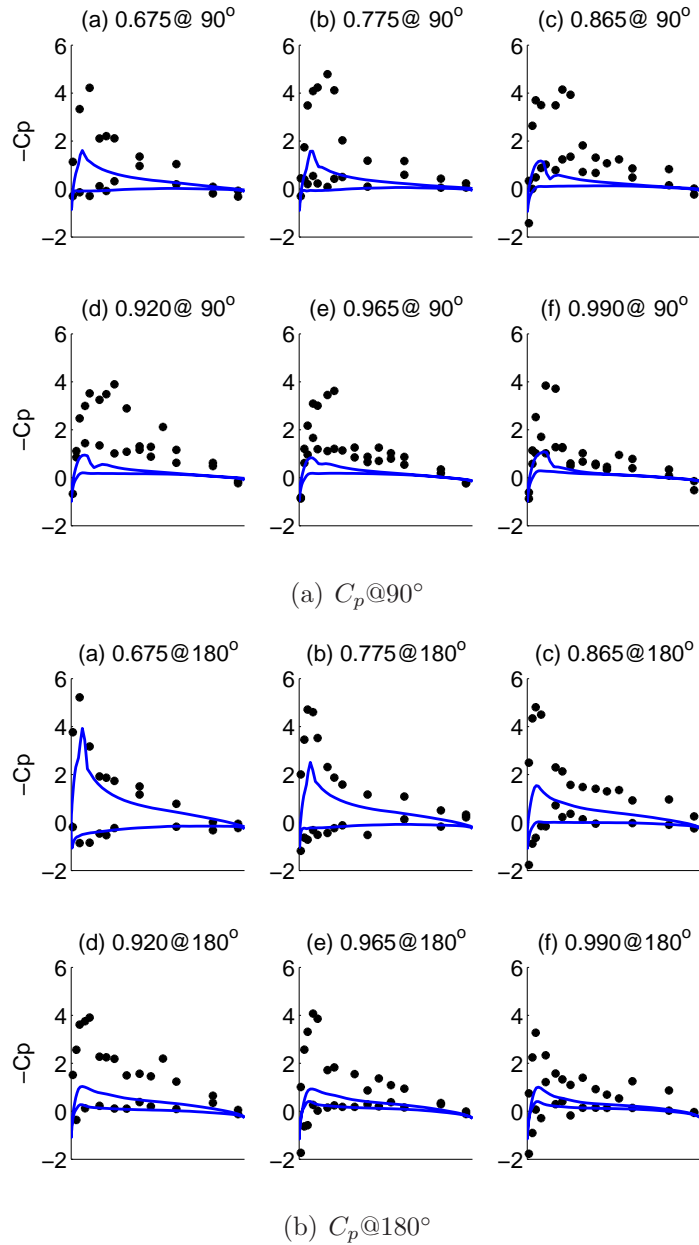
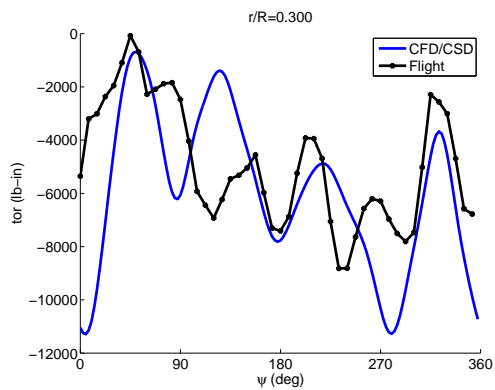


Figure 3.47: Surface pressure coefficient at different radial stations on advancing side of baseline UH-60A rotor in C9017 flight condition. Black dot: Flight test data, Blue solid: CFD-CSD with shaft-fixed trim.

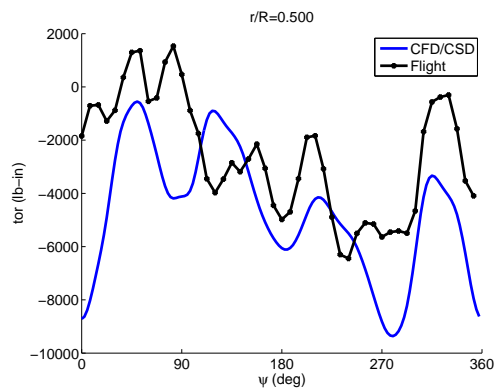
Figure 3.47 shows surface pressure profiles at two azimuth locations on the advancing side of the rotor. Consistently, the pressure values are under predicted by CFD/CSD computations compared to experiment. The predictions are relatively better at $\psi = 180^\circ$ than at $\psi = 90^\circ$. It must be noted here that, the experimental pressure values seem to be random and spurious at times. Further verification of the experimental data still needs to be done. While under prediction of the sectional pressure values at $\psi = 180^\circ$ are consistent with the under predicted normal sectional loads in Fig. 3.35, the pressure values at $\psi = 90^\circ$ are not as consistent.

Structural Dynamics: Torsional Moment and Pitch Link Loads

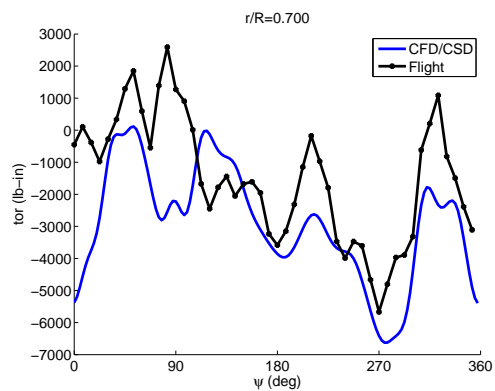
Figure 3.48 compares predicted sectional torsional moments at four radial stations with those from the flight test data. The trend of torsional moment time history is well predicted in terms of waveforms and peaks, except at the junction of the first and the second quadrant. The steady offset in mean value is an artifact of uncertainties in the test data. [88] The correlation is better at the inboard stations than outboard. However, the dominant $5/rev$ harmonics in sectional torsional moments, especially at the inboard stations, are not predicted by the CFD/CSD solver. Instead, the predicted moments show a dominant $4/rev$ trend. The discrepancy is due to the $4/rev$ harmonic over-prediction of the torsional section moments as demonstrated by Fig. 3.49. The figure shows the contribution of all harmonics ($1 - 10/rev$) to total torsional moment at the four radial stations. It is clearly observed that the fourth harmonic is dominantly over-predicted consistently across all radial stations. In these figures, it is further observed that except for $4/rev$ and $5/rev$ harmonic, the predicted amplitudes



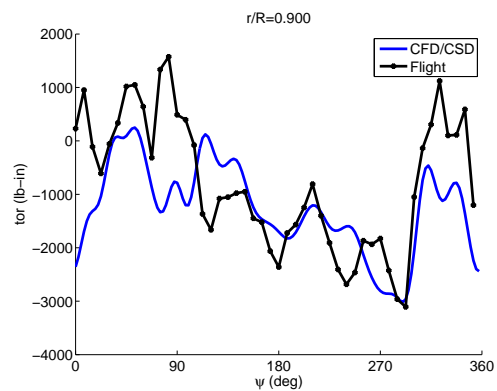
(a) Torsional moment @ $r/R = 0.30$



(b) Torsional moment @ $r/R = 0.50$

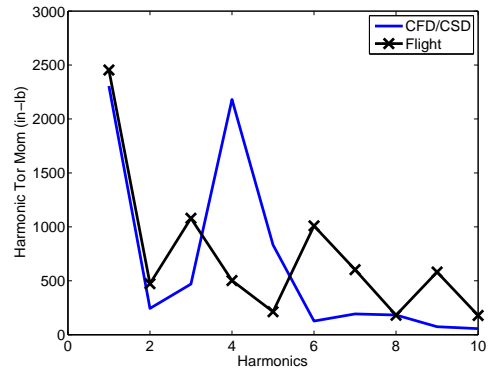
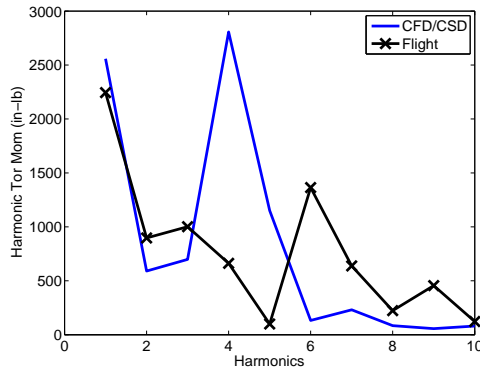


(c) Torsional moment @ $r/R = 0.70$



(d) Torsional moment @ $r/R = 0.90$

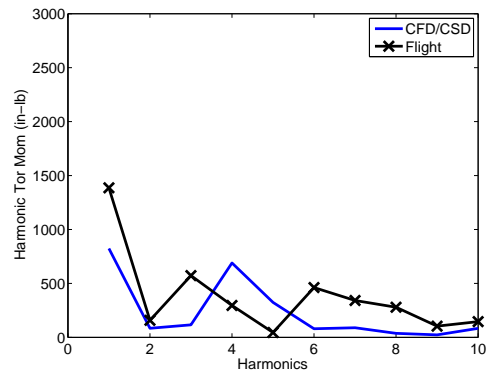
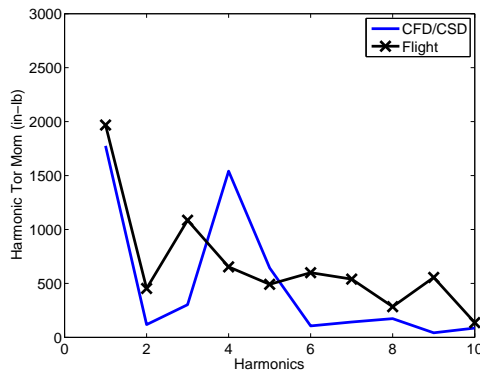
Figure 3.48: Comparison of CFD/CSD predicted sectional torsional moments with C9017 flight test data.



(a) Torsional moment Harmonics @ $r/R =$ (b) Torsional moment Harmonics @ $r/R =$

0.30

0.50



(c) Torsional moment Harmonics @ $r/R =$ (d) Torsional moment Harmonics @ $r/R =$

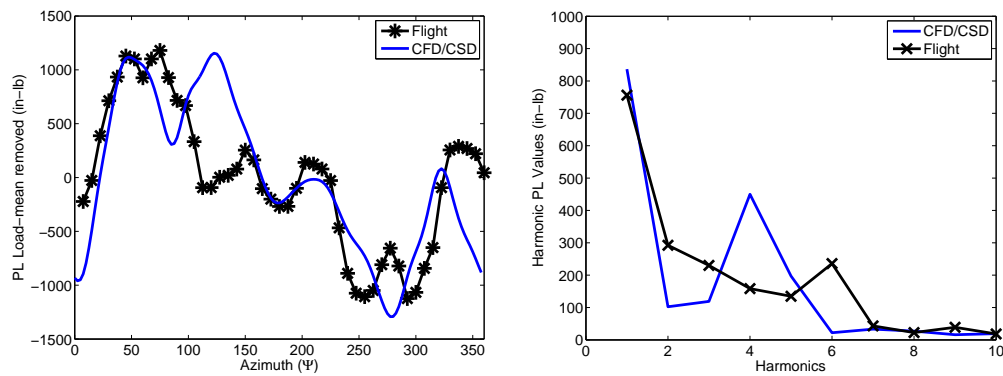
0.70

0.90

Figure 3.49: Comparison of CFD/CSD predicted amplitudes of harmonics of sectional torsional moments with C9017 flight test data.

of harmonics the moments are consistently comparable or under-predicted. This reflects in the overall under-prediction of the corresponding torsional moments. Moreover, the $4/rev$ amplitude monotonically diminishes towards the outboard stations and hence it can be observed that the outboard sectional torsional moments (3.49(c) and 3.49(d)) starts picking up the smaller harmonics.

However, the discrepancy is restricted only to the advancing side and not on the retreating side, as observed in 3.48. Thus, the error is not reflected in the torsional oscillations (combined $4/rev$ and $5/rev$ harmonics) on the retreating side, and hence does not jeopardize stall prediction at these azimuth locations. Further outboard, the discrepancy is more pronounced. The test data show an even larger harmonic content (upto $7/rev$ or larger) at the outboard station ($r/R = 0.90$), but computed values show still dominantly $4/rev$ content with only smaller amplitudes of higher harmonic oscillations.



(a) Pitch link (mean removed) vs azimuth ψ (b) Pitch link harmonic amplitudes vs harmonics

Figure 3.50: Comparison of CFD/CSD predicted pitch link load with C9017 flight test data.

Figure 3.50(a) compares the pitch link load time history (with mean removed) computed from the CFD/CSD analysis with the test data. To neglect the offset

in steady measurement error, the mean values are removed. Pitch link loads are the spanwise integrated torsional moment loads and therefore the trends and errors in pitch link loads are direct consequence of the trends and errors found in the sectional torsional moment predictions. The waveform and the peaks are well captured, except at the beginning of the second quadrant. Both the predicted and test data show a huge drop in values near azimuth locations, $\psi = 270^\circ$ and 360° , suggesting the presence of sharp moment stalls at these azimuths.

Similar to the observation made in torsional moments behavior the predicted pitch link loads show dominant $4/rev$ behavior, while the test data shows $5/rev$. As described before, the discrepancy is due to over-prediction of the $4/rev$ torsional sectional loads; mostly on the advancing side. Figure 3.50(b) shows the total pitch link load in terms of the amplitude contributions from its $1 - 10/rev$ harmonics. It clearly shows the dominant $4/rev$ harmonic over-prediction, which reflects on the pitch link load time history.

3.4 Summary

This chapter describes in detail the validation and verification of the CFD solver, which can handle multi-element airfoil (LE-Slats) configurations, against existing 2-D experimental wind tunnel data. It also demonstrates the superior advantages of slats in alleviating and/or eliminating dynamic stall on a pitching airfoil. Then, the computational model of the CFD solver is loosely coupled with a CSD (comprehensive) solver and validated against flight test data on a rotor in a moderate speed, high altitude and high thrust condition, namely, UH-60 for flight counter C9017. The predictions from the coupled analysis satisfactorily

capture the trends of the C9017 flight test condition both qualitatively, and quantitatively (to a limited accuracy). This establishes the coupled CFD/CSD model as a credible tool to analyze rotors with a slat.

Chapter 4

Rotor Performance Improvement using LE Slats

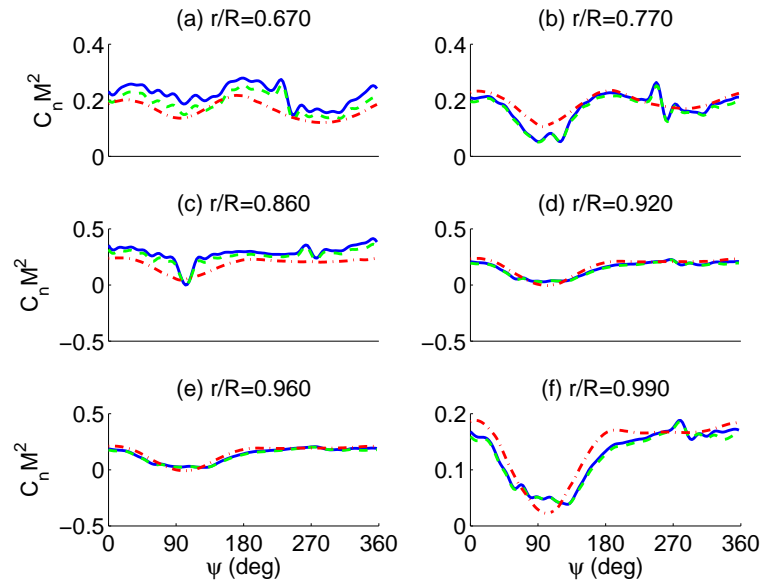
Having validated the coupled CFD/CSD solver for the UH-60A rotor, the solver is now used for evaluating the effectiveness of a slat on dynamic stall alleviation and thus analysing its effect on rotor performance improvement. A detailed analysis, using qualitative as well as quantitative parameters, is performed to demonstrate the slat capabilities in attaining better rotor performance. Further, studies are carried out to show the effectiveness of the slat in achieving higher thrust (pushing the thrust limit), which would allow expanding the flight envelope of the typical UH-60A rotor.

But, before the strategies to alleviate or eliminate dynamic stall are studied, it is vital to gain fundamental understanding of its dependence on rotor thrust itself. Dynamic stall is a performance compromise and a consequence of rotor wanting to achieve higher thrust limits. If the higher thrust requirement of the rotor were to be reduced, the retreating side dynamic stall problem could be totally eliminated. The first section explains this better by demonstrating the dependence of the rotor performance on rotor thrust settings.

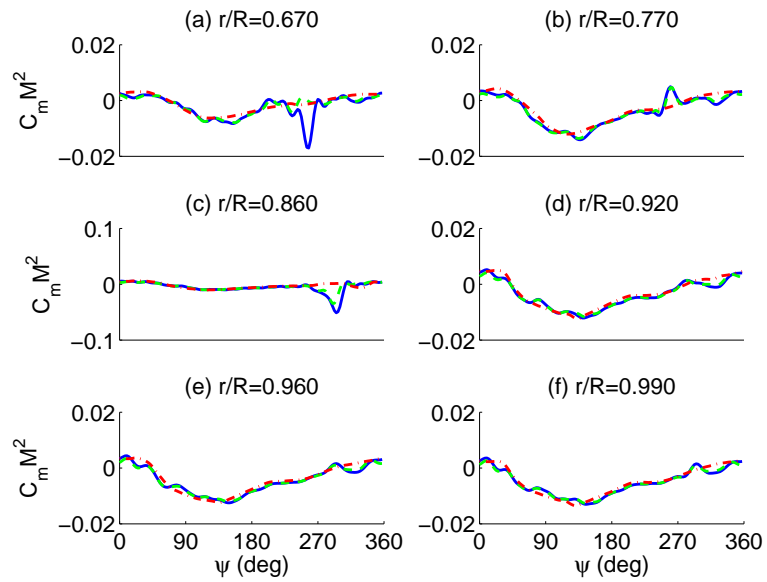
4.1 Effect of Thrust Setting on Dynamic Stall

To understand the onset of dynamic stall and its dependence on the rotor thrust setting, computations are performed at the same advance ratio ($\mu = 0.237$) as that of flight condition C9017, but at different C_T/σ settings. The conditions chosen are such that the rotor operated at 10% and 5% lower thrust than the baseline C9017 flight condition. A fair estimate of the thrust effect on stall events is first obtained through a comprehensive analysis using UMARC. Figure 4.1 shows the normal force and pitching moment time history predictions from the linearized aerodynamic model. While 5% thrust reduction mitigates the stall event by almost 50% (in terms of pitching moment drop near 300° azimuth location), 10% thrust reduction seems to eliminate the dynamic stall altogether. Figures 4.2–4.4 show the CFD prediction and comparison of the normal force, pitching moment, and the chord wise force time histories for these three thrust conditions at several radial stations. It is observed that even a 5% reduction in the thrust is sufficient to nearly eliminate the effect of dynamic stall on the pitching moment time histories in the retreating side of the rotor disk. As with UMARC predictions, considerable reduction in the variations of normal force and chord wise forces are observed at this reduced thrust condition. But, unlike UMARC, the CFD air load time histories do not vary appreciably with further reductions in the rotor thrust.

To obtain a quantitative parameter capable of indicating the onset of dynamic stall, two possible indicators are analyzed: (a) integrated vibratory torsional loads (4–17rev) near the blade root ($r/R = 22.5\%$), and (b) the blade pitch link loads. Figure 4.5 compares the time histories and the half peak-to-peak blade vibratory torsional moments at the blade root. UMARC underpredicts the peak-



(a) Normal Loads



(b) Pitching Moments

Figure 4.1: Variation of UMARC linearized aerodynamic airloads with thrust.

$C_T/\sigma = 0.1325$; $C_T/\sigma = 0.1258$; $C_T/\sigma = 0.1190$

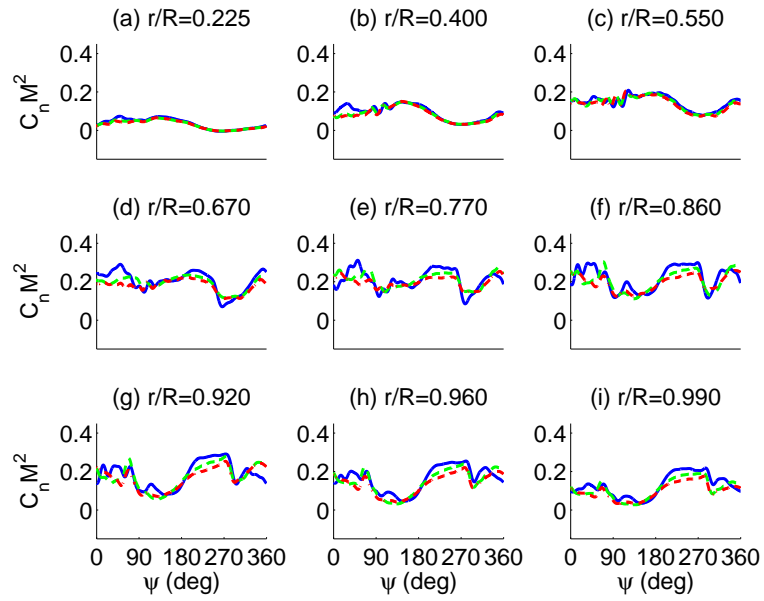


Figure 4.2: Variation of CFD normal loads with thrust. Blue solid: $C_T/\sigma = 0.1325$; Green dash: $C_T/\sigma = 0.1258$; Red dash-dot: $C_T/\sigma = 0.1190$

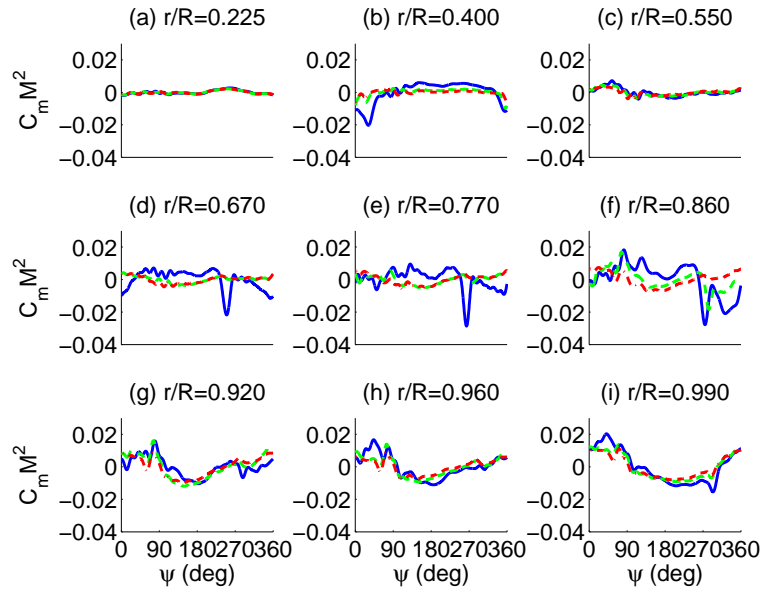


Figure 4.3: Variation of CFD pitching moments with thrust. Blue solid: $C_T/\sigma = 0.1325$; Green dash: $C_T/\sigma = 0.1258$; Red dash-dot: $C_T/\sigma = 0.1190$

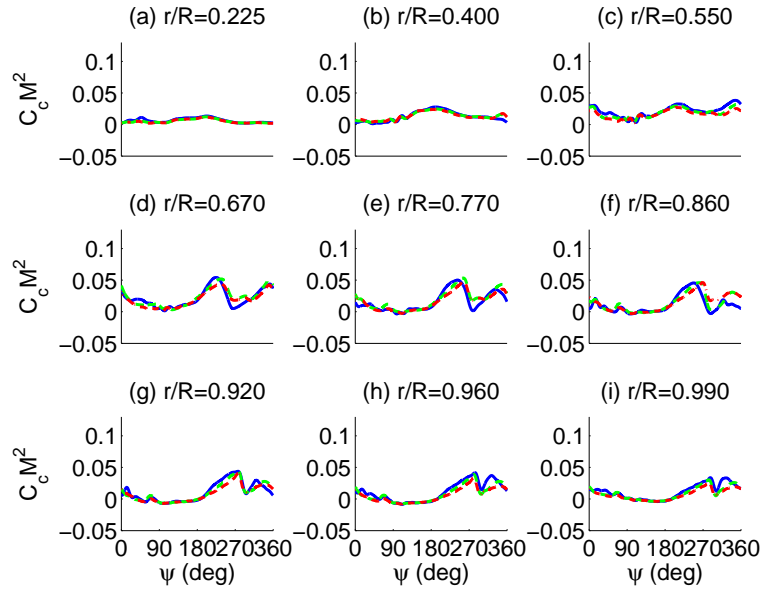
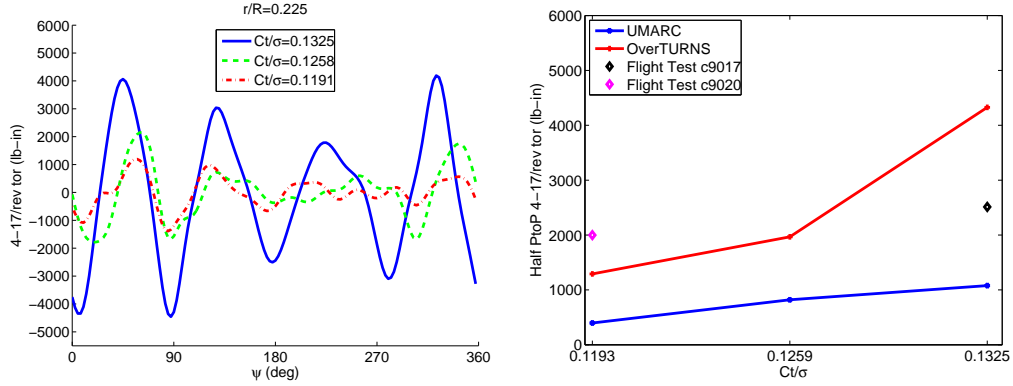


Figure 4.4: Variation of CFD chord wise forces with thrust. Blue solid: $C_T/\sigma = 0.1325$; Green dash: $C_T/\sigma = 0.1258$; Red dash-dot: $C_T/\sigma = 0.1190$

to-peak torsional moments as compared to CFD. For example, for the baseline $C_T/\sigma = 0.1325$, the half peak-to-peak predictions by the coupled analysis is 3347 lb-in, from UMARC it is 1419 lb-in while the flight test data is 2512 lb-in. It is observed that a reduction in thrust by as little as 5% results in a significant reduction (around 33%) in the half peak-to-peak moments. Favorable effects of thrust reduction are also observed in the pitch link loads (see Fig. 4.6), indicating that slight changes in the rotor lift distribution can significantly reduce or even completely eliminate the dynamic stall phenomena in the retreating side. This is well demonstrated by upto 55% reduction in peak-to-peak pitch link load observed for the lowest thrust case. See Fig. 4.6(a). Figure 4.6(b) also shows the measured values from the UH-60A flight counter C9020. This flight condition has approximately the same thrust as the lowest condition used in the present simulation. However, it must be emphasized that the flight conditions are not

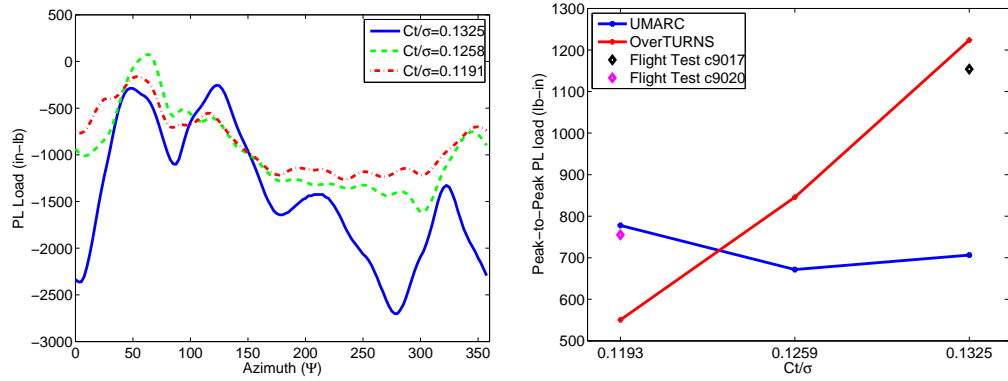


(a) CFD predicted Torsional 4 – 17/rev moment vs azimuth (Ψ) (b) Half peak-to-peak 4 – 17/rev torsional moments vs C_T/σ

Figure 4.5: Sectional 4 – 17/rev torsional moments at $r/R = 22.5\%$: effect of thrust on stall; Blue solid: $C_T/\sigma = 0.1325$; Green dash: $C_T/\sigma = 0.1258$; Red dash-dot: $C_T/\sigma = 0.119$

exactly identical and the comparison is strictly qualitative. Although, the drop in pitch link loads predicted by CFD with decreasing thrust is larger than measured, the trend is correct.

Finally, Fig. 4.7 compares the vibratory 4/rev rotor hub loads for the three cases. All quantities are non-dimensionalized by the baseline C9017 values. It is observed that there is a noticeable reduction in all three hub forces and hub moments (except for M_y) with reduced rotor thrust values. This is expected because, for the lower thrust conditions the dynamic stall events are weaker, and hence there is reduced unsteady load on the blade and consequently on the rotor hub. It must be emphasized that the absolute values of the rolling (M_x) and pitching (M_y) moments are relatively insignificant ($\leq 3\%$) compared to the rotor torque values (M_z) and hence their relative non-dimensional values are not as important as that of the rotor torque values while comparing the relative



(a) CFD predicted Pitch link load vs azimuth (Ψ) (b) Half peak-to-peak pitch link load vs C_T/σ

Figure 4.6: Pitch link loads: effect of thrust on stall; Blue solid: $C_T/\sigma = 0.1325$; Green dash: $C_T/\sigma = 0.1258$; Red dash-dot: $C_T/\sigma = 0.119$

merits of the various slat configurations. The reduced hub loads can be further explained by Figure 4.8 which compares the vibratory normal loads ($3 - 20/rev$) of the baseline condition with that of the two lower thrust conditions. The vibratory loads, especially the $3/rev$ and $3 \pm 1/rev$ ones, contribute towards the hub $4/rev$ loads. From the figure it is evident that the peak-to-peak values of these vibratory loads for the lower thrust settings are considerably smaller than for the baseline thrust setting and therefore, the hub loads are smaller for the lower thrust conditions compared to the baseline one as described in Figure 4.7.

Table 4.1 compares control angles and power loss for the various thrust cases. With reduced thrust, there is reduced lift requirement and therefore, correspondingly, reduced trim collective requirements. It is also observed that the power loss is better recovered for lower thrust conditions because of their attenuated dynamic stall events.

Table 4.1: CFD Predicted Trim Control Angles and Power for Three Thrust Cases

C_T/σ	θ_0	θ_{1c}	θ_{1s}	α	C_Q/σ
0.1325 (Baseline)	14.86	7.01	-8.55	-2.85	0.01120
0.1258	11.72	4.06	-6.95	-2.85	0.00666
0.1192	10.48	3.09	-5.99	-2.85	0.00514

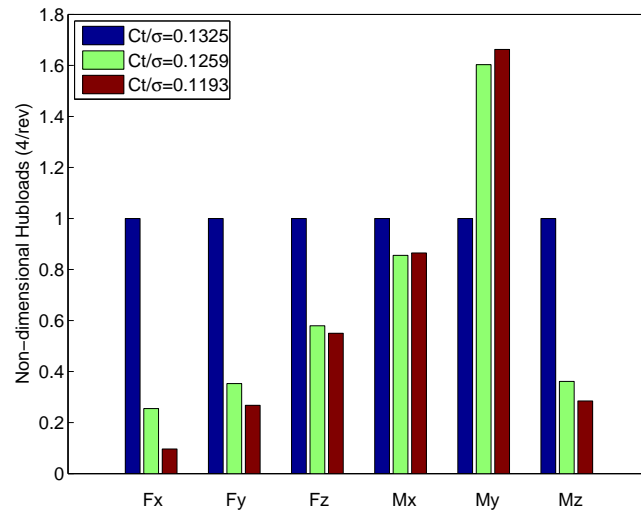


Figure 4.7: CFD predicted 4/rev Hub loads; $C_T/\sigma = 0.1325$; $C_T/\sigma = 0.1258$;
 $C_T/\sigma = 0.119$

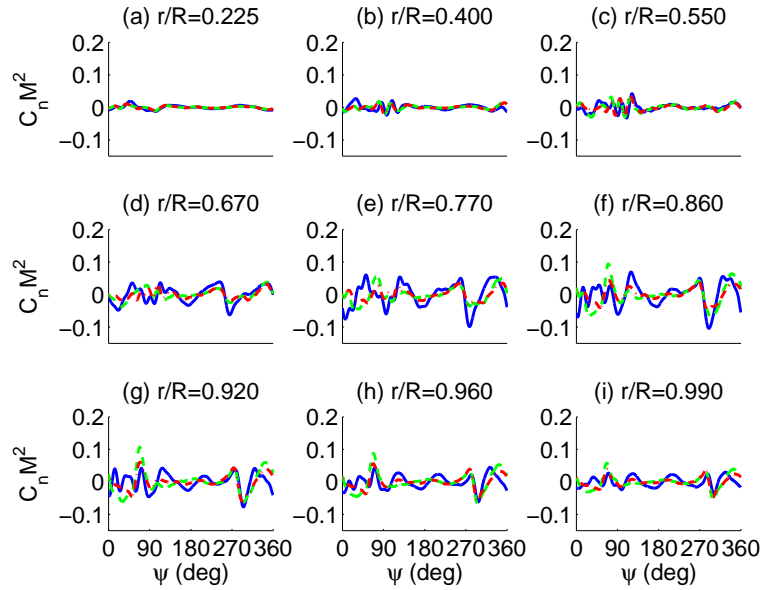


Figure 4.8: Variation of CFD vibratory normal loads ($3 - 20/rev$) with thrust. Blue solid: $C_T/\sigma = 0.1325$; Green dash: $C_T/\sigma = 0.1258$; Red dash-dot: $C_T/\sigma = 0.119$

4.2 Analysis of UH-60A with Slat

The results shown in the previous sections provide enough confidence in applying the coupled simulation to study the effectiveness of a leading-edge slat for mitigation of dynamic stall in helicopter rotors. The focus of this section is to study the performance of a modified UH-60A rotor blade with leading-edge slat for the C9017 flight condition, and determine if the benefits seen in 2-D computations translate into better aerodynamic characteristics for the rotor blade in high thrust flight conditions.

4.2.1 Modified UH-60A Rotor Blade with Slat

To analyze the effect of slat on rotor aerodynamics a modified UH-60A rotor blade is considered with a single slat that spans across 50% – 90% of the rotor radius. The slat geometry proposed by Lorber et al. [15] was specifically designed for a particular main airfoil section which is different from the SC1095-R8 sections in the midspan region of the baseline UH-60A blade. Using this slat geometry with the baseline UH-60A airfoil geometry will not provide the optimum channeling of the flow near the leading edge of the main airfoil section – see Fig. 4.9. Therefore, the modified blade geometry replaces the baseline airfoil sections in the region such that it uses the same airfoil-slat combination that was used in the 2-D experiments. Note that the modifications were purely restricted to the blade surface definition used by the CFD meshes only. The blade structural properties were not modified to account for the additional mass increase from slat or the change in the blade moments of inertia.

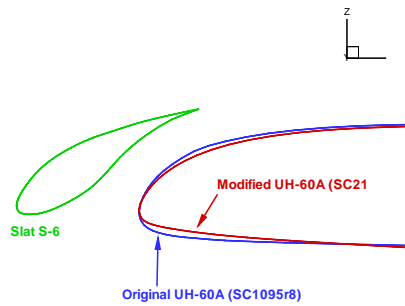


Figure 4.9: Modified UH60 Blade with Slat S-6

As a sanity check, to ensure that the modification of the rotor blade does not drastically alter the lift and pitching moment characteristics across the blade span at the C9017 flight condition, computations were performed with the modi-

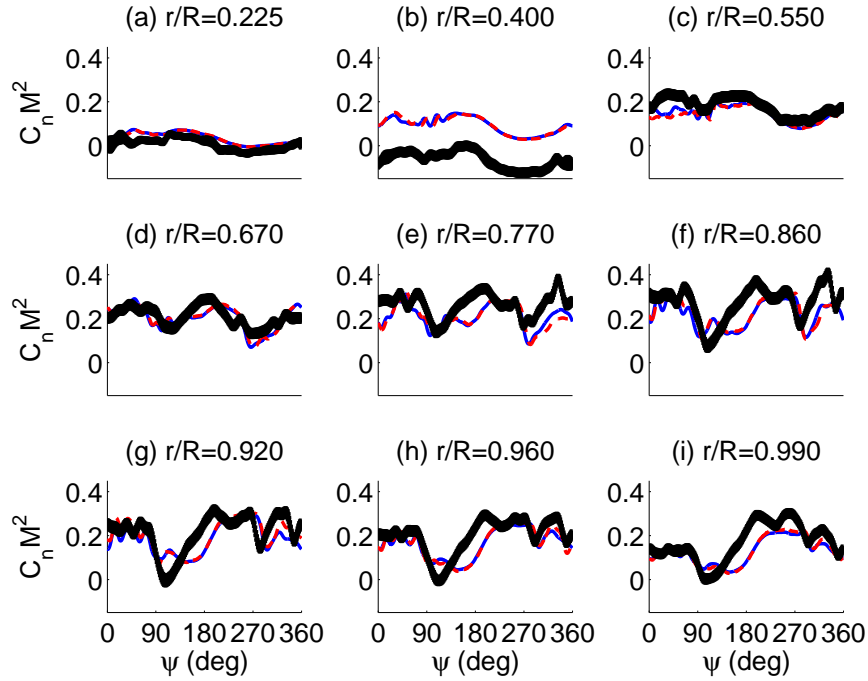


Figure 4.10: Predicted and measured sectional normal loads for C9017. Black dot: Flight Test Data; Blue solid: CFD UH60A Blade; Red dash: CFD UH60A-*mod* Blade.

fied UH-60A blade geometry without the slat and compared against the baseline UH-60A rotor results at this flight condition – see Figs. 4.10 and 4.11. While the normal load time histories show no noticeable affect, the moment load time history show a slight deterioration of the pitching moment stall at certain radial stations ($r/R = 0.86$) and an over prediction of the same at certain other stations ($r/R = 0.92, 96$) due to the modified blade geometry. However, the final trim control settings and the rotor power remain largely unchanged for the modified rotor geometry, as shown in Table 4.2.

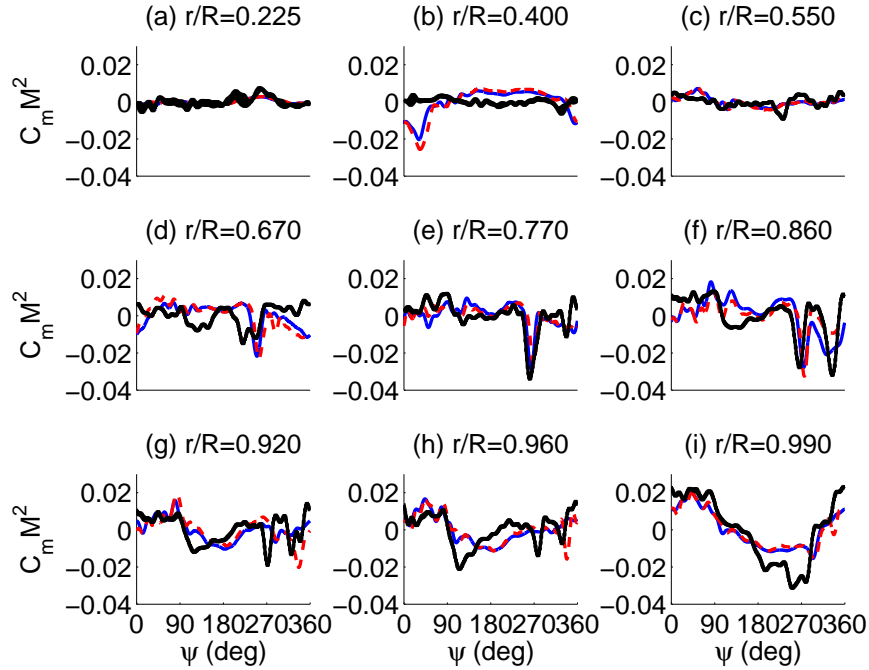


Figure 4.11: Predicted and measured sectional moment loads for C9017. Black dot: Flight Test Data; Blue solid: CFD UH60A Blade; Red dash: CFD UH60A-mod Blade.

Blade Type	θ_0	θ_{1c}	θ_{1s}	α	C_Q/σ
UH-60A	14.86	7.01	-8.55	-2.85	0.01120
UH60A-mod	14.63	6.69	-8.58	-2.85	0.01069

Table 4.2: Final trim control angles and the predicted rotor power for the baseline and the modified UH-60A rotor geometries without the slat.

4.2.2 2-D Dynamic Slat Actuation

So far the slat has been considered to be static with respect to the main blade. Actuating the slat with respect to the blade would introduce the active control feature to the blade design which would allow the blade more control authority

on its influence on flow physics. Appropriate actuation would lead to better performance of the multi-element airfoil. Therefore, taking a step back to two dimensional flows, this section analyses the fundamental advantages and the disadvantages of a dynamic slat for an airfoil undergoing pitching motion. No experimental measurements are available for such a situation, so the results are compared with the pitching motion results obtained with the two extreme static slat configurations.

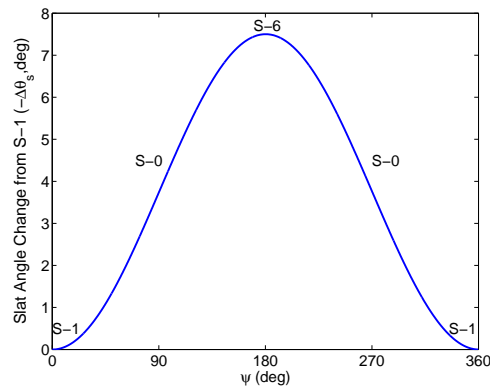


Figure 4.12: Time history of slat angle over one cycle ($-\Delta\theta_s$ versus ψ) due to $1/rev$ slat actuations

In order to determine the optimum dynamic slat actuation strategy that will provide us with the maximum performance gains over the entire cycle of the unsteady pitching motion, one must analyze the potential advantages and disadvantages of the S-1 and S-6 configurations. Both configurations have the advantage of increasing the stall margin compared to the baseline airfoil, but they are accompanied by a higher nose-down pitching moment penalty. Slat configuration S-6 is more effective in pushing the stall margin to higher angles of attack compared to the S-1 configuration. Consequently S-6 incurs larger nose-down pitching moment over a wider range of angle of attack than the S-1

configuration. However, the S-1 configuration has a lower nose-down pitching moment penalty and lower drag at low angles of attack (typical of blade sections on the advancing side). Thus, the dynamic actuation must be such that the slat is at the S-1 configuration when the airfoil is at its lowest pitch angle, and it is at S-6 configuration when the airfoil is at the maximum pitch attitude. Figure. 4.12 shows change in slat angle with respect to the S-1 position over one pitching cycle.

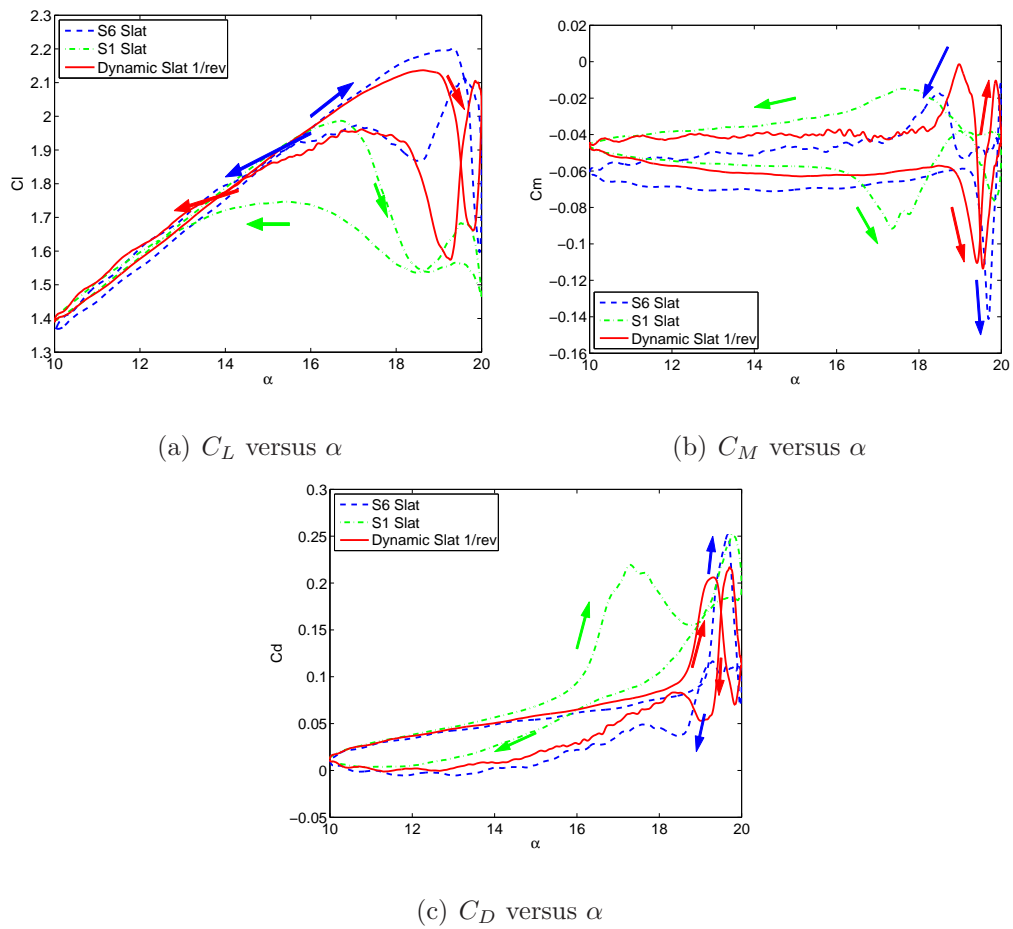


Figure 4.13: Airload comparisons for static and dynamic slat cases

Figure 4.13 compares the time histories of the lift, pitching moment, and drag variations predicted for a dynamic slat actuation with that predicted for

the two static slat configurations for an unsteady airfoil pitching motion. The overall behavior of the dynamic slat actuation represents a compromise between the S-1 and S-6 aerodynamic characteristics. The normal and drag loads for the dynamic slat case are better than those for the S-1 configuration throughout the cycle. The nose-down moments characteristics are much improved than either static configurations, but is comparable to the S-6 airload characteristics over most part of the cycle. At larger angles moment values tend towards that of the S-6 values, and are closer to the low S-1 values at lower angles of attack. Thus, at lower angles it overcomes the large moment penalty and at larger angles, it not only delays stall, but also improves its lift-to-drag ratio.

4.2.3 Effectiveness of Slat on Dynamic Stall Mitigation

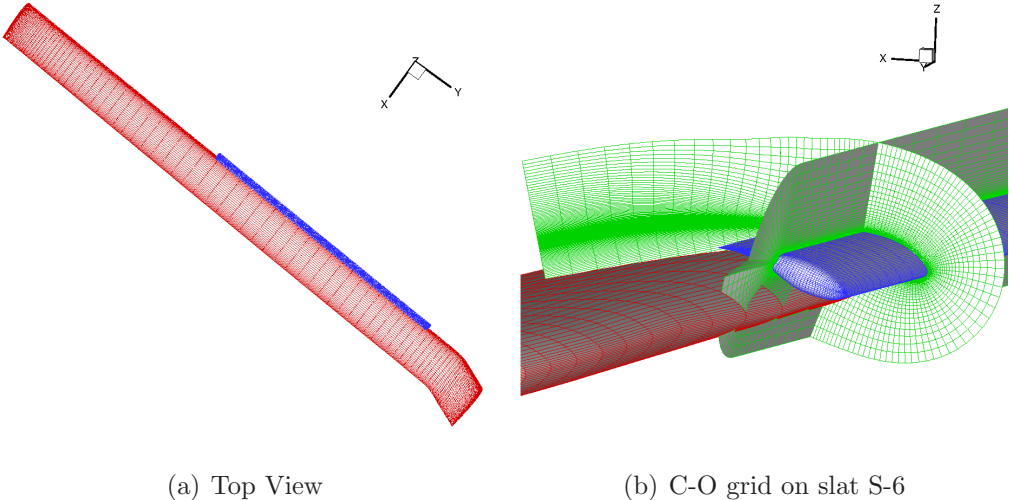


Figure 4.14: Slat S-6 Geometry

A coupled simulation of the C9017 flight condition for the modified UH-60A rotor blade is performed both with static and dynamic slat actuations. The slat spans 40% of the main rotor blade ($r/R = [0.5 : 0.9]$). See Fig. 4.14(a). The

computational mesh used for the slat is a C-O topology mesh with $129 \times 77 \times 65$ points along wrap around, span wise and normal direction, respectively – see Fig. 4.14(b). The surface spacing in the normal direction is 5×10^{-6} chords of the main element and the outer boundaries are 10% of the slat span away.

The existing CFD solver required both the blade mesh and the wake mesh in any quadrant to be in one single processor and the computation for the whole rotor was performed using only four processors. Current methodology improves upon this parallelization for further reduction in the cost of the CFD computation. Each of the blade and the wake meshes is now split into multiple mesh blocks to compute the solution in parallel. The mesh splitting is done so as to ensure the most optimal load balancing. For example, for a slatted rotor computation with 10 processors per quadrant (and 40 processors for the whole rotor), the slat mesh is split into 2, the blade mesh into 4 and the wake mesh into 4 processors. The slat mesh being smallest requires fewer split mesh blocks than is required for the blade and the wake meshes. Figure 4.15 summarizes the computational speed up due to the parallelization for the baseline as well as the slatted (S-6) rotor cases. The speed up values are obtained by comparing the computational time for a given number of processors (Np) with respect to the corresponding minimum number of processors ($Np0$) used for that particular rotor case. In the figure, $Np0 = 8$ for the baseline rotor, and $Np0 = 12$ for the slatted rotor computations. It is observed that the parallelization of the slatted rotor is less efficient than that of the baseline rotor. It can be attributed to additional communication time required for the airload information transfer from the slat processors to the main blade processors for rotor airload computation. The reduced efficiency of slatted rotor is also because of the overhead

computation required for obtaining connectivity information for a larger overset group (of three grids) as compared to the baseline rotor overset group (of two grids) during the hole cutting step. Overall, the baseline rotor clocks approximately 20 hours with 32 processors and the slat S-6 rotor clocks approximately 26 hours with 40 processors to compute solution for one rotor revolution (360°) on a Intel(R) Xeon(TM) CPU 3.20GHz machine. It must be noted here that the parallelization is performed only for computing the flow solution and not for obtaining the connectivity information in the hole cutting step.

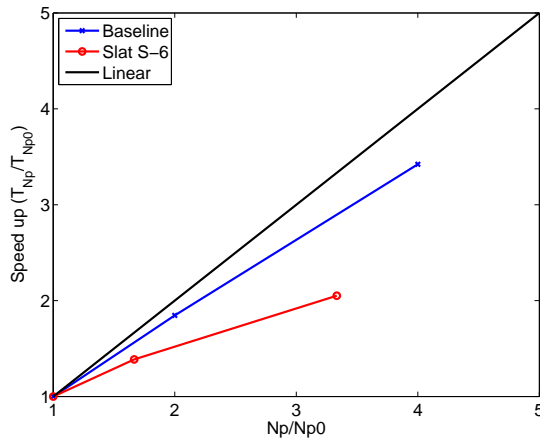


Figure 4.15: Computational time speed up for Np processors with respect to the corresponding minimum number of processors ($Np0$) used for baseline as well as slatted (S-6) rotors

The integrated sectional airloads at a given span, transferred to the CSD solver, is the vector sum of the slat and the main airfoil loads about the elastic axis. Note that the inertial effects of the slat are not modeled in the structural solver. However, the blade dynamics over the entire span is affected by the modified airloads at the sections where the slat is present. This in turn affects the aerodynamics over the entire blade span in the successive coupled trim it-

erations. The net effect is that the blade dynamic and aerodynamic response is considerably different compared to the baseline rotor at all blade sections when the coupling cycles converge.

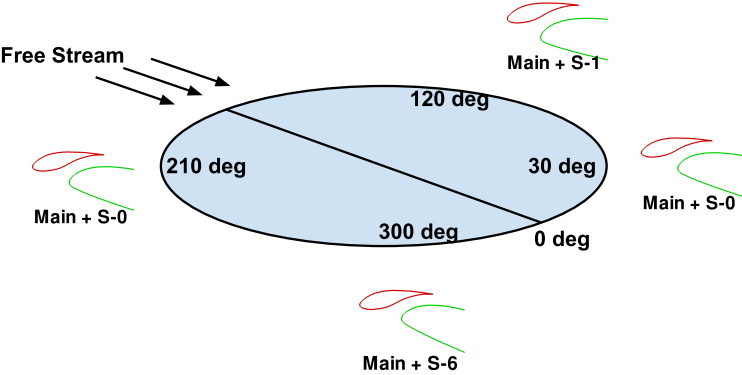


Figure 4.16: Schematic of slat actuation over a rotor revolution with appropriate phase offset.

For static slat analysis, both the S-6 and S-1 slat configurations were considered. For the dynamic slat actuation, the slat motion is prescribed such that the slat is at the S-6 configuration when the blade is at $\psi = 300^\circ$ and at the S-1 configuration on the advancing side at $\psi = 120^\circ$. This phase offset is to ensure the S-6 configuration during the deepest stage of the first dynamic stall event. A $1/rev$ actuation is introduced to transition the slat between these extremes as the blade rotates around the hub. See Fig. 4.16.

Figures 4.17–4.19 show the time histories of the non-dimensional normal force, pitching moment, and chord wise force at six outboard stations of the rotor blade. The normal forces show a slight alleviation of the severity of the dynamic stall at the outer sections with both static and dynamic slat actuations. However, the most significant difference is observed in the retreating blade pitch-

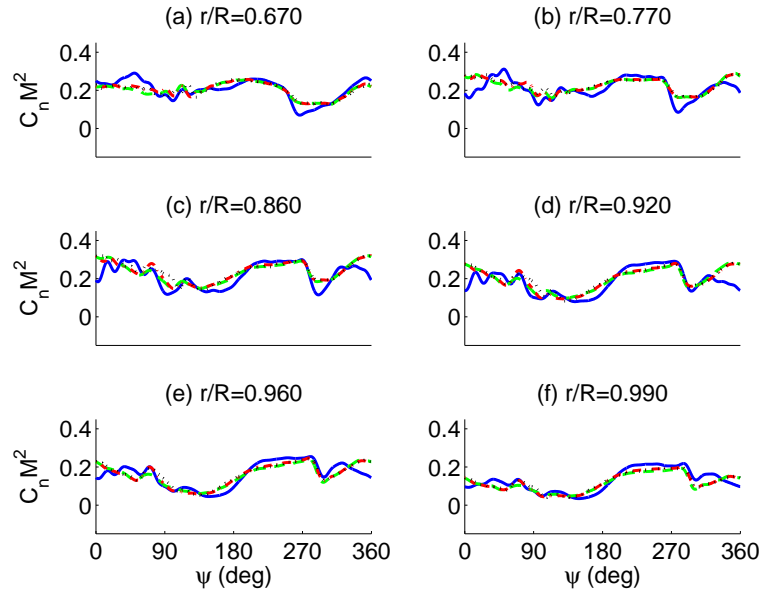


Figure 4.17: Time history of CFD normal loads with dynamic slat. **Blue solid:** no slat; **Green dash:** steady slat S-6; **Red dash dot:** steady slat S-1; **Black dot:** dynamic slat.

ing moment loads; the presence of the slat is able to completely eliminate the two moment stall cycles in the fourth quadrant. However, a slight increase in the nose-down pitching moment is observed on the advancing side. Moreover, all the slat configurations consistently incur larger drag penalty on the advancing side, arising mostly due to larger profile drag of the slatted airfoil.

The contour plots of the unsteady pitching moments (with means removed), shown in Fig. 4.20, over the rotor disk provides a better understanding of the relative differences between the baseline no-slat rotor, and the static and the dynamic slatted rotors. While the baseline rotor shows the presence of stalled regions (blue colored areas) on the retreating side, introduction of a slat seems to eliminate these moment stall regions completely over the entire rotor disk.

The trends are similar to those observed for the 2-D airfoil sections analyzed

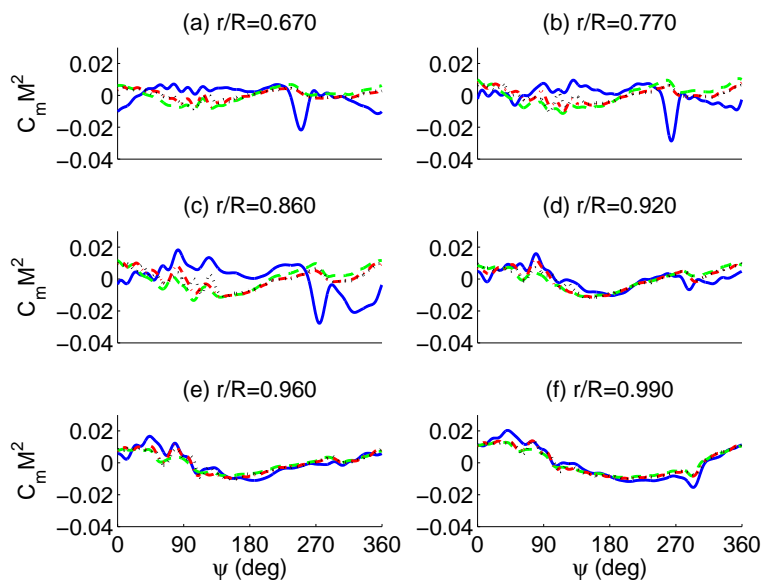


Figure 4.18: Time history of CFD pitching moments with dynamic slat. Blue solid: no slat; Green dash: steady slat S-6; Red dash dot: steady slat S-1; Black dot: dynamic slat.

previously. While the net integrated sectional normal forces look similar for the two slat actuations analyzed, examination of the vibratory loads show finer differences between the two actuations – see Fig. 4.21.

As mentioned previously, the presence of the slat also affects the blade dynamic response in the converged trimmed flight condition. These changes in the blade deformations is reflected in the final trim control settings, and the rotor power as shown in Table 4.3. The additional lift generation from the presence of the slat allows the rotor to achieve the same thrust at a lower collective setting compared to the baseline rotor. Even though the S-1 slat results in a lower collective and complete elimination of dynamic stall, it incurs a larger power loss than both the static S-6 slat and dynamic slat actuation cases.

Figure 4.22 shows the variation of the effective geometric angle of attack at

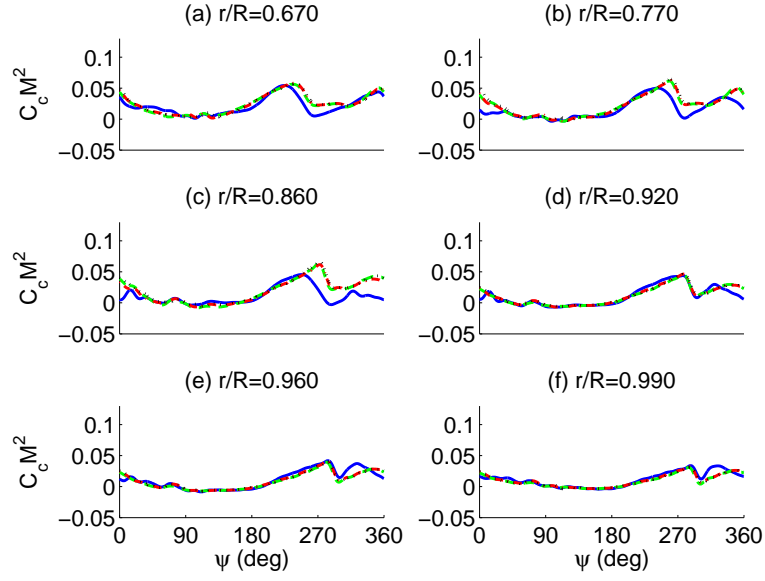


Figure 4.19: Time history of CFD chord wise forces with dynamic slat. Blue solid: no slat; Green dash: steady slat S-6; Red dash dot: steady slat S-1; Black dot: dynamic slat.

three radial stations across the span. The geometric angle of attack shown here includes the contribution from the blade collective and cyclic pitch ($\theta_{control}$), the built-in pre-twist (θ_{tw}), and the elastic twist response of the blade (ϕ), i.e. $\theta_{tot}(r, \psi) = \theta_{control}(r, \psi) + \theta_{tw}(r) + \phi(r, \psi)$, where (r, ψ) refer to any radial and azimuthal location, respectively. A reduction in the effective geometric angle of attack for the slatted-rotor configurations is clearly noticed, particularly in the fourth quadrant of the rotor disk. In addition to improving the sectional lift characteristics, the presence of the slat also introduces a beneficial blade dynamic response which reduces the effective angle of attack thereby delaying the onset of dynamic stall.

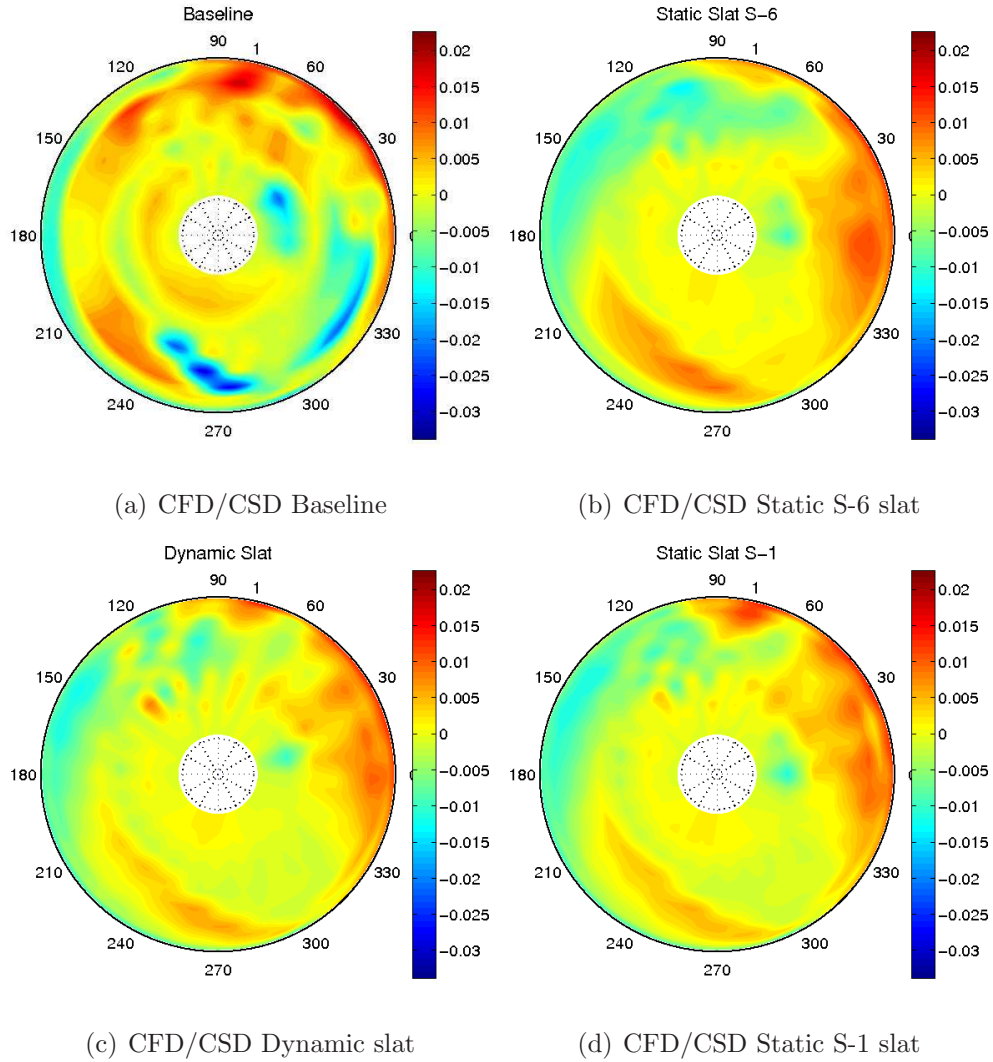


Figure 4.20: Comparison of the pitching moment variation across the rotor disk for the static and dynamic slat analyses with the baseline no-slat rotor.

Qualitative Analysis of Dynamic Stall Mitigation

The streamlines in Fig. 4.23 clearly shows how the introduction of any slat (S-1 and S-6) causes elimination of the strong dynamic stall vortex, otherwise present at outboard stations on the baseline rotor. The stations shown are at $r/R = 73\%$, 75% and 79% .

Figure 4.24 compares the Q-criterion iso surface for the baseline rotor with

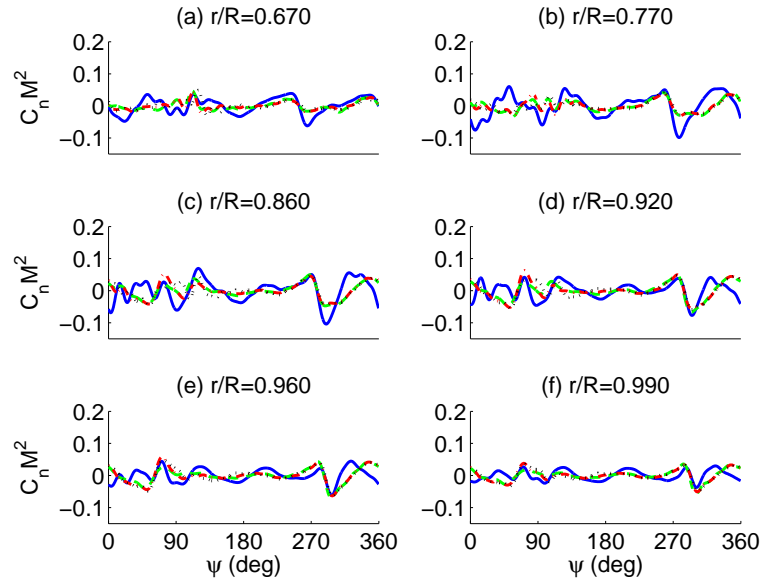


Figure 4.21: Time history of CFD vibratory normal loads ($3 - 20/rev$) with dynamic slat. **Blue solid:** no slat; **Green dash:** steady slat S-6; **Red dash dot:** steady slat S-1; **Black dot:** dynamic slat.

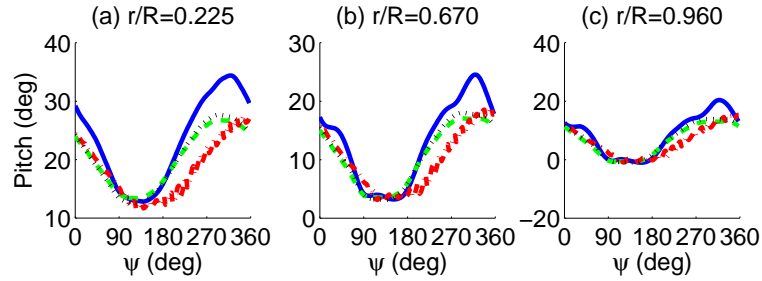


Figure 4.22: Variation of the effective geometric angle of attack as a function of azimuth at different radial stations. **Blue solid:** no slat; **Green dash:** steady slat S-6; **Red dash dot:** dynamic slat; **Black dot:** steady slat S-1.

the slat S-6 UH-60A blade. Due to the lower collective and reduced stall events, the vortex wake strength has reduced with the introduction of slat S-6.

The carpet surface pressure plots for the upper surface at relevant stations

Blade Type	θ_0	θ_{1c}	θ_{1s}	α	C_Q/σ
Baseline UH60A	14.86	7.01	-8.55	-2.85	0.01120
Slat S-6	11.41	3.52	-5.72	-2.85	0.00674
Slat S-1	11.25	3.89	-6.63	-2.85	0.00727
Dynamic Slat	11.29	3.95	-6.46	-2.85	0.00700

Table 4.3: Comparison of the final trimmed control pitch settings and the net rotor power for the modified UH-60A configurations and the baseline UH-60A rotor.

reveal the effectiveness of the slat – see Figs. 4.25 and 4.26. The first of these figures compares pressure peaks near the leading edge at rotor inboard stations where the slat is present. Due to the favorable gap effects due to slat S-6, the suction pressure peaks are significantly relieved on the upper surface of the airfoil at both the inboard stations shown in Fig. 4.25. The suction peak values seem to be reduced nearly by half. Even at the two stations outboard of the slat, the indirect influence of the slat is found; the suction pressure peaks relief is mild but noticeable.

Stall Indicators: Pitch Link Load and Root Torsional Moment

Pitch link loads and root sectional torsional moment loads serve as appropriate indicators for the onset of blade stall, and can be used as a quantitative metric for determining the effectiveness of a given slat configuration. Figure 4.27 shows the time histories of the vibratory torsional loads at the root (4 – 17/rev) and the corresponding pitch link loads in the hub frame. The severest pitch link loads occur in the advancing and retreating side. The presence of a slat clearly

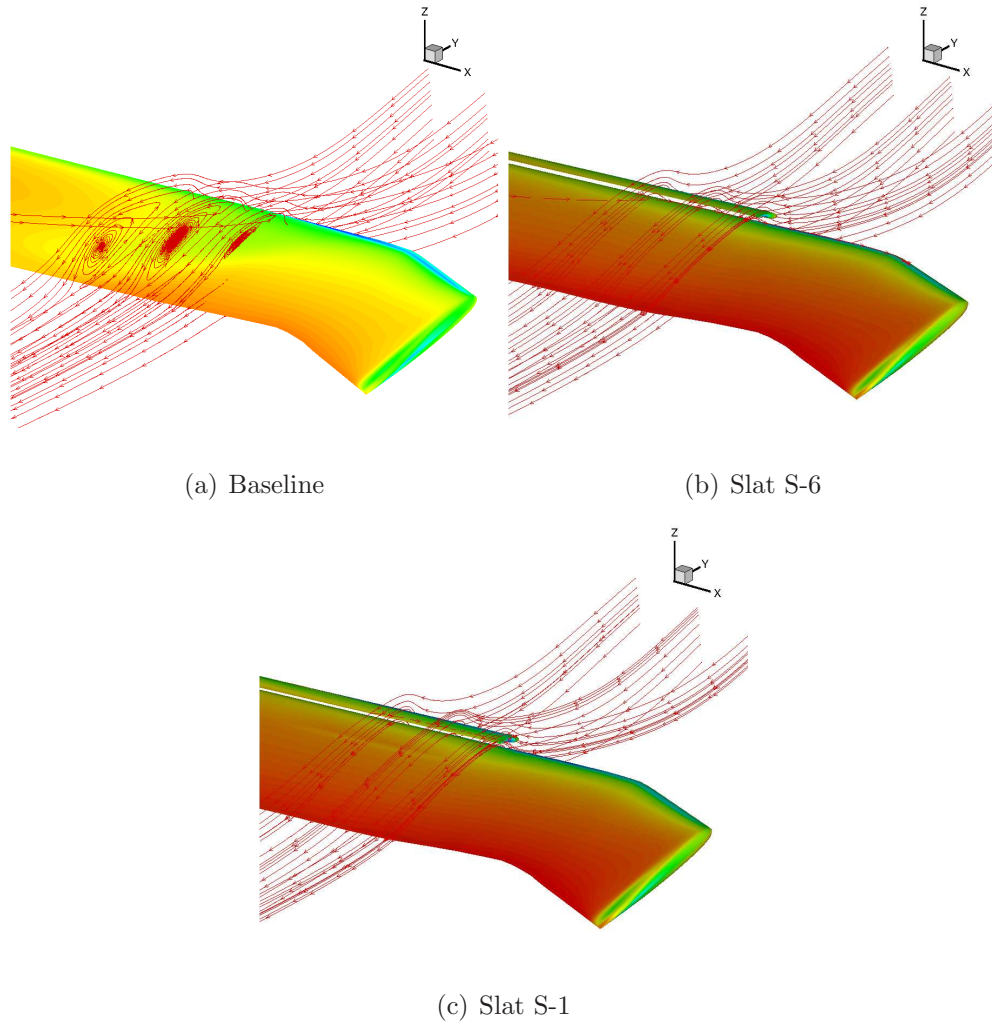


Figure 4.23: Streamlines comparisons for baseline and slatted rotor cases at three outboard stations, $r/R = 73\%$, 75% , and 79% .

shows a reduction of up to 73% in the vibratory root ($r/R = 22.5\%$) torsional loads, and a corresponding reduction of up to 62% in the pitch link loads (see Fig. 4.28). The level of vibration reduction that is gained by introducing a slat is significant. An interesting observation is that the static S-6 slat is the most effective in stall alleviation in terms of the mentioned quantifying parameters and the performance of the dynamic slat actuation ($1/rev$) in this regard is

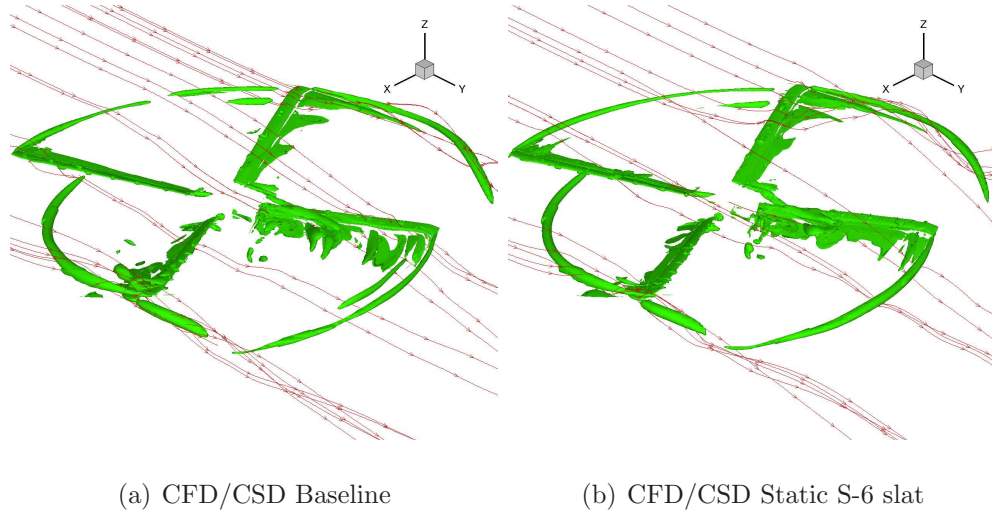


Figure 4.24: Comparison of Q-criterion iso-surface contours of baseline rotor with that having static S-6 slat.

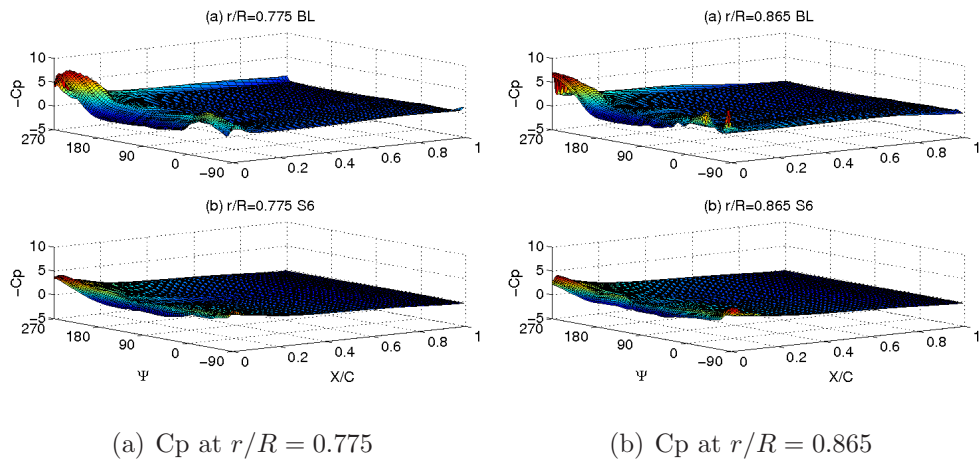


Figure 4.25: Mitigation of pressure peaks near leading edge of main blade due to slat S-6 in slat region.

almost comparable to that of the static S-1 configuration.

Finally, in Figure 4.29, the 4/rev hub loads predictions are compared for the baseline rotor with the two modified slat configurations. Once again all quantities are normalized by the predicted baseline rotor values. It is observed that the F_z loads remain largely unchanged with the introduction of the slat. It

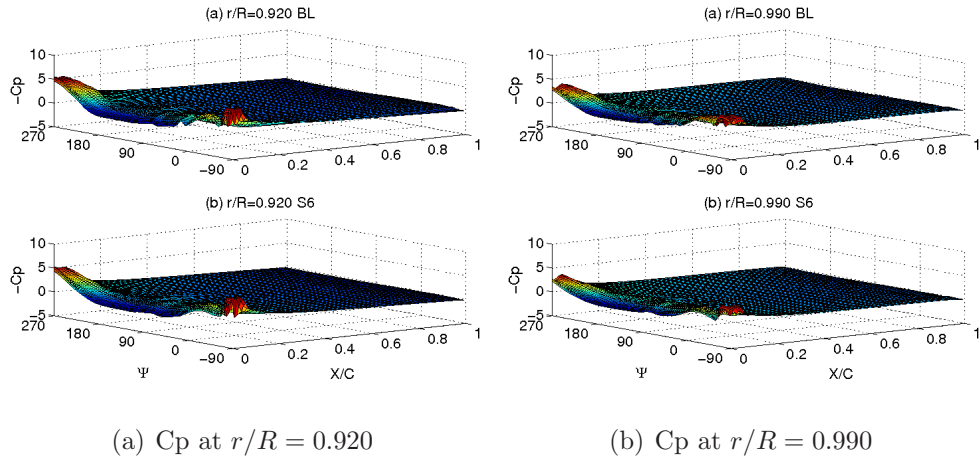
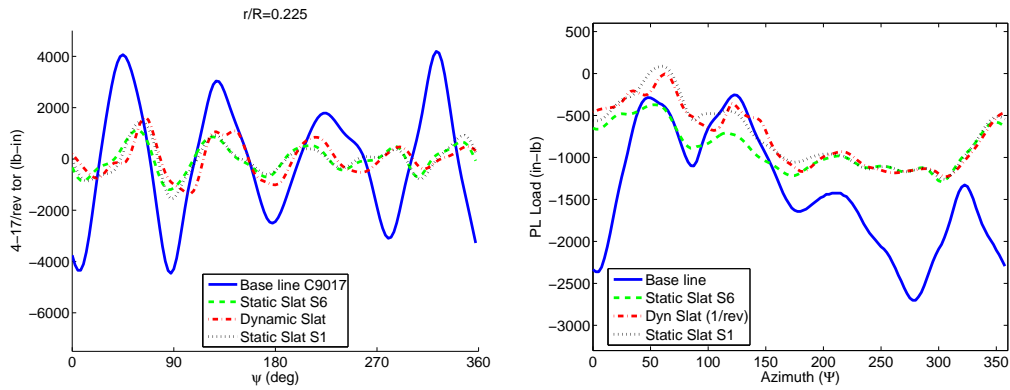


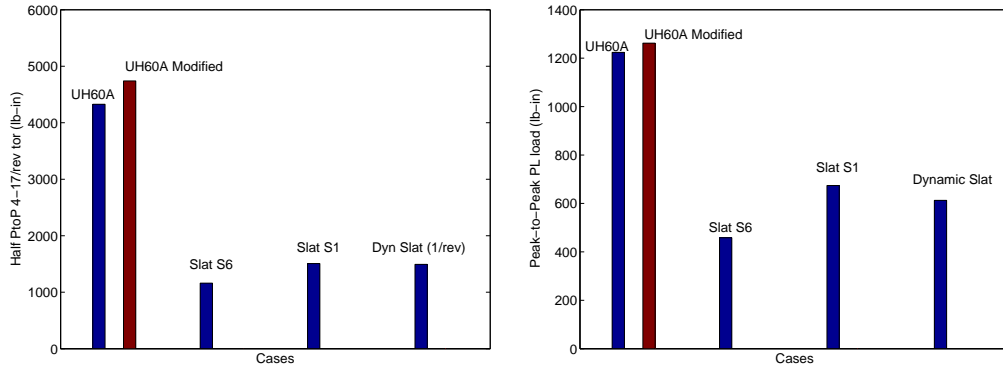
Figure 4.26: Mitigation of pressure peaks near leading edge of main blade due to slat S-6 outboard of slat.



(a) CFD predicted (4 – 17/rev) torsional load vs azimuth (Ψ) (b) CFD predicted Pitch link load vs azimuth (Ψ)

Figure 4.27: Comparison of the vibratory torsional loads (4 – 17/rev) and predicted pitch link loads showing the effect of slat on rotor structural loads. **Blue solid:** no slat; **Green dash:** steady slat S-6; **Red dash dot:** dynamic slat.; **Black dash:** steady slat S-1

should be mentioned that the absolute values of the rolling (M_x) and pitching (M_y) moments are very insignificant ($\leq 2\%$) as compared to the rotor torque (M_z) values and hence their relative non-dimensional values are not as important



(a) Vibratory (4 – 17/rev) root torsional load

(b) Pitch link load

Figure 4.28: CFD/CSD predicted peak-to-peak vibratory root torsional and pitch link loads for various blade configurations.

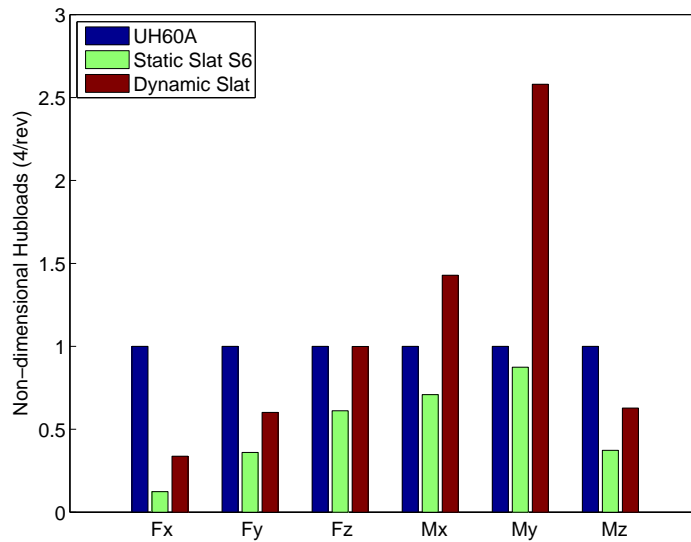


Figure 4.29: CFD predicted 4/rev Hub loads; no slat; **Steady Slat S-6**; **Dynamic Slat**

as that of the rotor torque values while comparing the relative merits of the three slat configurations.

4.2.4 Performance Improvement due to Slat

Figure 4.30 plots the thrust and torque time histories for a blade over one rotor revolution. A few interesting observations can be made from the time history plots of torque contribution (Fig. 4.30(a)) for the various blade configurations:

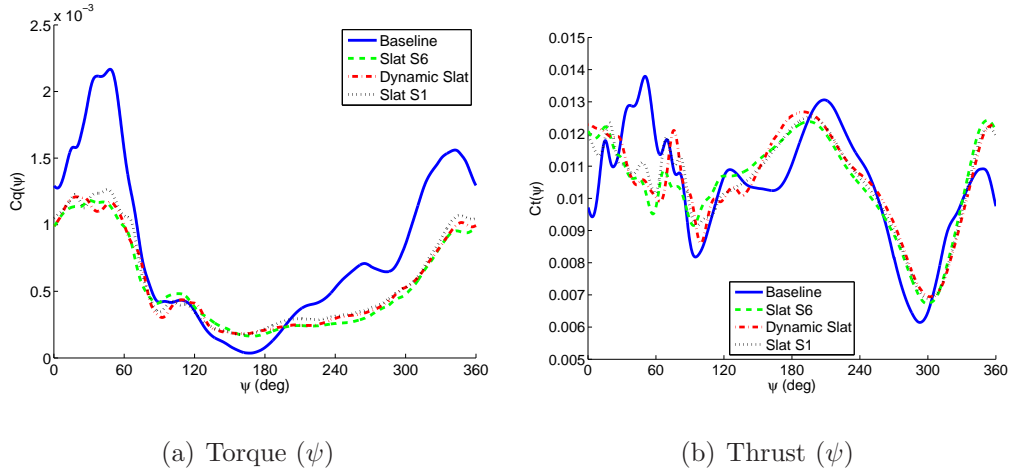


Figure 4.30: Non-dimensional torque and thrust time history over one rotor revolution.

- Slats help reduce the torque penalty otherwise observed in the baseline rotor. This results mainly due to the absence of dynamic stall events, besides due to the reduced trim control angles (collective pitch and cyclic angles) possible due to the enhanced lifting capability of slatted rotors.
- The presence of torque peaks, which consequently gets eliminated by slats, are not restricted to only the regions experiencing stall events. A strong torque peak is present also in the first quadrant, away from the stall region. This trend however corresponds well with the thrust peaks observed in Fig. 4.30(b).
- Rotor with the slat S-6 configuration is most effective and that with slat

S-1 is the least effective in alleviating the torque penalty. The dynamic slat consistently shows intermediate behavior between these two slat configurations. However, the differences between the slat configurations is relatively small.

4.3 Dynamic Slat Strategies

The dynamic slat actuation considered on the 2-D pitching airfoil was such that the slat is at the maximum upward position (S-1) at the smallest main element pitch angle and is at the maximum downward position (S-6) at the largest main element pitch angle. Thus, the direction of the slat motion is always in the opposite direction to that of the main element motion during the whole pitching cycle, which results in the slat imparting opposing momentum to the flow. Offsetting the phasing of the slat actuation with respect to the main blade would ensure that the direction of the slat motion is aligned along the main element direction of motion at least over a finite section of the pitching cycle. This in turn might favor flow augmentation on the main element to ultimately improve its stall characteristics. The following section discusses the effect of the phase offset on the airloads on a 2-D pitching SC2110 airfoil.

4.3.1 Phase Offset of Dynamic Slat Actuation on SC2110 Airfoil

For this study, a 2-D SC2110 airfoil pitching at $\alpha(t) = 15^\circ - 5^\circ \cos(\omega t)$ at a Reynolds number $Re = 4.14 \times 10^6$, and a freestream Mach number $M_\infty = 0.3$ is considered. Figure 4.31 shows the three slat actuation motions for two different

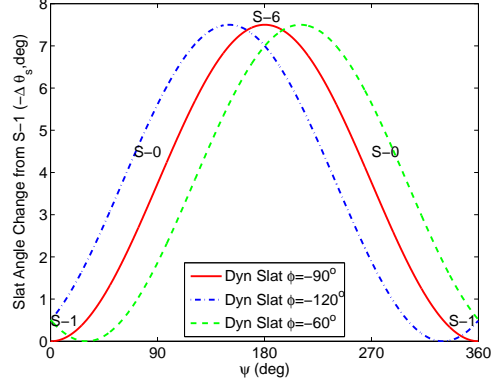


Figure 4.31: Time history of change of slat angle with respect to S-1 position over one cycle ($\Delta\theta_s$ versus ψ) due to three different phasing ($\phi = -60^\circ, -90^\circ, -120^\circ$) of slat actuation

phase offset values compared to the baseline dynamic slat motion considered earlier. The equation of slat motion is:

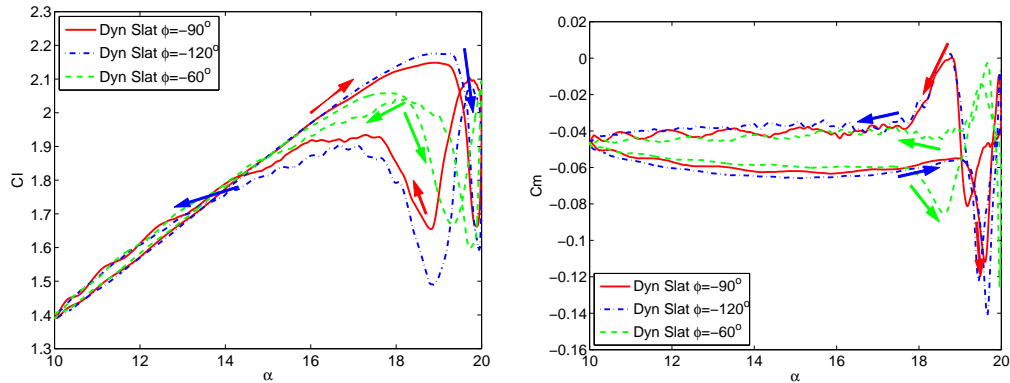
$$\Delta\theta = \Delta\theta_{max} [\sin(\psi - \phi)] \quad (4.1)$$

$$\theta = \theta_0 + \Delta\theta_i \quad (4.2)$$

where, $\Delta\theta_{max}$ is the amplitude of slat angle actuation and $\Delta\theta$ is the total slat angle displacement. Angles θ_0, θ are the initial and absolute slat angles, respectively, defined with respect to the main blade chord. As noted earlier, values of $\Delta\theta_{max} = 3.75^\circ$, $\phi = -90^\circ$ ensures that the slat is at S-1 position at smallest pitch angle and at S-6 at maximum pitch angle. Similar equations of motion can be used for rigid translation ($\Delta [xc, yc, zc]$) of the slat and the slat pivot point about which the slat pitches.

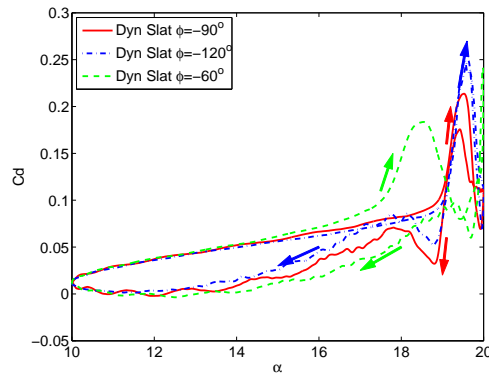
Current section looks at the effect of varying the ϕ values on the airfoil airload characteristics for the pitching airfoil. Two phase offset values are considered, such that the slat attains the S-6 position either 30° earlier ($\phi = -120^\circ$) or 30°

later ($\phi = -60^\circ$) than the baseline actuation scheme ($\phi = -90^\circ$).



(a) C_L versus α

(b) C_M versus α



(c) C_D versus α

Figure 4.32: Airload comparisons of the three phasing ($\phi = -60^\circ, -90^\circ, -120^\circ$) of slat actuations

Figure 4.32 compares the airloads time history values from the three slat actuations. It is observed that the slat actuation that leads ($\phi = -120^\circ$, dash-dot blue) the baseline slat actuation (solid red) allows for increased Cl_{max} , but only very marginally (less than 2%). Moreover, the stall delay is very negligible and in fact, both the pitching moment drop as well as drag loss post stall is more than what is found with the baseline slat actuation. Delaying the phasing of slat actuation ($\phi = -60^\circ$, dash green), however, seem to have strong influence on the

airload behavior. This actuation not only reduces Cl_{max} value, but also causes early stall events in the moment (Fig. 4.32(b)) as well as the drag (Fig. 4.32(c)) time history plots.

The airload behavior from the three slat actuations definitely demonstrates the effect of phase offset on underlying flow physics during the pitching cycle. However, it still does not show distinctly superior advantage of any one slat phasing over the other slat phasing strategies. While the lead phasing offset (by $+30^\circ$) results in slight Cl_{max} improvement, it comes at an expense of larger oscillatory airloads post stall, besides resulting in overall larger airload hysteresis loops. Similarly, the delayed phase offset ((by -30°) may result in lower Cl_{max} values and early stall, but it also provides reduced overall airload hysteresis loops, reduced extent of stall events, reduced oscillatory behavior post stall, and early recovery to attached flow. Therefore it is not expected to have significant influence on the full scale rotor airloads and hence no slat phase offset computations on actual rotor are considered any further.

The slat actuation considered so far consists of only a $1/rev$ harmonic. To further exploit the airload characteristic of the S-1 and S-6 configurations, a logical next step in dynamic slat actuation strategy would be to prolong the duration of these extreme slat positions during the actuation cycle. This can be achieved by including higher harmonic (e.g. $3, 5/rev$ or higher) actuations of the slat. The following sections explore these actuation methods as potential stall alleviation strategies.

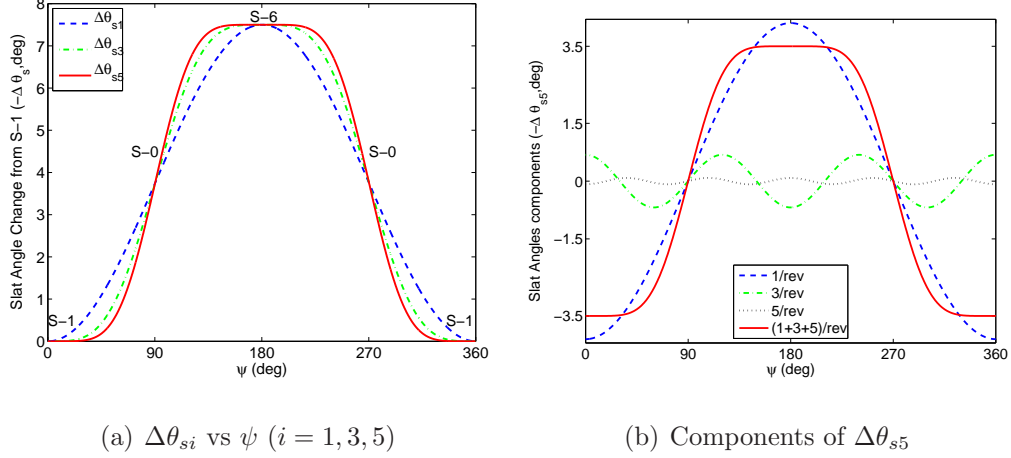


Figure 4.33: Time history of change of slat angle with respect to S-1 over one cycle ($\Delta\theta_s$ versus ψ) due to three (up to 1, 3, 5/rev) slat actuations and build up of the $\Delta\theta_{s5}$ slat actuation

4.3.2 Higher Harmonic Slat Actuation on SC2110 Airfoil

As mentioned earlier, it is possible that there could be some benefit to allowing the slat to remain in their extreme slat positions (S-1 and S-6) for longer durations, thereby enhancing the corresponding airload behavior of the airfoil at these positions during a pitching cycle.

The following motions of these slat angles (see Methodology Chapter for a more general form) are given by:

$$\Delta\theta_{s1} = \Delta\theta_{max} [\sin(\psi - \phi)] \quad (4.3)$$

$$\Delta\theta_{s3} = \Delta\theta_{max} \frac{9}{8} \left[\sin(\psi - \phi) + \frac{1}{9} \sin(3\psi - 3\phi) \right] \quad (4.4)$$

$$\Delta\theta_{s5} = \Delta\theta_{max} \frac{75}{64} \left[\sin(\psi - \phi) + \frac{1}{6} \sin(3\psi - 3\phi) + \frac{1}{50} \sin(5\psi - 5\phi) \right] \quad (4.5)$$

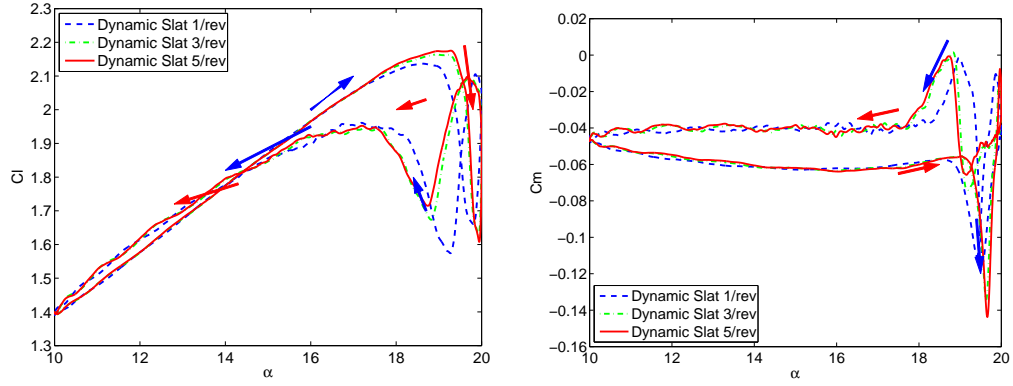
$$\theta = \theta_0 + \Delta\theta_i \quad (4.6)$$

where, $\Delta\theta_{max}$ is the amplitude of slat angle actuation and $\Delta\theta_i$ is the up to i 'th

harmonic total slat angle displacement. Angles θ_0 , θ are the initial and absolute slat angles, respectively, defined with respect to the main blade chord. For the present work, values of $\Delta\theta_{max} = 3.75^\circ$, $\phi = -90^\circ$ ensures that the slat is at the S-1 position at smallest pitch angle and at S-6 at maximum pitch angle, and thus maintains the airload characteristics required of the airfoil at those angles. Similar equations of motion can be used for rigid translation ($\Delta [xc, yc, zc]$) of the slat and the slat pivot point about which the slat pitches.

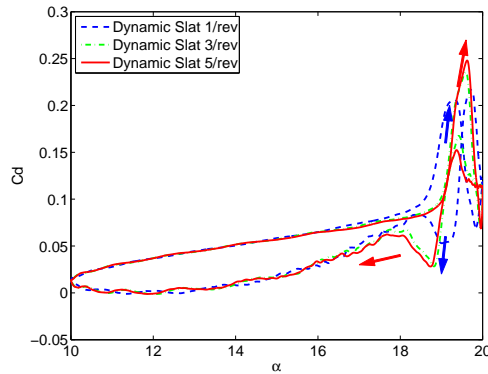
The magnitude chosen for the 1, 3 and 5/*rev* harmonics is such that no new minima or maxima occur and higher derivatives at global maximum and minimum are progressively set to zero (e.g. for upto 3/*rev* the first, second and third derivatives are zero at extrema); this results in flatter curves near extrema and more rapid change in slat angles in between extrema (see Fig. 4.33(a)). The relative magnitude of the components for the actuation that includes up to 5/*rev* is shown in Fig. 4.33(b).

The airloads due to these three actuation strategies are compared with each other in Fig. 4.34. The addition of the higher harmonic content in the slat motion leads to a small but noticeable delay in all airload stall events. With increasingly higher harmonic content, the pitching moment penalty keeps increasing. At larger angles, the airload behavior of the largest harmonic actuation is closest to that of the S-6 slat characteristics. At lower angles, there is no significant advantage of sustaining longer S-1 state using these higher harmonic actuations.



(a) C_L versus α

(b) C_M versus α



(c) C_D versus α

Figure 4.34: Airload comparisons of the three (up to 1, 3, 5/rev) harmonic dynamic slat actuations

4.3.3 Higher Harmonic Slat Actuation on Modified UH-60A Rotor

The higher harmonic actuations (3, 5/rev) discussed in the previous section are now implemented for a slat on the UH-60A rotor blades. As mentioned earlier, the phase offset for all slat actuations is chosen so as to ensure slat configuration of S-6 at 300° and S-1 at 120° . This allows S-6 position at deepest stage of first dynamic stall event, as shown in Fig. 4.35. In the figure, the $\Delta\theta_{s1}$, $\Delta\theta_{s3}$, $\Delta\theta_{s5}$ slat actuations, respectively, refer to the up to 1/rev, 3/rev and 5/rev frequency

content during one rotor revolution.

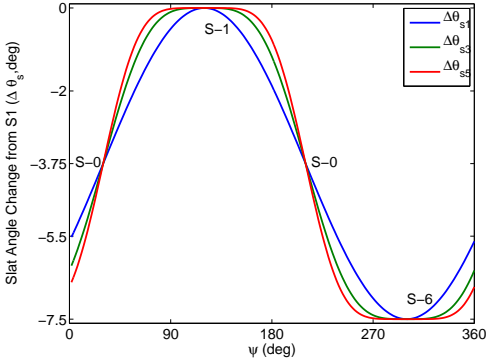


Figure 4.35: Slat actuation (up to 1, 3, 5/rev) with respect to S-1 position over one rotor revolution ($\Delta\theta_s$ vs ψ)

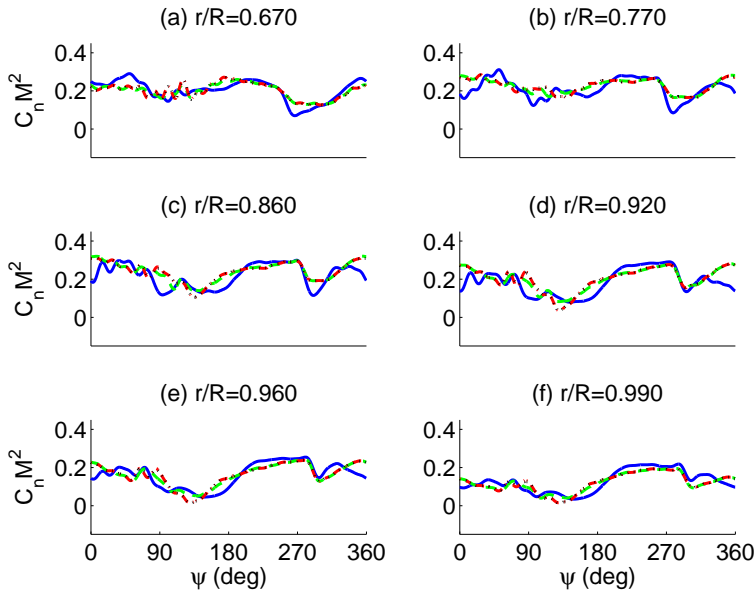


Figure 4.36: Time history of CFD normal loads all dynamic slat actuations. Blue solid: no slat; Green dash: 1/rev dynamic slat; Red dash dot: up to 3/rev dynamic slat; Black dot: up to 5/rev dynamic slat.

The airloads resulting from the above mentioned slat actuation strategies are presented in Fig. 4.36 (lift) and Fig. 4.37 (pitching moment). As the figures

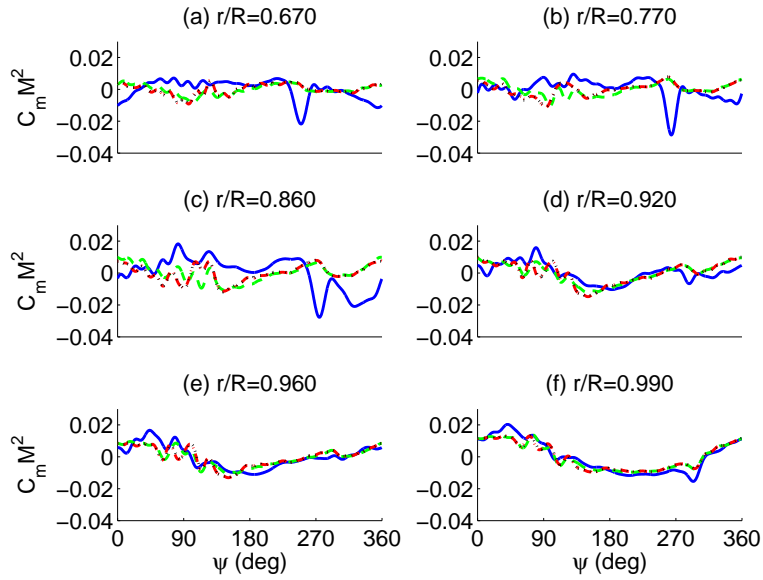
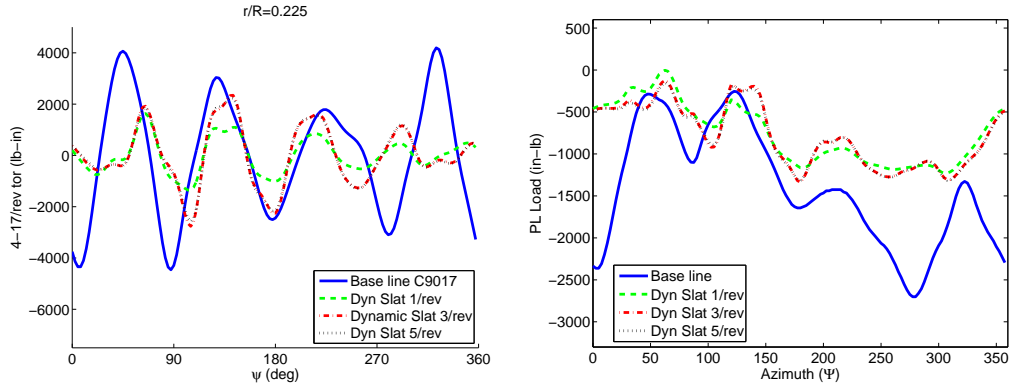


Figure 4.37: Time history of CFD pitching moments with dynamic slat actuations. Blue solid: no slat; Green dash: $1/rev$ dynamic slat; Red dash dot: up to $3/rev$ dynamic slat; Black dot: up to $5/rev$ dynamic slat

show, while all the slat actuation methods are successful in mitigating stall on the retreating side, their relative performance in doing so is not very clear.

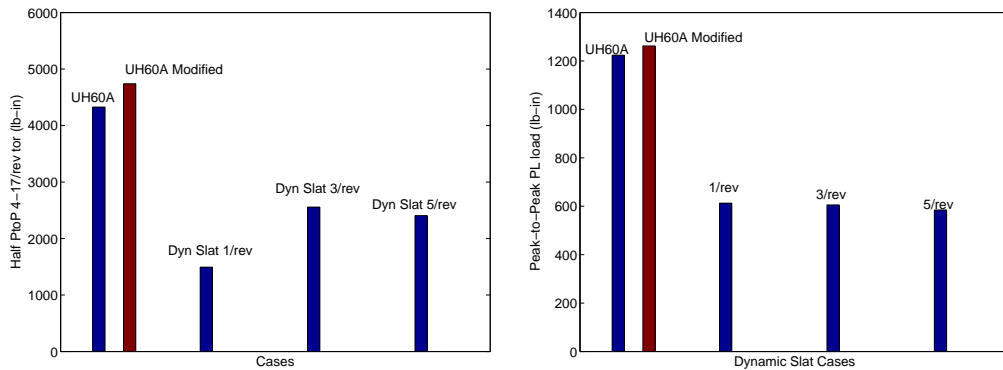
Quantitative Estimate of Stall Alleviation

Figure 4.38 compare the three slat actuation schemes in terms of quantities measuring the extent of stall, such as, vibratory ($4 - 17/rev$) root torsional moment and pitch link loads. Similar to observations made for rotors with static slat, all three slat actuations result in predominantly $5/rev$ torsional sectional loads. The distinctly different characteristics of load due to $1/rev$ from the other two higher harmonic actuations is apparent from Fig. 4.38(a). Interestingly, unlike in the airload plots, this plot is clearer in demonstrating relatively better performance of $1/rev$ actuation in reduction of vibratory torsional loads (approximately 64%)



(a) CFD predicted $(4 - 17/rev)$ torsional load vs azimuth (Ψ) (b) CFD predicted Pitch link load vs azimuth (Ψ)

Figure 4.38: Comparison of the vibratory torsional loads $(4 - 17/rev)$ and predicted pitch link loads showing the effect of dynamic slat actuations on rotor structural loads. **Blue solid:** no slat; **Green dash:** $1/rev$ dynamic slat; **Red dash dot:** up to $3/rev$ dynamic slat; **Black dot:** up to $5/rev$ dynamic slat.



(a) Vibratory root $(4 - 17/rev)$ torsional load (b) Pitch link load

Figure 4.39: CFD/CSD predicted peak-to-peak vibratory root torsional and pitch link loads for various slat actuations.

than other higher harmonic actuations (approximately 40% for both). It is possible that the higher harmonic actuations are actually causing some vibratory

loads.

Only pitch link load time history, shown in Fig. 4.38(b), shows comparable (or better at times) performance of higher harmonic actuations than $1/rev$ actuation. The peak-to-peak pitch link load reduction of the baseline pitch link load due to all slat actuations are $\approx 50\%$. Figures 4.39 compares the relative half peak-to-peak values of root vibratory torsional moment and pitch link loads due to all slat actuation schemes and corroborate the observations made about the relative performance of higher harmonic actuations. Table 4.4 further demonstrates that there is no advantage of using higher harmonics of slat actuation, either in terms of reduced collective, or power reduction, at least at the baseline thrust value.

Blade Type	θ_0	θ_{1c}	θ_{1s}	α	C_Q/σ
Baseline UH60A	14.86	7.01	-8.55	-2.85	0.01120
Dynamic Slat $1/rev$	11.29	3.95	-6.46	-2.85	0.00700
Dynamic Slat $3/rev$	11.37	4.35	-6.35	-2.85	0.00701
Dynamic Slat $5/rev$	11.39	4.36	-6.31	-2.85	0.00701

Table 4.4: Comparison of the final trimmed control pitch settings and the net rotor power for different slat actuations.

4.4 Effectiveness of Slat on Achieving Higher Thrust

From the analysis so far, LE-Slats have been found to be very effective in controlling and alleviating dynamic stall. However, there seems to be little benefit

to higher harmonic actuation and at least for the baseline C9017 condition, little benefit to dynamic actuation. Therefore, only a static slat strategy is examined. The flight operational envelope can be expected to be pushed to a higher thrust regime, and therefore to a higher rotor performance state, which is otherwise limited by losses incurred due to dynamic stall. This section explores the possible use of slats for two possible higher thrust settings of $C_T/\sigma = [0.1391, 0.1458]$, i.e. 105% and 110% of baseline thrust, respectively. Based on earlier results only the static S-6 slat configuration is considered for achieving trimming of rotors at higher thrust settings.

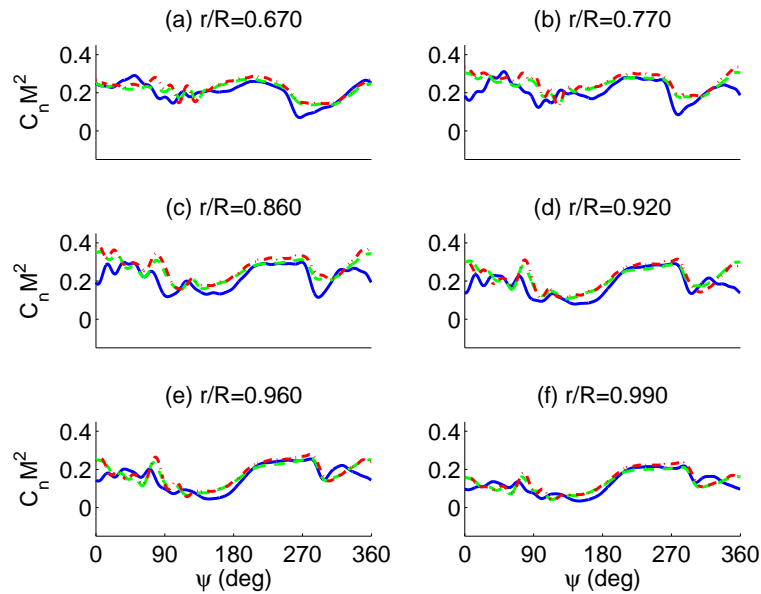


Figure 4.40: Variation of predicted normal loads with thrust setting; Blue solid: $C_t/\sigma = 0.1325$ baseline; Green dash: $C_t/\sigma = 0.1391$ with S-6; Red dash dot: $C_t/\sigma = 0.1458$ with S-6

Figures 4.40 and 4.41 demonstrate the effect of the slat on stall characteristics in normal and pitching moment loads, respectively. While the baseline rotor airloads are without slat, the other two higher thrust cases are with slat S-6.

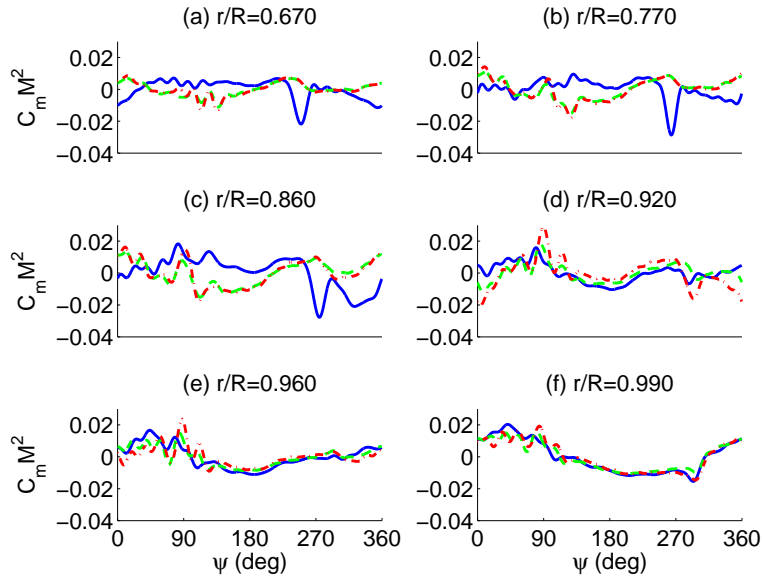


Figure 4.41: Variation of predicted pitching moment with thrust setting; Blue solid: $C_T/\sigma = 0.1325$ baseline; Green dash: $C_T/\sigma = 0.1391$ with S-6; Red dash dot: $C_T/\sigma = 0.1458$ with S-6

The presence of the slat helps alleviate the lift as well as power limits of the baseline rotor, which is otherwise present due to dynamic stall. This allows for trimming the rotor at the higher thrust values. Even at 105% baseline thrust setting, the rotor is able to trim to a control setting such that there are no significant stall events, except the radial stations immediately outboard of the slat ($r/R = 0.92$). As expected, the stall event at this station for the even higher thrust setting (110% of baseline thrust) is more severe. The stall features at these higher thrust values with slat are similar to that of the lower baseline thrust setting but without any slat, emphasizing the fact that prominent unsteady dynamic stall features develop. It can be recalled that similar phenomenon was observed even for the baseline thrust setting with S-1 slat configuration. This could be attributed to the interaction of the slat wake with the main blade flow.

Although the static slat is effective in alleviating stall and reducing pitching moments on the retreating side, it also comes with a penalty of higher negative pitching moment on the advancing side. However, the moment penalty is only in the spanwise stations over which the slat is present, i.e. $r/R = [0.5 : 0.9]$ and no significant moment loss is observed beyond $r/R = 0.9$ – see Fig. 4.41. The presence of the slat also incurs larger drag loss, especially on the advancing side (Fig. 4.42), but this too is restricted to the region of the rotor where the slat is present, i.e. $r/R = [0.5 : 0.9]$.

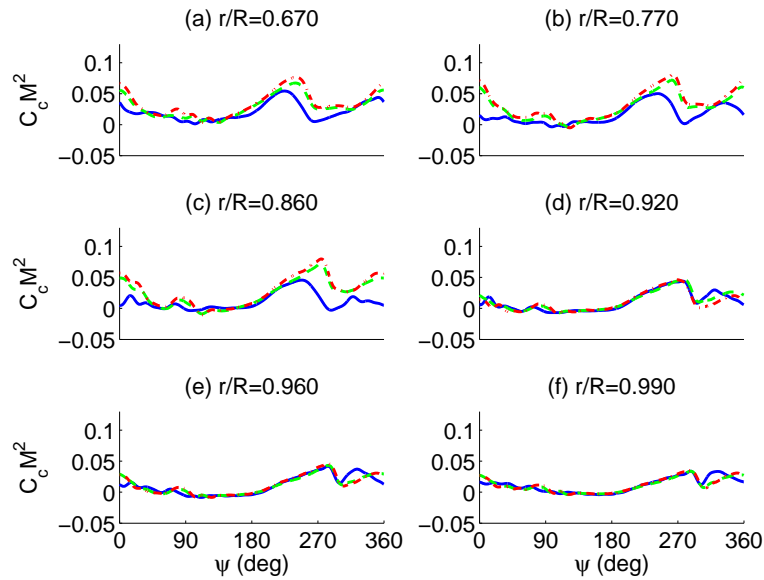


Figure 4.42: Variation of predicted chordwise force with thrust setting; Blue solid: $C_T/\sigma = 0.1325$ baseline; Green dash: $C_T/\sigma = 0.1391$ with S-6; Red dash dot: $C_T/\sigma = 0.1458$ with S-6

Vibratory normal load ($3 - 20/rev$) time history, which is predominantly $5/rev$, in Fig. 4.43 reveals that introduction of the slat dampens out the higher harmonic content of the normal loads throughout the rotor cycle except near stall. The lift stall events are comparatively more mitigated due to slat at

the higher thrust settings when compared to the baseline case, at the inboard stations. However, the vibratory components are larger for the higher thrust cases at the stations which are further outboard of the slat. This again could be due to the aerodynamic interaction between the slat wake with the blade boundary layer. The presence of slat tip vortices creates a suction peak which might cause enhanced vortex shedding near the baseline blade leading edge, thereby initiating larger stall compared to the baseline.

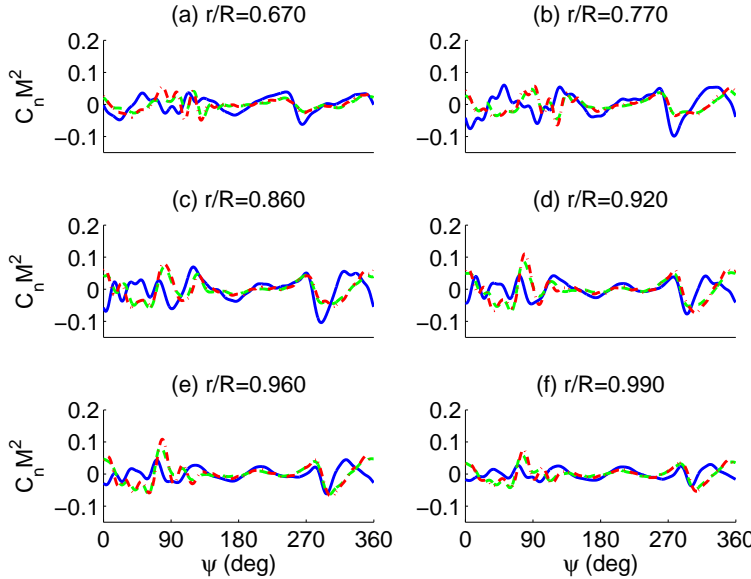
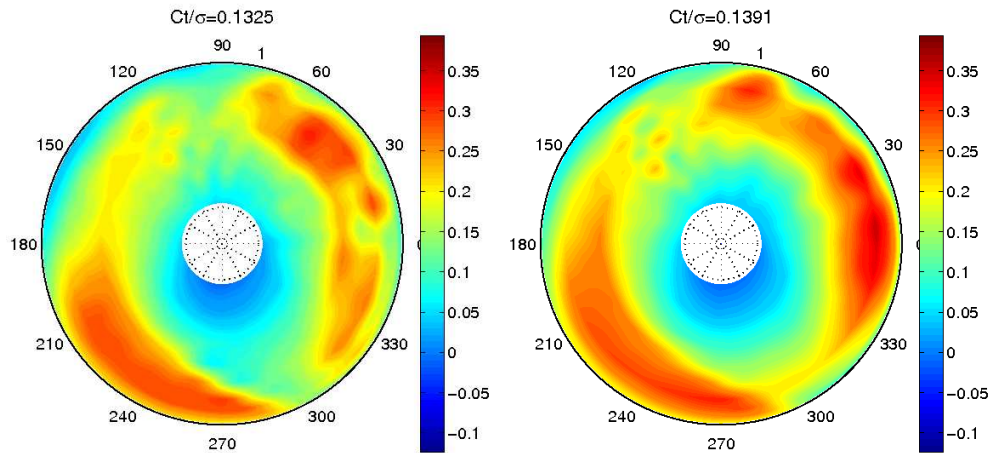


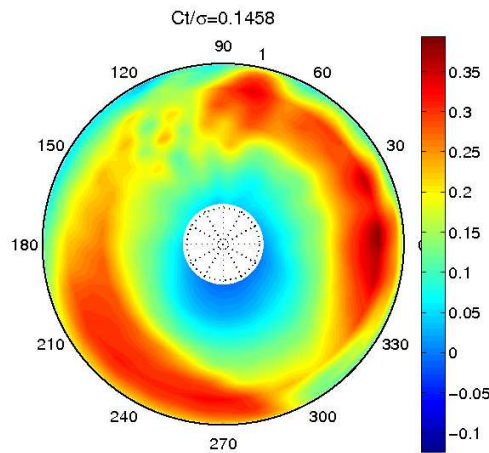
Figure 4.43: Variation of predicted normal ($3-20/rev$) loads with thrust setting; Blue solid: $C_T/\sigma = 0.1325$ baseline; Green dash: $C_T/\sigma = 0.1391$ with S-6; Red dash dot: $C_T/\sigma = 0.1458$ with S-6

Polar plots of normal loads for these cases over the entire rotor disk shows the portion of the rotor disk that contributes the most to increased lift. Figures. 4.44 shows the trend of reduced negative lift values in the fourth quadrant and increasingly positive lift values on the front (mostly third quadrant) and rear portion of the disk. These results relate well with the normal load time his-



(a) $Ct/\sigma = 0.1325$ Baselin

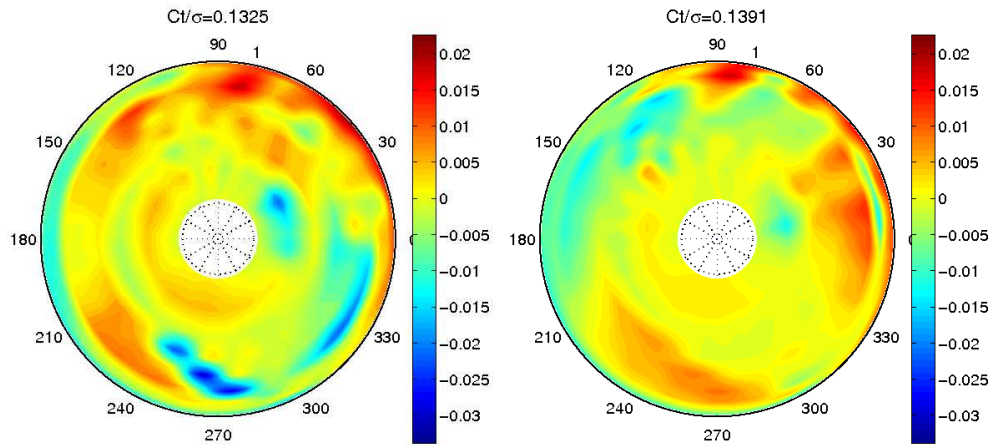
(b) $Ct/\sigma = 0.1391$ Slat S-6



(c) $Ct/\sigma = 0.1458$ Slat S-6

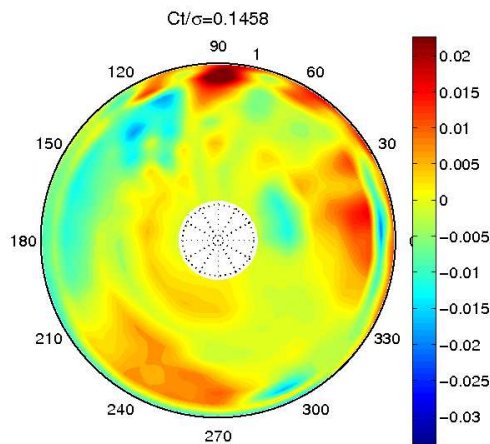
Figure 4.44: Variation of the polar normal load over whole rotor disk with higher thrust values

tory plots discussed earlier. Similarly, the corresponding polar plots of pitching moment loads for these three thrust cases confirm the observations made earlier with the pitching moment time history plots. Figure 4.45 clearly shows the absence of large negative moment values observed in the baseline rotor retreating side at the inboard stations. However, there is a region of large negative pitching moment at the outboard stations for higher thrust cases even with the slat. But,



(a) $Ct/\sigma = 0.1325$ Baseline

(b) $Ct/\sigma = 0.1391$ Slat S-6



(c) $Ct/\sigma = 0.1458$ Slat S-6

Figure 4.45: Comparison of the polar pitching moment (mean removed) load over whole rotor disk of higher thrust settings with the baseline thrust.

this region spans only a small portion of the rotor disk in the fourth quadrant and hence does not deteriorate the overall performance of the slat.

From a broad perspective, the overall effectiveness of the slat can be best judged when the final trim control angles and power required are analysed. Table 4.5 shows that with the addition of the slat, even the high thrust settings results in lower collective as well as cyclic values. Consequently, the power

penalty is also reduced for both the high thrust conditions. As expected 110% larger thrust condition results in larger trim control angles and power than the 105% larger thrust condition.

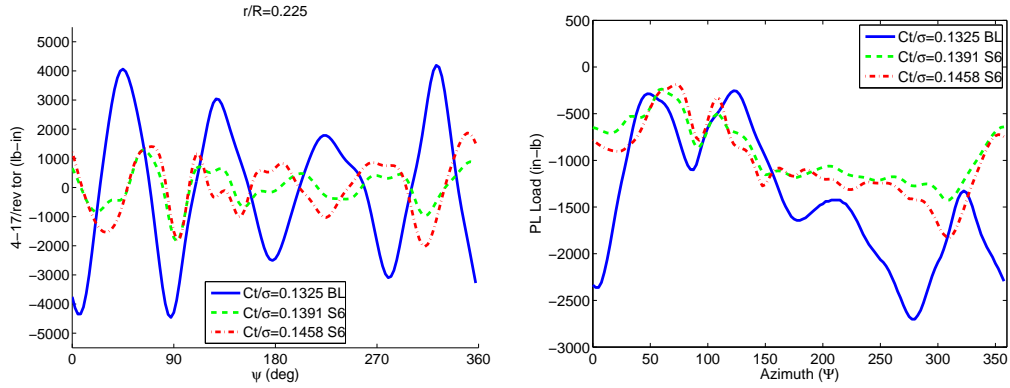
Blade Type	θ_0	θ_{1c}	θ_{1s}	α	C_Q/σ
$Ct/\sigma = 0.1325$ Baselin	14.86	7.01	-8.55	-2.85	0.01120
$Ct/\sigma = 0.1391$ Slat S-6	12.16	4.15	-6.53	-2.85	0.00797
$Ct/\sigma = 0.1458$ Slat S-6	13.09	4.82	-7.17	-2.85	0.00973

Table 4.5: Comparison of the final trimmed control pitch settings and the net rotor power of higher thrust settings with the baseline thrust.

4.4.1 Quantifying Stall at Higher Thrust settings: Pitch Link Load and Root Torsional Moment

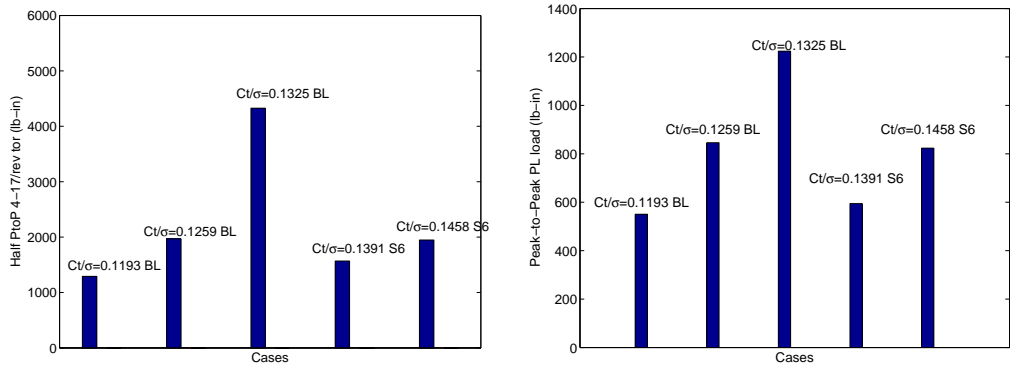
A measure of dynamic stall intensity is obtained looking at the vibratory torsional moment at the root section ($r/R = 22.5\%$) as well as the pitch link load time history over one rotor revolution. Figure. 4.46(a) shows how introduction of the slat has successfully brought down the amplitude of torsional vibratory moments even at these higher thrust settings. Two interesting observations: a) vibratory torsional moments due to rotors at high C_T/σ with slat are predominantly $5/rev$, and b) both the high thrust rotor cases with slat produce increasingly sharper negative drop in vibratory torsional moment near the 300° azimuth or near the second stall event. This could be arising due to pitching moment (4.41) and vibratory lift (4.43) drops observed at outboard stations.

However, as Fig. 4.47(a) shows, due to dynamic stall mitigating effect of the slat, the final trimmed state results in damped vibratory half peak-to-peak



(a) CFD predicted $(4 - 17/rev)$ torsional load vs azimuth (Ψ) (b) CFD predicted Pitch link load vs azimuth (Ψ)

Figure 4.46: Comparison of the vibratory torsional loads $(4 - 17/rev)$ and predicted pitch link loads of higher thrust settings with the baseline thrust. Blue solid: $C_T/\sigma = 0.1325$ baseline; Green dash: $C_T/\sigma = 0.1391$ with S-6; Red dash dot: $C_T/\sigma = 0.1458$ with S-6.



(a) Vibratory root $(4 - 17/rev)$ torsional load (b) Pitch link load

Figure 4.47: Comparing CFD/CSD predicted peak-to-peak vibratory root torsional and pitch link loads of higher thrust settings with the baseline thrust.

values at both the high thrust settings. The slat enables 63% and 40% reduction in vibratory root torsional moments for 105% and 110% larger thrust settings,

respectively.

Slat effectiveness is further appreciated from Fig. 4.46(b), which compares the pitch link time histories for the three case. The use of the slat allows the rotor to trim with reduced amplitude for the higher thrust settings. Similar to torsional vibratory moments, pitch-link loads due to the slat tends to show $5/rev$ periodic behavior and the maximum negative pitch link drop is again around 300° azimuth (near second stall event) and is offset from the similar drop observed in baseline case by about 30° . Ultimately, the slat is effective in relieving the pitch-link loads by 42% and 22% for the 105% and 110% larger thrust settings, respectively. See Fig. 4.47(b).

Another interesting observation that can be made from Fig. 4.47 is that, the peak-to-peak values of the root torsional loads and the pitch link loads on slatted rotor at these high thrust cases are, in fact, comparable to those at the two lower thrust flight conditions (at 5% and 10% lower than the baseline thrust) considered for the baseline rotor. The common factor contributing to the reduced loads in both the cases is the alleviated dynamic stall events in these conditions.

4.5 Performance Prediction for Slatted Rotor

The ultimate aim of using a slat on the UH-60A rotor was to push the flight envelope by pushing the performance limits otherwise imposed due to dynamic stall events. For the measure of performance, L/D_e value of the rotor is considered. It is defined as:

$$\frac{L}{D_e} = \frac{C_T \cos(\alpha_s)}{[C_Q/\mu - C_T \sin(\alpha_s)]}$$

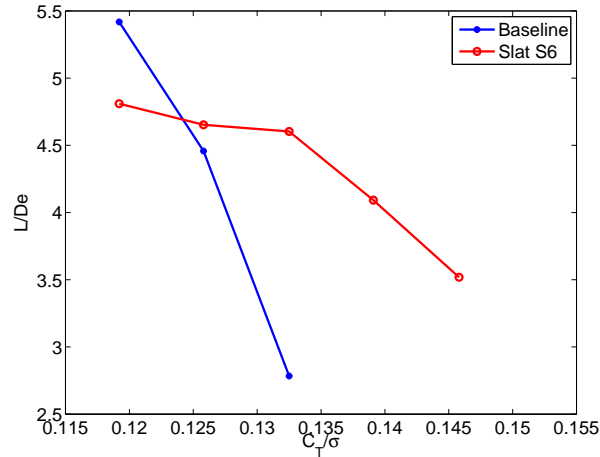


Figure 4.48: Comparing L/D_e for baseline rotor with that having slats S-6 and S-1

which is nothing but the ratio of ‘rotor lift’ and ‘propulsive power’. Here, C_T, C_Q are the rotor thrust and torque, respectively, μ is the rotor advance ratio, and α_s is the shaft tilt angle, where $\alpha_s < 0$ implies shaft tilt towards the direction of flight. As Fig. 4.48 demonstrates, the use of slat has enabled the rotor performance to improve in the region of high thrust by a significant margin, e.g. the L/D_e values due to slat S-6 improves by almost one and half times (or six times in C_T/C_Q values) than baseline UH-60A at baseline thrust of $C_T/\sigma = 0.1325$. However, the performance of the slatted rotor degrades compared to the baseline rotor at lower values of rotor thrust (around $C_T/\sigma \leq 0.125$).

Chapter 5

Conclusion

The operational flight envelope of modern rotorcraft is limited due to its rotors thrust, torsional and power limits. For a rotor in a forward flight, an unsteady phenomenon that severely limits the rotor performance is *dynamic stall*, which occurs on the retreating side of the rotor disk. There have been extensive research in devising dynamic stall alleviation techniques in the past, and recently the active control methods have become more popular than others.

The active control of the dynamic stall on rotors using flow control devices, although potentially highly effective, is more complex to implement than that using variable geometry or multi-element airfoil concepts. Among various multi-element and variable geometry concepts studied in the literature, leading edge slats (LE-Slat) have been shown to have superior effectiveness in alleviating dynamic stall. These studies on LE-slats, however, were mostly on two dimensional pitching airfoils. The few studies conducted on rotors only used a simplified linearized aerodynamic model. The present work aims to demonstrate the effectiveness of a LE-Slat on improving rotor performance by alleviating dynamic stall on a full scale rotor, by developing a platform that couples a computational structural solver with a high-fidelity CFD solver.

This chapter summarizes the key contributions made towards achieving the mentioned objectives of the present work, and discusses key observations made and conclusions drawn in the process. Then it presents the significance of the present work and then finally concludes with a few recommendations for future studies.

5.1 Summary

The objective of the thesis was to extend and validate an existing coupled CFD/CSD model to investigate the effectiveness of LE-Slats in delaying the onset of dynamic stall on rotors to increase the flight envelope. Various methodologies were improved over existing RANS code to include the capability to analyse a multi-element bladed rotor instead of just a single element bladed rotor. These improvements included that of an improved overset grid connectivity using the so-called Implicit Hole Cutting approach and a generalized force transfer routine for transferring loads from the LE-Slat onto the main blade.

The CFD solver was extensively validated against available 2-D experimental measurements for both steady and unsteady flight conditions with and without slats. Two major slat configurations, so-called S-1 and S-6, were considered for extensive experimental validations, besides investigating their flow physics to understand the possible aerodynamic advantages over a baseline airfoil in regards to dynamic stall control. The solver was further used to study the effectiveness of dynamically actuating the slat in mitigating dynamic stall on airfoils. Here, the capability of implicit hole cutting to handle a dynamically moving mesh in the case of the actuating slat mesh, allowed for ease in establishing connectivity across multiple grids. These studies laid the foundation for the later analysis of

slats on a full scale rotor in actual flight conditions.

The modified CFD solver was then coupled with the CSD solver (UMARC) to analyze the UH-60A rotor in a high-altitude, high-thrust flight condition, namely C9017, characterized by distinct dynamic stall events in the retreating side of the rotor disk. The coupled CFD/CSD model was validated with existing C9017 flight test data. Finally, a modified UH-60A rotor blade with leading-edge slat was analyzed to determine the effectiveness of leading-edge slats in mitigating dynamic stall on helicopter rotors. As in the case of the 2-D study, two main slat configurations, S-1 and S-6, were considered for rotor analysis. The nature of the flow physics for a full scale rotor and the change of its behavior due to slat at appropriate rotor span location were studied. Further, various dynamic slat actuation strategies, with more than $1/rev$ harmonic content, were studied for their effectiveness in alleviating dynamic stall on a rotor.

5.2 Observations and Conclusions

Key observations and conclusions from the development of the methodology and the studies involving the use of a slat with a 2-D airfoil as well as rotors are discussed here.

5.2.1 Methodology

The implicit hole cutting technique is found to be an ideal candidate for determining overset connectivities in complicated overset mesh systems containing more than two meshes, in both static and dynamic flight conditions. It could even handle the mesh system where more than one mesh were moving relative

to each other, such as, in the case of a dynamically actuating slat both for a 2-D airfoil as well as rotors. Maintaining good connectivity across mesh boundaries required good overlap between them.

The generalized force transfer was found to be useful for seamless transfer of airloads from slats to the corresponding blade. The routine was parallelized and airload transfer with a multi-block partition of the blade and slat was found to be equally as accurate as for a single block airload transfer.

5.2.2 Validation of CFD Solver

The CFD solver, OVERTURNS, was validated against available experimental wind tunnel data for the two dimensional baseline airfoil and that with S-1 and S-6 slat configurations, for both steady and unsteady flight. Furthermore, the UH-60A rotor flight condition with dynamic stall, C9017, was also examined to validate the ability of the code to predict dynamic stall on a 3-D rotor. The key conclusions drawn from this study are:

1. Predictions from the CFD solver captured the trends of airload measurements for static angles of attack sweep with and without the slat, but it predicted delayed stall events in both lift and moment. Interestingly, the moment stall delay was more severe for the baseline airfoil (around 4°) than for the slatted airfoil (around 2°). The discrepancy between the prediction and measurement was explained using surface pressure comparisons. The predictions were more accurate in attached flow conditions at lower angles than separated flow conditions at larger angles.
2. The multi-element airfoil was shown to have a higher lift margin compared to the baseline airfoil, but also had a higher nose-down pitching moment

at all angles of attack studied.

3. The higher static stall margin for the slatted airfoil (e.g. around 4° delayed moment stall) is because of the better flow characteristics over the upper surface of the main airfoil section promoted by the favorable five major gap effects of a slat. This greatly reduces the adverse pressure gradient on the upper surface and delays the onset of boundary layer separation on the main airfoil.
4. Appropriate turbulent transition fix was found to be successful in improving the drag prediction in steady flow conditions, due to otherwise assumed fully turbulent flow. It was concluded that, in dynamic flow conditions, such as airfoil pitching, appropriate turbulent transition could help capture the leading edge separation bubble more accurately, thereby improving the prediction accuracy of the vortex size, intensity and associated flow physics.
5. For unsteady pitching airfoil motion, the presence of the slat was shown to delay the lift stall to higher angles of attack, e.g. by around 2° . More importantly, the severity of the moment stall was greatly reduced by both slat configurations compared to the baseline airfoil. The S-6 slat configuration was observed to have better lift and moment characteristics at high angles of attack than S-1. Although these trends were modeled adequately by the CFD simulations, the delay in stall predictions were still present.
6. The predictions from the coupled CFD-CSD simulation showed good qualitative and quantitative correlation with flight test data for the baseline UH-60A rotor operating at a high-altitude, high-thrust flight condition (C9017). A grid convergence study showed that $\frac{1}{4}^\circ$ time step and grid size

of $133 \times 130 \times 61$ was sufficient to capture the salient airload trends in flight test data. Consequent analysis of the flow physics explained the observed trends in airload time histories.

5.2.3 Rotor Performance Improvement using LE Slats

After the coupled CFD-CSD platform was validated, it was successfully used to analyze and show the favorable effects of LE-Slats in dynamic stall alleviation. The following presents a few observations and conclusions from the analysis.

1. It was observed that the use of fixed-shaft angle trim (or wind tunnel trim) allowed the simulation to capture the pitching moment predictions during dynamic stall better. For example, the second moment stall cycles at the outboard stations are better captured in wind tunnel trim analysis than free flight trim. The inability of free-flight trim to capture the moment stall as accurately as wind tunnel trim is possibly because of the low-fidelity modeling of the fuselage, empennage and the tail rotor in the comprehensive helicopter model.
2. Dynamic stall is a high thrust phenomenon on rotors in forward (and maneuver) flights. The effect of thrust setting on rotor airloads demonstrated that dynamic stall could be eliminated with sufficient reduction in thrust values.
3. Static slat configurations (S-1 and S-6) are highly effective in mitigating the severity of the dynamic stall at the C9017 flight condition. With the modified UH-60A blade geometry with slats, the dynamic stall events for the C9017 flight condition are completely eliminated. This is accompanied

by upto 73% reduction in the peak-to-peak values of the vibratory ($4 - 17/rev$) root torsional load and upto 62% reduction in peak-to-peak values of pitch link loads.

4. Three different slat actuation strategies with various combinations of higher harmonic content (up to $[1, 3, 5]/rev$), were studied, first for the 2-D pitching airfoil and then for the actual rotor, to show the effectiveness of dynamic slat actuation on dynamic stall suppression. Higher harmonic content during dynamic slat motion on pitching airfoil ensured that its airload characteristics were comparable with that of S-1 and S-6 configurations at corresponding extreme up and down slat positions, respectively. This motivated its use in the full scale rotor study later. The $1/rev$ slat actuation was found to perform relatively better than other higher harmonic actuations. Overall it was observed that, the dynamic slat actuation did not necessarily out perform the static slat configurations in terms of overall rotor performance improvement.
5. Use of slat S-6 position allowed achieving higher thrust values (upto 10% higher) beyond the thrust limit value ($C_T/\sigma = 0.1325$) of flight condition C9017. Presence of slat S-6 alleviated dynamic stall occurring at these larger thrust settings and still allowed the rotor to trim by sustaining attached flow and sufficient lift till larger blade section angles. The attenuated dynamic stall events was apparent from the reduced peak-to-peak values of the vibratory root torsional loads (upto 54%) as well as the pitch link loads (upto 32%) even at the 10% higher thrust flight condition. Besides pushing the flight envelope of the rotor, the use of the slat also resulted in improving the rotor performance at these higher thrust values.

Even at the baseline thrust level, the L/De value of the slatted rotor was found to be 65% larger than the baseline rotor.

5.3 Significance of the Work

The present work contributes not only towards the improvement of the methodology development of the CFD solver, but also on validating and understanding the fundamentals of the physical mechanism involved in a MEA analysis. A brief description of the significance of the work is:

1. Methodology Development:

- (a) An existing coupled CFD/CSD solver was extended to incorporate the capability to analyse an MEA design, namely, an airfoil with LE-slat. Dynamically moving LE Slat on a helicopter blade was also successfully implemented.
- (b) For improved connectivity across meshes in the overset frame work required for the multi-element bladed rotor, an efficient hole cutting procedure, Implicit Hole Cutting (IHC), was implemented. The hole cutting procedure was also optimized by appropriate parallel implementation.
- (c) A generalized force transfer routine for an MEA configuration was also developed.

2. Computational validation and determining physical mechanisms and benefits:

- (a) Improved prediction and understanding of two dimensional MEA airfoils as well as a three dimensional rotor (UH60 flight test case C9017) undergoing dynamic stall phenomena was obtained with the improved aerodynamic modeling. This included realizing the need for accurate modeling of turbulence and turbulence transition for improved prediction of the solver.
- (b) Static and dynamic LE slat mechanisms were implemented to mitigate and/or eliminate rotor dynamic stall.
- (c) Increase in stall margin was determined. Moreover, performance and pitch link load as well as torsional load benefits were also quantified.

5.4 Recommendations and Future Work

The present study demonstrates the robustness of the computational methodology for reliable prediction of a slatted-rotor aerodynamics, and its usefulness as a design tool to determine the optimum amplitude and phasing of dynamic slat actuation for stall alleviation in rotorcraft applications. However, certain aspects of the analysis can be improved. These improvements and recommendations for future studies are discussed in this section.

Regarding methodology, the following are recommended:

1. Present study assumed fully turbulent flow for all its analyses. However, as noted in Chapter 3, an appropriate turbulent transition model would help predict the flow better. Future studies, especially involving a 2-D pitching airfoil experiencing dynamic stall, should use transition modeling for better prediction of dynamic stall, dynamic stall vortex strength and

related physics.

2. Implicit hole cutting can be further improved by incorporating an improved donor search algorithm, which is one of the computationally most expensive steps. Further, the hole cutting procedure needs to be parallelized to overcome a computational bottle neck.
3. The slat inertia effect as well as its own structural modeling is required to simulate a more correct slat effect in a coupled CFD/CSD framework.

From the present study, the following suggestions can be made regarding the use of a slat in rotor performance improvements:

1. A static slat appears to be nearly as effective as the dynamically moving slat in rotor performance enhancement, i.e. in terms of stall alleviation, reduction in pitch link and torsional moment loads.
2. For a dynamically moving slat, it appears that higher harmonic slat actuation is no more efficient than $1/rev$ actuation. The static slat configuration S-6 is more efficient than either static S-1 or dynamic slat actuation strategies regarding overall rotor performance improvement.

5.4.1 Future Work

The present CFD/CSD analysis tool handling MEA airfoil can be used for the following future studies:

1. Perform detailed thrust sweeps to determine new stall boundaries.
2. Study slat edge effects through appropriate grid refinement strategies.

3. Perform an advance ratio sweep to determine if there exists any performance penalty at high advance ratios with the static or moving slat.
4. Obtain optimum amplitude and phasing of dynamic slat actuation for dynamic stall alleviation as well as structural load and vibration reductions.
5. Explore the use of moving slat actuations for achieving higher thrust and expanding flight envelope.

Appendix A

LE-Slat versus Other High-lift Devices: A Numerical Investigation

Besides LE-Slat, some other active control devices that have gained popularity in recent years are: Trailing Edge Flap (TEF) and drooping leading edge device (a deforming leading edge concept). As mentioned earlier, thrust capability of a rotor can be evaluated to a reasonable extent from its blade airfoil load characteristics. Therefore, the above mentioned high-lift devices are compared with a LE-Slat on the basis of their static flow characteristics. To get a quantitative estimate of their relative performance, these devices are judged on their relative lift-to-drag ratio properties, static stall characteristics and suction pressure peak relief capabilities using a simple numerical experiment.

For the numerical experiment, an SC2110 airfoil in a fully turbulent free stream Mach number of $M = 0.3$ and Reynold number $Re = 4.14$ million is considered. This represents a typical flow condition encountered by a blade mid-span station on the retreating side of a rotor in forward flight. The trailing edge flap considered has a 10% chord flap deflected down by 10° . The drooping LE has its 10% chord near leading edge drooped down by 10° . For slatted airfoil,

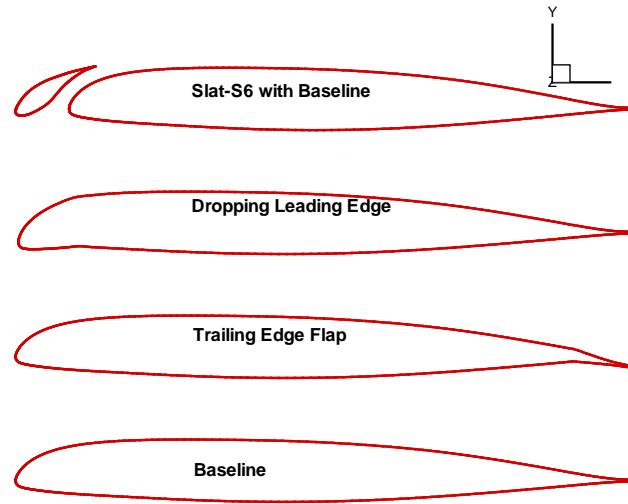


Figure A.1: Various high lift devices

a so called S-6 slat configuration (originally designed at UTRC) is considered (see Figs.A.1). Figure A.2 compares airloads for these devices for an angle of attack range of, $\alpha \in [4^\circ : 24^\circ]$. These figures clearly demonstrate that a LE-slat has the best static airfoil characteristics among the three devices considered when evaluated in terms of the following airfoil characteristics:

- **Lift-to-drag ratio (L/D):**

- A TEF provides increased lift through improved circulation due to the camber effect resulting from the flap deflection. But, the large drag penalty at larger angles of attack (α) results in reduced L/D .
- A drooping LE provides only moderate lift improvement but incurs large drag even at lower angles, which results in its low L/D values.
- A LE slat results in significant L/D improvement. Besides producing extra lift as a separate blade element (due to the presence of more

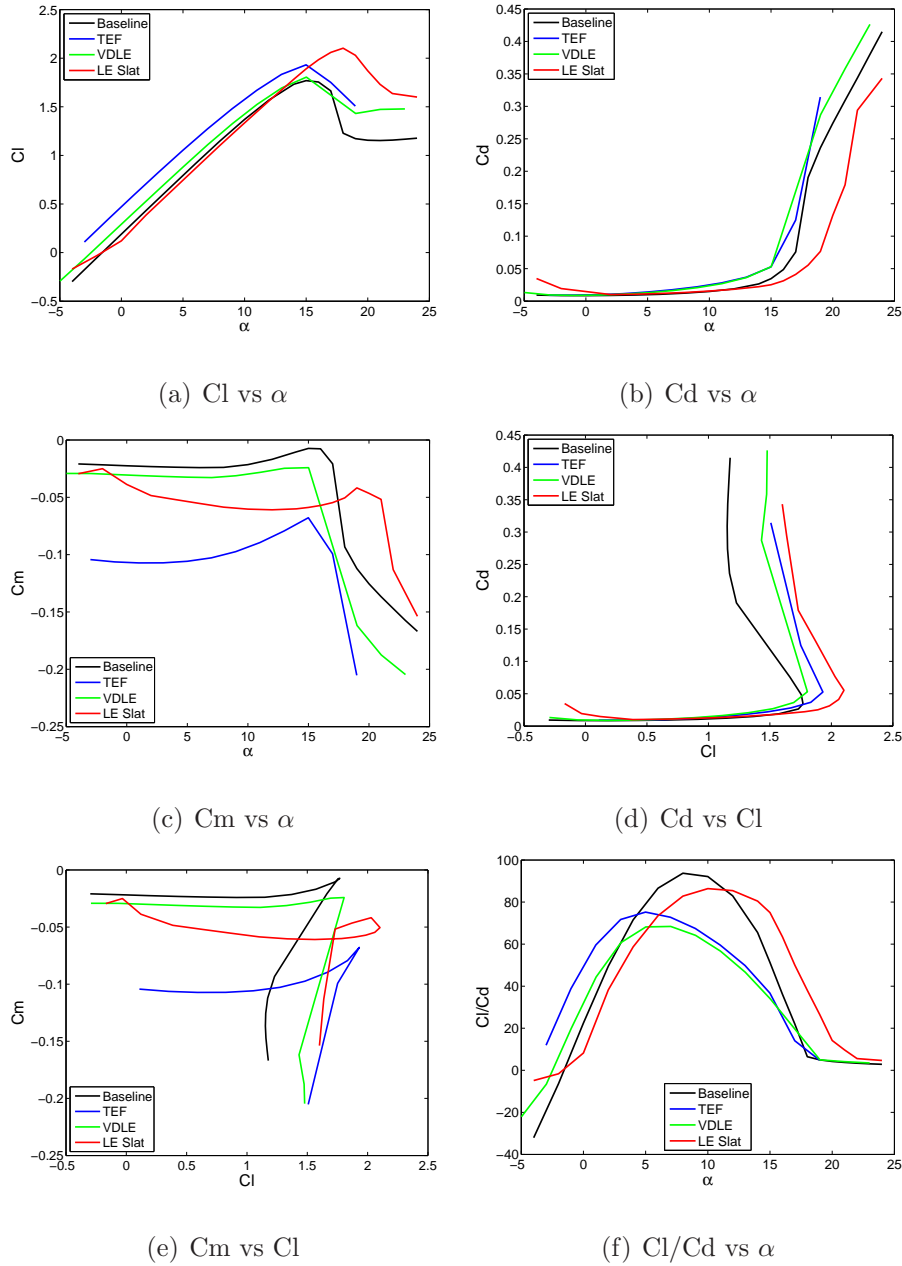
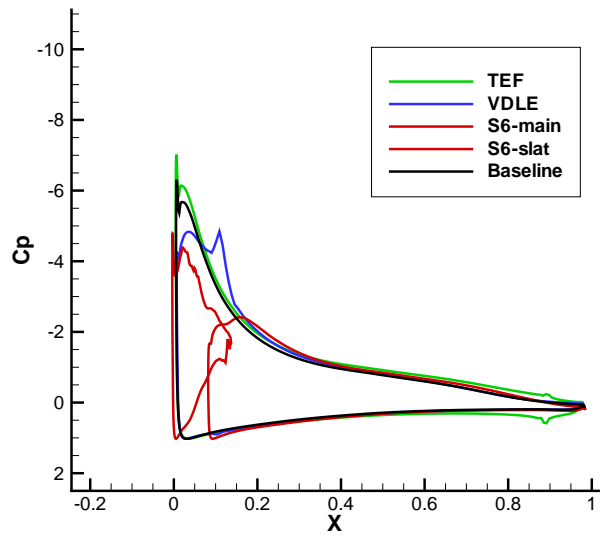
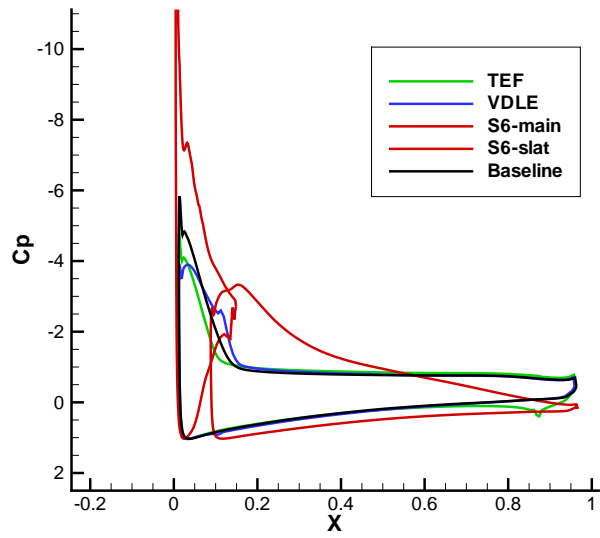


Figure A.2: Comparing airloads on various high lift devices ($M = 0.3, Re = 4.14 \times 10^6$)

than one boundary layer), the slat also incurs low drag penalty and sustains larger lift even at larger angles.



(a) C_p at $\alpha = 12^\circ$



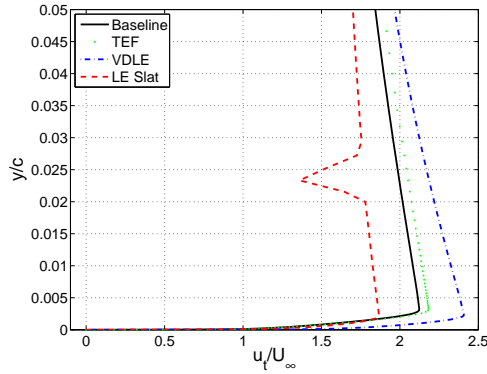
(b) C_p at $\alpha = 18^\circ$

Figure A.3: C_p on various high lift devices at free stream $M = 0.3, Re = 4.14 \times 10^6$

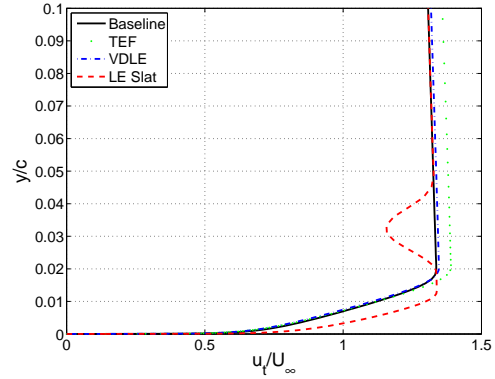
- **Suction pressure peak relief** (see Fig A.3)
 - A TEF only indirectly augments the fluid momentum near the leading edge through circulation. Therefore, the suction pressure peak remains high at large angles. Because of this, there is a sharp drop in the suction pressure, which leads to a severe stall event.
 - A drooping LE helps in only delaying the adverse pressure gradient by turning the flow through its leading edge droop, but cannot avoid large suction pressure peak and subsequent sharp drop of suction pressure at larger angles.
 - A LE slat through its favorable 'slat effects' reduces the suction pressure peak near the main element LE. Thus, the slat relieves the main element off of large suction peak, and the flow remains more attached even at larger angles.

- **Static stall characteristics**
 - A TEF has larger lift at lower angles but shows earlier stall compared to the baseline airfoil. It also incurs largest drag and moment loads.
 - A drooping LE has mild stall and separation delay with very little lift and drag advantages.
 - A LE-slat demonstrates best stall behavior: a) it delays the stall to the maximum angle, b) it has largest lift near stall, and c) it has minimum drag and moment penalty at higher angles.

- **Boundary layer profile** (see Figs. A.4 and A.5)

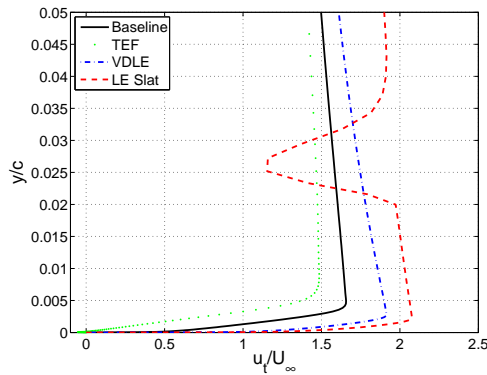


(a) $u_t/U_{\infty bl}$ at 10% chord

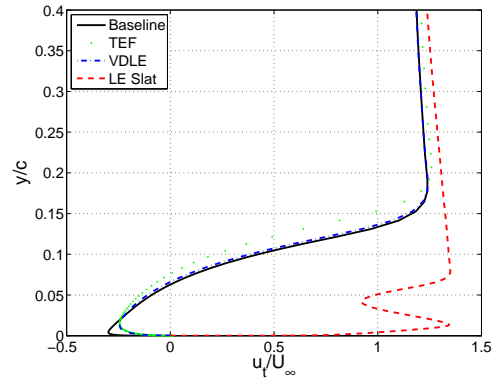


(b) $u_t/U_{\infty bl}$ at 50% chord

Figure A.4: Boundary layer profile on various high lift devices at $M = 0.3$, $Re = 4.14 \times 10^6$, $\alpha_{eff} = 12.0^\circ$



(a) $u_t/U_{\infty bl}$ at 10% chord



(b) $u_t/U_{\infty bl}$ at 50% chord

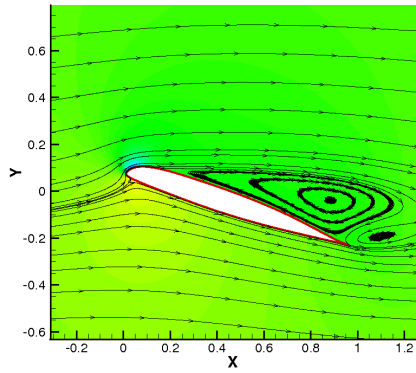
Figure A.5: Boundary layer profile on various high lift devices at $M = 0.3$, $Re = 4.14 \times 10^6$, $\alpha_{eff} = 18.0^\circ$

- Boundary layer profiles further explain how a TEF, compared to the baseline airfoil, help accelerate the flow only marginally and only at lower angles (e.g. at $\alpha_{eff} = 12^\circ$). At larger angles (e.g. at $\alpha_{eff} = 18^\circ$), it is totally ineffective and in fact, results in early leading edge stall (see Fig. A.5(a)).
- A drooping LE helps accelerate the flow near the leading edge, and

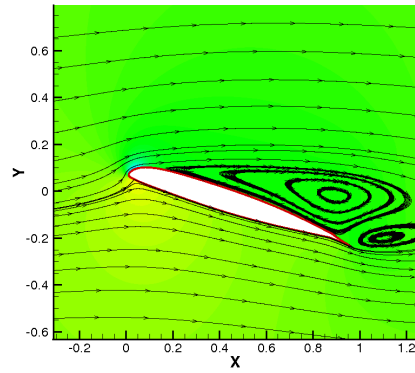
to a small extent even farther aft of the airfoil (i.e. at 50% chord), till large angles of attack. Although it is more effective than the TEF in maintaining accelerated flow near the leading edge, it still can not avoid separation and stalled flow at large angles (e.g. at $\alpha_{eff} = 18^\circ$). See Fig. A.5(b)).

- A LE-slat is the most effective device in maintaining attached flow through very large angles. As Fig. A.5 shows, the flow is separated for all the devices except for the LE-slat. Favorable 'slat effects' relieve the suction pressure peak on the main element LE. Moreover, the CBL, developed due to the slat wake interaction with the main element BL, is effective in the off-surface pressure recovery above the main element. These two slat flow features are effective in reducing separation. Figure A.6, which compares streamlines for all the devices at $\alpha_{eff} = 18^\circ$, exemplify the improved attached flow capability of a slatted airfoil compared to other devices.

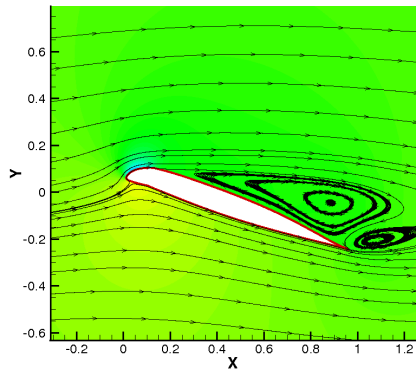
The numerical experiment discussed above demonstrates that a LE-Slat has the best steady airfoil characteristics among the existing major control devices, especially TEFs and deforming leading edge devices. In the following sections, the slat effectiveness is further investigated in dynamic flow conditions.



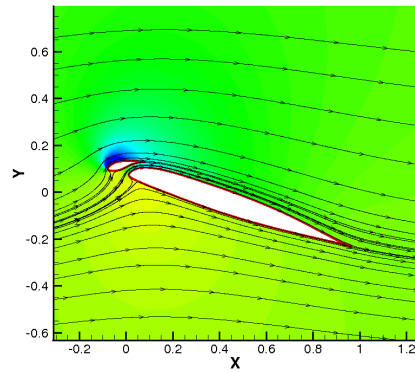
(a) Baseline



(b) TEF



(c) VDLE



(d) Slat-6

Figure A.6: Stream lines on various high lift devices at $M = 0.3$, $Re = 4.14 \times 10^6$, $\alpha_{eff} = 18.0^\circ$

Appendix B

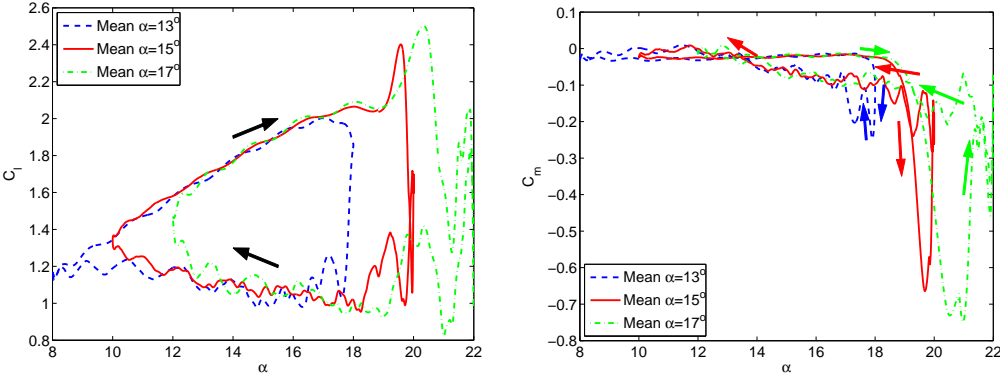
Numerical Studies of the Unsteady Effects in a Pitching Airfoil

This chapter carries out numerical studies of the unsteady effects of a moving slat with respect to the main airfoil on the airfoil dynamic stall. But, before evaluating the effectiveness of a slat in alleviating dynamic stall, it is valuable to understand the effects of the free stream angle of attack on the properties of dynamic stall.

B.1 Effect of Varying Mean Pitching Angle

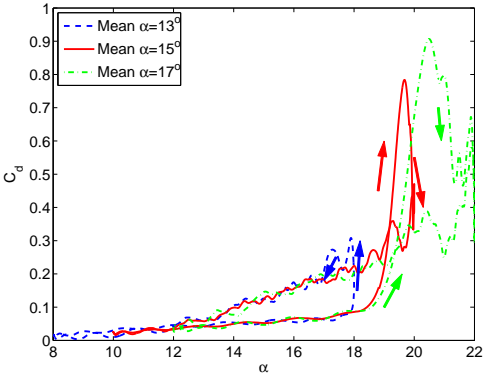
Figure. B.1 shows the effect of a mean pitching angle on the dynamic stall on a baseline airfoil. It is clearly observed that with increasing mean angle, the dynamic stall events get stronger and ‘deeper’ because of stronger vortex shedding. In all the cases, the airload values are comparable to each other in the attached region before stall. Invariably, the hysteresis effects of the airloads get larger with increasing mean pitch angle. It must be noted here that the lowest mean angle produces a clock-wise moment loop resulting in a negative torsional damping

factor, but with larger mean angles the moment loops become counter-clockwise, thereby providing more positive torsional damping; a negative torsional damping promotes aerolastic divergence or flutter. The drag hysteresis effects are similar to the pitching moment hysteresis effects. The general conclusion from this numerical experiment is that, a reduced mean angle is overall more favorable in ameliorating dynamic stall.



(a) C_l versus α

(b) C_m versus α



(c) C_d versus α

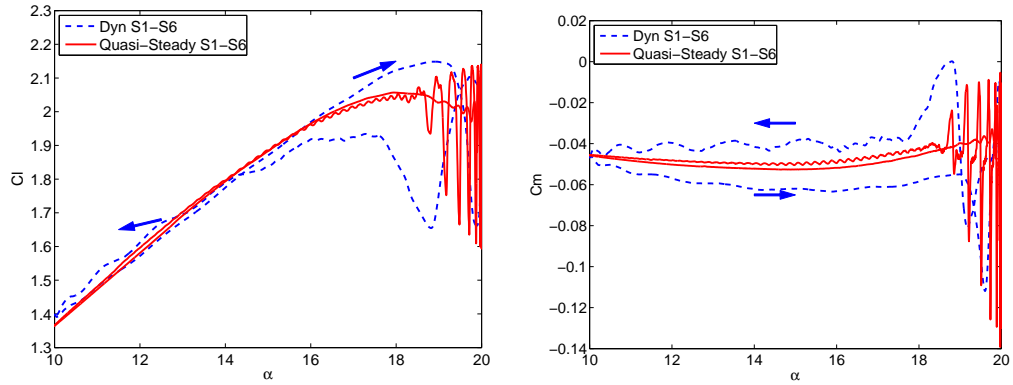
Figure B.1: Effect of varying mean angle of pitching

B.2 Quasi-steady Versus Dynamic Slat Actuation

Figure B.2 compares the dynamic slat actuation with pitching airfoil with the corresponding quasi-steady run. As expected the quasi-steady airloads show very small or no hysteresis effects at all, i.e. the upstroke and down stroke airload values do not show any unsteady effects. Although at larger angles of attack near stall the flow characteristic becomes highly unsteady, the effects subside very soon after the angle is lower than the maximum value. The flow reattaches much sooner than the case of unsteady pitching. Another noteworthy observation is that the airload values from quasi-steady run are almost always bounded by those from unsteady run. This figure demonstrates the combined unsteady effect of moving slat on a pitching airfoil.

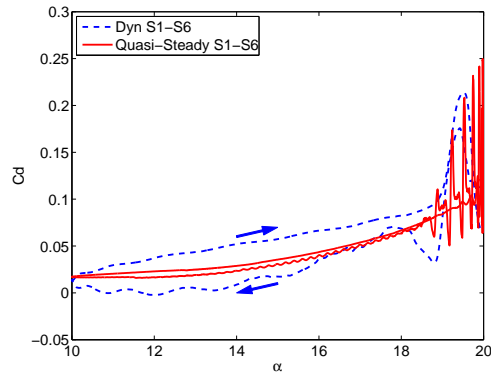
B.3 Unsteady Effect of Slat Actuation

To clearly understand the favorable effects of slat actuation, it would be more appropriate to see how the flow physics and the airload characteristics vary with the motion of just the slat while the main element stays stationary. To carry out this numerical experiment, the slat is actuated between the S-1 and S-6 positions with reduced frequency of $k = 0.07$ at a free stream conditions of $M = 0.3$ and $Re = 4.14 \times 10^6$. The unsteady effects are examined at three different free stream angles of attack, i.e. at $\alpha = [0^\circ, 10^\circ, 15^\circ]$. Figures B.3 and B.4 summarize the unsteady effects of slat actuation at these three different angles. For the ease of comparison, the mean values of airloads are removed from the plots. The abscissa represents values of slat angle α_s , which vary from $\alpha_s = -20^\circ$ at the S-1



(a) C_L versus α

(b) C_M versus α

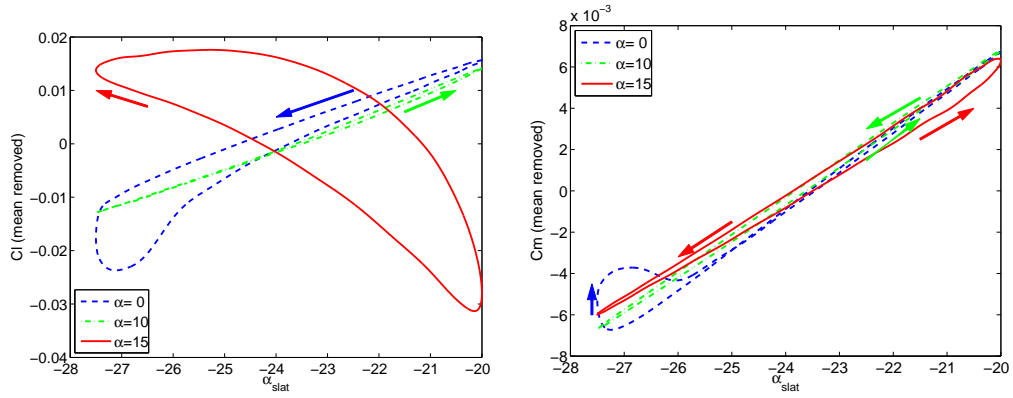


(c) C_D versus α

Figure B.2: Comparing airloads of dynamic slat actuation with corresponding quasi-steady run

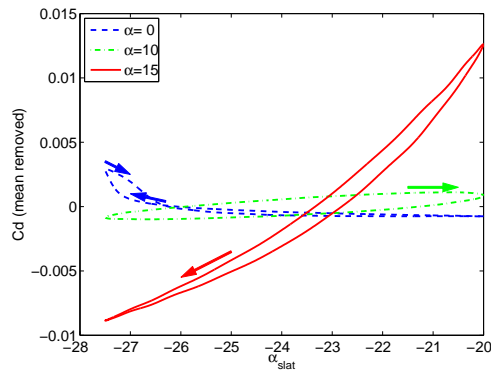
position to $\alpha_s = -27.5^\circ$ at the S-6 position. Figure B.3(a) shows the hysteresis loop direction changes from counter clockwise at the lowest angle ($\alpha = 0^\circ$) to clockwise at the maximum angle ($\alpha = 15^\circ$). The figure also shows that at lower free stream angles, the S-1 configuration has better lift characteristics than the S-6 configuration, but at larger free stream angle, the S-6 configuration becomes a more effective lifting element than the S-1 configuration.

Similar to the lift time history, the drag and moment airloads also show reversal of the direction of hysteresis loop from clockwise to counter clockwise



(a) C_L (mean removed) versus α_s

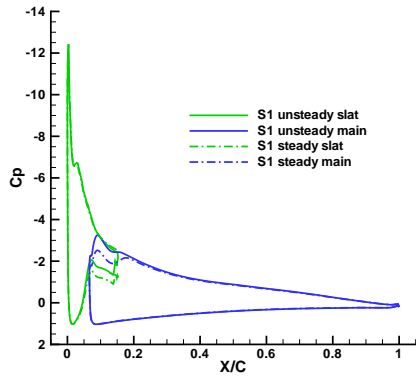
(b) C_M (mean removed) versus α_s



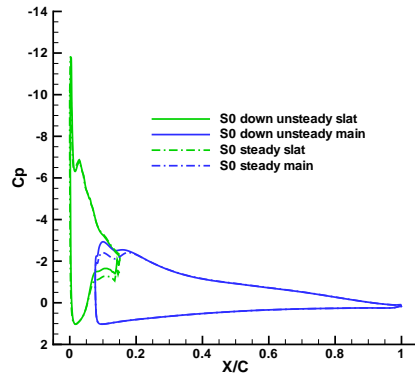
(c) C_D (mean removed) versus α_s

Figure B.3: Comparing mean removed airloads of unsteady slat on static main airfoil at $\alpha = [0^\circ, 10^\circ, 15^\circ]$

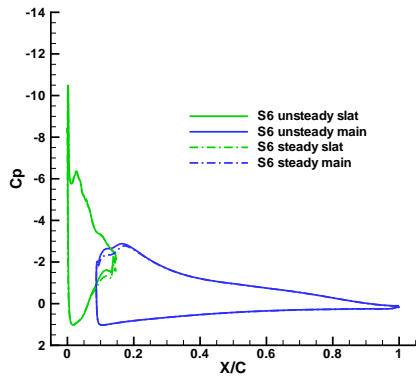
with increasing free stream angles. The hysteresis effects, however, are more limited than what was found in the lift time histories. The counter clockwise loops in moment plot suggest positive aerodynamic torsional damping at larger angles ($\alpha = [10^\circ, 15^\circ]$). Comparing relative behavior of the slat at positions S-1 and S-6 during actuation cycle it is noted that, invariably the slat at the S-6 position incurs larger nose-down pitching moment throughout the range of free stream angles. The drag characteristics at these two slat positions, however, are dependent upon the free stream angle; for example, at lower angles the slat



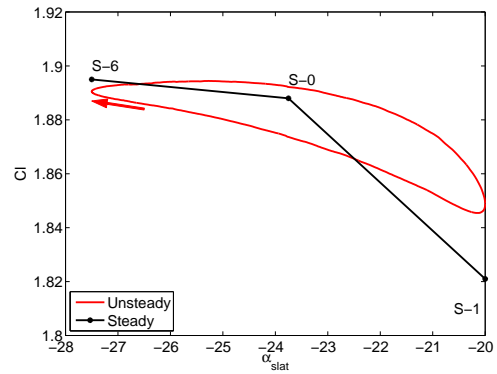
(a) C_p for S1



(b) C_p for S0 down stroke



(c) C_p for S6



(d) C_l versus α_s

Figure B.4: Comparing C_p and lift values of unsteady slat on static main airfoil with steady values of the corresponding slat configurations at $\alpha = 15^\circ$

position at S-1 results in lower drag loss, whereas at larger angles the drag loss is minimum at the S-6 position.

In general, the above investigation on the unsteady effects of slat reveals that, more favorable airload characteristics of S-6 slat configuration is found at larger free stream angles, and that of S-1 is found at lower free stream angles.

Figure B.4 compares the surface pressure values on the slatted airfoil at various stages of unsteady slat actuation with the pressure values of the corre-

sponding steady slat configurations, all at a main element free stream angle of attack at $\alpha = 15^\circ$. The difference in C_p values clearly show the unsteady effect of the slat actuation. The slat in its down stroke produces larger area under C_p curve, for both the slat and the main element, which results in an increased lift value (B.4(d)). The lift time history characteristics in Fig. B.4(d) relates well with the surface pressure characteristics of the airfoil at the corresponding slat positions during the actuation cycle. The nature of the hysteresis loop of the lift curve over the slat actuation cycle reflects the unsteady effects of the variable slat configuration.

Bibliography

- [1] Bousman, W. G., “Airfoil Dynamic Stall and Rotorcraft Maneuverability,” NASA/TM-2000-209601, AFDD/TR-00-A-008, NASA Technical Memorandum, July 2000.
- [2] Leishman, J. G., “Principles of Helicopter Aerodynamics,” Cambridge University Press, 2002.
- [3] Smith, A. M. O., “High-Lift Aerodynamics,” *Journal of Aircraft*, Vol 12, No. 6, June 1975, pp. 501–530.
- [4] Harris, T. A. and Lowry, J. G., “Pressure Distribution over an NACA 23012 Airfoil with a Fixed Slot and a Slotted Flap,” NACA-732, July 30, 1941.
- [5] Rogers, S. E., “Progress in High-Lift Aerodynamic Calculations,” 31st Aerospace Sciences Meeting & Exhibit, Reno, NV, Jan 11-14, 1993.
- [6] Rumseya, C. L. and Yingb, S. X., “Prediction of High Lift: Review of Present CFD Capability,” *Progress in Aerospace Sciences*, Vol 38, 2002, pp. 145–180.
- [7] Gauvain, W. E., “Wind-tunnel Tests of a Clark Y Wing with ”Maxwell” Leading Edge,” NACA-598, April 1937.

- [8] Davenport, F. J. and Front, J. V., "Airfoil Sections for Rotor Blades - A Reconsideration," American Helicopter Society 22nd Annual Forum, May 12, 1966, Washington, D.C.
- [9] McCloud, J. L. III and McCullough, G. B., "Wind-Tunnel Tests of a Full-Scale Helicopter Rotor with Symmetrical and with Cambered Blade Sections at Advance Ratios from 0.3 to 0.4," NASA TN 4367, September 1958.
- [10] McCroskey, W. J., "Some Current Research in Unsteady Fluid Dynamics - The 1976 Freeman Scholar Lecture," *Journal of Fluids Engineering*, Vol. 99, March 1977, pp. 8 – 387.
- [11] Carr, L. W., "Progress in Analysis and Prediction of Dynamic Stall," *Journal of Aircraft*, Vol. 25, No. 1, January 1988, pp. 6 – 17.
- [12] McCroskey, W. J., McAlister, K. W., Carr, L. W. and Pucci, S. L., "An Experimental Study of Dynamic Stall on Advanced Airfoil Sections Volume 1. Summary of Experiments," NASA TM 84245, July 1982.
- [13] McAlister, K. W., Pucci, S. L., McCroskey, W. J. and L. W. Carr, "An Experimental Study of Dynamic Stall on Advanced Airfoil Sections Volume 2. Pressure and Force Data," NASA TM 84245, September 1982.
- [14] Carr, L. W., McCroskey, W. J., McAlister, K. W., Pucci, S. L. and Lambert, O., "An Experimental Study of Dynamic Stall on Advanced Airfoil Sections Volume 3. Hot-Wire and Hot-Film Measurements," NASA TM 84245, December 1982.

- [15] Lorber, P. F., “Compressibility Effects on the Dynamic Stall of a Three-Dimensional Wing,” AIAA Paper 92-0191, AIAA 30th Aerospace Sciences Meeting, January 1992, Reno, NV.
- [16] Lorber, P. F., Carta, F. O. and Covino, A. F., “An Oscillating Three-dimensional Wing Experiment: Compressibility, Sweep, Rate, Waveform and Geometry Effects on Unsteady Separation and Dynamic stall,” AIAA Paper 91-1795, June 1991.
- [17] Piziali, R. A., “2-D and 3-D Oscillating Wing Aerodynamics for a Range of Angles of Attack Including Stall,” NASA TM 4632, USAATCOM Technical Report 94-A-011, September 1994.
- [18] Carr, L. W., and Chandrasekhara, M. S., “Compressibility effects on dynamic stall,” *Progress in Aerospace Sciences*, Vol 32, 1996, pp. 523 – 573.
- [19] Spentzos, A., Barakos, G. N., Badcock, K. J., Richards, B. E., Coton, F. N., Galbraith, R. A. McD., Berton, E. and Favier, D., “Computational Fluid Dynamics Study of Three-Dimensional Dynamic Stall of Various Planform Shapes,” *Journal of Aircraft*, Vol. 44, No. 4, July-August, 2007, pp. 1118–1128.
- [20] Brocklehurst, A. and Duque, E. P. N., “Experimental and Numerical Study of the British Experimental Rotor Programme Blade,” NASA, Ames Research Center, AIAA-1990-3008.
- [21] Fradenburgh, E. A., Jepson, W. D. and Moffitt, R. C., “Helicopter Blade With A Tip Having A Selected Combination Of Sweep, Taper AND An-

- hedral To Improve Hover Efficiency,” United States Patent 4,324,530, 13 April 1982.
- [22] Yeager, W. T., Noonan, Jr K. W., Singleton, J. D., Wilbur, M. L., and Mirick, P. H., “Performance and Vibratory Loads Data From a Wind-Tunnel Test of a Model Helicopter Main Rotor Blade With a Paddle-Type Tip,” , NASA Technical Memorandum 4754, May 1997.
- [23] Yee, K., Joo, W., and Lee, D., “Aerodynamic Performance Analysis of a Gurney Flap for Rotorcraft Application,” *Journal of Aircraft*, Vol. 44, No. 3, May - June 2007, pp. 1003–1014.
- [24] Chandrasekhara, M. S., “Compressible Dynamic Stall Performance of a Variable Droop Leading Edge Airfoil with a Gurney Flap,” 42nd AIAA Aerospace Sciences Meeting and Exhibit 5 - 8 January 2004, Reno, Nevada.
- [25] Martin, P. B., Wilson, J. S., Berry, J. D., Wong, T.-C., Moulton, M., and McVeig, M. A., “Passive Control of Compressible Dynamic Stall,” AIAA 2008-7506, 26th AIAA Applied Aerodynamics Conference, Honolulu, Hawaii, 18 - 21 August 2008.
- [26] Karim, M., and Achyara, M., “Control of the Dynamic Stall Vortex Over a Pitching Airfoil by Leading Edge Suction,” AIAA Paper 1993- 3267, July 1993.
- [27] Yu, Y., McAlister, K., Tung, C., and Wang, C., “Dynamic Stall Control for Advanced Rotorcraft Application,” *AIAA Journal*, vol. 33, issue 2, 1995, pp. 289–295.

- [28] Lewington, N.P., Peake, D.J., Henry, F.S., Kokkalis, A. and Perry, J., “The Application of Air-Jet Vortex Generators to Control the Flow on Helicopter Rotor Blades,” private communication.
- [29] Shih, C., Beahn, J., Krothapalli, A., and Chandrasekhara, M.S., “Control of Compressible Dynamic Stall using Microjets,” Proceedings of FEDSM03 4TH ASME JSME Joint Fluids Engineering Conference, Honolulu, Hawaii, USA, July 611, 2003.
- [30] Lorber, P.F., McCormick, D. C., Anderson, T. J., Wake, B. E., MacMartin, D. G., Pollack, M. J., Corke, T. C., Breuer, K., “Rotorcraft Retreating Blade Stall Control,” AIAA- 2000-2475, FLUIDS 2000 Conference and Exhibit, Denver, CO, 19-22 June 2000.
- [31] Seifert, A., Bachar, T., Koss, D., Shepshelovich, M., and Wygnanski, I., “Oscillatory Blowing A Tool to Delay Boundary Layer Separation,” *AIAA Journal*, Vol. 31, No. 11, 1993, pp. 2052–2060.
- [32] Hassan, A. A., “Applications of Zero-Net-Mas Jets for Enhanced Rotorcraft Aerodynamic Performance,” *Journal of Aircraft*, Vol. 38, No. 3, 2001, pp. 478–485.
- [33] Traub, L. W., Miller, A. and Rediniotis, O., “Effects of Active and Passive Flow Control on Dynamic-Stall Vortex Formation,” *Journal of Aircraft*, Vol. 41, No. 2, Engineering Notes, 2003, pp. 405–408.
- [34] Fulton, M. and Ormiston, R., “Hover Testing on Small Scale Rotor with On-Blade Elevons,” *Journal of the American Helicopter Society*, Vol. 46, No. 2, 2001, pp. 96–106.

- [35] Koratkar, N. and Chopra, I., “Closed-Loop Wind Tunnel Testing of a Smart Rotor Model with Trailing-Edge Flaps,” *Journal of the American Helicopter Society*, Vol. 47, No. 4, 2002, pp. 263-272.
- [36] Roget, B. and Chopra, I., “Trailing Edge Flap Control Methodology for Vibration Reduction of Helicopter With Dissimilar Blades,” 42nd AIAA/ASME/ASCE/AHS/ASC Structures, Structural Dynamics, and Materials Conference and Exhibit, AIAA-2001-1433, Seattle, WA, 2001, pp. 16–19.
- [37] Davis, G., Feszty, D., and Nitzsche, F., “Trailing edge flow control for the mitigation of dynamic stall effects,” 31st European Rotorcraft Forum, European Rotorcraft Forum, Florence, Italy, September 12-16 2005.
- [38] Mishra, A. and Sitaraman, J. and Baeder, J. and Opoku, D. G., “Computational Investigation of Trailing Edge Flap for Control of Vibration,” 25th AIAA Applied Aerodynamics Conference, Miami, Florida, June 25-28, 2007.
- [39] Chandrasekhara, M. S., “Fluid Mechanics of Compressible Dynamic Stall Control using Dynamically Deforming Airfoils,” Final Report, U.S. Army Research Office, NAVAL Postgraduate School, Monterey, CA, Dec 4, 2001.
- [40] Sahin, M., Sankar, L. N., Chandrasekhara, M.S., and Tung, C., “Dynamic Stall Alleviation Using a Deformable Leading Edge Concept—A Numerical Study,” *Journal of Aircraft*, Vol. 40, No. 1, Jan. – Feb., 2003, pp. 77–85.
- [41] Chandrasekhara, M. S., Martin, P. B., and Tung, C., “Compressible Dynamic Stall Control Using a Variable Droop Leading Edge Airfoil, 41st

- Aerospace Sciences Meeting and Exhibit, Reno, NV, AIAA Paper 2003-48, Jan. 2003.
- [42] Kerho, M., “Adaptive Airfoil Dynamic Stall Control,” 43rd Aerospace Sciences Meeting and Exhibit, Reno, NV, AIAA Paper 2005-1365, Jan. 2005.
- [43] Martin, P. B., McAlister, K. W., Chandrasekhara, M. S., and Geissler, W., “Dynamic Stall Measurements and Computations for a VR-12 Airfoil with a Variable Droop Leading Edge,” American Helicopter Society 59th Annual Forum, AHS International, Alexandria, VA, May 68, 2003.
- [44] Carr, L. W., and McAlister, K., “The Effect of a Leading Edge Slat on the Dynamic Stall of an Oscillating Airfoil,” AIAA/AHS Aircraft Design Systems and Operation Meeting, 1983, AIAA-83-2533.
- [45] McAlister, K. W., and Tung, C., “Suppression of Dynamic Stall with a Leading-Edge Slat on a VR-7 Airfoil,” NASA Technical Paper 3357 and ATCOM Technical Report 92-A0-013, March 1999.
- [46] Noonan, K. W., Allison, D. O., and Stanaway, S., “Investigation of a Slotted Rotorcraft Airfoil at Mach Numbers from 0.20 to 0.88 at Full-Scale Rotor Reynolds Number,” AHS Aeromechanics Specialist’s Conference, San Francisco, CA, January 1994.
- [47] Noonan, K. W., Yeager, J. W. T., Singleton, J. D., Wilbur, M. L., and Mirick, P. H., “Evaluation of Model Helicopter Main Rotor Blade with Slotted Airfoils at the Tip,” Proceedings of the 55th Annual Forum of the American Helicopter Society, Montreal, Quebec, Canada, May 25-27 1999.

- [48] Carr, L. W., Chandrasekhara, M. S., Wilder, M. C., and Noonan, K. W., “Effect of Compressibility on Suppression of Dynamic Stall using a Slotted Airfoil,” *Journal of Aircraft*, Vol. 38, No. 2, April 2001, pp. 296–301.
- [49] Narramore, J., McCroskey, W. J., and Noonan, K. W. “Design and Evaluation of Multi-Element Airfoils for Rotorcraft,” Proceedings of the 55th Annual Forum of the American Helicopter Society, Montreal, Quebec, Canada, May 25 - 27 1999.
- [50] Narramore, J. C., “High-Lift Multi-Element Airfoil for Tilt Rotor Vehicles,” Proceedings of The American Helicopter Society Aerodynamics, Aeroacoustics, and Test and Evaluation Technical Specialists Meeting, San Francisco, CA, January 23-25 2002.
- [51] Yeo, H., and Lim, J. W., “Application of a Slotted Airfoil for UH-60 A Helicopter Performance,” Proceedings of The American Helicopter Society Aerodynamics, Aeroacoustics, and Test and Evaluation Technical Specialists Meeting, San Francisco, CA, January 23-25 2002.
- [52] Chaffin, M.S., “Application of Adjoint Optimization Method to Multi-Element Rotorcraft Airfoils,” Presented at the AHS Vertical Lift Aircraft Design Conference, San Francisco, CA, 2000.
- [53] Lorber, P. F., Bagai, A., and Wake, B. E., “Design and Evaluation of Slatted Airfoils for Improved Rotor Performance,” 62nd Annual Forum and Technology Display of the American Helicopter Society International, Phoenix, AZ, May 9-11 2006.

- [54] Cole, S. R., and Rivera, J. R., "The New heavy Gas Testing capabilities in the NASA Langley Transonic Dynamics Tunnel," Royal Aeronautical Society Wind Tunnel and Wind Tunnel Test Techniques Forum, Paper 4, April 1997.
- [55] Mishra, A., Ananthan, S., Baeder, J. D., Opoku, D. G., Wake, B. E., and Lin, R-S., "Coupled CFD/CSD Prediction of the Effects of Leading Edge Slat on Rotor Performance," 65th Annual Forum and Technology Display of the American Helicopter Society International, Dallas, TX, May 27 - 29, 2009.
- [56] Lee, Y., and Baeder, J. D., "Implicit Hole Cutting – A New Approach to Overset Grid Connectivity," 16th AIAA Computational Fluid Dynamics Conference, Washington, DC, June 2003.
- [57] Torok, M.S., Moffitt, R.C., Lorber, P.F., Davis, G.C.R, Bernhard, A.P.F., Welsh, W.A., and Wake, B.E., "Active Control of Multi- Element Rotor Blade Airfoils," U.S. Patent 6,769,872 B2, Aug 3, 2004.
- [58] Torok, M. S., Moffitt, R. C., Bagai, A., "Active Control of Multi- Element Rotor Blade Airfoils," U.S., Patent 6,932,569 B2, August 23,2005.
- [59] Bernhard, A.P.F., Torok, M.S., Moffitt, R.C., Lorber, P.F., Davis, G.C.R,, Welsh, W.A., and Wake, B.E., "Directional Elastomeric Coupler," US Patent 6,666,648, Dec 2003.
- [60] White, F. M., "Viscous Fluid Flow," McGraw-Hill, 1991.

- [61] Srinivasan, G. R., and Baeder, J. D., "TURNS: A Free-wake Euler/ Navier-Stokes Numerical Method for Helicopter Rotors," *AIAA Journal*, Vol. 31, No. 5, May 1993, pp. 959–961.
- [62] Lakshminarayan, V. K., "Computational Investigation of Micro-Scale Coaxial Rotor Aerodynamics in Hover," Ph.D. Dissertation, Department of Aerospace Engineering, University of Maryland at College Park, 2009.
- [63] Hinze, J. O., "Turbulence," McGraw-Hill Series in Mechanical Engineering, 1975.
- [64] Duraisamy, K. and Sitaraman, J. and Baeder, J., "High Resolution Wake Capturing Methodology for Accurate Simulation of Rotor Aerodynamics," 61st Annual Forum of the American Helicopter Society, Dallas, Texas, June 8-11, 2005.
- [65] Roe, P., "Approximate Riemann Solvers, Parameter Vectors and Difference Schemes," *Journal of Computational Physics*, Vol. 135, No. 2, August 1997, pp. 250–258.
- [66] Vatsa, V.N., and Thomas, J.L., and Wedan, B.W., "Navier-Stokes Computations of Prolate Spheroids at Angle of Attack," AIAA Paper 87-2627, Aug. 1987.
- [67] Van Leer, B., "Towards the Ultimate Conservative Difference Scheme V. A Second-Order Sequel To Godunov's Method," *Journal of Computational Physics*, Vol. 135, No. 2, August 1997, pp. 229–248.

- [68] Jameson, A., and Yoon, S., “Lower-Upper Implicit Schemes with Multiple Grids for Euler Equations,” *AIAA Journal*, Vol. 25, No. 7, July 1987, pp. 929-935.
- [69] Yoon, S. and Jameson, A., “Lower-Upper Symmetric-Gauss-Seidel Method for Euler and Navier-Stokes Equations,” *AIAA Journal*, Vol.26, 1988, pp. 1025-1026.
- [70] Koren, B., “Upwind Schemes, Multigrid and Defect Correction for the Steady Navier-Stokes Equations,” Proceedings of the 11th International Conference on Numerical Methods in Fluid Dynamics, Williamsburg, VA, June 1988.
- [71] Hoffman, K. A., and Chiang, S. T., “Computational Fluid Dynamics, Vol. 2,” EES Books, 2000.
- [72] Pulliam, T., “Time Accuracy and the use of Implicit Methods,” 11th AIAA Computational Fluid Dynamics Conference, AIAA Paper 1993-3360, Orlando, FL, July 1993.
- [73] Baldwin, B., and Lomax, H., “Thin Layer approximation and Algebraic Model for Separated Flows,” 16th AIAA Aerospace Sciences Meeting, AIAA paper 1978-257, Huntsville, AL, January 1978.
- [74] Durbin, P., “A Reynolds Stress Model for Near Wall Turbulence,” *Journal of Fluid Mechanics*, Vol. 249, 1993, pp. 465-498.
- [75] Srinivasan, G.R., Ekaterinaris J. A., and McCroskey, W. J., “Evaluation of Turbulence Models for Unsteady Flows of an Oscillating Airfoil,” *Computers and Fluids*, Vol. 24, No. 7, 1995, pp. 833–861.

- [76] Spalart, P. R. and Allmaras, S. R., “A One Equation Turbulence Model for Aerodynamics Flow,” AIAA Paper 1992-0439, 1992.
- [77] Menter, F. R. , “Two-Equation Eddy-Viscosity Turbulence Models for Engineering Applications,” AIAA Journal, Vol. 32, No 8., 1994, pp. 1598–1605.
- [78] Barth, T. J., Puliam, T. H., and Buning P. G., “Navier-Stokes Computations for Exotic Airfoils,” 23rd AIAA Aerospace Sciences Meeting, AIAA Paper 1985-0109, Reno, NV, January 1985.
- [79] Gupta, V., “An Investigation of Quad Tilt Rotor Aerodynamics in Helicopter mode,” Ph.D. Dissertation, Department of Aerospace Engineering, University of Maryland at College Park, 2005.
- [80] Duraisamy, K., “Studies in Tip Vortex Formation, Evolution and Control,” Ph.D. Dissertation, Department of Aerospace Engineering, University of Maryland at College Park, 2005.
- [81] Chopra, I. and Bir, G., “University of Maryland Advanced Rotor Code: UMARC,” American Helicopter Society Aeromechanics Specialists Conference, San Francisco, January, 1994.
- [82] Sitaraman, J., “CFD Based Unsteady Aerodynamic Modeling for Rotor Aeroelastic Analysis,” Ph.D. Dissertation, Department of Aerospace Engineering, University of Maryland at College Park, 2003.
- [83] Tung, C. and Caradonna, F. X. and Johnson, W., “Conservative Full Potential Model for Unsteady Transonic Rotor Flows,” AIAA Journal, Vol.25, No.2, 1987, pp. 193–198.

- [84] Datta, A., “Fundamental Understanding, Prediction and Validation of Rotor Vibratory Loads in Steady Level Flight,” Ph.D. Dissertation, Department of Aerospace Engineering, University of Maryland at College Park, 2004.
- [85] Lee, Y., “On Overset Grids Connectivity and Automated Vortex Tracking in Rotorcraft CFD,” Ph.D. Dissertation, Department of Aerospace Engineering, University of Maryland at College Park, 2008.
- [86] Bousman, W. G. and Kufeld, R. M., “UH-60A Airloads Catalog,” NASA/TM-2005-212827, August 2005.
- [87] Frank J. McHugh, “What Are the Lift and Propulsive Force Limits at High Speed for the Conventional Rotor?”, American Helicopter Society 34th Annual National Forum, May 15 - 17, 1978, Washington, D.C.
- [88] Datta, A. and Chopra, I., “Prediction of UH-60A Dynamic Stall Loads in High Altitude Level Flight using CFD/CSD Coupling,” Proceedings of the 61st Annual Forum of the American Helicopter Society, June 1-3, 2005, Grapevine, TX.
- [89] Datta, A., Nixon, M., and Chopra, I., “Review of Rotor Loads Prediction with the Emergence of Rotorcraft CFD,” Journal of the American Helicopter Society, Vol. 52, (4), October 2007, pp. 287–217.
- [90] Sitaraman, J., Datta, A., Baeder, J. and Chopra, I., “Coupled CFD/CSD Prediction of Rotor Aerodynamic and Structural Dynamic Loads for Three Critical Flight Conditions,” 31st European Rotorcraft Forum, Florence, Italy, September 13-15, 2005.

- [91] Potsdam, M., Yeo, Hyeonsoo, and Johnson, W. “Rotor Airloads Prediction using Loose Aerodynamic/Structural Coupling,” Proceedings of the 60st Annual Forum of the American Helicopter Society, June 7-10, 2004, Baltimore, MD.
- [92] Ananthan, S. and Baeder, J. D. and Sitaraman, J. and Hahn, S. and Iaccarino, G., “Hybrid Unsteady Simulation of Helicopters: HUSH,” 26th AIAA Applied Aerodynamics Conference, Honolulu, Hawaii, August 18-21, 2008.